

**SYNTHESIS OF NANOSTRUCTURED SILICA FOR USE  
AS A SUPPORT FOR IRON FISCHER-TROPSCH  
CATALYSTS**

**KENEILOE KHOABANE**

**SYNTHESIS OF NANOSTRUCTURED SILICA FOR USE  
AS A SUPPORT FOR IRON FISCHER-TROPSCH  
CATALYSTS**

**KENEILOE KHOABANE**

A thesis submitted to the Faculty of Science, University of the Witwatersrand,  
Johannesburg, in fulfilment of the requirements for the degree of **Doctor of  
Philosophy**

Johannesburg, 2007

## **DECLARATION**

I declare that this thesis is my own, unaided work. It is being submitted for the degree of Doctor of Philosophy in the University of the Witwatersrand, Johannesburg. It has not been submitted before for any degree or examination in any other University.

---

Keneiloe Khoabane

22<sup>nd</sup> Day of May 2007

## **ABSTRACT**

Nanostructured silica materials were synthesised by the sol-gel process using simple hydroxyacids as template precursors, and these materials were employed as supports for a low temperature iron Fischer-Tropsch (FT) catalyst. Thus, this thesis is divided into two parts: (I) the synthesis of nanostructured silica gels, and (II) their use as catalyst supports in the FT reaction.

## **PART I**

The effects of synthesis conditions, acidic and basic template precursors and their amounts, synthesis temperature, duration of hydrolysis and ageing, solvent concentration, organic co-solvent, and the synthesis procedure used on the morphology of the silica materials were studied. The synthesised silica gels were characterised by TEM, SEM, BET, TGA, and XRD.

Mixtures of different morphologies were obtained with all the hydroxyacids used and the studies revealed that the morphology of the resultant silica gels was largely determined by the type of the hydroxyacid used. The use of oxalic acid produced materials with 4-9 % micropores and a mixture of meso- and macropores mainly consisting of hollow tubes and hollow spheres; the use of D-gluconic and L-tartaric acids produced mesoporous materials mainly consisting of hollow spheres and sheets with folds, respectively; while the use of stearic and cinammic acids produced macroporous materials mainly consisting of solid spheres and undeveloped particles, respectively. The silica gels formed were found to be amorphous in nature, despite the different morphologies that existed in them, and were also thermally stable.



Studies involving the use of oxalic and D-gluconic acids showed that the key to the shape of the resultant morphologies resided in the shape of the template crystals formed in solution under specific synthesis conditions. The template shape depended on the type of the template precursor (i.e. both the acid and the base) and its amount. It was also observed that under certain conditions, both at elevated temperatures ( $\geq 55\text{ }^{\circ}\text{C}$ ) and at high water concentrations ( $> 50\%$ ), the template dissolved and this led to low yields of shaped morphologies (i.e. hollow spheres and tubes). The solvent concentration to produce a maximum tube yield (in the case of oxalic acid) and hollow sphere yield (in the case of D-gluconic acid) was found to require about 25-50 % water. Very well-developed tubes were also obtained at this concentration (i.e. with oxalic acid).

Long hydrolysis and ageing times (i.e.  $> 2\text{ h}$ ) of the sols and gels, respectively, resulted in the formation of surface attached colloidal particles and of tubes and hollow spheres with decreased wall thicknesses. Pre-formation of the template prior to addition of TEOS produced materials with lower surface areas, higher tube yields and bigger tube sizes when compared with materials synthesised by forming the template together with the silica gel.

## **PART II**

Two types of silica gels were used as supports for an iron FT catalyst; the nanostructured silica gels (tubes with surface area  $109\text{ m}^2/\text{g}$  and spheres with surface area  $245\text{ m}^2/\text{g}$ ) and a commercial silica gel (Davisil silica, surface area  $273\text{ m}^2/\text{g}$  - consisting of undeveloped particles). The effect of varying the potassium promotion levels and of the support morphology on the catalyst activity and selectivity in the FT reaction was studied at  $250\text{ }^{\circ}\text{C}$ , in a slurry operated CSTR.

It was observed that an increase in the potassium loading up to 0.5 wt % in the Davisil silica catalyst led to a decrease in the catalyst FT and water gas shift (WGS) activity, and methane selectivity. However, the efficiency of the catalyst to produce hydrocarbons increased with an increase in potassium loading up to 0.5 wt %. Increasing the potassium level up to 0.9 wt % led to a slight increase in both the catalyst activity and methane selectivity, and a decrease in the catalyst efficiency. For the silica tubes catalyst, increasing the potassium loading to 0.5 wt % led to an increase in the catalyst activity and methane selectivity, while increasing the potassium level up to 0.9 wt % led to a decrease in the catalyst activity. For both supports, increasing the potassium loading led to an increase in the selectivity towards high molecular weight hydrocarbons, olefins (relative to paraffins) and terminal olefins (relative to internal olefins).

While the Davisil silica and the silica tube catalysts remained more or less stable throughout the reaction, the activity of the silica spheres catalyst declined rapidly with time. The nanostructured silica gel supported catalysts both showed higher activities and methane selectivities, but lower efficiencies when compared to the Davisil silica catalyst. Although the selectivity of all three catalysts towards olefins were similar, their selectivity towards high molecular weight hydrocarbons decreased in the order Davisil silica > silica spheres > silica tubes. Elongated needle-like Fe nanoparticles (NPs) were obtained in the silica tubes catalyst, semi hexagonal Fe NPs were formed in the silica spheres catalyst, while the Fe NPs could not be distinguished from the support in the Davisil silica catalyst.

After the reaction, the surface areas of all three catalysts were found to have decreased and the catalysts to have sintered. The nanostructured silica supported catalysts showed the presence of Fe nanozones surrounded by a layer of amorphous carbon, while only agglomerated particles of Fe and some carbon rich regions were observed in the Davisil silica catalyst. No evidence of alteration of the morphology of the nanostructured silica supports was observed after the reaction.

*This thesis is dedicated to my parents;*  
*Ben Buti and Seanokeng Johanna Khoabane*

## ACKNOWLEDGEMENTS

I would like to express my sincere gratitude to the following people:

My supervisor; Prof. Neil John Coville, for giving me the opportunity to learn from him, for his priceless support, patience, guidance, countless suggestions and undivided attention. Prof, your knowledge of catalysis, materials chemistry and chemistry in general will never cease to inspire me.

My co-supervisor; Dr. Wolfgang. H. Meyer, for his support.

My parents for their patience, unconditional love and unwavering support, for being with me through the hardships I encountered during my studies. My brothers; Floyd, Oupa and Tshepo for their support and for always believing in me. My little girl; Tshimologo *ya di* Tshegofatso, for her love, patience and understanding that “mama” had to study - your presence in my life gave me the courage to complete this work.

My best friend, my pillar of strength, without whom this work would not have been completed - my husband; Lucky M. Sikhwivhilu, for all his help with editing the manuscript, encouragement, advice, immeasurable support, understanding, love and for being a part of my life.

Prof. Hartmut Winkler and Prof. Lawrence M. Nxumalo, of the former Vista University Soweto campus, for laying a solid foundation and for developing the love for chemistry in me.

Prof. Burtron H. Davis, of the University of Kentucky Centre for Applied Energy Research (CAER), USA, for giving me the opportunity to utilise his research facilities for the Fischer-Tropsh studies and for his invaluable advice and input.

Members of the CAER Clean Fuels and Chemicals group (CFC); Dr Gary Jacobs for physisorption analysis of the catalysts, Dr. Uschi Graham for the HRTEM analysis of the catalysts, Dr. Mingsheng Luo, Mr Shiqi Bao and Mr Dennis E. Sparks for teaching me how to run the reactors. The rest of the CFC group for all the assistance they provided and for making me feel at home in a foreign country.

Miss Gugulethu Mpungose for synthesising some of the silica gels presented in Chapter 3.

Prof. Mike Witcomb, Mr. Abe Seema, and Ms. Caroline Lalkhan of the Electron Microscope Unit at the University of the Witwatersrand for their assistance with the electron microscopy work.

All members of the Catalysis-Organometallic-Ceramics/Materials group for creating a stimulating and enjoyable environment in which to learn, and for the lively forums we used to have.

NRF, DoL Scarce Skills, DAAD, CoE C\*Change and the University of the Witwatersrand for financial support

Last but not least, God Almighty, for granting me the strength to overcome obstacles and for guiding me throughout this journey.

## **PUBLICATION EMANATING FROM THIS WORK**

Keneiloe Khoabane, Emma M. Mokoena, Neil J. Coville, *Synthesis and study of ammonium oxalate templated sol-gel templated silica gels*, Microporous and Mesoporous Materials 83 (2005) 67.

## **ORAL PRESENTATION**

Keneiloe Khoabane, Neil J. Coville, *Systematic study of the synthesis of ammonium oxalate sol-gel templated silica gels*. Catalysis South Africa (CATSA) conference, November 2004, University of North West, Potchefstroom

## **POSTER PRESENTATIONS**

1. Keneiloe Khoabane, Neil J. Coville, Burtron H. Davis, Uschi M. Graham, *Low temperature Fischer-Tropsch synthesis studies over a silica supported iron catalyst: effect of support morphology*, CATSA conference, November 2006, Diaz Beach Hotel, Mosselbay.
2. Keneiloe Khoabane and Neil J. Coville, *Synthesis of silica by sol-gel method in the presence of citric acid*, CATSA conference, November 2003, Riverside Hotel, Durban.
3. Keneiloe Khoabane and Neil J. Coville, *Synthesis of silica by sol-gel method in the presence of citric acid*, African Materials Research Society conference, December 2003, University of the Witwatersrand, Johannesburg.

## ABBREVIATIONS AND ACRONYMS

Abbreviation or Acronym	Description
$\alpha$	Alpha (chain growth probability)
$^{\circ}\text{C}$	Degrees Celsius
$\mu\text{m}$	Micrometer
%	Percent/percentage
ASF	Anderson-Schulz-Flory
BET	Brunauer-Emmett-Teller
BJH	Barret, Joyner and Halenda
$\text{cm}^3$	Cubic centimetres
Co	Cobalt
CO	Carbon monoxide
$\text{CO}_2$	Carbon dioxide
CSTR	Continuously stirred tank reactor
EDX	Energy dispersive X-ray
Fe	Iron
FID	Flame ionisation detector
Fig.	Figure
FT	Fischer-Tropsch
FTS	Fischer-Tropsch synthesis
g	Grams
GC	gas chromatograph
GHSV	gas hourly space velocity
$\text{H}_2$	Hydrogen
$\text{H}_2\text{O}$	Water
h	Hour
HRTEM	High resolution transmission electron microscopy

HTFT	high temperature Fischer-Tropsch
K	Potassium
L	Litre
LTFT	low temperature Fischer-Tropsch
min	Minute
ml	Millilitre
NH <sub>3</sub>	Ammonia
NH <sub>4</sub> OH	Ammonium hydroxide
Ni	Nickel
nm	Nanometre
rpm	Revolutions per minute
Ru	Ruthenium
SEM	Scanning electron microscopy
SiO <sub>2</sub>	silicon dioxide/silica
SMSI	strong metal-support interaction
STP	standard temperature and pressure
TEM	Transmission electron microscopy
TEOS	Tetraethylorthosilicate
TGA	Thermogravimetric Analysis
TCD	Thermal Conductivity Detector
NP	nanoparticle
NT	Nanotube
TOS	time-on-stream
TPD	Temperature programmed desorption
TPR	Temperature Programmed Reduction
WGS	Water gas shift
WHSV	Weigh hourly space velocity
wt %	Weight percent
XRD	X-Ray Diffraction



## **TABLE OF CONTENTS**

### **PART 1: SOL-GEL SYNTHESIS OF NANOSTRUCTURED SILICA GEL**

#### **CHAPTER 1: SOL-GEL CHEMISTRY AND NANOSTRUCTURED SILICA- LITERATURE REVIEW**

1.1. INTRODUCTION	1
1.2. SILICA	2
1.2.1. Forms of Silica	2
1.3. SOL-GEL PROCESSING	4
1.3.1. Sol-gel Processing; A Brief History	4
1.3.2. The Chemistry of Sol-Gel Processing of Silica	7
1.3.3. Applications of Silica gel	11
1.3.4. Advantages of Sol-Gel Processing	12
1.4. NANOSTRUCTURED MATERIALS	13
1.4.1. Nanotubes and related nanostructures	14
1.5. GENERAL REMARKS	20
1.6. SCOPE OF THIS WORK	20
1.7. REFERENCES	22

#### **CHAPTER 2: A SYSTEMATIC STUDY OF PARAMETERS GOVERNING MORPHOLOGIES OF OXALATE ION SOL-GEL TEMPLATED SILICA GELS**

2.1. INTRODUCTION	27
-------------------	----

2.2. EXPERIMENTAL	29
2.2.1 Reagents and Chemicals	29
2.2.2. Synthesis Procedure	29
2.2.3. Characterisation	36
2.2.3.1. Transmission Electron Microscopy	36
2.2.3.2. Scanning Electron Microscopy	36
2.2.3.3. N <sub>2</sub> Physisorption	36
2.2.3.4. Powder X-Ray Diffraction	37
2.2.3.5. Thermal Analysis	37
<b>Part A: A Systematic Study of Parameters Governing Morphologies of Ammonium Oxalate Sol-Gel Templated Silica Gels</b>	
2.3. RESULTS AND DISCUSSION	38
2.3.1. General Comments	38
2.3.2. Variation of temperature	40
2.3.3. Variation of oxalic acid concentration	43
2.3.4. Variation of water amount	45
2.3.5. Variation of ammonia concentration	48
2.3.6. Effect of length of TEOS hydrolysis time	49
2.3.7. Effect of length of ageing time	50
2.3.8. Variation of co-solvent and water amount	53
2.3.9. The ‘Long method’ v/s the ‘Short method’ Synthesis Procedure	58
2.3.10. Reaction Mechanism	62
<b>Part B: Synthesis of Silica Materials by the Templated Sol-Gel Method: Effect of Different Base Catalysts</b>	
2.4. RESULTS AND DISCUSSION	66
2.4.1. Variation of Oxalic Acid amount in different base catalysts	66
2.4.2. Variation of base amount/concentration	70
2.4.3. Variation of water to ethanol amount	73
2.4.4. The ‘Long Method’ v/s the ‘Short Method’ Synthesis Procedure	77
2.4.5. General remarks on the use of different base catalysts	80

2.5. CONCLUSION	83
2.5. REFERENCES	85

### **CHAPTER 3: SYSTEMATIC STUDY OF THE USE OF D-GLUCONIC ACID AND OTHER HYDROXYACIDS IN THE SYNTHESIS OF SILICA GEL BY THE TEMPLATED SOL-GEL METHOD**

3.1. INTRODUCTION	87
3.2. EXPERIMENTAL	89
3.2.1. Reagents and Chemicals	89
3.2.2. Synthesis Procedure	89
3.2.3. Characterisation	91
3.2.3.1. Transmission Electron Microscopy	91
3.2.3.2. N <sub>2</sub> Physisorption	92
3.2.3.3. Powder X-Ray Diffraction	92
3.2.3.4. Thermal Analysis	92

#### **Part A: Systematic Study of the use of D-gluconic Acid in the Synthesis of Silica Gel by the Templated Sol-Gel Method**

3.3. RESULTS AND DISCUSSION	93
3.3.1. General Comments	93
3.3.2 Effect of Temperature	96
3.3.3. Effect of varying D-gluconic acid concentration	99
3.3.4. Effect of varying NH <sub>4</sub> OH amount	101
3.3.5. Effect of variation of water amount	104
3.3.6. The effect of hydrolysis and ageing time	105
3.3.7. Variation of synthesis procedure: The ‘long method’ versus the ‘short method’ synthesis procedure	109
3.3.8. Effect of variation of organic co-solvent	113

**Part B: A Study of the use of other Hydroxyacids in the Synthesis of Silica Gel  
by the Templated Sol-Gel Method**

3.4. RESULTS AND DISCUSSION	118
3.5. CONCLUSION	123
3.6. REFERENCES	125

**PART 2: FISCHER-TROPSCH STUDIES OF SILICA  
SUPPORTED IRON CATALYST**

**CHAPTER 4: FISCHER-TROPSCH SYNTHESIS: LITERATURE  
REVIEW**

4.1. INTRODUCTION	126
4.2. THE FISCHER-TROPSCH REACTION	127
4.3. FISCHER-TROPSCH CATALYSTS	130
4.3.1. Active Metals	130
4.3.1.1. Iron	131
4.3.1.2. Cobalt	132
4.3.1.3. Nickel	133
4.3.1.4. Ruthenium	134
4.3.1.5. Other FT catalysts	134
4.3.2. Promoters	135
4.3.2.1. Chemical Promoters	136
4.3.2.2. Structural Promoters	138
4.4. FISCHER-TROPSCH REACTION TEMPERATURE	140
4.5. APPLICATION OF FISCHER-TROPSCH PRODUCTS	140
4.6. SCOPE OF THIS WORK	141
4.7. REFERENCES	143

## **CHAPTER 5: EXPERIMENTAL**

5.1. INTRODUCTION	147
5.2. REAGENTS AND CHEMICALS USED	147
5.2.1 Supports	147
5.2.2. Metals	148
5.2.3. Gases	149
5.3. CATALYST PREPARATION	149
5.4. THE FISCHER-TROPSCH REACTOR SYSTEM	150
5.5. FISCHER-TROPSCH SYNTHESIS	152
5.5.1. Product Analysis	153
5.5.2. Fischer-Tropsch Data Calculations	156
5.5.3. Catalyst Extraction	159
5.6. SUPPORT AND CATALYST CHARACTERISATION	159
5.6.1. Transmission Electron Microscopy	159
5.6.2. Scanning Electron Microscopy	160
5.6.3. Ammonia Temperature Programmed Desorption	160
5.5.4. Carbon Monoxide Temperature Programmed Reduction	160
5.5.5. Nitrogen Physisorption	161
5.5.5. Elemental Analysis of catalysts	161
5.7. REFERENCE	162

## **CHAPTER 6: LOW TEMPERATURE FISCHER-TROPSCH SYNTHESIS REACTOR STUDIES OVER A COMMERCIAL SILICA AND SILICA TUBES SUPPORTED IRON CATALYSTS: EFFECT OF POTASSIUM LOADING.**

6.1. INTRODUCTION	164
6.2. EXPERIMENTAL	166

6.2.1. Catalyst Preparation	166
6.2.2. Fischer-Tropsch Synthesis	168
6.2.3. Extraction of used catalysts	168
6.2.4. Catalyst Characterisation	168
<b>Part A: The Effect of Potassium Loading on the Activity and Selectivity of a Commercial Silica Supported Iron Catalyst.</b>	
6.3. RESULTS AND DISCUSSION	169
6.3.1. Carbon monoxide conversion	169
6.3.2. Methane Selectivity	173
6.3.3. Reaction Rates and Catalyst Efficiency	175
6.3.4. Product Distribution and Selectivity	180
6.3.5. Catalyst Characterisation	185
6.4. CONCLUSION	187
<b>Part B: The Effect of Potassium Loading on the Activity and Selectivity of Silica Tubes Supported Iron Catalyst.</b>	
6.5. RESULTS AND DISCUSSION	188
6.5.1. Carbon monoxide conversion	188
6.5.2. Methane Selectivity	190
6.5.3. Reaction Rates	190
6.5.4. Product Distribution and Selectivity	192
6.5.5. Catalyst Characterisation	197
6.6. CONCLUSION	198
6.7. REFERENCES	200
 <b>CHAPTER 7: LOW TEMPERATURE FISCHER-TROPSCH SYNTHESIS</b>	
<b>STUDIES OVER A SILICA SUPPORTED IRON CATALYST:</b>	
<b>EFFECT OF SILICA SUPPORT TYPE</b>	
7.1. INTRODUCTION	203
7.2. EXPERIMENTAL	205

7.2.1. Catalyst Support Preparation	205
7.2.2. Catalyst preparation	206
7.2.3. Fischer-Tropsch Synthesis	207
7.2.4. Extraction of used catalysts	208
7.2.5. Catalyst Characterisation	208
7.3. RESULTS AND DISCUSSION	209
7.3.1. Characterisation of supports	209
7.3.2. Carbon monoxide conversion	215
7.3.3. Reaction Rates	216
7.3.4. Carbon dioxide selectivity	220
7.3.5. Methane Selectivity	221
7.3.6. Product Distribution and Selectivity	223
7.3.7. Characterisation of catalysts	227
7.4. CONCLUSION	239
7.5. REFERENCES	241

## **CHAPTER 8: GENERAL CONCLUSION**

## LEGEND OF FIGURES

Figure 2.1:	Chemical structure of Oxalic Acid	28
Figure 2.2:	Powder XRD pattern of calcined material, synthesised with 42.5mmol oxalic acid at 25 °C.	38
Figure 2.3:	Nitrogen adsorption-desorption isotherm and (inset) BJH pore size distribution (determined from the adsorption arm) of silica material synthesized with 42.5 mmol oxalic acid, 170 mmol NH <sub>4</sub> OH and 2.3% H <sub>2</sub> O at 25 °C.	39
Figure 2.4:	TEM images of silica materials synthesised in the absence of oxalic acid at (a) 25 °C and (b) 75 °C.	40
Figure 2.5:	An SEM image of a typical material synthesised at 25 °C.	41
Figure 2.6:	TEM images of (a) tubes synthesised at 25 °C, (b) hollow spheres and (c) a mixture of tubes and amorphous material synthesised at 75 °C. Materials were synthesized using oxalic acid (42.5 mmol).	42
Figure 2.7:	TEM images showing the effect of water/ethanol ratio on silica formation. (a) 0 %, (b) 2.3 %, (c) 25 %, (d) 50 %, (e) 75 %, (f) 100 % water; synthesized at 25 °C.	47
Figure 2.8:	TEM images showing the effect of length of TEOS hydrolysis at 25 °C on silica structure formation and dissolution. (a) 1 min, (b) 2 h (tubes), (c) 2 h (spheres), (d) 6 h, (e) 24 h (tubes), (f) 24 h (spheres).	50
Figure 2.9:	TEM images showing effect of ageing time at 75 °C on silica formation and dissolution. (a) 1 min, (b) 2 h, (c) 6 h and (d) 24 h.	52
Figure 2.10:	HRTEM images showing effect of ageing at 75 °C	



on silica tubes. (a) 2 h and (b) 6 h.	52
Figure 2.11: BJH pore size distributions of silica materials synthesised in methanol, ethanol and isopropanol, with 50 % water.	56
Figure 2.12: TEM images of tubes synthesised in 50 % water and (a) methanol, (b) ethanol, and (c) isopropanol.	56
Figure 2.13: TEM images showing the effect of water amount on the tubes synthesised by the ‘short method’ synthesis procedure with (a) 2.3, (b) 25, (c) 50 and (d) 75 % water relative to ethanol amount.	60
Figure 2.14: TGA profiles of silica materials synthesised by the ‘short method’ and ‘long method’ synthesis procedures. Materials were prepared with 2.3 % H <sub>2</sub> O.	62
Figure 2.15: TEM images of silica materials synthesised with 85 mmol oxalic acid and (a) 85 mmol KOH, (b) 85 mmol NaOH, and (c) 170 mmol NH <sub>4</sub> OH.	67
Figure 2.16: TEM images of silica materials synthesised with (a) 85 mmol KOH, (b) 170 mmol KOH, (c) 85 mmol NaOH, and (d) 170 mmol NaOH.	72
Figure 2.17: TEM images of tubes synthesised with NaOH as base catalyst in (a) and (b) 2.3 , (c) 25 and (c) 50 % water.	75
Figure 2.18: SEM images of (a) low and (b) higher magnification of potassium oxalate, (c) low and (d) higher magnification of sodium oxalate, and (e) low and (f) higher magnification of ammonium oxalate salts precipitated in water/ethanol mixtures.	82
Figure 3.1: Chemical structures of template precursor molecules used in this study	88
Figure 3.2: Powder X-ray Diffractogram of a calcined and uncalcined typical material, synthesised at 25 °C with	

85 mmol D-gluconic acid, 170 mmol NH <sub>4</sub> OH in ethanol containing 2.3 % H <sub>2</sub> O.	94
Figure 3.3: Nitrogen isotherm and BJH pore size distribution, calculated from the adsorption arm of the isotherm (inset) of a material synthesised at room temperature, with 85 mmol D-Gluconic acid, 170 mmol NH <sub>4</sub> OH and 2.3 % H <sub>2</sub> O.	95
Figure 3.4: TGA profile of an uncalcined material synthesised at 25 °C with 85 mmol d-gluconic acid, 170 mmol NH <sub>4</sub> OH, and 2.3 % H <sub>2</sub> O in ethanol.	96
Figure 3.5: BJH pore size distributions (calculated from the adsorption arms of the isotherms) of silica gels synthesised at different temperatures.	98
Figure 3.6: TEM images of hollow spheres synthesised at (a) 25 °C, (b) 55 °C and (c) 75 °C.	99
Figure 3.7: TEM images of hollow spheres synthesised in (a) 170, (b) 340, and (c) 510 mmol NH <sub>4</sub> OH.	103
Figure 3.8: TEM images of hollow spheres synthesised after hydrolysis for different times. (a) 1 min; developing spheres, (b) 2 h; well-defined hollow spheres (c) 4 h; enlarged spheres, (d) 6h; cloudy and enlarged hollow spheres, and (e) 8 h; bursting sphere and (d) 8 h bursting sphere.	106
Figure 3.9: Effect of hydrolysis time on the hollow spheres average wall thickness.	107
Figure 3.10: TEM images of hollow spheres aged for (a) 1 min, smooth and well-defined hollow spheres, and (b) 8 h, very cloudy, thin-walled hollow spheres.	108
Figure 3.11: Effect of length of ageing time on hollow sphere average wall thickness	109

Figure 3.12: TEM images of hollow spheres and tubes synthesised by (a) and (b) the ‘short method’, (c) and (d) ‘long method’ synthesis procedures.	111
Figure 3.13: BJH pore size distributions (calculated from the adsorption arms of the isotherms) of materials synthesised by the ‘long method’ and the ‘short method’ synthesis procedures.	113
Figure 3.14: TEM images of hollow spheres synthesised in different organic co-solvents. (a) Methanol, (b) Ethanol, (c) Isopropanol, and (d) 1-Butanol.	115
Figure 3.15: BJH pore size distributions (calculated from the adsorption arm of the isotherms) of silica gels synthesised in different organic co-solvents.	117
Figure 3.16: TEM images of (a) solid smooth tube obtained with stearic acid, (b) solid tubes and (c) sheet with folds obtained with L - tartaric acid.	120
Figure 3.17: Nitrogen isotherms and (inset) BJH pore size distributions (calculated from the adsorption arms) of the materials synthesised with (a) L-tartaric acid, (b) cinammic acid and (c) stearic acid.	122
Figure 4.1: The change in composition of iron catalysts during FT reaction.	132
Figure 5.1: Schematic diagram of the slurry CSTR set-up used in the study. P- pressure gauge, A- pressure controller, N- needle valve, MFC- mass flow controller, T/C- thermocouple, S/M- stirrer motor, F- sintered metal filter, K <sub>1</sub> - heavy wax trap (200 °C), K <sub>2</sub> - light wax trap (100 °C), K <sub>3</sub> - liquid trap (0 °C).	151

Figure 5.2:	Picture of the reactor used for FT synthesis. K <sub>1</sub> , K <sub>2</sub> , K <sub>3</sub> , S/M and 1L CSTR described in Fig. 5.1.	152
Figure 5.3:	Hewlett Packard Refinery Gas Analyser, used for analysing on-line gas samples, equipped with four TCD type detectors and four columns: 10 m x 0.32 mm molecular sieve 5Å @ 110 °C, 8 m x 0.32 mm Poraplot U @ 80 °C, 10 m x 0.32 mm Al <sub>2</sub> O <sub>3</sub> @ 140 °C, 10 m x 0.15 mm OV-1 @ 120 °C.	154
Figure 5.4:	Agilent 6890 Capillary GC used for oil and wax analysis, equipped with an FID type detector, column: 60 m DB-5, 0.32 mm ID, 0.25 µm film. Programme: 35 °C hold 10 min, 4 °C/min to 325 °C, hold 52 min.	154
Figure 5.5:	Hewlett Packard 5790 packed column GC for water samples analysis, equipped with a TCD type detector, column: 0.154m x 3.2 mm 80/100 mesh Porapak Q. Programme: 100 °C hold 1 min, 10 °C/min to 390 °C, hold 40 min.	155
Figure 5.6:	Agilent 5890 Series II Capillary GC used for the analysis of heavy wax, equipped with an FID type detector. Column: 25 m HT-5 Aluminum clad 0.53mm I.D, 0.15 µm film. Operation Programme: 50 °C no hold, 10 °C/min to 390 °C, hold 40 min.	155
Figure 6.1:	Effect of potassium loading on CO conversion over iron supported on Davisil SiO <sub>2</sub> .	170
Figure 6.2:	Effect of potassium loading on methane selectivity.	175
Figure 6.3:	Effect of potassium loading on Fischer-Tropsch reaction rate.	176
Figure 6.4:	Effect of potassium loading on water-gas-shift reaction rate.	177
Figure 6.5:	Effect of potassium loading on CO <sub>2</sub> selectivity.	177

Figure 6.6:	Effect of potassium loading on catalyst efficiency.	179
Figure 6.7:	Anderson-Shultz-Flory plot for a 0.5 % potassium promoted catalyst.	181
Figure 6.8:	Effect of potassium loading on hydrocarbon product distribution.	182
Figure 6.9:	Effect of potassium loading on 1-olefin selectivity.	185
Figure 6.10:	Effect of potassium loading on CO conversion over Fe supported on silica tubes.	189
Figure 6.11:	Effect of potassium loading on methane selectivity.	190
Figure 6.12:	Effect of potassium loading on (a) Fischer-Tropsch and (b) water-gas shift reaction rates.	191
Figure 6.13:	Effect of potassium loading on CO <sub>2</sub> selectivity.	192
Figure 6.14:	Anderson-Schultz-Flory distribution plot of 0.5 % K loaded catalyst.	193
Figure 6.15:	Effect of potassium loading on hydrocarbon product distribution.	194
Figure 6.16:	Effect of potassium loading on 1-olefin selectivity.	197
Figure 7.1:	The distribution of morphology in the silica supports.	209
Figure 7.2:	SEM images of the supports used. (a) commercial Davisil silica, (b) ammonium oxalate templated silica tubes, and (c) ammonium citrate templated silica spheres.	210
Figure 7.3:	TEM images of the supports used. (a) commercial Davisil silica, (b) ammonium oxalate templated silica tubes, and (c) ammonium citrate.	211
Figure 7.4:	(a) Nitrogen adsorption-desorption isotherms (closed symbols-adsorption, open symbols-desorption) and (b) BJH pore size distributions of the supports, calculated from the adsorption arm.	213

Figure 7.5:	Effect of silica support type on carbon monoxide conversion.	215
Figure 7.6:	Cumulative amount of iron lost during reaction.	216
Figure 7.7:	The effect of silica support type on the rate of the (a) Fischer-Tropsch reaction and (b) water gas shift reaction.	219
Figure 7.8:	The effect of silica support type on the catalyst efficiency for production of hydrocarbons.	220
Figure 7.9:	The effect of support type on carbon dioxide selectivity.	221
Figure 7.10:	Effect of silica support type on methane selectivity.	222
Figure 7.11:	Ammonia-TPD of the used supports.	223
Figure 7.12:	Effect of silica support type on hydrocarbon product distribution.	224
Figure 7.13:	The Anderson-Schulz-Flory plot of a silica spheres supported potassium promoted iron catalyst.	226
Figure 7.14:	BJH pore size distributions of fresh catalysts calculated from the adsorption arm.	228
Figure 7.15:	HRTEM images of (a) fresh and (b) used Davisil silica supported catalyst.	230
Figure 7.16:	HRTEM images of a fresh silica tubes supported iron catalyst, showing (a) Fe nanoparticles occurring both inside and outside a silica tube, and (b) column arrangements of needle-like Fe nanoparticles.	231
Figure 7.17:	HRTEM images of a used silica tubes supported catalyst, (a) showing agglomerated Fe NPs inside a tube, (b) agglomerated Fe NPs some occurring outside the tube walls, and (c) silica tube not damaged during the reaction.	232
Figure 7.18:	HRTEM images of a fresh and used silica spheres supported iron catalyst. Fresh catalyst (a) Fe nanoparticles on spheres,	

	and (b) high magnification image showing semi-hexagonal Fe nanoparticles, Used catalyst (c) silica sphere still intact, and (d) high magnification image showing disorganised and agglomerated Fe nanoparticles.	234
Figure 7.19:	HRTEM image showing (a) agglomerated Fe nanoparticles, and (b) a high magnification of a 'doughnut shaped' particle.	236
Figure 7.20:	HRTEM image of Davisil silica supported catalyst after FT synthesis, showing amorphous carbon particle.	237
Figure 7.21:	CO TPR profile of silica supported iron catalysts.	239

## INDEX OF TABLES

Table 1.1:	Some of the elements that have been used to date in sol-gel processing.	7
Table 2.1:	Effect of the amount of oxalic acid and the synthesis temperature on particle distribution and surface area of the silica materials.	43
Table 2.2:	Effect of the amount of oxalic acid and temperature on the silica particle size	44
Table 2.3:	Effect of water amount on the silica particle distribution.	45
Table 2.4:	Effect of water amount on silica tube size	46
Table 2.5:	Effect of concentration of $\text{NH}_3$ on the silica particle distribution.	48
Table 2.6:	Effect of $\text{NH}_3$ concentration on the silica particle size.	49
Table 2.7:	Effect of organic co-solvent and water amount	

	(relative to co-solvent) on silica particle distribution.	55
Table 2.8:	Effect of co-solvent type on silica particle size	58
Table 2.9:	Effect of water/ethanol ratio on silica particle distribution	59
Table 2.10:	Effect of water/ethanol ratio on silica particle size	61
Table 2.11:	Effect of oxalic acid amount on silica particle distribution. (85 mmol NaOH and KOH, 170 mmol NH <sub>4</sub> OH, 2.3 % H <sub>2</sub> O).	68
Table 2.12:	Effect of oxalic acid amount on silica particle size (NaOH, KOH and NH <sub>4</sub> OH)	69
Table 2.13:	Effect of base amount on silica particle distribution. KOH and NaOH: 85 mmol oxalic acid and 2.3 % H <sub>2</sub> O, NH <sub>4</sub> OH: 42.5 mmol oxalic acid and 50 % H <sub>2</sub> O.	71
Table 2.14:	Effect of base catalyst concentration on silica particle size (NaOH, KOH and NH <sub>4</sub> OH)	73
Table 2.15:	Effect of water amount (relative to ethanol) on silica particle distribution 85 mmol base (170 mmol for NH <sub>4</sub> OH only) and 42.5 mmol oxalic acid, 25 °C.	74
Table 2.16:	Effect of water amount (relative to ethanol) on silica particle size (NaOH, KOH and NH <sub>4</sub> OH)	76
Table 2.17:	The effect of variation of the synthesis procedure with the use of different base catalysts on silica particle distribution. Base 85 mmol (170 mmol for NH <sub>4</sub> OH), oxalic acid 42.5 mmol, 2.3 % H <sub>2</sub> O.	78
Table 2.18:	Effect of variation of synthesis procedure on silica particle size (NaOH, KOH and NH <sub>4</sub> OH)	80
Table 3.1:	Effect of temperature on silica particle distribution and size.	97
Table 3.2:	The effect of synthesis temperature on silica particle size and physisorption properties	98
Table 3.3:	Effect of variation of D-gluconic acid amount on silica	



	particle distribution.	101
Table 3.4:	Effect of varying $\text{NH}_4\text{OH}$ amount on silica particle distribution and size.	102
Table 3.5:	Effect of variation of water (relative to ethanol) amount on silica particle distribution and size.	105
Table 3.6:	Effect of variation of synthesis procedure on silica particle distribution.	110
Table 3.7:	Effect of variation of synthesis procedure on particle size and nitrogen physisorption properties of the silica gels.	112
Table 3.8:	Effect of variation of organic co-solvent on silica particle distribution.	114
Table 3.9:	Effect of variation of organic co-solvent on silica particle size and surface area.	117
Table 3.10:	Particle distributions of silica materials synthesised with the different template precursors.	119
Table 4.1:	Approximate relative cost of metals active for Fischer-Tropsch in 2004.	131
Table 6.1:	Metal contents of the prepared promoted iron catalysts (Fe/Davisil $\text{SiO}_2$ ).	169
Table 6.2:	Effect of potassium loading on the decrease in catalyst activity with time on stream.	170
Table 6.3:	Details of reaction conditions used by other researchers.	172
Table 6.4:	Effect of potassium promotion on chain growth probability and olefin selectivity.	184
Table 6.5:	Physisorption data and carbon content of fresh and used catalysts.	187

Table 6.6:	Metal contents of the prepared promoted iron catalysts (Fe/SiO <sub>2</sub> tubes).	188
Table 6.7:	Amount of C <sub>19+</sub> hydrocarbons in reactor contents at the end of reaction.	194
Table 6.8:	Effect of potassium promotion on chain growth probability and olefin selectivity.	196
Table 6.9:	Physisorption data and carbon content of the fresh and used catalysts.	198
Table 7.1:	Details of catalyst preparation procedure.	207
Table 7.2:	Physisorption data of the supports.	214
Table 7.3:	Actual metal contents of the prepared promoted iron catalysts	214
Table 7.4:	Overall change in FT reaction rate, WGS reaction rate and catalyst efficiency with time on stream.	218
Table 7.5:	Amount of C <sub>19+</sub> hydrocarbons in reactor contents at the end of the reaction.	225
Table 7.6:	Effect of silica support type on chain growth probability and olefin selectivity.	227
Table 7.7:	Physisorption data and carbon content of the fresh and used catalysts.	229

# **PART I**

## **SOL-GEL SYNTHESIS OF NANOSTRUCTURED SILICA GEL**

# **CHAPTER 1**

## **SOL-GEL CHEMISTRY AND NANOSTRUCTURED SILICA- LITERATURE REVIEW**

### **1.1. INTRODUCTION**

The observation of the carbon nanotubes by Iijima in 1991<sup>1</sup> sparked the world's interest in nanoarchitected materials, especially due to their potential applications in material manufacture and design. Although different methods of synthesising these materials have been found, studies into the improvement of these methods and the synthesis of novel structures of various compositions are still continuing. One method to make nanoarchitected materials is by the sol-gel process, a simple and straightforward method of synthesis. The process readily affords materials with controlled structure, surface area and porosity.

This chapter provides a brief review of the sol-gel process with particular reference to the synthesis of silica nanotubes and related nanostructures. This chapter begins with a brief introduction to silicon dioxide, followed by a description of the sol-gel processing of silica materials which includes a brief history of sol-gel, the chemistry of silica synthesis by sol-gel processing, the applications of silica gel and advantages of the sol-gel method. An introduction of nanostructured materials is also included, and this section describes some of the synthesis procedures available for the synthesis of nanostructured silica materials.

## 1.2. SILICA

The term silica denotes the compound silicon dioxide,  $\text{SiO}_2$ . It is the most common binary compound of silicon and oxygen, the two elements of greatest terrestrial abundance. Silica constitutes about 60 weight % of the earth's crust, occurring either alone or combined with other oxides that form silicates. It is of great geological importance and is a ubiquitous chemical substance with a rich chemistry. Commercially, silica is the source of elemental silicon and is used in large quantities as a constituent of building materials, as a desiccant, adsorbent, reinforcing agent, filler, and catalyst component. Silica also has numerous specialised applications, e.g. as piezoelectric crystals, in optical elements, and as glassware. Silica is a basic material of the glass, ceramics, and refractories industries, and an important raw material for the production of soluble silicates, silicon and its alloys, silicon carbide, silicon-based chemicals and silicones<sup>2</sup>.

### 1.2.1. Forms of Silica

By far, the commonest form of silica is crystalline quartz, the main constituent of common sand. However, under certain conditions in nature and in the laboratory, other forms are produced. These forms may be divided into the following classes<sup>2</sup>:

- (1) Anhydrous crystalline silica
- (2) Hydrated crystalline silica ( $\text{SiO}_2 \cdot x\text{H}_2\text{O}$ )
- (3) Anhydrous amorphous silica of microporous anisotropic form such as found in fibres or sheets
- (4) Anhydrous and hydrous amorphous silica of colloidally subdivided or microporous isotropic form, such as found in sols, gels, and fine powders.
- (5) Massive dense amorphous silica glass

***Anhydrous Crystalline Silica***

This type of silica can either occur by transformation of other forms of silica or can be found naturally, e.g. in meteor craters and volcanic deposits. According to the conventional view of the polymorphs of silica, there are three main forms of crystalline silica. These are quartz, stable below about 870 °C, tridymite, stable from about 870 – 1470 °C, and cristobalite, stable from about 1470 °C to the melting point of about 1723 °C. Other forms of anhydrous crystalline silica include keatite, coesite, stishovite, silica W, melanophlogite, silica O, silica X, and silicalite<sup>2,3</sup>

***Hydrated Crystalline Silica***

Silicas with one or more molecules of hydrated water such as  $\text{Na}_2\text{SiO}_3 \cdot 4\text{H}_2\text{O}$  and  $\text{NaSi}_7\text{O}_{13} \cdot 3\text{H}_2\text{O}$ , can be formed by chemical and/or heat treatment of compounds such as sodium disilicate  $\text{Na}_2\text{Si}_2\text{O}_5$ , gillipsite  $\text{BaFeSi}_4\text{O}_{10}$ , chrysolite asbestos  $(\text{HO})_8\text{Mg}_6\text{Si}_4\text{O}_{10}$ , and mordenite  $(\text{Na}_2\text{CaK}_2)\text{Al}_2\text{Si}_{10}\text{O}_{24} \cdot 7\text{H}_2\text{O}$ <sup>2,4,5</sup>.

***Amorphous Silicas***

Frondel<sup>6</sup> showed that amorphous silica is not truly amorphous but consists of regions of local atomic order, or crystals of extremely small size, which, by careful X-ray diffractogram studies, appear to have the cristobalite structure. Otherwise, by ordinary diffractogram procedures, these materials give only a broad band, with no multiple peaks as are ordinarily obtained with macroscopic crystals.

Amorphous silica can be broadly divided into 3 classes:

- (i) vitreous silica or silica glass, made by fusion of crystalline quartz or quartz sand,
- (ii) silica M, an amorphous silica formed when either amorphous or crystalline silicas are irradiated with high speed neutrons,
- (iii) microamorphous silica, which includes sols, gels, powders, and porous glasses.

These are characterised by small ultimate particle size (less than a micron) and high specific surface areas.

***Hydrated Amorphous Silica***

This type of polymeric structure is obtained if monosilicic acids in water are concentrated and polymerised at ordinary or low temperature and in slightly acidic conditions. An example of this is natural opal, which contains 5.25-13.5 % water locked within the structure and does not evaporate<sup>7</sup>.

**1.3. SOL-GEL PROCESSING**

*Sol-gel* can be broadly defined as the preparation of ceramic materials by preparation of a sol, gelation of the sol, and removal of the solvent<sup>8</sup>.

A *colloid* is a suspension in which the dispersed phase is so small (~1-1000 nm) that gravitational forces are negligible and interactions are dominated by short-range forces, such as the van der Waals attraction and surface charges. A *sol* is a dispersion of colloidal particles suspended in Brownian motion within a fluid matrix. In the sol-gel process, the precursors for the preparation of a colloid consist of a metal or metalloid element surrounded by ligands, (appendages *not* including another metal or metalloid atom). For example, an inorganic salt  $\text{Al}(\text{NO}_3)_3$  or an alkoxide  $\text{Al}(\text{OC}_4\text{H}_9)_3$  can be used as precursors for the preparation of aluminium oxide. A *gel* is a substance that contains a continuous solid skeleton enclosing a continuous liquid phase, with both the solid and liquid phases having colloidal dimensions.

**1.3.1. Sol-gel Processing; A Brief History<sup>8,9</sup>**

Sol-gel processing methods were first used historically for decorative and constructional materials. However, many new applications for sol-gel prepared materials were developed in the 20<sup>th</sup> century. Today sol-gel methods are reaching their full potential, enabling the preparation of new generations of advanced

materials not easily accessible by other methods, yet using mild, low-energy conditions.

The earliest use of colloids to prepare functional materials was seen in the cave paintings at Lascaux in France, dating back 17 000 years; the pigments used were based on iron oxide, carbon and clays, ground into fine powders, graded by sedimentation and dispersed in water using natural oils as surface active stabilisers. The next major development was some 8000 years ago as seen by early examples of the use of plaster and bricks. These include the bricks produced through burning and held together with bitumen for the building of the tower of Babel. In Egypt in 4000 BC, an aqueous paste of crushed sand and a sodium flux and binder was moulded and fired to produce *faience* by binding silica particles together with the molten flux. Glazing methods were developed to seal the surfaces of porous clay vessels, and these were used in China and Mesopotamia as far back as 2000 BC<sup>10</sup>. The idea of using chemically-linked particles as a matrix to form a composite with other particulate materials led to the development of concrete in about 700 BC in Iran. This process was later improved by the Romans between 200 BC and 400 AD, and in Britain, France and in Germany in the 18<sup>th</sup> century. However, many of these early technologies became lost in the Dark Ages after the decline of the Roman Empire.

The next significant development was the discovery of ‘water glass’ by von Helmont in 1644. He dissolved silicate materials (stones, sand, etc.) in alkali and found that on acidification, a precipitate of silica equal in weight to the original silicate materials was obtained. In 1779 Bergman found that the mixture gelled upon addition of the correct amount of dilute acid. In the 19<sup>th</sup> century, many oxide materials, such as zirconium gels and uranium oxide were prepared from hydroxide gels. In 1846, Ebelman prepared the first silicon alkoxide by reacting silicon tetrachloride and alcohol, and he found that the product gelled on prolonged exposure to the atmospheres with normal humidity. This discovery was then followed by the preparation of hydrolysed derivatives of silicon alkoxide and silicic acid between



1876 and 1884. Meanwhile, studies of inorganic gels from aqueous salts were under study. For example, Graham<sup>11</sup> showed that the water in silica gel could be exchanged for organic solvents. In the 1930s, Hurd<sup>12</sup> showed that a silica gel must consist of a polymeric skeleton of silicic acid enclosing a continuous liquid phase, while Kistler<sup>13</sup> invented the process of supercritical drying to produce aerogels. The use of sols and gels for the preparation of homogeneous powders was later done in the mineralogy and ceramics industry<sup>14,15</sup>. However, this early work was not directed at understanding the mechanism of the reaction and the gelation process.

Much more sophisticated work, both scientifically and technologically, was carried out in the nuclear industry in the 1970's. The goal of the work was to prepare small spheres (tens of  $\mu\text{m}$  in diameter), by sol-gel processing, of radioactive oxides that would be packed into fuel cells for nuclear reactors<sup>16</sup>. The preparation of small spheres was achieved by dispersing the aqueous sol in a hydrophobic organic liquid, so that the sol would form into small droplets, each of which would subsequently gel. The ceramics industry began to show interest in gels in the late 1960s and 1970s; when controlled hydrolysis and condensation of alkoxides for preparation of multicomponent glasses was developed<sup>17,18</sup>. Simultaneously ceramic fibres were made from metal-organic precursors on a commercial basis by several companies<sup>19,20</sup>.

Today, sol-gel processing finds application in the synthesis of many metal and semi-metal oxide gels and ceramics. **Table 1.1** shows some of the metals that have been used to date in sol-gel processing.

**Table 1.1.** Some of the elements that have been used to date in sol-gel processing<sup>8</sup>.

Li	Be	Ti	Ta	Ni
Na	Mg	Zr	Cr	In
K	Ca	Hf	Mn	Ga
Rb	Sr	V	Fe	Ge
Cs	Ba	Nb	Co	

However in this chapter focus will be based on the sol-gel synthesis of silica.

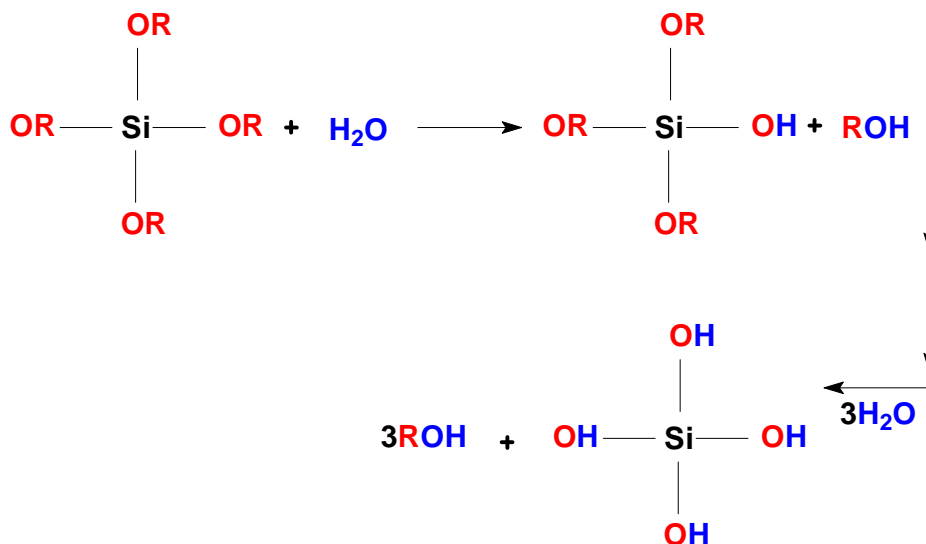
### 1.3.2. The Chemistry of Sol-Gel Processing of Silica

Silicon is the most abundant metal on the earth's crust, and evidence of silicate hydrolysis and condensation to form polysilicate gels and particles is seen in many naturally occurring systems such as precious opal. Readily soluble silica, when it comes in contact with water, undergoes repeated hydrolysis and condensation to give aqueous polysilicate species occur that under appropriate chemical conditions can evolve into amorphous silica particles. These when glued together by a low-density silicate gel form precious opal<sup>2</sup>. Flint, a hard type of stone, was apparently formed from the siliceous skeletons of ancient sponges. It was also discovered in the 1970s that soluble trace amounts of silica play a major role in the development of mammals<sup>8</sup>.

The sol-gel process involves three fundamental reactions; hydrolysis, alcohol condensation and gelation (accompanied by crosslinking).

#### *Hydrolysis*

The first step in sol-gel processing of SiO<sub>2</sub> is hydrolysis of a silicon alkoxide to form a hydroxylated product and a corresponding alcohol (see **Scheme 1.1**).



**Scheme 1.1.** Schematic representation of hydrolysis of tetraalkylorthosilicate (R=alkyl).

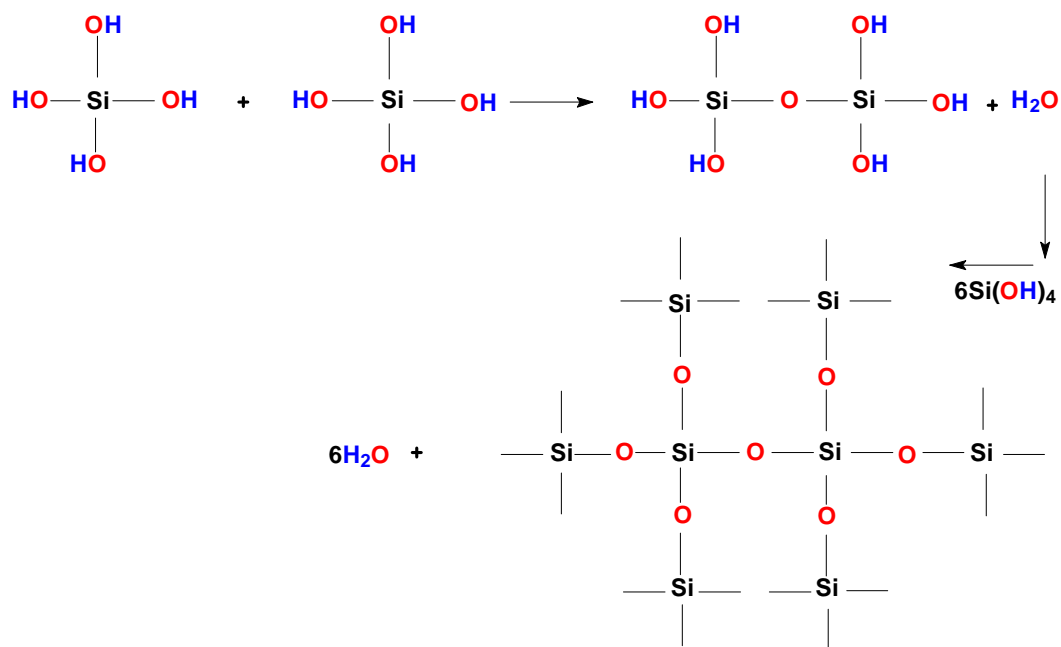
This process is most rapid and complete when an acidic or basic catalyst is employed. The most commonly used catalysts are mineral acids and ammonia.

A number of factors can affect the rate of hydrolysis of a silicon alkoxide, and these include the steric bulkiness of the alkoxy group; larger alkoxy groups lead to more steric hindrance and thus lead to slower reactions. The rate of hydrolysis of a silicon alkoxide can be affected by the hydrophobic or hydrophilic character of the precursor. If a hydrophobic silicon alkoxide is employed, a co-solvent needs to be added to achieve miscibility with water, to facilitate hydrolysis. Many different organic solvents can be used to achieve miscibility, such as different alcohols, tetrahydrofuran, and formamide. However, the choice of the organic co-solvent is important since use of a different alcohol from that generated by hydrolysis can lead to trans-esterification and this can affect the reaction. Another determining factor for the rate of hydrolysis of a silicon alkoxide is the water:alkoxide ratio. The stoichiometric ratio of water:alkoxide for complete hydrolysis is 4. However, less water than this can still be used since some water may form in the condensation step.

If the amount of water becomes very small, however, the hydrolysis rate slows down due to the reduced reactant concentration. Similarly, if very large amounts of water are used, the alkoxide becomes diluted, leading to increased gel times.

### Condensation

After hydrolysis of the alkoxide groups into silanol groups, condensation reactions occur, producing siloxane bonds. As with hydrolysis reaction, condensation reactions can be either acid or base catalysed. Silicon hydroxide molecules can react to form siloxane bonds, thereby releasing water in the process, as shown in **Scheme 1.2**. This reaction is called water condensation.



**Scheme 1.2.** Schematic representation of water condensation reaction of hydrolysed tetraalkylorthosilicate molecules.

$$\begin{array}{c}
 \begin{array}{c} \text{OR} \\ | \\ \text{RO}-\text{Si}-\text{OR} \\ | \\ \text{RO} \end{array} + \begin{array}{c} \text{OH} \\ | \\ \text{HO}-\text{Si}-\text{OH} \\ | \\ \text{OH} \end{array} \longrightarrow \begin{array}{c} \text{OR} \quad \text{OH} \\ | \quad | \\ \text{RO}-\text{Si}-\text{O}-\text{Si}-\text{OH} \\ | \quad | \\ \text{RO} \quad \text{OH} \end{array} + \text{ROH} \\
 \\
 \begin{array}{c} \text{OR} \\ | \\ \text{RO}-\text{Si}-\text{OR} \\ | \\ \text{O} \\ | \\ \text{RO}-\text{Si}-\text{O}-\text{Si}-\text{O}-\text{Si}-\text{OR} \\ | \quad | \quad | \\ \text{OR} \quad \text{O} \quad \text{OR} \\ | \\ \text{RO}-\text{Si}-\text{OR} \\ | \\ \text{OR} \end{array} \xleftarrow{\quad} 3\text{Si(OR)}_4
 \end{array}$$

Under most conditions, condensation commences before hydrolysis is complete. Just as with hydrolysis, the relative rates of reaction of different species depend on steric effects of the substituent on the silicon alkoxide.

Polycondensation and gelation occurs when links form between silica sol particles, produced by hydrolysis and condensation, to such an extent that a giant spanning cluster reaches across the containing vessel. Gelation only increases the viscosity of the mixture but not the chemical composition. Following gelation, further cross-

linking and chemical inclusion of isolated sol particles into the spanning cluster continues, leading to an increase in the elasticity of the sample.

Ageing of the gel leads to a gradual increase in the number of  $Q^3$  and  $Q^4$  species ( $Q^3$  species are Si atoms attached via four oxygen links to three other silicon atoms, while  $Q^4$  species are Si atoms attached via four oxygen links to four other silicon atoms) due to cross-linking via trans-pore condensation reactions of pore-surface hydroxyl groups. The net effect of this process is a stiffening and shrinkage of the sample, the latter caused by new bonds forming where there were formerly only weak interactions between surface hydroxyl and alkoxy groups.

After ageing of the gel, it is normally dried to remove the solvent and so leaves a porous network. Drying by evaporation under normal conditions gives rise to capillary pressure that causes shrinkage of the gel network. The resulting gel, called a *xerogel*, is often reduced in volume by a factor of 5 to 10 compared to the original wet gel. However, if the water in the gel is exchanged for alcohol, which is then removed by supercritical drying, no capillary stresses occur and thus relatively very little shrinkage of the gel occurs, in that case the gel is called an *aerogel*. These gels may indeed be mostly air, having volume fractions of solid as low as ~1%.

### 1.3.3. Applications of Silica Gel

The largest application areas for silica gels synthesised by the sol-gel method include their uses in health care products, such as thixotropic agents in cosmetics and dentrifices, as selective absorbents to maintain clarity during the brewing of beer, as desiccants, as a thixotrope and flattening agent in coatings<sup>21</sup>; and as a support for polymerisation catalysts. Specialised silica gels that have uniform pore structure, and which are often surface-treated, are used in the production of chromatography columns for gas- and liquid-phase separations. Amorphous silica gels<sup>22</sup> and

aerogels<sup>23</sup> are also used as insulating materials and sol-gel coatings for optical applications<sup>24</sup>.

#### 1.3.4. Advantages of Sol-Gel Processing

One of the advantages of using sol-gel processing for the synthesis of inorganic oxides is that the temperatures required for almost all the stages of synthesis are low, usually close to room temperature. Thus, thermal degradation of both the material itself and any entrapped species is minimised and so high purity and stoichiometry in syntheses can be achieved. Also, this advantage allows for the production of unusual amorphous materials as the low-temperatures used in this process are generally below the crystalline temperature for oxide materials.

High purity products can be formed from this method, as the precursors, i.e. metal alkoxides and mixed alkyl/alkoxides, are frequently volatile and easily purified to very high levels. Also, mild chemical conditions are normally used. Although hydrolysis and condensation reactions are catalysed by acids and bases, extreme pH conditions can easily be avoided, by rapid neutralisation or buffering of the synthesis mixture after hydrolysis.

By appropriate chemical modification of the precursors, control of the rates of hydrolysis, condensation, and colloid particle size, as well as pore size, porosity and pore wall chemistry of the final material can be achieved. Also, by controlling the ageing and drying conditions, further pore size and mechanical strength of the material can be controlled.

Covalent attachment of organic and biological species to porous silicate glass structures can be achieved by using functionalised precursors, while by using organometallic precursors containing polymerisable organic ligands, materials containing both organic and inorganic polymer networks can be produced. Organic

species may be entrapped in the gel to create pores with controlled size and shape, subsequent removal of these species can leave ‘molecular footprints’ with potential application as catalytic sites.

#### 1.4. NANOSTRUCTURED MATERIALS

Nanotechnology is the design, fabrication and application of nanostructures or nanomaterials, and the fundamental understanding of the relationship between physical properties or phenomena and material dimensions<sup>25</sup>. These new physical properties not only satisfy human curiosity, but also promise new advances in technology. Physical and chemical properties of substances can be considerably altered when they are exhibited on a nanoscopic scale, and this opens up a completely new perspective for material design that benefits from the introduction of particle size as a new powerful parameter.

Nanotechnology also promises the possibility of creating nanostructures of metastable phases with non-conventional properties including superconductivity and magnetism. Yet another very important aspect of nanotechnology is the miniaturisation of current and new instruments, sensors, and machines that will greatly impact on the world we live in, such as computers, biosensors, nanorobots, and nanoscaled electronics.

A nanometre (nm) is one billionth of a metre, i.e.  $10^{-9}$  m. Materials in this size range exhibit some remarkable specific properties. A transition from atoms or molecules to bulk form takes place in this range. Nanostructured or nanoscale materials are any solid materials that have a nanometer dimension: three dimensions; e.g. nanoparticles, two dimensions, e.g. thin films, and one dimension, e.g. thin wires<sup>26</sup>.



Synthesis and processing of nanostructures and nanomaterials are an essential aspect of nanotechnology studies. New physical properties and applications of nanomaterials and nanostructures are possible only when nanostructured materials are made available with *desired size, morphology, crystal and microstructure, and chemical composition*.

Nanomaterials with anisotropic morphology are particularly advantageous. Nanotubes, especially, possess several different areas of contact (borders, inner and outer surfaces, and structured tube walls) that in principle can be functionalised in several ways. Their basic hollow morphology is almost directly associated with their usage as nanoscale host materials. Below is a summary of some of the methods of synthesising silica nanotubes and related nanostructures that are used today.

#### 1.4.1. Nanotubes and Related Nanostructures

The discovery of carbon nanotubes (CNTs)<sup>1</sup> has catalysed a fruitful and still growing interest in nanotubes (NTs), both in application-oriented industrial and basic research. Although CNTs are still the most widely investigated examples of such materials, especially regarding potential applications, the world-wide search for other systems is steadily increasing this family of nanostructured materials. These include BN<sup>27</sup> and (BN)<sub>x</sub>C<sub>y</sub><sup>28</sup> Mo and W dichalcogenides<sup>29</sup>, NbS<sub>2</sub><sup>30</sup>, HfS<sub>2</sub><sup>31</sup>, ZrS<sub>2</sub><sup>31</sup>, TaS<sub>2</sub><sup>30</sup>, and NbSe<sub>2</sub><sup>32</sup>, VO<sub>x</sub><sup>33</sup>, Mn-V oxide<sup>34</sup>, SiO<sub>2</sub><sup>35</sup>, TiO<sub>2</sub><sup>36</sup>, Al<sub>2</sub>O<sub>3</sub><sup>37</sup>, ZnO<sup>38</sup>, In<sub>2</sub>O<sub>3</sub> and Ga<sub>2</sub>O<sub>3</sub><sup>39</sup> and oxides of Er, Tm, Yb and Lu<sup>40</sup>, BaTiO<sub>3</sub> and PbTiO<sub>3</sub><sup>41</sup>, NiCl<sub>2</sub><sup>42</sup>, and Au<sup>43</sup>, Co<sup>44</sup>, Ni<sup>45</sup>, and Te<sup>46</sup>.

Among oxide NTs, SiO<sub>2</sub>-NTs are of special interest because of their hydrophilic nature, easy colloidal suspension formation and facile surface functionalisation. SiO<sub>2</sub>-NTs and related structures find wide applications in processes such as drug delivery<sup>47</sup>, enzyme encapsulation<sup>48</sup>, as templates for CNT synthesis<sup>49</sup>, bioseparation<sup>50</sup> and in catalysis<sup>51</sup>.

There are two main pathways for the synthesis of oxide NTs. One straightforward method is conducted by employing porous or fibrous materials as templates to guide formation of single oxide NTs. The other method involves the use of organic molecules where the interaction and/or self-assembly between inorganic precursors and organic templates may offer unique alternatives in the development of inorganic nanotube materials.

Sol-gel techniques have been extensively used to synthesise silica nanotubes. In one of the methods most commonly employed, formation of silica nanotubes takes place by transcription of a template. The template can either be preformed or formed *in situ*. Carboxylic acids have been employed for the purpose of transcription of tubular shapes into silica materials. Nakamura and Matsui<sup>35</sup> prepared hollow SiO<sub>2</sub>-NTs as a spin-off product of sol-gel synthesis wherein, TEOS was hydrolysed in the presence of ammonia and racemic DL-tartaric acid. They obtained mixtures of cylindrical and square-shaped tubes with outer diameters ranging from 0.8 to 1.0 µm and lengths of 200-300 µm. The authors speculated that chains of hydrogen-bonded DL-tartaric acid molecules acted as templates for the deposition of the silica nanotubes. Miyaji and co-workers<sup>52</sup> found that incipient crystallisation of ammonium dl-tartrate into needle-like crystals was responsible for the formation of the nanotubes through a mechanism involving inorganic deposition on the external surface of the organic crystal filaments. The mechanism was later confirmed when needle-like crystals of ammonium oxalate, L-tartrate and succinate were able to produce SiO<sub>2</sub>-NTs<sup>53</sup>. Wang *et al*<sup>54</sup> used citric acid and obtained hollow single SiO<sub>2</sub>-NTs with diameters of 50 to 500 nm and lengths ranging from hundreds of nanometers to tens of micrometers, while Mokoena<sup>51(a)</sup> obtained hollow spheres with outer diameter of about 200 nm during her synthesis of SiO<sub>2</sub> materials in the presence of citric acid. The advantages of synthesising SiO<sub>2</sub>-NTs using a carboxylic acid as a template precursor is that the synthesis is carried out under mild conditions, and can be done even at room

temperature, furthermore, the template can be easily removed by washing or calcination at elevated temperatures in air.

Anodic alumina membranes have also been used in the sol-gel synthesis of SiO<sub>2</sub>-NTs<sup>50(a),55</sup>. In a typical synthesis, pores of the alumina membrane are filled with an acid hydrolysed silica precursor, aged for a few days, and the membrane dissolved by alkaline treatment. Textor and Roewer<sup>55(b)</sup> obtained hollow SiO<sub>2</sub>-NTs with outer diameters less than 200 nm when they filled the alumina membrane by spin coating, and they obtained silica fibrils when they used dip-coating procedures. In their study, Zhang *et al*<sup>55(c)</sup> obtained SiO<sub>2</sub>-NTs with an outer diameter in the range of 30-50 nm, that could emit stable, high brightness visible light at room temperature. They suggested that the visible light emission from the SiO<sub>2</sub>-NTs may be linked to the large surface area that is covered with a high density Si-OH complex.

SiO<sub>2</sub>-NTs can also be produced by sol-gel methods using inorganic templates such as needle-like CaCO<sub>3</sub><sup>56(a)</sup> particles, nanowires of [Pt(NH<sub>3</sub>)<sub>4</sub>(HCO<sub>3</sub>)<sub>2</sub>]<sup>56(b)</sup>, Ag<sup>56(c)</sup>, ZnO<sup>56(d)</sup> and V<sub>3</sub>O<sub>7</sub>·H<sub>2</sub>O<sup>56(e)</sup>, and Au nanorods<sup>56(f)</sup>. Tetrapod-like SiO<sub>2</sub>-NTs were also obtained by using tetrapod-like ZnO nanowires<sup>56(d)</sup>. In these methods, removal of the template can be achieved by dissolution in an acidic and/or alkaline solution. Apart from large scale synthesis of SiO<sub>2</sub>-NTs, the thickness of their outer walls can be controlled by changing the TEOS hydrolysis time and/or its concentration. Synthesis of SiO<sub>2</sub>-NT arrays has also been achieved through a thermal oxidation approach in the ‘absence’ of a template; the growth of the hollow SiO<sub>2</sub>-NTs was suggested to occur by a vapour-liquid-solid mechanism<sup>57</sup>.

SiO<sub>2</sub>-NTs, nanofibers and nanorods have been synthesised by sol-gel procedure in the presence of surfactants<sup>58</sup>. Dong *et al*<sup>58(a)</sup> used kaolin clay as a source of silica and cetyltrimethylammonium bromide (CTAB) as template. They obtained hollow silica nanotubes with outer diameters of up to 150 nm. Single crystal-like nanofibers with diameters ranging between 50 and 300 nm and lengths from tens of micrometres up

to several millimeters, with hexagonally organised pores possessing either a circular or longitudinal architecture have been synthesised by sol-gel procedure in the presence of the surfactant hexadecyltrimethylammonium chloride ( $C_{16}TMACl$ )<sup>58(b)</sup>. Nanorods with outer diameters of up to about 1000 nm and lengths of up to 6  $\mu m$  have been obtained in the presence of the mixed surfactants, CTAB and cetyltrimethylammonium chloride (CTAC)<sup>58(c)</sup>. Mesostructured silica hollow spheres have been synthesised by using a double-templating method. In the process  $CaCO_3$  was employed as a structure-directing template for the spheres and hexadecyltrimethylammonium bromide ( $C_{16}TMABr$ ) as a meso-structure directing agent. Hollow spheres with inner diameters of about 40 nm and with mesostructured walls were obtained from the procedure<sup>59</sup>.

Organogelators have also been used to transcribe shape into silica gels<sup>60</sup>. The non-hydrogen bond based gelators, have been shown to create various hollow silica fibers with linear<sup>60(a)</sup>, helical<sup>60(b)</sup> and multilayered<sup>60(c) and (d)</sup> structures. Novel structures such as linear<sup>60(e)</sup>, helical<sup>60(e),(f)</sup>, bundled<sup>60(f)</sup>, multi-layered cigar-like<sup>60(g)</sup>, vesicular<sup>60(g)</sup>, hollow spherical<sup>60(h)</sup> and lotus<sup>60(h)</sup> type structures have been obtained with hydrogen bond based gelators.

Another structure closely related to the NT is the nanowire.  $SiO_2$  nanowires which show intensive blue light emission have been synthesised by laser ablation<sup>61</sup>. Large scale synthesis of  $SiO_x$  nanowires has been achieved by physical evaporation of the mixture of mesoporous silica containing iron nanoparticles and silicon powder<sup>62</sup>. They have also been prepared through a vapour phase transport process via the vapour-liquid-solid mechanism using silicon powder and a Au colloid catalyst<sup>63</sup>.

It has been shown that an external electric field, magnetic field or a shear can alter the structure and morphology of crystalline mesoporous silica materials<sup>64</sup>. This is achieved by orientation of the template micelles in the desired form followed by  $SiO_2$  growth on these oriented micelles. Fiber/rod-like  $SiO_2$  structures with diameters

in the size range of hundreds of nanometres up to a few micrometres have been obtained by this method. In their synthesis of  $\text{SiO}_2$  gel, Patwardhan *et al*<sup>65</sup> used a cationically charged polymer, polyallylamine hydrochloride (PAH) to produce solid spheres. However, upon perturbation of the reaction mixture by shaking, stirring, flowing in a tube or applying shear, they obtained  $\text{SiO}_2$  fiber-like structures with diameters of about 100 nm. The authors proposed that PAH orients into elongated chains, thus facilitating formation of fiber-like  $\text{SiO}_2$  structures, while globule-like conformations of PAH formed in unperturbed systems.

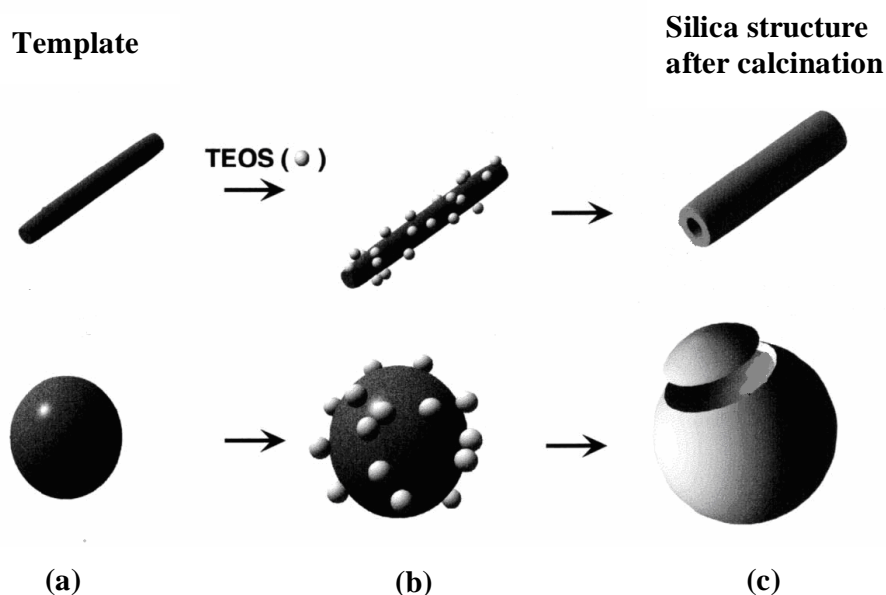
Electrohydrodynamically generated coaxial liquid jets combined with sol-gel chemistry have been used to produce hollow nanofibers<sup>66</sup>. In the method coaxial liquid nanojets are made of a shell-forming liquid on the outside and inert poorly miscible liquid (such as olive oil and glycerine) on the inside, the latter containing a very broad and general range of liquid nanotubular templates requiring no molecular-level assembly. Gelation of the sol (shell) constituent prior to electrical charge-mediated breakup of the coaxial nanojet yields hollow nanofibers, with diameters in the order of 500 nm, having a liquid template-filled core, which can be removed by evaporation.

It has been suggested that for a template to be able to transcribe its shape into the inorganic material, interaction between the inorganic material precursor and the template has to exist. The interaction has been proposed to occur in one the following ways<sup>67,68</sup>:

- (i) the negatively charged prehydrolysed precursor moieties in solution (partially hydrolysed TEOS, oligomers, or small  $\text{SiO}_2$  particles) can interact with the positively charged moieties on the template surface,
- (ii) hydrogen bonding can occur between donating moieties on the template and the negatively charged precursor moieties in solution, or

(iii) if the surface of the template contains moieties that can catalyse the formation of small amounts of inorganic material on the surface,  $\text{SiO}_2$  growth will proceed on the surface of these nuclei.

Thus, in the templated synthesis of nanostructured  $\text{SiO}_2$  materials, the silica precursor polymerises and assembles itself over the surface of the template, and after removal of the template (e.g. by calcination, acid/alkaline treatment) a structured hollow material is left behind (see illustration in **Scheme 1.4**).



**Scheme 1.4.** Schematic representation of creation of the various silica structures from a rod-like and spherical templates by sol-gel polymerisation: (a) template crystal, (b) sol-gel polymerisation of TEOS and adsorption on surface of template (c) single hollow tube or spherical structure obtained after removal of the template<sup>60(h)</sup>.

### 1.5. GENERAL REMARKS

There is no doubt that silica is one of the most widely used inorganic oxide, particularly in catalysis, and that sol-gel processing, being a method that offers many advantages, can be used to synthesise silica gels with ease. Now that nanotechnology approaches can be applied to the silica gels, different nanostructures of silica have been found and synthesised and these have proven to be useful in many applications.

By using different templates, and different synthesis procedures more novel nanostructured silica materials can be formed in the years ahead.

### 1.6. SCOPE OF THIS WORK

Since nanostructured silica materials find wide applications and still show the potential for increased applications, methods of synthesising them need to be improved. In particular, they need to be obtained with ease, in large scale, under mild conditions. More importantly, cost effective ways of synthesising them must be found. Sol-gel processing provides a facile method of synthesis of these materials as it offers many advantages. These include the purity of the final product, the mild conditions employed and the control of porosity. Thus, this method still is the best method for synthesising such materials.

In this work, synthesis of nanostructured silica gels by the sol-gel process, using simple hydroxyacids as structure directing template precursors was done. In particular, the effects of variation of synthesis procedures, conditions and template precursors on the morphology of the resultant silica gels were investigated. Studies on the control of the porosity of the resultants gels were, however, not done in this work. The synthesised nanostructured silica gels were then used as supports for the low temperature iron Fischer-Tropsch catalyst, the effect of potassium promotion on

the activity and selectivity of the catalyst was studied and the catalyst was compared to that supported on a commercial silica gel.



**1.7. REFERENCES**

1. S. Iijima, *Nature*, 354 (1991) 56.
2. R.K. Iler, *The Chemistry of Silica: Solubility, Polymerisation, Colloid and Surface Properties, and Biochemistry*, Wiley, New York, 1979.
3. (a) P.P. Keat, *Science*, 120 (1954) 328.  
(b) L.Coes, Jr., US Patent, 2,876,072 (Norton Co.) 1959.  
(c) R.W. Crose, E.M. Flanigen, U.S. Pat. 4,061,724 (Union Carbide Corp.) 1977.
4. N.Y. Chen, F.A. Smith, *Inorg. Chem.*, 15 (1976) 295.
5. H.P. Eugster, *Science*, 57 (1967) 1177.
6. C. Frondel, *The System of Mineralogy of DANA*, 7<sup>th</sup> Ed., Vol 3, Silica Minerals, Wiley, New York, 1962, p.154.
7. W.H. Huang, D.L. Vogler, *Nature, Phys. Sci.*, 235 (1972) 157.
8. C.J. Brinker, G.W. Scherer, *Sol-Gel Science- The Physics and Chemistry of Sol-Gel Processing*, Academic Press, Carlifornia, 1990.
9. J.D. Wright, N.A.J.M. Sommerdijk, *Sol-Gel Materials, Chemistry and Applications*, Taylor and Francis, London, 2001.
10. P.B. Vandiver, *Scientific American*, 262 (1990) 106.
11. T. Graham, *J. Chem. Soc.*, 17 (1864) 318.
12. C.B. Hurd, *Chem. Rev.*, 22 (1938) 403.
13. S.S. Kistler, *J. Phys. Chem.*, 36 (1932) 52.
14. R.M. Barrer, L. Hinds, *Nature*, 166 (1950) 562.
15. R. Roy, *J. Am. Cer. Soc.*, 39 (1956) 145.
16. J.L. Woodhead, *Silicates Ind.*, 37 (1972) 191.
17. L. Levene, I.M. Thomas, U.S. Patent 3,640,093 (1972).
18. H. Dislich, *Angew. Chem.*, 10 (1971) 363.
19. H.G. Sowman, U.S. Patent 3,795,524 (1974).
20. S. Horikuri, K. Tsuji, Y. Abe, A. Fukiu, E. Ichiki, Japanese Patent 49,108325 (1974).
21. L. Kutik, *J. Coat. Technol.*, 58 (1986) 91.

22. C.J. Brinker, Mater. Res. Soc. Symp. Proc., 284 (1993) 469.
23. J. Fricke, A. Emmerling, Adv. Mater., 3 (1991) 504.
24. L.L. Hench, Ceram. Trans., 29 (1993) 591.
25. G. Cao, *Nanostructures and Nanomaterials: Synthesis, Properties and Applications*, Imperial College Press, London, 2004.
26. K.J. Klabunde, *Nanoscale Materials in Chemistry*, Wiley-Interscience, New York, 2001, p.11.
27. N.G. Chopra, R.G. Luyken, K. Cherry, V.H. Crespi, M.L. Cohen, S.G. Louie, A. Zettl, Science, 269 (1995) 966.
28. W. Han, P.-K. Redlich, F. Ernst, M. Rühle, Chem. Mater., 11 (1999) 3620.
29. (a) R. Tenne, L. Margulis, M. Genut, G. Hodes, Nature, 360 (1992) 444.  
(b) L. Margulis, G. Salitra, R. Tenne, Nature, 365 (1993) 113.  
(c) Y. Feldman, E. Wasserman, D.J. Srolovitch, R. Tenne, Science, 267 (1995) 222.
30. M. Nath, C.N.R. Rao, J. Am. Chem. Soc., 123 (2001) 4841.
31. M. Nath, C.N.R. Rao, Angew. Chem. Int. Ed., 41 (2002) 3451.
32. D.H. Galván, J.-H. Kim, M. Maple, M. Avalos-Berja, E. Adem, Fullerene Sc. Technol., 8 (2000) 143.
33. (a) P.M. Ajayan, O. Stephane, P. K. Redlich, C. Colliex, Nature, 375 (1995) 564.  
(b) M.E. Spahr, P. Bitterli, R. Nesper, M. Müller, F. Krumeich, H.U. Nissen, Angew. Chem. Int. Ed., 37 (1998) 1263.  
(c) M. Niederberger, H.-J. Muhr, F. Krumeich, F. Bieri, D. Günther, R. Nesper, Chem. Mater., 12 (2000) 1995.
34. A. Doble, K. Ngala, S. Yang, P.Y. Zavalji, M.S. Whittingham, Chem. Mater., 13 (2001) 4382.
35. H. Nakamura, Y. Matsui, J. Am. Chem. Soc., 117 (1995) 2651.
36. (a) H. Imai, Y. Takei, K. Shimizu, M. Matsuda, H. Hirashima, J. Mater. Chem., 9 (1999) 2971.  
(b) D. Gong, C.A. Grimes, O.K. Varghese, W. Hu, R.S. Singh, Z. Chen, E.C.

- Dickey, J. Mater. Res., 16 (2001) 3331.
37. L. Pu, X. Bao, J. Zou, D. Feng, Angew. Chem. Int. Ed., 40 (2001) 1490.
38. J. Zhang, A. Reller, Chem. Commun., (2002) 606.
39. B. Cheng, E.T. Samulski, J. Mater. Chem., 11 (2001) 2901.
40. M. Yada, M. Mihara, S. Mouri, M. Kuroki, T. Kijima, Adv. Mater., 14 (2002) 309.
41. B.A. Hernandez, K.-S. Chang, E.R. Fischer, P.K. Dorhout, Chem. Mater., 14 (2002) 480.
42. Y.R. Hachohen, E. Grunbaum, R. Tenne, J. Sloan, J.L. Hutchison, Nature, 395 (1998) 337.
43. C.J. Brumlik, C.R. Martin, J. Am. Chem. Soc., 113 (1991) 3174.
44. G. Tourillon, L. Pontonnier, J.P. Levy, V. Langlais, Electrochem. Solid State Lett., 3 (2000) 20.
45. J. Bao, C. Tie, Z. Xu, Q. Zhou, D. Shen, Q. Ma, Adv. Mater., 13 (2001) 1631.
46. B. Mayers, Y. Xia, Adv. Mater., 14 (2002) 279.
47. J.-F. Chen, H.-M. Ding, J.-X. Wang, L. Shao, Biomater., 25 (2004) 723.
48. (a) H.-M. Ding, L. Shao, R.-J. Liu, Q.-G. Xiao, J.-F. Chen, J. Colloid and Interface Sc., 290 (2005) 102.
- (b) Q.-G. Xiao, X. Tao, J.-P. Zhang, J.-F. Chen, J. Mol. Catal. B: Enzym., 42 (2006) 14.
49. M. Kim, K. Sohn, J. Kim, T. Hyeon, Chem. Commun., (2003) 652.
50. (a) D.T. Mitchell, S.B. Lee, L. Trofin, N. Li, T.K. Nevanen, H. Söderlund, C.R. Martin, J. Am. Chem. Soc., 124 (2002) 11864.
- (b) S.J. Son, J. Reichel, B. He, M. Schuchman, S.B. Lee, J. Am. Chem. Soc., 127 (2005) 7316.
51. (a) E.M. Mokoena, *Synthesis and use of Silica Materials as Supports for the Fischer-Tropsch reaction*, PhD thesis, University of the Witwatersrand, Johannesburg (2005).
- (b) S. Naito, K. Minoshima, T. Miyao, Top. Catal., 39 (2006) 131.

52. F. Miyaji, S.A. Davis, J.P.H. Charmant, S. Mann, *Chem. Mater.*, 11 (1999) 3021.
53. F. Miyaji, Y. Watanabe, Y. Suyama, *Mater. Res. Bull.*, 38 (2003) 1669.
54. L. Wang, S. Tomura, F. Ohashi, M. Maeda, M. Suzuki, K. Inukai, *J. Mater. Chem.*, 11 (2001) 1465.
55. (a) B.D. Yao, D. Fleming, M.A. Morris, S.E. Lawrence, *Chem. Mater.*, 16 (2004) 4851.
- (b) F.S.M. Textor, U.G.G. Roewer, *J. Mater. Sc. Lett.*, 18 (1999) 599.
- (c) M. Zhang, E. Ciocan, Y. Bando, K. Wada, L.L. Cheng, P. Pirouz, *Appl. Phys. Lett.*, 80 (2002) 491.
56. (a) J.-X. Wang, L. -X. Wen, Z.-H. Wang, M. Wang, L. Shao, J.-F. Chen, *Scripta Mater.*, 51 (2004) 1035.
- (b) C. Hippe, M. Wark, E. Lork, G. Schulz-Ekloff, *Microporous and Mesoporous Mater.*, 31 (1999) 235.
- (c) S.O. Obare, N.R. Jana, C.J. Murphy, *Nanolett.*, 1 (2001) 601.
- (d) Y. Chen, X. Xue, T. Wang, *Nanotechnol.*, 16 (2005) 1978.
- (e) Y.D. Lin, Y. Lu, Y.G. Sun, Y. N. Xia, *Nanolett.*, 2 (2002) 427.
- (f) J. Zygmunt, F. Krumeich, R. Nesper, *Adv. Mater.*, 15 (2003) 1538.
57. (a) R. Fan, Y.Y. Wu, D.Y. Li, M. Yue, A. Majumdar, P.D. Yang, *J. Am. Chem. Soc.*, 125 (2003) 5254.
- (b) C. Liang, Y. Shimizu, T. Sasaki, H. Umehara, N. Koshizaki, *J. Mater. Chem.*, 14 (2004) 248.
58. (a) W. Dong, W. Li, K. Yu, K. Krishna, L. Song, X. wang, Z. wang, M.-O. Coppens, S. Feng, *Chem. Commun.*, (2003) 1302.
- (b) J. Wang, J. Zhang, B.Y. Asoo, G.D. Stucky, *J. Am. Chem. Soc.*, 125 (2003) 13966.
- (c) S. Han, W. Hou, W. Dang, J. Xu, J. Hu, D. Li, *Mater. Lett.*, 57 (2003) 4520.
59. Y. Le, J.-F. Chen, J.-X. Wang, L. Shao, W.-C. Wang, *Mater. Lett.*, 58 (2004) 2105.
60. (a) Y. Ono, K. Nakashima, M. Sano, Y. Kanekiyo, K. Inoue, J. Hojo, S. Shinkai,

- Chem. Commun., (1998) 1477.
- (b) J.H. Jung, Y. Ono, S. Shinkai, *Angew. Chem. Int. Ed.*, 39 (2000) 1862.
- (c) J.H. Hung, Y. Ono, S. Shinkai, *J. Chem. Soc. Perkin Trans.*, 2 (1999) 1289.
- (d) J.H. Jung, Y. Ono, S. Shinkai, *Langmuir*, 16 (2000) 1643.
- (e) N. Amanokura, Y. Kanekiyo, S. S. Shinkai, D.N. Reinhoudt, *J. Chem. Soc. Perkin Trans.*, 2 (1999) 1995.
- (f) R.J.H. Hafkamp, M.C. Freiters, R.J.M. Nolte, *J. Org. Chem.*, 64 (1999) 412.
- (g) U. Beginn, S. Keinath, M. Möller, *Macromol. Chem. Phys.*, 199 (1998) 2379.
- (h) J.H. Jung, M. Amaike, K. Nakashima, S. Shinkai, *J. Chem. Soc. Perkin Trans.*, 2 (2001) 1938.
61. D.P. Yu, Q.L. Hang, Y. Ding, H.Z. Zhang, Z.G. Bai, J.J Wang, Y.H. Zou, W. Qian, G.C. Xiong, S.Q. Feng, *Appl. Phys. Lett.*, 73 (1998) 3076.
62. C.H. Liang, L.D. Zhang, G.W. Meng, Y.W. Wang, Z.Q. Chu, *J. Non-Cryst. Solids*, 277 (2000) 63.
63. Y.W. Wang, C.H. Liang, G.W. Meng, X.S. Peng, L.D. Zhang, *J. Mater. Chem.*, 12 (2002) 651.
64. W.J. Kim, S.M. Yang, *Chem. Mater.*, 12 (2000) 3227.
65. S.V. Patwardhan, N. Mukherjee, S.J. Clarson, *J. Inorg. Organomet. Polymers*, 11 (2002) 117.
66. I.G. Loscertales, A. Barrero, M. Márquez, R. Spretz, R. Valerde-Ortiz, G. Larsen, *J. Am. Chem. Soc.*, 126 (2004) 5376.
67. R.A. Caruso, M. Antonietti, *Chem. Mater.*, 13 (2001) 3272.
68. K.J.C. Bommel, S. Shinkai, *Langmuir*, 18 (2002) 4544.

## **CHAPTER 2**

### **A SYSTEMATIC STUDY OF PARAMETERS GOVERNING MORPHOLOGIES OF OXALATE ION SOL-GEL TEMPLATED SILICA GELS**

#### **2.1. INTRODUCTION**

The shaping and synthesis of both inorganic and organic materials can be achieved at both the macroscopic and microscopic levels and indeed today the general principles to make ‘shaped’ materials are even to be found in the popular scientific literature<sup>1</sup>. Two generic procedures to make molecules with ‘shape’ represent the ‘top down’ and ‘bottom up’ approaches to materials synthesis, both with advantages and disadvantages determined by the final product composition, product properties, cost etc<sup>2</sup>. The recent advances in the ‘bottom up’ approach to molecular shape control, driven by self-assembly, templating and dendrimer synthesis has led to new strategies to materials synthesis where fine control of structure is possible. Thus, the synthesis of inorganic-organic hybrids in which the components are linked together in a precise relationship permits the synthesis of naturally occurring bio-minerals and hence a biomimetic approach to materials synthesis<sup>3</sup>.

Recently it has been shown that templates can be used to transfer structural information, from the template to inorganic molecules/ions such that the shape (and even the chirality) of the newly formed material can now be predicted<sup>4,5</sup>. An excellent review by Shinkai and co-workers has recently summarised the current status of templating procedures on inorganic materials<sup>4</sup>

One of the procedures used to transfer shape to inorganic molecules and ions is via the use of organic crystals as templates. This approach, although currently limited to

the synthesis of spheres and rods/tubes/fibres, generally leads to facile template removal from the final structure (heating, solvent extraction). Indeed, Nakamura and Matsui<sup>6</sup> were the first to reveal the utility of this approach in the synthesis of silica tubes starting from TEOS (tetraethylorthosilicate) and using DL-tartaric acid as template precursor. Since this study, a number of other reports have appeared extending the approach to other similar template precursors, both organic (e.g. citric acid)<sup>7,8,9</sup> and inorganic ( $[\text{Pt}(\text{NH}_3)_4(\text{HCO}_3)_2]$ )<sup>10</sup>, as well as to produce transition metal oxides ( $\text{TiO}_2$ ,  $\text{Nb}_2\text{O}_5$ ,  $\text{ZrO}_2$  and  $\text{Ta}_2\text{O}_5$ <sup>11</sup>,  $\text{V}_3\text{O}_7$ <sup>12</sup>).

The shape of the inorganic material formed in the synthesis has been shown to relate to the shape of the crystalline template with the diameter and length of tubular materials determined by the synthesis conditions<sup>7,8</sup>. For example, transcription of shape by use of ammonium tartrate as template is proposed to occur via an interaction between the  $\text{NH}_4^+$  ions in the template and the silicate ions in basic solution<sup>6,8</sup>.

In this study oxalic acid (chemical structure shown in **Fig. 2.1**), a dicarboxylic acid, was used as a template-precursor to prepare silica gels. In particular, silica gels were synthesised using a range of synthesis conditions in order to study their effects on formation of different morphologies of silica gel.

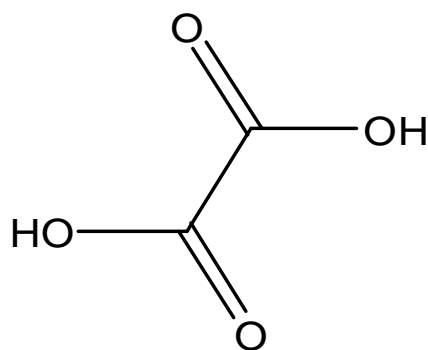


**Figure 2.1.** Chemical structure of Oxalic Acid

This chapter is divided into two parts, in Part A the study of the effect of synthesis conditions on the morphology of synthesised silica in the presence of ammonia as a base catalyst for the condensation reaction was done, and in Part B the use of potassium hydroxide and sodium hydroxide as base catalysts for the condensation reaction in comparison to ammonium hydroxide was studied.

## 2.2. EXPERIMENTAL

### 2.2.1. Reagents and Chemicals

Ethanol (Saarchem, 99.9%), methanol (Saarchem, 99%), isopropanol (Saarchem, 99%), distilled water, tetraethylorthosilicate (TEOS); (Aldrich, 98%), oxalic acid (Saarchem, 99%), ammonium hydroxide (Fluka, 28%), sodium hydroxide pellets (Saarchem, 98%), and potassium hydroxide pellets (Saarchem, 85 %) were used as chemical sources. All chemicals were used as received. The synthesis procedure followed a standard approach and a typical synthesis is outlined below. Both the yield and product morphology were determined after each synthesis.

### 2.2.2. Synthesis Procedure

#### *Part A: A Systematic Study of Parameters Governing Morphologies of Ammonium Oxalate Templated Sol-Gel Silica Gels*

In a typical synthesis, 42.5 mmol of template precursor, oxalic acid, was dissolved in a mixture of 0.7 ml of distilled water and 30 ml of ethanol. The silicon precursor, TEOS (6 ml), was then added to the mixture to form a sol, which was magnetically stirred at a speed of 300 rpm for 2 h at room temperature (25 °C). Finally, 12 ml of  $\text{NH}_4\text{OH}$  (containing 170 mmol  $\text{NH}_3$ ) was added drop-wise over 30 min to the



mixture to form a gel. The gel was then aged for 2 h at room temperature, dried in an oven at 100 °C for 48 h and then calcined under static air at 600 °C for 6 h (see **Scheme 2.1**).

**(a) Blank experiments:** The synthesis was carried out at 25 °C and 75 °C, in the absence of oxalic acid. All other parameters were kept constant.

**(b) Variation of temperature:** The synthesis procedure outlined above was performed as described except that the synthesis temperature was varied (75 °C, 55 °C, 25 °C, and 0 °C).

**(c) Variation of amount of oxalic acid:** All parameters were kept constant, as described above except for the amount of oxalic acid used (42.5, 63.8, and 85.0 mmol). The synthesis was also carried out at 25 °C, 55 °C, and 75 °C .

**(d) Variation of amount of water:** The synthesis was carried out at room temperature and all parameters except the amount of water were kept constant. The total solvent volume was kept constant at 30.7 ml. The percentage of water in ethanol used was 100 %, 75 %, 50 %, 25 %, and 0 % (by volume).

**(e) Variation of  $\text{NH}_4\text{OH}$  concentration:** The synthesis was carried out at room temperature with a 1:1 ratio of water:ethanol; concentrations of  $\text{NH}_3$  used were 7 %, 14 %, 21 % and 28 % (by volume) in water. All other parameters were kept constant.

**(f) Variation of length of TEOS hydrolysis time:** The synthesis was carried out at room temperature; all parameters were kept constant except for TEOS hydrolysis time (i.e. time before addition of  $\text{NH}_4\text{OH}$ ); which was varied from 1 min to 24 h.

**(g) Variation of length of ageing time:** The synthesis was carried out at 75 °C; all parameters were kept constant except for the length of ageing time, which was varied from 1 min to 24 h.

**(h) Variation of organic co-solvent:** The synthesis was carried out at room temperature; the organic co-solvent and the amount of water relative to the organic co-solvent were varied. Methanol, ethanol and isopropanol were used as organic cosolvents, and the water amount relative to the organic co-solvent used were 75, 50, 25 and 2.3 % (by volume). All other parameters were kept constant.

**(i) Variation of synthesis procedure:** The ‘short method’ synthesis procedure presented in **Scheme 2.2** was used. In this method, hydrolysis and condensation of TEOS were done simultaneously. The materials were synthesised at room temperature. An amount of 42.5 mmol of oxalic acid was dissolved in 30.7 ml of an ethanol and water mixture, the water relative to ethanol amount used was 2.3, 25, 50 and 75 %. To the acidic mixture, 12 ml of ammonium hydroxide, containing 170 mmol NH<sub>3</sub> was added all at once without stirring, and a white precipitate of ammonium oxalate was formed. Subsequently, 6 ml (27 mmol) of TEOS was added rapidly, and the resulting gel stirred for 30 min, and was then aged for 2 h. After ageing, the gel was dried at 100 °C for 48 h, and then calcined in static air at 600 °C for 6 h.

***Part B: Synthesis of Silica Gel by the Templated Sol-Gel Procedure - Effect of Different Base Catalysts***

The materials were synthesised by the ‘long method’ synthesis procedure, unless otherwise stated. The silica materials synthesised with KOH and NaOH, after ageing, were washed with distilled water by centrifugation until the conductivity remained constant, and then dried at 100 °C for 48 h, prior to calcinations in static air at 600 °C for 6 h.

**(j) Variation of oxalic acid amount:** Materials were synthesised at room temperature, 42.5 or 85 mmol of oxalic acid, 12 ml of base (85mmol of KOH, 85 mmol of NaOH, or 170 mmol of NH<sub>4</sub>OH) was used.

**(k) Variation of base catalyst and amount thereof:** Materials were synthesised at room temperature, 85 mmol of oxalic acid (42.5 mmol in the case of NH<sub>4</sub>OH), water relative to ethanol amount of 2.3 % (50 % in the case of NH<sub>4</sub>OH), and 12 ml of base (potassium hydroxide, sodium hydroxide, or ammonium hydroxide) with amounts of either 85 or 175 mmol were used.

Synthesis of silica materials with 42.5 mmol oxalic acid and 170 mmol KOH/NaOH, 2.3, 25 and 50 % H<sub>2</sub>O, were attempted but the silica that precipitated dissolved during addition of base.

**(l) Variation of water relative to ethanol amount with different base catalysts:** Materials were synthesised at room temperature; 42.5 mmol of oxalic acid, 12 ml of base KOH (85 mmol), NaOH (85 mmol), or NH<sub>4</sub>OH (170 mmol) and amounts of water relative to ethanol 50, 25, and 2.3 % (by volume), were used in the synthesis. All other parameters were kept the same.

**(m) Variation of synthesis procedure:**

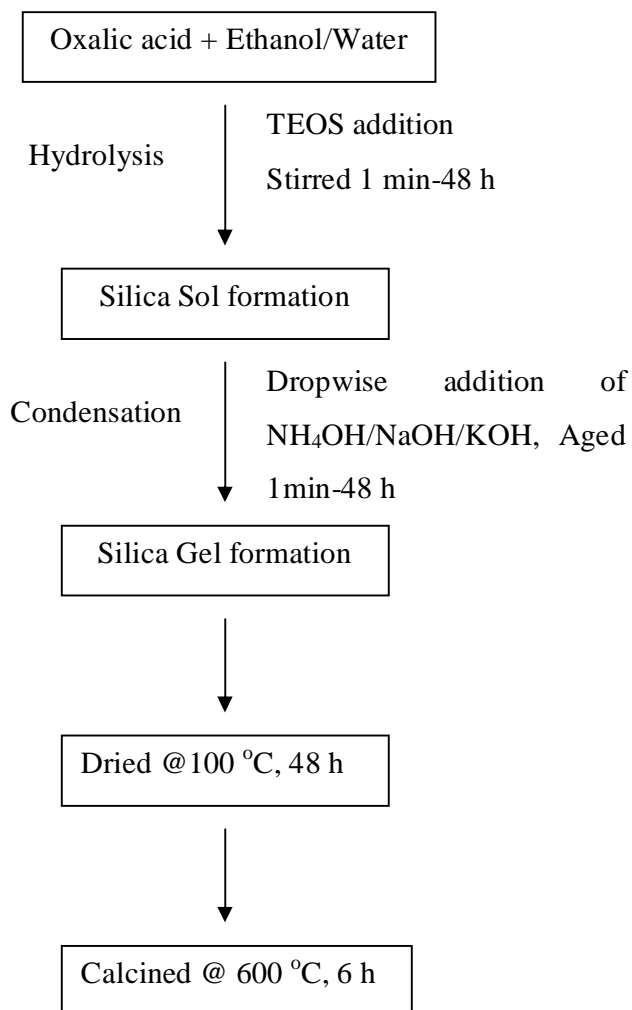
**(i) Long method (see Scheme 2.1)**

Materials were synthesised at room temperature; Oxalic acid, 42.5 mmol, was dissolved in an ethanol and water mixture, containing 2.3 % H<sub>2</sub>O. TEOS (27 mmol) was added and the mixture stirred for 2 h. A volume of 12 ml of base (85 mmol of KOH, 85 mmol of NaOH, or 170 mmol of NH<sub>4</sub>OH) was added dropwise for 30 min to form a gel, and the resulting gel aged for 2 h. The gel was dried at 100 °C for 48 h, and then calcined in static air at 600 °C for 6 h.

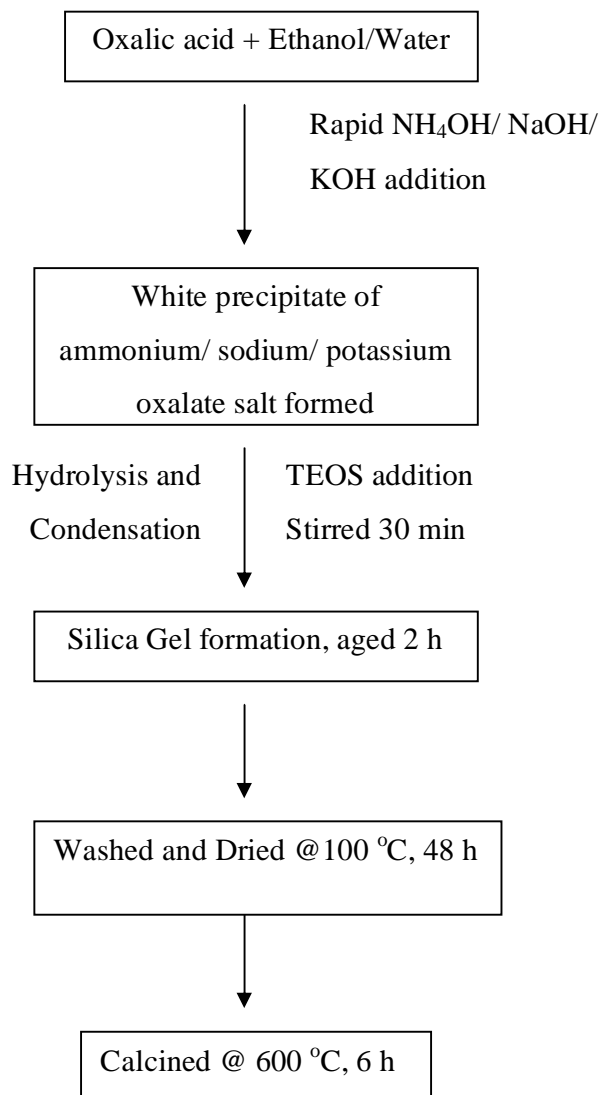
**(ii) Short method (see Scheme 2.2)**

Materials were synthesised at room temperature; Oxalic acid, 42.5 mmol, was dissolved in an ethanol and water mixture, containing 2.3 % H<sub>2</sub>O. A volume of 12 ml of base (85 mmol KOH, 85 mmol KOH, or 170 mmol NH<sub>4</sub>OH) was then added rapidly without stirring. This was followed by subsequent addition of 27 mmol TEOS and the resulting gel was stirred for 30 min, followed by ageing for 2 h. The resulting gel was dried at 100 °C for 48 h, and then calcined in static air at 600 °C for 6 h.

**(n) *Precipitation of potassium, sodium and ammonium oxalate salts:*** The salts were precipitated at room temperature; 85 mmol (42.5 mmol in the case of ammonium oxalate) oxalic acid was dissolved in a 30 ml water/ethanol mixture containing 2.3 % H<sub>2</sub>O (50 % H<sub>2</sub>O in the case of ammonium oxalate), and 12 ml of NaOH, KOH, or NH<sub>4</sub>OH, containing 170 mmol Na<sup>+</sup>, K<sup>+</sup>, and NH<sub>4</sub><sup>+</sup> ions was added dropwise for 30 min, with concurrent stirring of the mixture. The resulting salt was then filtered and dried on a frit at room temperature.



**Scheme 2.1.** Schematic representation of the ‘long method’ synthesis procedure used to make the templated silica.



**Scheme 2.2.** Schematic representation of the ‘short method’ synthesis procedure used to make the templated silica.

### 2.2.3. Characterisation

**2.2.3.1. Transmission Electron Microscopy.** Transmission electron microscopy images were observed with a JEOL-100S electron microscope with an acceleration voltage of 80 kV. Samples were prepared by sonicating about 100 mg of sample in 2 ml of ethanol for at least 5 minutes and then 2 drops of the suspension were placed on a Cu grid coated with carbon film. After approximately one minute, excess liquid was removed by touching one edge of the grid with a Whatman filter paper.

**2.2.3.2. Scanning Electron Microscopy.** The silica samples were coated with gold coating prior to analysis. A Hitachi S-2700 scanning electron microscope (SEM) fitted with a LaB<sub>6</sub> gun was used for photo imaging. The microscope was run at a voltage of 15 keV and a current of 75  $\mu$ A.

For the analysis of potassium, sodium and ammonium oxalate salts, scanning electron microscopy images were recorded on a JSM 840 electron microscope with an acceleration voltage of 10 kV and a working distance of 15 mm. Prior to analysis, samples were coated with a gold-palladium coating.

**2.2.3.3. N<sub>2</sub> Physisorption.** The nitrogen adsorption and desorption isotherms were measured at -196 °C (77 K) using a Micromeritics ASAP 2010 instrument. The Brunauer-Emmet-Teller (BET) surface area was calculated from the adsorption isotherms and Barret-Joyner-Halenda (BJH) method was used to determine the pore size distribution. Degassing of the samples for 24 h at 0.1 Pa at 120 °C preceded every measurement. Specific adsorption pore volumes were calculated by the BJH method that is assumed to cover the cumulative adsorption pore volume of pores in the range 1.7 to 300 nm in diameter.

**2.2.3.4. Powder X-Ray Diffraction.** X-Ray powder diffraction measurements were carried out on a Philips PW 1830 Diffractometer generator, equipped with a Ni-filtered CuK $\alpha$  radiation source. The measurements were carried out in the 1.5-60 ° 2 $\theta$  range at a generator voltage of 40 kV and a current of 20 mA. A scan rate of 2 ° per step was used.

**2.2.3.5. Thermal Analysis.** Thermogravimetric analyses were performed with a Perkin Elmer Pyris 1 TGA Thermogravimetric Analyser using nitrogen as the purge gas, at a flow rate of 20 ml per minute, and a heating rate of 5 °C per minute.

The amounts and sizes of the various silica shapes produced in the syntheses were estimated (as percentages) by standard measurement/counting procedures from TEM photographs. The distribution data was divided amongst four different morphological types: hollow spheres, solid spheres, tubes and irregularly shaped (referred to as ‘amorphous’ in the text and tables) material.



---

***PART A: A SYSTEMATIC STUDY OF PARAMETERS  
GOVERNING MORPHOLOGIES OF AMMONIUM OXALATE  
SOL-GEL TEMPLATED SILICA GELS***

## **2.3. RESULTS AND DISCUSSION**

### **2.3.1. General Comments**

**Fig. 2.2** shows the powder X-Ray diffractogram of a typical silica product produced in the presence of oxalic acid after calcination. The calcined material shows only one broad peak centred at 22 degrees  $2\theta$ , indicating that the silica framework is noncrystalline. All samples measured in this work gave a similar XRD profile.

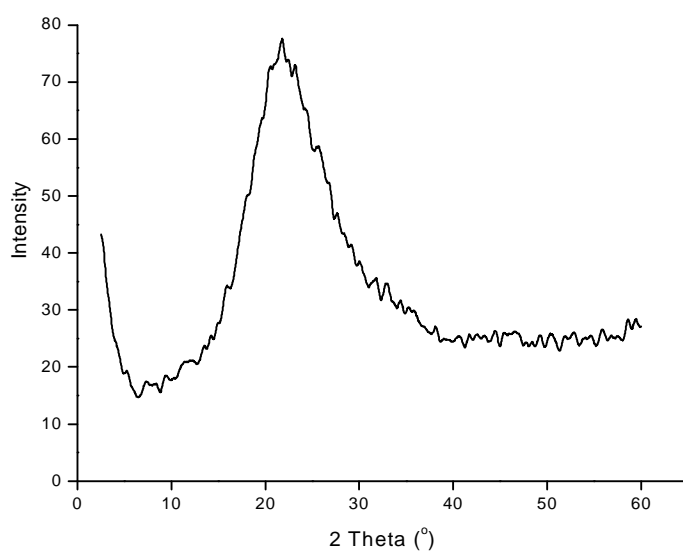


**Figure 2.2.** Powder XRD pattern of calcined material, synthesized with 42.5mmol oxalic acid at 25 °C.

**Fig. 2.3** shows a typical isotherm of a calcined silica sample. It reveals a type II isotherm which is typical of non-porous or macroporous materials<sup>13,14</sup>. A BJH pore size distribution determined from the adsorption arm, shown in the inset in **Fig. 2.3**, indicated the presence of some micropores and a range of mesopores (4-8 nm), and the presence of macropores was indicated by the hysteresis loop not levelling off at the x-axis. Similar results were noted in the pore size distribution determined from the desorption arm but the data also indicated a meniscus instability at about 3 nm for most samples. In general, surface areas obtained from micropores were 4-9 % of the total surface area of the materials.

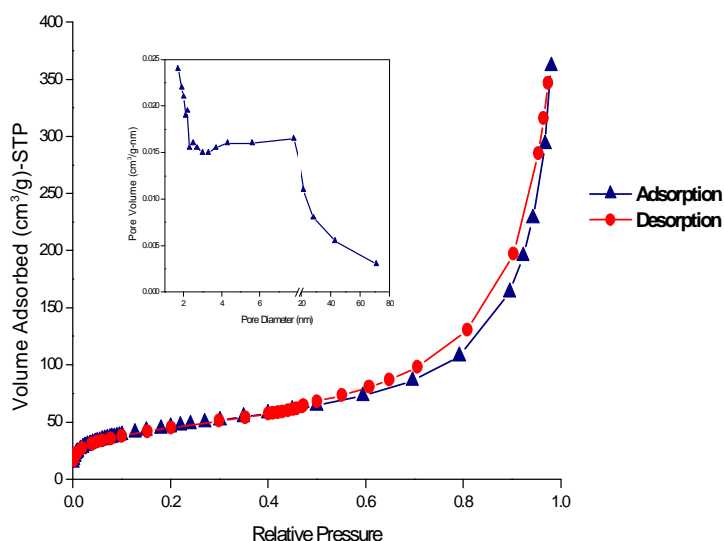


**Figure 2.3.** Nitrogen adsorption-desorption isotherm and (inset) BJH pore size distribution (determined from the adsorption arm) of silica material synthesized with 42.5 mmol oxalic acid, 170 mmol  $\text{NH}_4\text{OH}$  and 2.3%  $\text{H}_2\text{O}$  at 25 °C.

### 2.3.2. Variation of Temperature

Blank syntheses were performed for comparison purposes. At room temperature in the absence of oxalic acid only solid spheres were obtained, shown in **Fig. 2.4a**, while at 75 °C about 5 % solid spheres were obtained with the rest being amorphous material, shown in **Fig. 2.4b**. Conditions used in these syntheses are similar to those used to prepare Stöber spheres<sup>15</sup>. No tubes or hollow spheres were obtained in the absence of template.

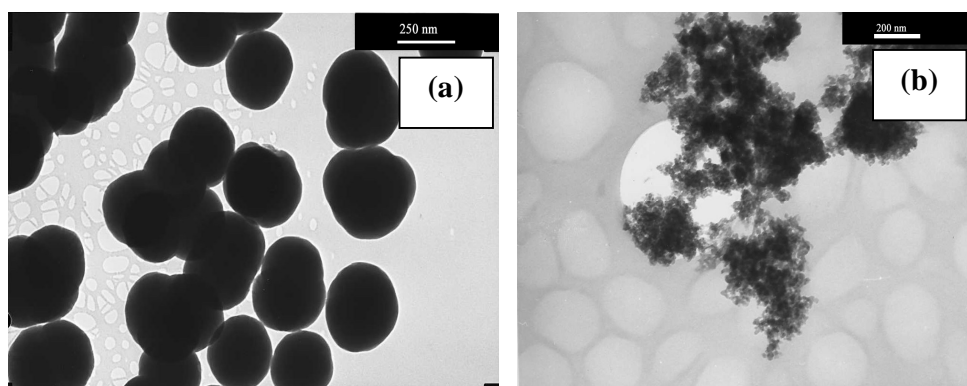


**Figure 2.4.** TEM images of silica materials synthesised in the absence of oxalic acid at (a) 25 °C and (b) 75 °C.

The syntheses at a constant oxalate concentration (42.5 mmol) were performed at four different temperatures (75, 55, 25, and 0 °C) – the upper and lower bounds being set by the boiling point of ethanol and freezing point of water respectively.

The materials were analysed by TEM and SEM. **Fig. 2.5** shows the SEM image of a typical material. It shows the presence of tubes, spheres and some undeveloped particles.



**Figure 2.5.** An SEM image of a typical material synthesised at 25 °C.

**Fig. 2.6a** and **2.6b** show the TEM images of a typical material that comprises predominantly tubes and hollow spheres (and some amorphous material). The numerous long hollow tubes and hollow (and solid) spheres all have ‘clean’ surfaces. However, temperature had a significant effect on the appearance of the materials formed. Both the tubes and the hollow spheres obtained at 55 and 75 °C were found to have surface attached colloidal particles (e.g. **Fig. 2.6c**, 75 °C) as was found by other workers<sup>8</sup>. This is indicated in **Table 2.1** where the amorphous material content increases with an increase in temperature.

The distribution of the material amongst the various shapes as a function of synthesis conditions is given in **Table 2.1**. It is clear that increasing temperature (at fixed oxalate/silica ratio) led to an increase in amorphous material and a decrease in solid spheres and tubes.

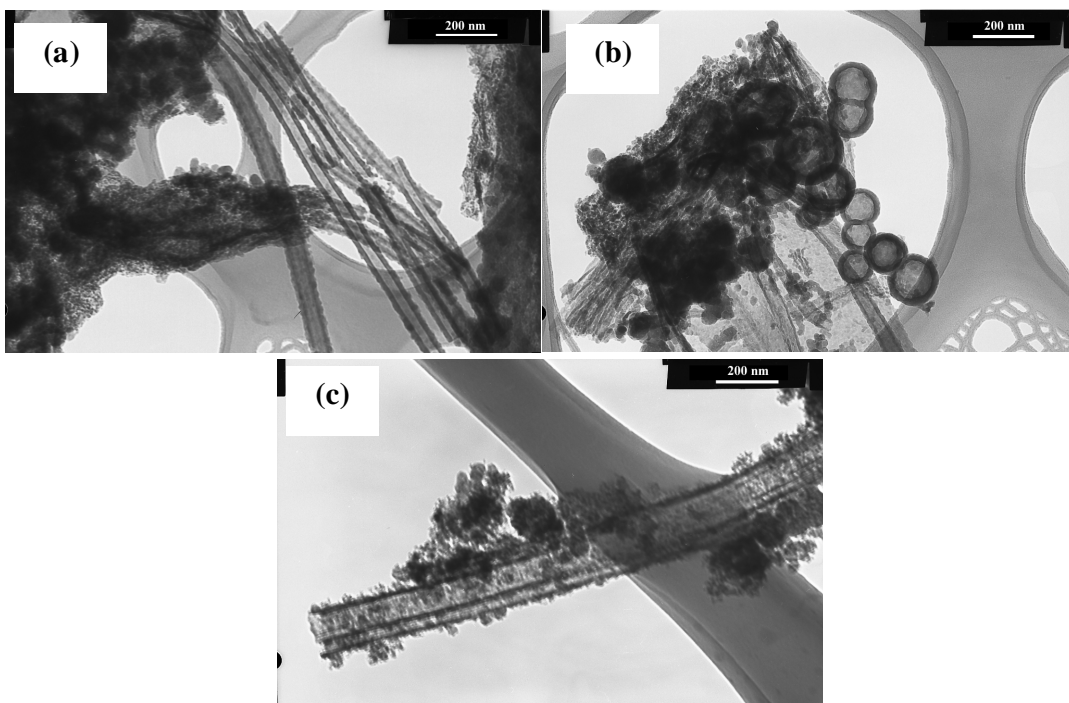


**Figure 2.6.** TEM images of (a) tubes synthesised at 25 °C, (b) hollow spheres and (c) a mixture of tubes and amorphous material synthesised at 75 °C. Materials were synthesized using oxalic acid (42.5 mmol).

Syntheses at different temperatures but as a function of oxalate ion concentration were also performed (63.8 and 85 mmol oxalate ions; **Table 2.1**). In general similar trends were found at all concentrations. However, a sharp increase in hollow sphere formation at 75 °C (85 mmol oxalic acid) was observed. This is believed to arise from the high concentration of oxalic acid and some evaporation of ammonia leading to the presence of less ammonium oxalate rod-like template crystals for tube formation.

**Table 2.1.** Effect of the amount of oxalic acid and the synthesis temperature on particle distribution and surface area of the silica materials.

Temp °C	Acid Amount (mmol)	Tubes (%)	Hollow Spheres (%)	Solid Spheres (%)	Amorph* Material (%)	BET S.A. <sup>#</sup> (m <sup>2</sup> /g)
75	42.5	35	5	0	60	318
75	63.8	30	20	5	40	231
75	85.0	15	60	0	25	250
55	42.5	25	30	5	45	210
55	63.8	30	25	5	35	172
55	85.0	35	20	5	35	194
25	42.5	35	35	15	15	160
25	63.8	40	20	25	15	106
25	85.0	45	20	30	5	115
0	42.5	15	55	10	20	236

\*-Amorphous, <sup>#</sup> - Surface area

### 2.3.3. Variation of Oxalic Acid Concentration

From **Table 2.1** above it can be observed that increasing the oxalate ion concentration affected both tube and sphere formation. At high temperature (75 °C) tube formation decreased while sphere formation increased as the oxalate ion concentration was increased. At the lower temperatures a reverse situation was seen. The results suggest that at low oxalate ion concentration there were less ammonium oxalate rod crystals available for the silica to assemble around, hence leading to preferential formation of spheres. This suggests that the oxalate ions formed two

types of templates, with rod-like templates favoured at high concentration and sphere shaped templates at lower concentrations.

**Table 2.2** shows the effect of the amount of oxalate ion on tube size. The longest tubes were obtained at 25 °C, which implies that at higher temperatures, (i) template crystals were smaller and/or (ii) template dissolution was faster. Shorter tubes were found at 0 °C when compared to tubes formed at 25 °C. It is suggested that this relates to the slow diffusion/mobility of the reactants at this low temperature.

**Table 2.2.** Effect of the amount of oxalic acid and temperature on the silica particle size.

Temp (°C)	Acid Amount (mmol)	Hollow Sphere O.D* (nm)	Tube O.D* (nm)	Tube Length (µm)
75	42.5	50-220	34-104	0.94-7.5
75	85	86-234	36-140	0.24-8.1
55	42.5	90-313	80-337	0.20-9.0
55	63.8	125-350	83-133	0.30-12
55	85	120-288	75-100	0.25-16.8
25	42.5	165-388	50-120	0.45-22
25	63.8	80-150	30-300	1.0-19
25	85	84-240	50-225	0.44-26
0	42.5	20- 175	44-150	0.22-14.2

\* Outer diameter

### 2.3.4. Variation of Water Amount.

**Table 2.3** shows the effect of water amount on particle distribution. It was observed that the tube yield increased with an increase in the amount of water and reached a maximum between 25 – 50 %  $\text{H}_2\text{O}$ , and then decreased. It was also observed that the tube outer diameter increased with an increase in the amount of water and that the maximum tube length was found with 25 %  $\text{H}_2\text{O}$  (shown in **Table 2.4**).

TEM images from this study are shown in **Fig. 2.7**. It can be seen that the best-developed tubes were formed in ethanol rich solvent mixtures ( $\geq 50$  % ethanol). Indeed the tubes with the best-defined walls were obtained from a one-to-one water/ethanol ratio (i.e. 50 %  $\text{H}_2\text{O}$ ), shown in **Fig. 2.7d**. It is clear from the figure that both ethanol and water are necessary in the synthesis as poorly formed tubes were obtained when one of the solvents was omitted. Water is necessary for hydrolysis of the TEOS. However, since the ethoxy groups are hydrophobic, and the TEOS and water are immiscible in all proportions, it is necessary to add ethanol as a co-solvent to achieve miscibility and to facilitate hydrolysis<sup>16</sup>.

**Table 2.3.** Effect of water amount on the silica particle distribution.

<b>H<sub>2</sub>O Amount (%)</b>	<b>Tubes (%)</b>	<b>Hollow Spheres (%)</b>	<b>Solid Spheres (%)</b>	<b>Amorphous Material (%)</b>
0	10	35	5	50
2.3	35	35	15	15
25	50	5	35	10
50	50	10	30	10
75	30	5	35	30
100	20	5	40	35



**Table 2.4.** Effect of water amount on silica tube size.

<b>H<sub>2</sub>O</b> <b>Amount (%)</b>	<b>Tube O.D<sup>*</sup></b> <b>(nm)</b>	<b>Tube Length (μm)</b>
0	50-175	0.64-6.6
2.3	52-120	0.45-22
25	38-307	0.21-25
50	100-325	0.35-20.7
75	33-633	0.60-7.8
100	24-800	1.3-12.5

\* – outer diameter

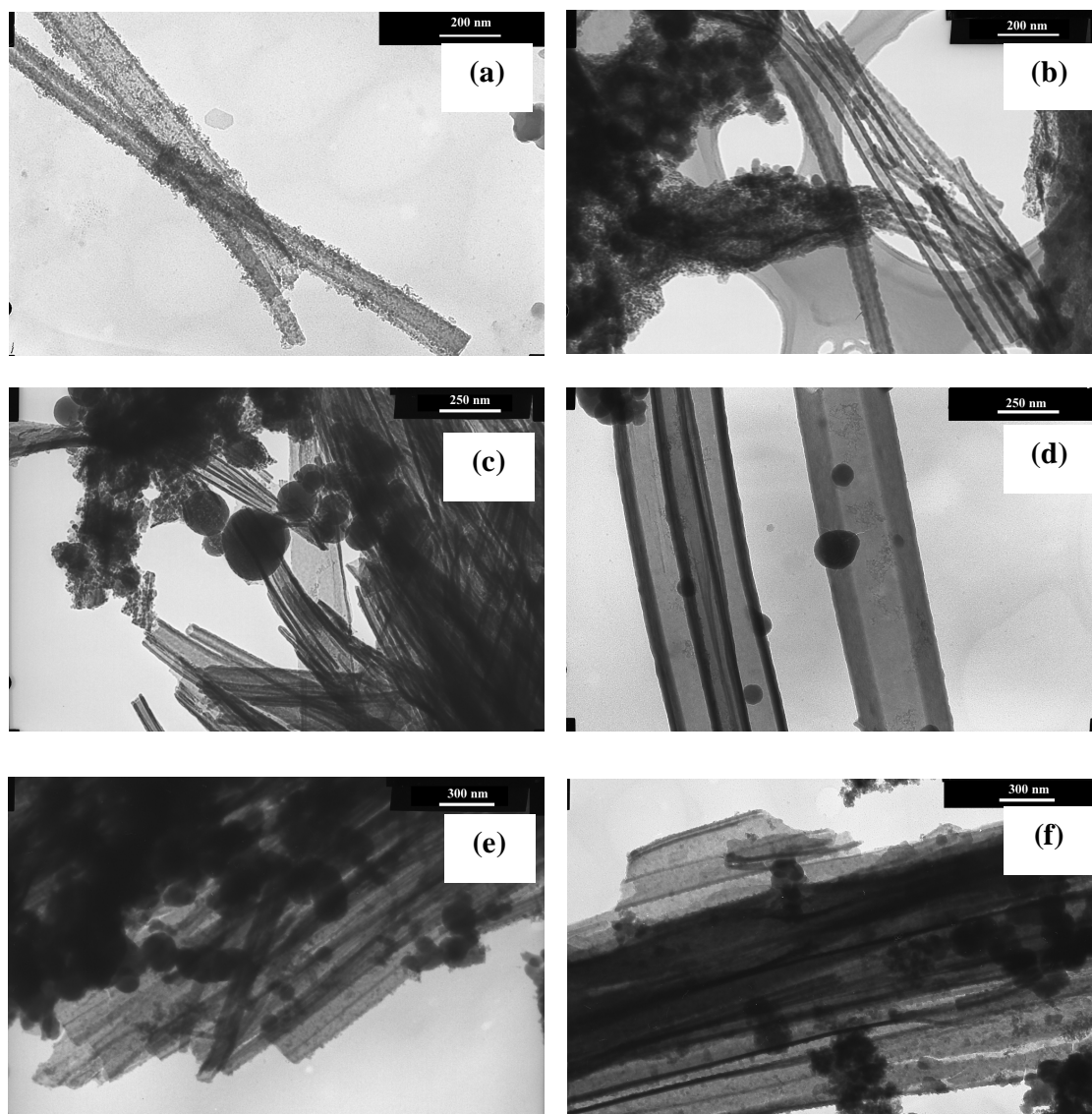


**Figure 2.7.** TEM images showing the effect of water/ethanol ratio on silica formation.

(a) 0 %, (b) 2.3 %, (c) 25 %, (d) 50 %, (e) 75 %, (f) 100 % water;  
synthesized at 25 °C.

### 2.3.5. Variation of Ammonia Concentration

The effect of ammonia concentration on the silica particle distribution is shown in **Table 2.5**. The tube yield was found to increase with an increase in the concentration of  $\text{NH}_3$  while the solid sphere yield decreased. At higher  $\text{NH}_3$  concentration there were sufficient tubular ammonium oxalate crystals for TEOS to assemble around, and the TEOS preferentially formed tubes rather than solid spheres that are normally found in the absence of oxalic acid. At 7 %  $\text{NH}_3$  more amorphous material and fewer tubes were formed due to the large amount of water present in the synthesis mixture.

**Table 2.5.** Effect of concentration of  $\text{NH}_3$  on the silica particle distribution.

<b><math>\text{NH}_3</math> Amount (%)</b>	<b>Tubes (%)</b>	<b>Hollow Spheres (%)</b>	<b>Solid Spheres (%)</b>	<b>Amorphous material (%)</b>
7	10	20	35	35
14	30	10	50	10
21	40	10	40	10
28	50	10	30	10

**Table 2.6** shows the effect of ammonia concentration on tube size. It can be seen that a significant increase in the length of the tubes occurred as the concentration of  $\text{NH}_3$  was increased. Presumably at high  $\text{NH}_3$  concentration there was less template dissolution and hence larger template crystals were formed. There was not much difference seen in the tube outer diameter when 14 to 28 %  $\text{NH}_3$  was used. However, tubes obtained with 7 %  $\text{NH}_3$  were thinner. This suggests that the thinner tubes were templated from smaller crystals that formed when less oxalate ions were ‘crystallised’. The increase in the number and length of tubes with an increase in the

concentration of  $\text{NH}_3$  observed is similar to previous results found in the presence of DL-tartaric acid <sup>9</sup>, but different to the concentration effects reported by Miyaji and co-workers <sup>8</sup>. This suggests that small changes in synthesis conditions will lead to significant changes in silica morphology.

**Table 2.6.** Effect of  $\text{NH}_3$  concentration on the silica particle size.

<b><math>\text{NH}_3</math> Amount (%)</b>	<b>Hollow Sphere O.D* (nm)</b>	<b>Tube O.D* (nm)</b>	<b>Tube Length (<math>\mu\text{m}</math>)</b>
7	66-560	20-233	2.8-8.1
14	75-300	160-320	0.7-12.4
21	80-420	40-320	0.24-16
28	100-266	100-325	0.35-20.7

\*- Outer diameter

### 2.3.6. Effect of Length of TEOS Hydrolysis Time.

When TEOS hydrolysis time (i.e. before  $\text{NH}_4\text{OH}$  addition to the oxalic acid solution) was increased from 1 min to 2 h, tubes and spheres with well-defined structure were formed during the ageing process as seen in **Fig. 2.8a, 2.8b** and **2.8c**. However, when the TEOS hydrolysis time was prolonged even further ( $> 3$  hours) fragmented and dissolving tubes with surface attached particles, and hollow spheres with thinner walls were observed (shown in **Fig. 2.8d, 2.8e, 2.8f**). A similar effect was mentioned previously for tubes formed in the presence of DL-tartaric acid<sup>9</sup>. The data suggest that templating must occur immediately and occurs more rapidly than the silica condensation reactions. Once formed, the tube and sphere walls thicken but after a certain time, dissolution of the metastable silica tubes/spheres commences.

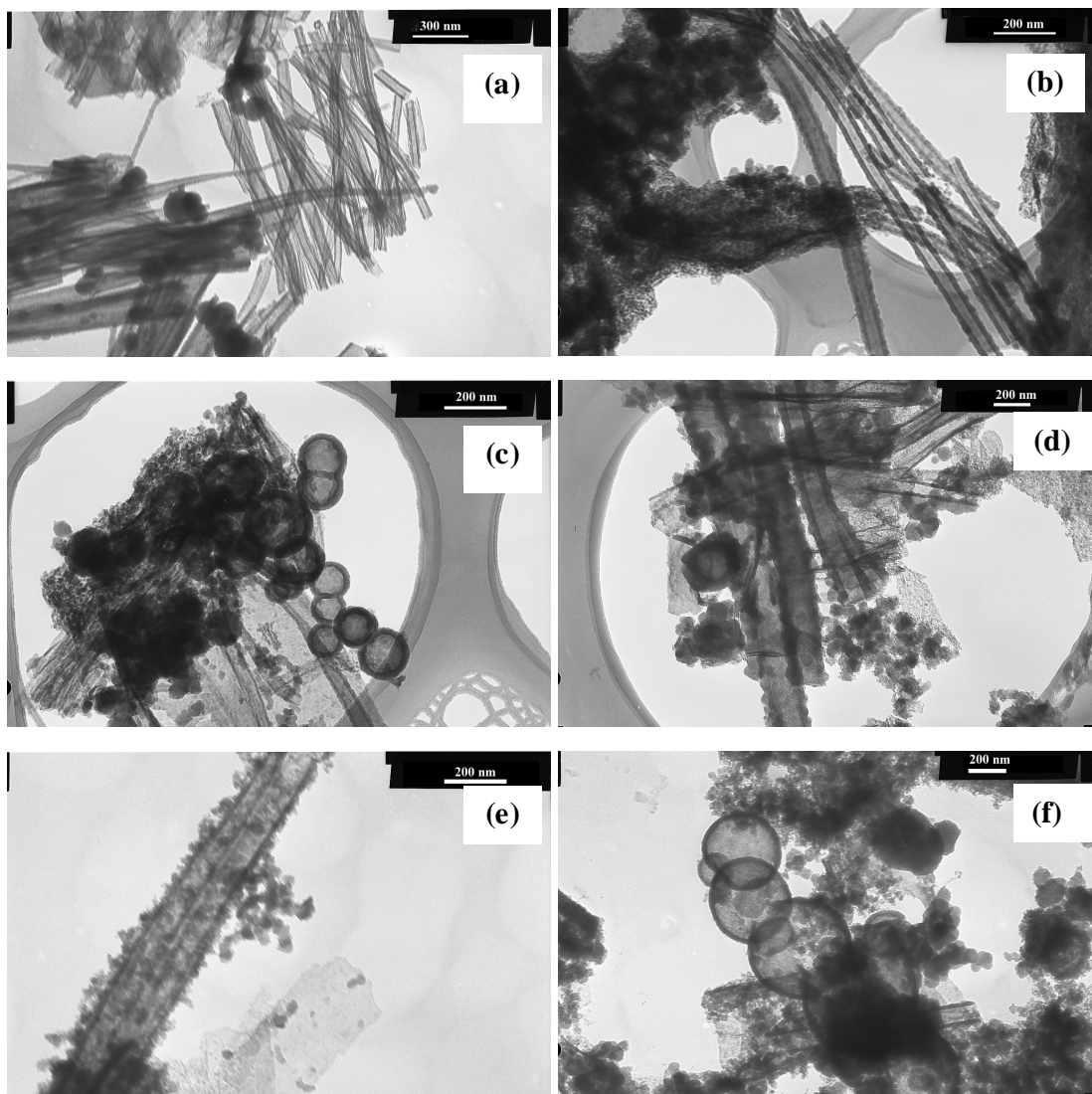


**Figure 2.8.** TEM images showing the effect of length of TEOS hydrolysis at 25°C on silica structure formation and dissolution. (a) 1 min, (b) 2 h (tubes), (c) 2 h (spheres), (d) 6 h, (e) 24 h (tubes), (f) 24 h (spheres).

### 2.3.7. Effect of Length of Ageing Time

The length of ageing time (after all reagents were added together) was also used to study the formation/dissolution effects on the silica structures. A high temperature

was used to enhance any secondary effects that would occur. TEM images of the silica materials (synthesized at 75 °C) as a function of time are shown in **Fig. 2.9**. **Fig. 2.9a** indicates that well developed tubes (and spheres) were formed rapidly as described above (1 min ageing). However, after 2 h (**Fig. 2.9b**) the tubes already showed the presence of amorphous material. These tubes had also commenced dissolving. Further, analysis of the TEM images revealed that when ageing was carried out for longer than 3 hours at 75 °C (and even 25 °C) fragmented tubes and hollow spheres were produced. After 24 h ageing the tubes were still present but the amount of amorphous material had increased substantially (**Fig. 2.9d**). Indeed the tubes were then covered by large amounts of amorphous material, which is similar to what was obtained by other workers <sup>11</sup>.

**Fig. 2.10** shows HRTEM images of the tubes after 2 and 6 h. Clearly the tubes aged for 2 h had well-defined thick walls, the walls of those aged for 6 h had started dissolving and were covered by very fine colloidal particles.

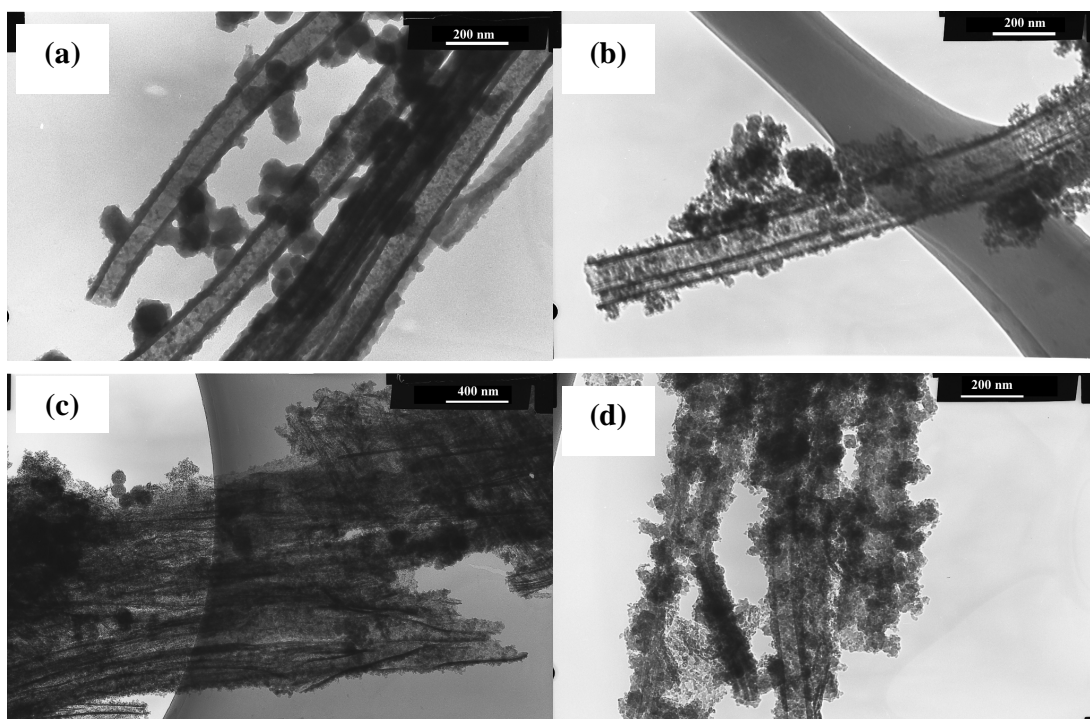


**Figure 2.9.** TEM images showing effect of ageing time at 75 °C on silica formation and dissolution. (a) 1 min, (b) 2 h, (c) 6 h and (d) 24 h.

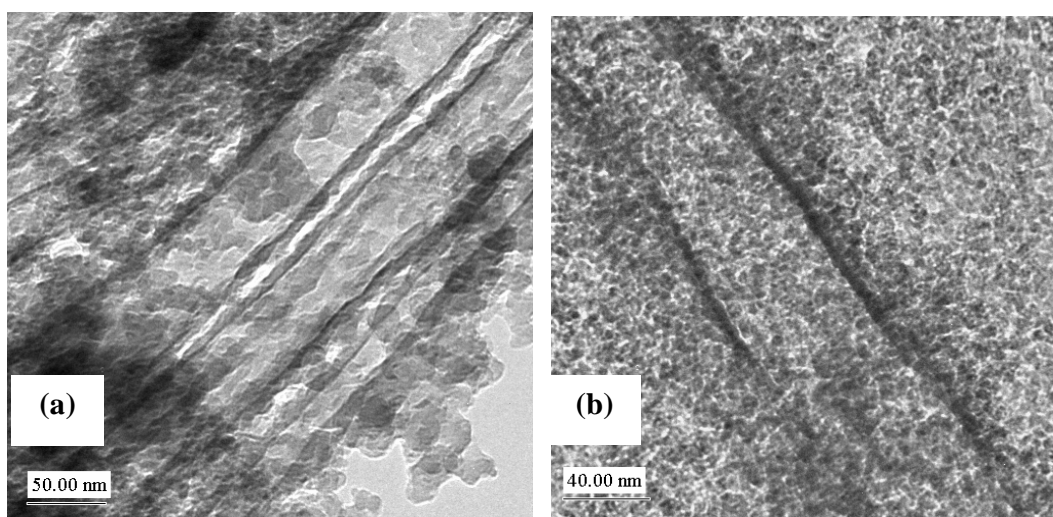


**Figure 2.10.** HRTEM images showing effect of ageing at 75 °C on silica tubes. (a) 2 h and (b) 6 h.

### 2.3.8. Variation of Organic Co-solvent and Water Amount

**Table 2.7** shows the particle distribution of silica materials synthesised in different co-solvents and water amounts. It can be deduced from the table that the type of co-solvent used affected the particle distribution as; in general, more tubes were formed in the presence of methanol than in any other co-solvent. It is also clear from the table that for all three co-solvents employed, as the amount of water was changed in the synthesis, so did the particle distribution, as it can be seen that for both ethanol and isopropanol, the tube yield increased with an increase in water amount up to 50 %  $\text{H}_2\text{O}$ , whereas for methanol the maximum tube yield was obtained with 2.3 %  $\text{H}_2\text{O}$ , beyond which the tube yield decreased. The difference in the maximum tube yield is probably due to different solubilities of oxalic acid, and hence ammonium oxalate, in the different co-solvents; thus implying that more needle-like ammonium oxalate template crystals occurred in methanol than in ethanol and isopropanol. Lower hollow sphere yields were obtained in methanol than in both ethanol and isopropanol. This could imply that oxalic acid dissolved easier in methanol than in ethanol or isopropanol. Thus, the amount of ‘oxalate ion spherical templates’ became less in solution, and instead the amount of needle-like ammonium oxalate template crystals increased.

The surface areas obtained from the materials synthesised in all three co-solvents were found to be comparable. It was also found that increasing the water amount in the synthesis when both isopropanol and ethanol were used as co-solvents, led to a decrease in the surface area of the material, mainly due to an increase in the amount of tubes formed with a corresponding decrease in amorphous material yield. The decrease in surface area observed when water amount in ethanol was increased from 50 to 75 %, despite an increase in the yield of amorphous material, which was expected to lead to an increase in the surface area of the material, was due to the



slight decrease in hollow sphere yield and probably due to changes in the particle sizes.

The gradual decrease in surface area with an increase in the water amount, observed with the materials synthesised in methanol, was not expected as it led to a decrease in the tube yield, which was expected to have led to an increase in the surface area. However, the materials synthesised in methanol all gave BJH pore size distributions slightly different from those obtained from materials synthesised in both ethanol and isopropanol, as shown in **Fig. 2.11**. The distribution of the former showed that, in addition to the micropores and a wide distribution of mesopores, also observed with ethanol and isopropanol, an increased amount of mesopores with diameters between 8 and 15 nm, occurred. **Fig. 2.12** shows TEM images of materials synthesised in all three co-solvents. It shows that while materials synthesised in both ethanol and isopropanol had smooth surfaces, the material synthesised in methanol had tubes with surface attached colloidal particles. Thus, the increased amount of mesopores with diameters between 8 and 15 nm observed with the materials synthesised in methanol was due to the presence of the surface attached colloidal particles, as they generally have higher surface areas. This implies that when the tube yield is increased, so does the amount of surface attached colloidal particles in the material. This will therefore lead to an overall increase in the surface area of the material. The presence of the surface attached colloidal particles in materials synthesised in methanol show that the type of co-solvent used, not only affects the solubility of the template and its precursors, but also the hydrolysis and condensation rates of TEOS.

The increase in surface area observed with the material synthesised in methanol with 75 % water was due to a decrease in the tube yield with a corresponding increase in the amorphous material yield.

**Table 2.7.** Effect of organic co-solvent and water amount (relative to co-solvent) on silica particle distribution.

Co-solvent	H <sub>2</sub> O amount (%)	Tubes (%)	Hollow Spheres (%)	Solid Spheres (%)	Amorphous (%)	BET S.A* (m <sup>2</sup> /g)
Methanol	2.3	80	0	10	10	133
Methanol	25	55	10	25	10	106
Methanol	50	50	5	25	20	73
Methanol	75	35	5	25	35	95
Isopropanol	2.3	25	45	5	25	100
Isopropanol	25	35	5	50	10	58
Isopropanol	50	43	2	45	10	53
Isopropanol	75	43	2	45	10	65
Ethanol	2.3	35	35	15	15	160
Ethanol	25	50	5	35	10	75
Ethanol	50	50	10	30	10	81
Ethanol	75	30	5	35	30	63

\*-surface area

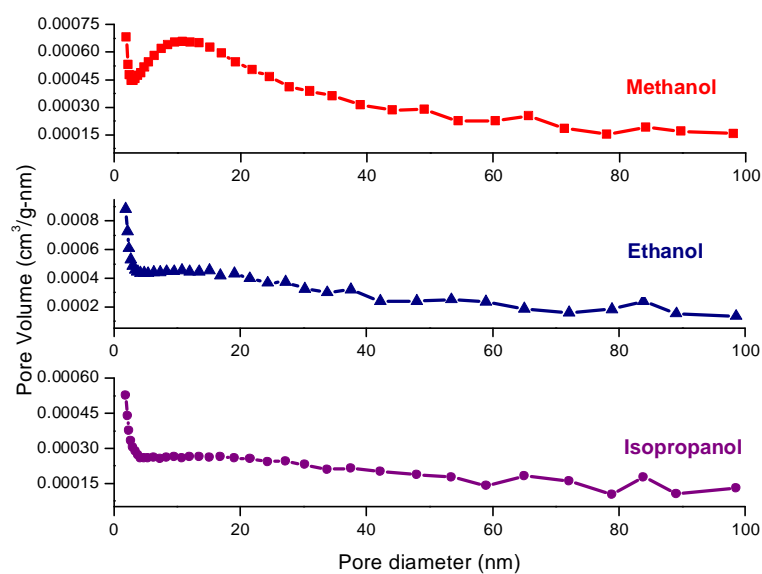


**Figure 2.11.** BJH pore size distributions of silica materials synthesised in methanol, ethanol and isopropanol, with 50 % water.

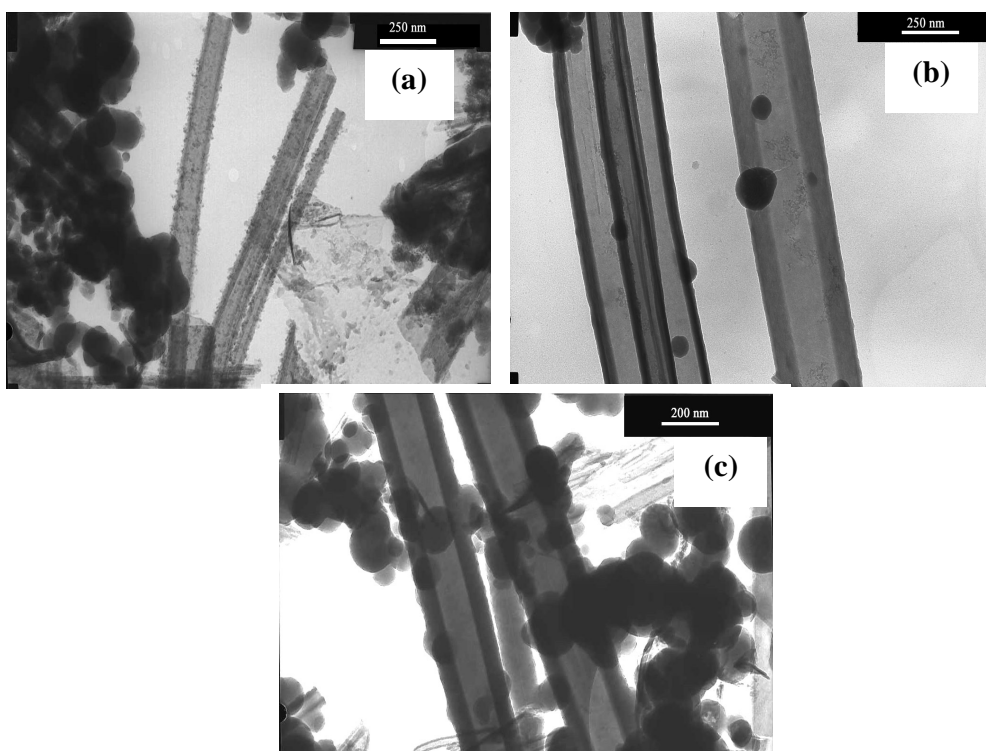


**Figure 2.12.** TEM images of tubes synthesised in 50 % water and (a) methanol, (b) ethanol, and (c) isopropanol.

**Table 2.8** shows the effect of co-solvent type and water amount on particle size. The general trend that can be deduced is that for all co-solvents, the tube width and length increased with an increase in water amount and reached a maximum at 50 % water. However, with the materials synthesised in ethanol, an increase in tube width with a further increase in water amount to 75 % was observed, this increase led to a decrease in the surface area of the material despite an increase in the amorphous material yield observed in **Table 2.7**.

Although the tube width was more or less the same in all co-solvents, methanol produced slightly longer tubes. Also, in all three co-solvents, the best-developed tubes were obtained with 50 % water. For all three co-solvents, increasing the water amount not only affected the tube size but the hollow sphere outer diameter as well. It was found that, increasing the water amount from 2.3 to 25 % increased the hollow sphere outer diameter, which decreased when the water amount was increased further. It is, however, not clear what the effect of the water amount was on the solid sphere diameter. In general, methanol looked to be a better co-solvent amongst the three, in terms of high tube yield, although it produced tubes with surface attached colloidal particles.

**Table 2.8.** Effect of co-solvent type on silica particle size.

Co-Solvent	H <sub>2</sub> O amount (%)	Hollow Sphere O.D* (nm)	Solid Spheres (nm)	Tube O.D* (nm)	Tube length (μm)
Methanol	2.3	-	100-260	40-195	0.36-13.8
Methanol	25	100-244	70-240	60-260	0.6-20
Methanol	50	50-160	90-333	36-750	8.8-37
Methanol	75	50-120	116-233	30-300	0.2-12.6
Isopropanol	2.3	64-320	120-200	24-175	0.72-20.3
Isopropanol	25	70-388	32-220	25-256	0.3-17.5
Isopropanol	50	72-255	50-366	30-833	0.11-30
Isopropanol	75	110-275	60-500	36-375	0.2-20.7
Ethanol	2.3	165-388	75-200	52-120	0.45-22
Ethanol	25	150-400	75-375	38-307	0.21-25
Ethanol	50	100-375	75-325	100-325	0.35-20.7
Ethanol	75	175-200	75-200	33-633	0.60-7.8

\*- outer diameter

### 2.3.9. The ‘Long Method’ versus the ‘Short Method’ Synthesis Procedure

In the ‘short method’ synthesis procedure, TEOS was hydrolysed and condensed simultaneously. **Table 2.9** shows the effect of increasing the water amount (relative to ethanol) on the particle distribution; results for the ‘long method’ were included for comparison. It shows that, contrary to the results found for the ‘long method’, increasing the water amount from 2.3 to 50 % did not affect the tube yield, but only the development of the tubes was affected, as shown in **Fig. 2.13**. The most developed tubes were obtained with 50 % water (**Fig. 2.13c**). Increasing the water amount to 75 % decreased the tube yield and even the appearance of the tubes was found to have deteriorated (**Fig. 2.13d**). Unlike in the ‘long method’, the ‘short

method' produced a very high tube yield and no hollow spheres. Very low surface area materials were obtained with this synthesis method. Also increasing the water amount was found to lead to a gradual decrease in surface area of the materials, even though the yields of the constituents were not affected.

**Table 2.9.** Effect of water/ethanol ratio on silica particle distribution.

Method	H <sub>2</sub> O (%)	Tubes (%)	Hollow Spheres (%)	Solid Spheres (%)	Amorphous Material (%)	BET Surface Area (m <sup>2</sup> /g)
<b>'Short'</b>	2.3	90	0	5	5	39
	25	90	0	5	5	31
	50	90	0	5	5	12
	75	70	0	15	15	5
<b>'Long'</b>	2.3	35	35	15	15	160
	25	50	5	35	10	75
	50	50	10	30	10	81
	75	30	5	35	30	63

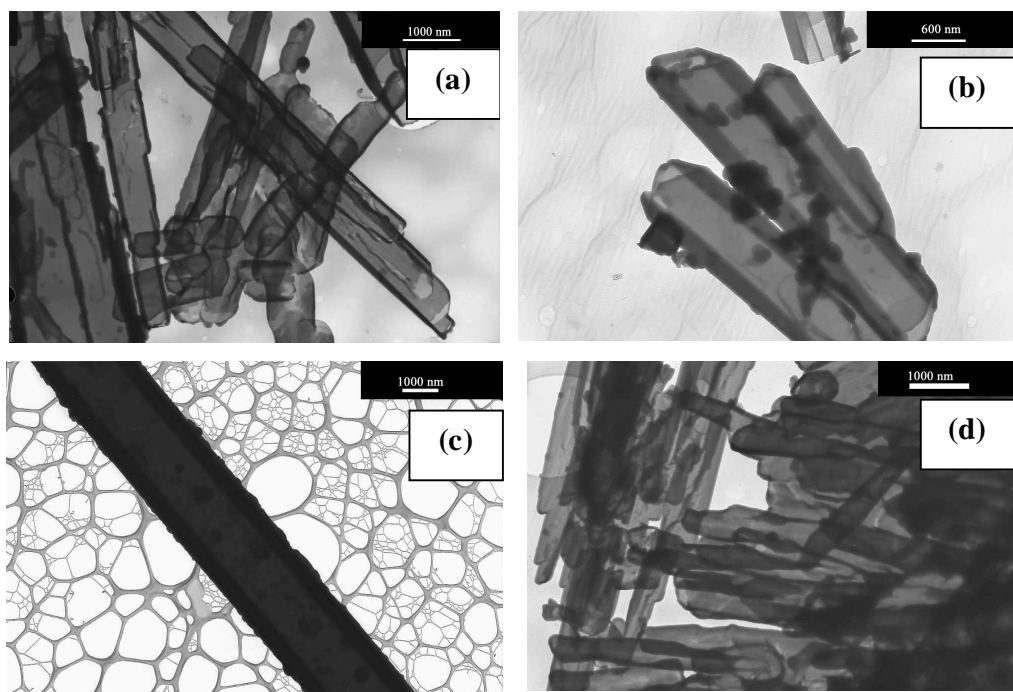


**Figure 2.13.** TEM images showing the effect of water amount on the tubes synthesised by the ‘short method’ synthesis procedure with (a) 2.3, (b) 25, (c) 50 and (d) 75 % water relative to ethanol amount.

**Table 2.10** shows the effect of increasing the water amount on the particle size in the synthesis with the ‘short method’ procedure. As was found with the ‘long method’, increasing the water amount led to an increase in the tube outer diameter and length. However, unlike with the long method, the tube length increased with water amount without reaching a maximum. The continued increase in the tube size with an increase in water amount could explain the observed decrease in surface area observed. This occurred despite a constant yield in the morphology of the materials, particularly after changing the water content from 25 to 50 % water. Not only did the ‘short method’ produce a high tube yield, but also the tubes were about 5 times wider and 7 times longer, when compared to those synthesised by the ‘long method’ synthesis procedure.

**Table 2.10.** Effect of water/ethanol ratio on silica particle size.

Method	H <sub>2</sub> O (%)	Tube O.D <sup>*</sup> (nm)	Tube Length (μm)
<b>Short</b>			
	2.3	88-400	1.3-21
	25	125-1250	4.5-72
	50	1100-2300	11-90
	75	450-4000	31-154
<b>Long</b>			
	2.3	52-120	0.45-22
	25	38-307	0.21-25
	50	100-325	0.35-20.7
	75	33-633	0.60-7.8

<sup>\*</sup> - outer diameter

Thus, it is clear from this study that the ‘short method’ synthesis procedure produced high tube yields that could not be attained by the ‘long method’ procedure. TGA curves of materials prepared by the two methods are shown in **Fig. 2.14**. The figure shows that two weight losses were obtained with an increase in temperature. The first weight loss of 6 % and 13 % for the ‘long method’ and the ‘short method’ synthesis procedures, respectively, occurred around 65 °C and was due to loss of moisture in the materials. The second weight loss of 44 % for the ‘long method’ and 65 % for the ‘short method’, which occurred around 200 °C, was due to loss of the template. Both synthesis procedures produced thermally stable materials, as no further weight loss was observed. However, by the end of the TGA program, the material prepared by the ‘short method’ synthesis procedure had lost 78 % of its original weight, while the one prepared by the ‘long method’ synthesis procedure had only lost 50 % of its original weight. Thus, the difference in the amount of weight lost observed with the two synthesis procedures, despite the same amounts of



reactants used, shows that there was more template formed in the ‘short method’ than in the ‘long method’ synthesis procedure.

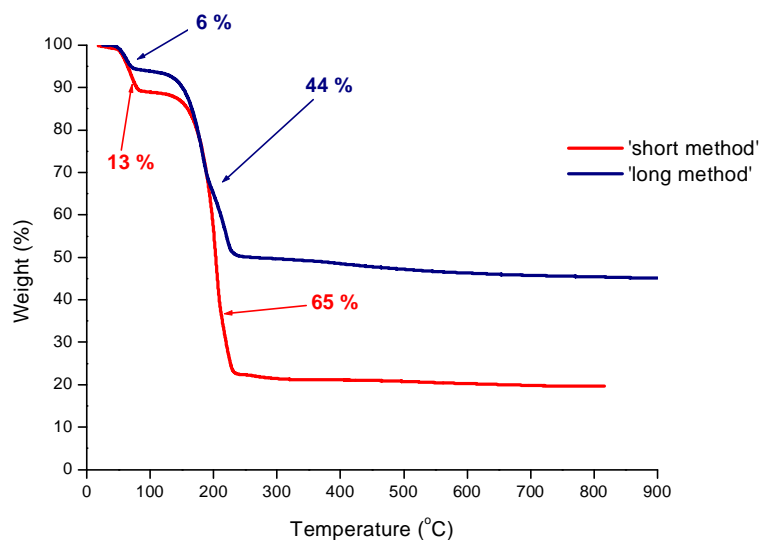


**Figure 2.14.** TGA profiles of silica materials synthesised by the ‘short method’ and ‘long method’ synthesis procedures. Materials were prepared with 2.3 % H<sub>2</sub>O.

### 2.3.10. Reaction Mechanism

The results obtained in this study indicate the meta-stable nature of the tubes/spheres formed in the templated synthesis. The data are entirely consistent with earlier proposals about templating on crystal surfaces, *but* the data presented here reveal a much more complex range of products are formed in the templated synthesis.

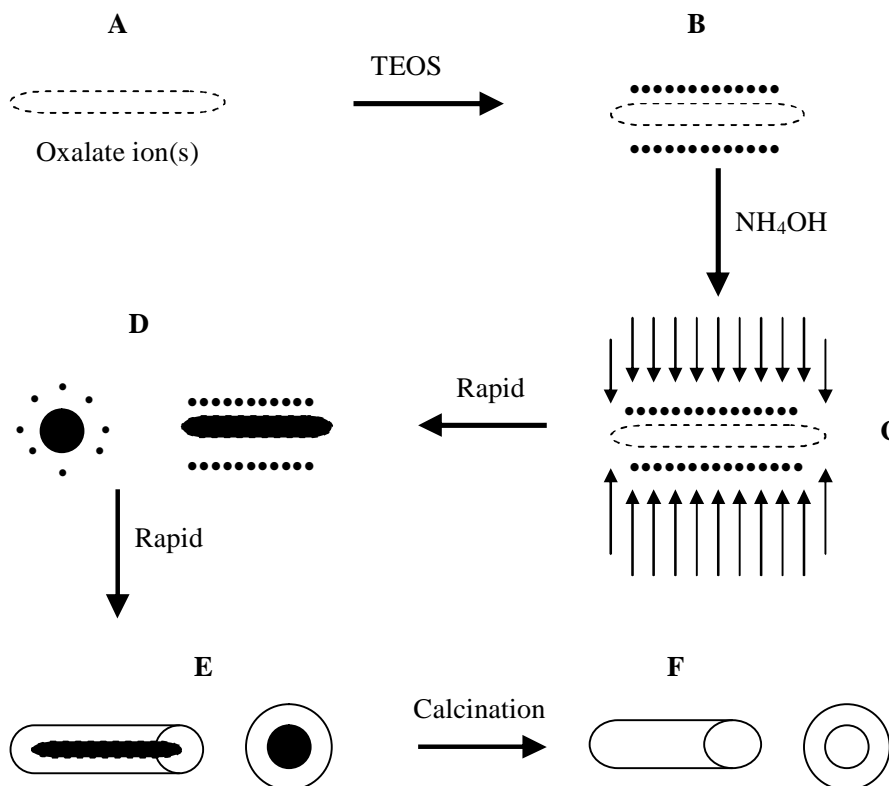
Ammonium oxalate crystal formation is dependent on many factors (temperature, reactant concentrations, etc) such that there will always be a mixture of ions as well as crystals of different sizes in solution. This is highlighted by recent reports that indicate different crystal morphologies of tartrate ions grown in silica media with the

morphologies affected by pH, counter ions, concentration, etc.<sup>17,18</sup>. It is proposed that the morphology of the crystals generated in this study is determined by the *various shapes* of the ammonium oxalate crystals. Addition of a silica source to this solution will result in silica hydrolysis and condensation around the oxalate ions/crystals (acting as both a template and a catalyst) with competition to silica tube formation. It is to be noted that:

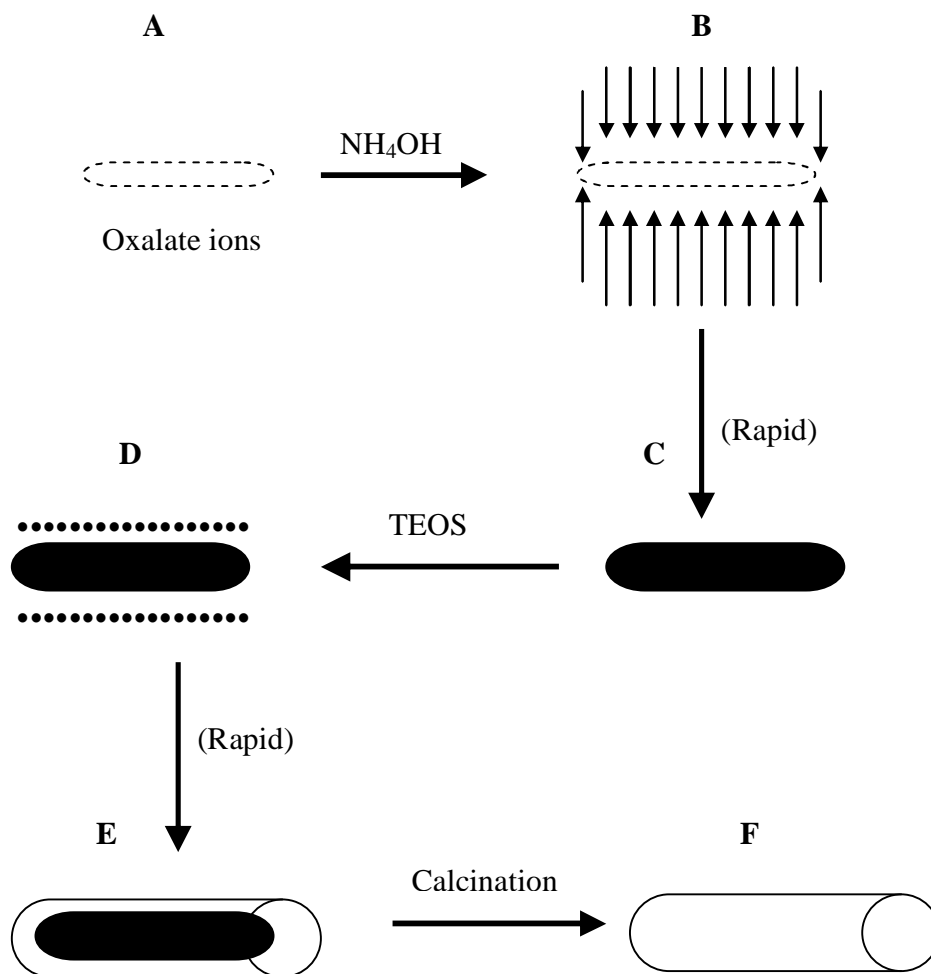
- (i) the formation of rod like crystals, as found by others<sup>7,8</sup>, led to the tubular silica materials formed.
- (ii) the presence of ‘hollow silica spheres’ indicates that when high oxalate ion concentrations are present (i.e. when there are fewer  $\text{NH}_4^+$  ions, e.g. at 75 °C with 85 mmol oxalic acid), the oxalate ions form spherical ‘micelle like’ structures.
- (iii) if the template concentration is low, or template crystallisation is disrupted (temperature, water amount) the silica ions will condense to give alternative morphologies and yield amorphous or filled spherical particles.
- (iv) since the syntheses were carried out in basic media the silica tubes/spheres formed reacted with excess  $\text{OH}^-$  ions, resulting in the tubes/spheres losing their smooth shape as the silica was dissolved away from the tube surface. Further, this dissolved silica re-precipitated on the tubes, generating the attached colloidal particles observed by TEM.

The reason for the major disparity in the tube yields observed between the ‘long method’ and the ‘short method’ synthesis procedures is that in the ‘long method’ synthesis procedure, the acidic oxalate ions were kept in solution for a longer period of time, thus allowing the oxalate ions to catalyse the hydrolysis of TEOS, and these were then coated with the hydrolysed TEOS. Thus upon addition of ammonium hydroxide, contact between the oxalate ions and the ammonium ions was reduced, (see illustration in **Scheme 2.3**). However, in the ‘short method’ synthesis procedure, ammonium hydroxide was added directly to the oxalate ions, which were in solution. Formation of needle-like ammonium oxalate templates occurred immediately, and as there was no obstruction between the two ions the needle-like templates that were

formed were therefore much more than in the long method and were wider and longer, (see illustration in **Scheme 2.4**). The maximised formation of the ammonium oxalate template in the ‘short method’ synthesis procedure is supported by the higher weight loss observed in the TGA profile of the ‘short method’-synthesised material.



Scheme 2.3. Schematic diagram of formation of hollow spheres and tubes by the ‘long method’ synthesis procedure. A: oxalate ion(s) in solution, B: TEOS sols covering surface of oxalate ion(s), C: interaction of ammonium and oxalate ions (sols reduce the interaction), D: sols on surface of ammonium oxalate template, template molecules thin and part of template broken into near spherical shape, E: condensation of sols over template crystals, F: hollow SiO<sub>2</sub> spheres and tubes remain after calcination.



Scheme 2.4. Schematic diagram of formation of tubes by the 'short method' synthesis procedure. A: oxalate ion (s) in solution, B: ammonium ions directly interacting with oxalate ion(s), C: strong rod-like ammonium oxalate template formed, D: TEOS sols covering surface of ammonium oxalate template, E: condensation of sols over template crystal, F: bigger hollow SiO<sub>2</sub> tube remain after calcination.

***PART B: SYNTHESIS OF SILICA MATERIALS BY THE  
TEMPLATED SOL-GEL METHOD- EFFECT OF DIFFERENT  
BASE CATALYSTS***

## **2.4. RESULTS AND DISCUSSION**

### **2.4.1. Variation of Oxalic Acid amount in Different Base Catalysts**

The use of different base catalysts was found to have an effect on the morphology of the particles formed. When KOH was used as a base catalyst, no tubes were formed at all, instead straight sheets, which could probably roll into tubes, were formed (shown in **Fig. 2.15a**). Tubes were formed in the case of both NaOH and NH<sub>4</sub>OH, although tubes formed from NaOH were not as well developed and defined as those formed from NH<sub>4</sub>OH, (**Fig. 2.15b** and **2.15c**). The latter observation could have been due to the low oxalic acid amount used in the synthesis with NaOH.

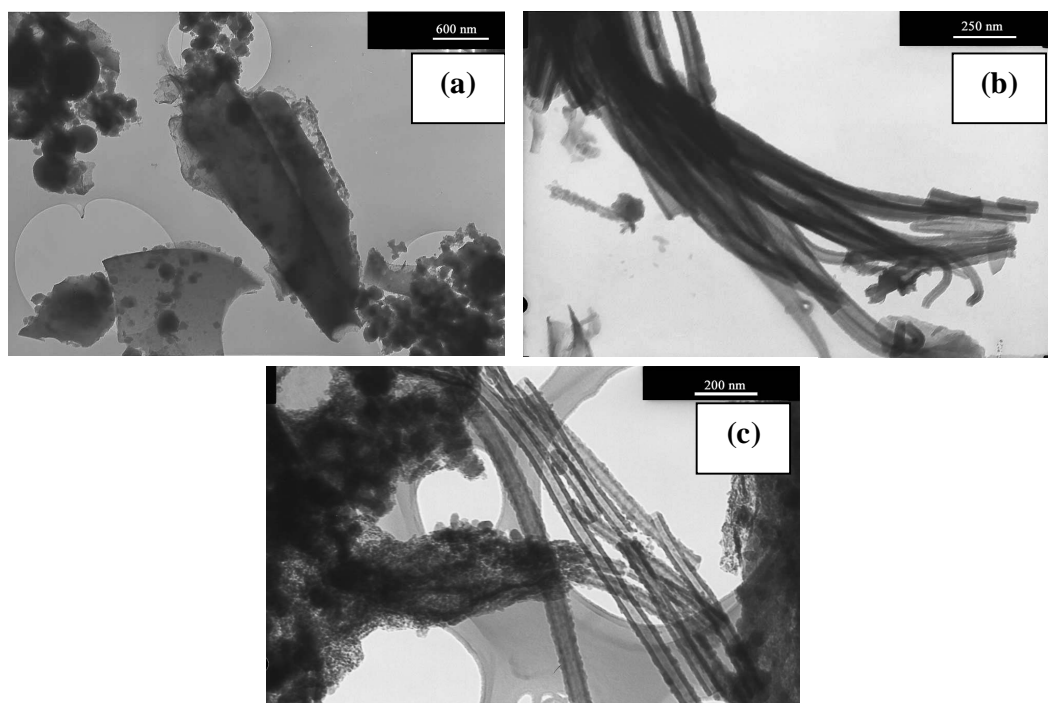


**Figure 2.15.** TEM images of silica materials synthesised with 85 mmol oxalic acid and (a) 85 mmol KOH, (b) 85 mmol NaOH, and (c) 170 mmol  $\text{NH}_4\text{OH}$ .

The effect of varying the base catalyst and the oxalic acid amount on particle distribution is shown in **Table 2.11**. Results for  $\text{NH}_4\text{OH}$ , which have already been discussed in part A above, were included for comparison. When KOH was used; increasing the amount of oxalic acid increased formation of sheets and of amorphous material; at the same time hollow and solid sphere yields decreased. When NaOH was used; increasing the oxalic acid amount considerably increased formation of tubes and decreased formation of hollow spheres considerably and slightly decreased formation of both solid spheres and amorphous material, while when  $\text{NH}_4\text{OH}$  was used; increasing oxalic acid amount increased both tube and solid sphere yields and correspondingly decreased both hollow sphere and amorphous material. The increase in sheet/tube yield and a corresponding decrease in hollow sphere yield, observed with all three bases with an increase in oxalic acid amount, shows that at high

template-precursor concentrations, the template preferably formed sheet/needle-like structures rather than spherical structures, the latter being a template for formation of hollow spheres. The amount of amorphous material formed was expected to decrease with an increase in the amount of oxalic acid used, as was observed with both NaOH and  $\text{NH}_4\text{OH}$ . In both cases as there was more template for the silica to build around. However, it is not clear why the amorphous material increased as was found when KOH was used. However, the increase in the yield of the solid spheres with an increase in oxalic acid amount observed with  $\text{NH}_4\text{OH}$  could be due to the higher base concentration used.

**Table 2.11.** Effect of oxalic acid amount on silica particle distribution. (85 mmol NaOH and KOH, 170 mmol  $\text{NH}_4\text{OH}$ , 2.3 %  $\text{H}_2\text{O}$ ).

Base	Acid amount (mmol)	Tubes (%)	Hollow spheres (%)	Solid spheres (%)	Amorphous (%)
KOH	42.5	sh* 15	20	35	30
KOH	85	sh* 25	10	20	45
NaOH	42.5	40	15	20	25
NaOH	85	63	2	15	20
$\text{NH}_4\text{OH}$	42.5	35	35	15	15
$\text{NH}_4\text{OH}$	85	45	20	30	5

\*- sheets.

**Table 2.12** shows the effect of variation of base catalyst and of oxalic acid amount on the particle size of the silica gels. When KOH was used; increasing oxalic acid amount decreased both the hollow and solid spheres outer diameters, although no major change was observed in the sheet length. This observation is in line with results given in **Table 2.11** as both hollow and solid sphere yields decreased with an increase in template precursor amount. When NaOH was used; increasing oxalic acid

amount did not affect the tube thickness but increased their length. At the same time a decrease in the solid sphere diameter was observed. However, hollow spheres were not affected by this parameter. This observation is in line with the results shown in **Table 2.11** where an increase in tube yield and a decrease in solid sphere and amorphous material yield were observed with an increase in oxalic acid amount. When  $\text{NH}_4\text{OH}$  was used; increasing the oxalic acid amount led to an increase in both tube outer diameter and length, a slight increase in solid sphere diameter and a decrease in hollow sphere outer diameter, which is in line with the results in **Table 2.11**. The observed increase in tube length with an increase in oxalic acid amount, observed with both  $\text{NaOH}$  and  $\text{NH}_4\text{OH}$ , implies that longer rod/needle-like templates were formed at higher template precursor concentrations.

**Table 2.12.** Effect of oxalic acid amount on silica particle size.

Base	Acid amount (mmol)	Hollow spheres O.D <sup>#</sup> (nm)	Solid spheres (nm)	Tubes O.D <sup>#</sup> (nm)	Tubes Length (μm)
KOH	42.5	50-605	200-800	-	sh* 7.0
KOH	85	84-425	140-600	-	sh* 6.8
NaOH	42.5	96-380	320-740	36-200	0.12-4.6
NaOH	85	84-360	80-380	38-205	0.4-6.3
$\text{NH}_4\text{OH}$	42.5	165-388	75-200	50-120	0.45-22
$\text{NH}_4\text{OH}$	85	84-240	75-250	50-225	0.44-26

<sup>#</sup> - outer diameter, \*- sheets



### 2.4.2. Variation of Base Amount

The results for the effect of varying the base catalyst amount on the particle distribution are detailed in **Table 2.13**. When KOH was used; increasing the amount of base increased the formation of sheets, (some folded sheets were also obtained, as shown in **Fig. 2.16a** and **2.16b**) and hollow spheres, but decreased the formation of solid spheres and amorphous material. When NaOH was used; increasing the base concentration increased tube yield with more well-developed tubes formed as shown in **Fig. 2.16c** and **2.16d**, and considerably decreased solid sphere formation. However, hollow sphere and amorphous material yields were not affected by this parameter. When  $\text{NH}_4\text{OH}$  was used; increasing the base concentration led to an increase in tube yield and a corresponding decrease in solid sphere, hollow sphere and amorphous material yields. The increase in the amount of tubes with an increase in base concentration, observed with both NaOH and  $\text{NH}_4\text{OH}$ , was expected as high template-precursor concentrations lead to the increased formation of rod-like templates.

**Table 2.13.** Effect of base amount on silica particle distribution. KOH and NaOH: 85 mmol oxalic acid and 2.3 % H<sub>2</sub>O, NH<sub>4</sub>OH: 42.5 mmol oxalic acid and 50 % H<sub>2</sub>O.

Base	pH After base addition	Base amount (mmol)	Tubes (%)	Hollow spheres (%)	Solid spheres (%)	Amorphous (%)
KOH	2.9	85	sh*25	10	20	45
KOH	5.1	170	sh*30	30	10	30
NaOH	2.5	85	63	2	15	20
NaOH	3.5	170	72	0	5	23
NH <sub>4</sub> OH	4.1	85	30	10	50	10
NH <sub>4</sub> OH	10.7	170	50	10	30	10

\*-sheets

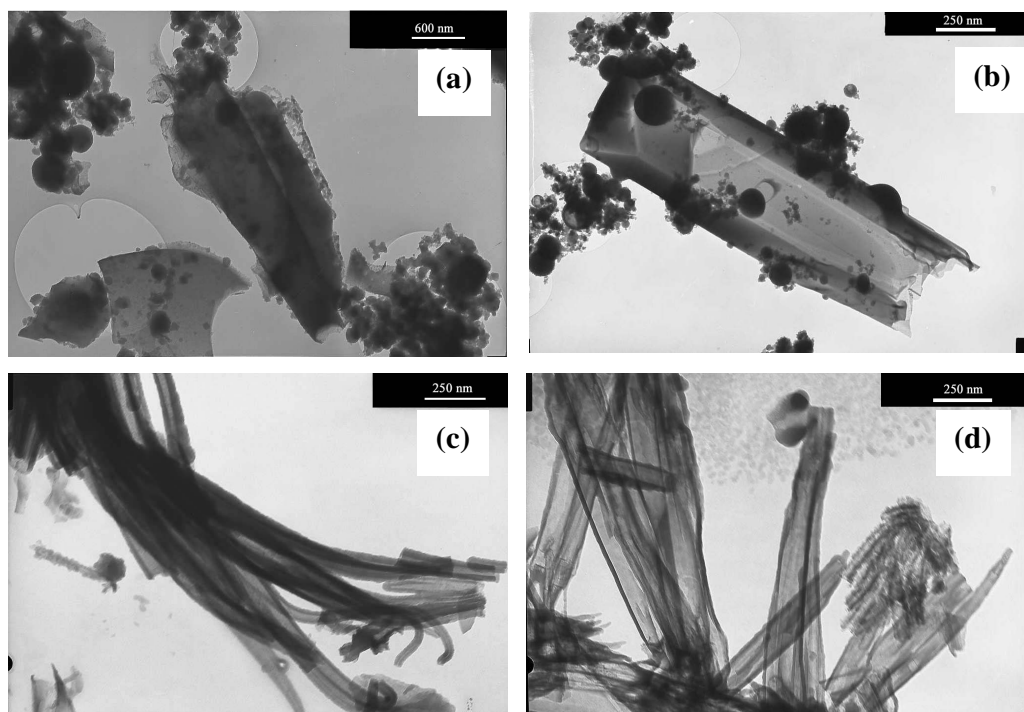


**Figure 2.16.** TEM images of silica materials synthesised with (a) 85 mmol KOH, (b) 170 mmol KOH, (c) 85 mmol NaOH, and (d) 170 mmol NaOH.

**Table 2.14** lists the results of the effect of varying the base concentration on the particle size. When KOH was used; increasing the concentration of the base catalyst increased the hollow sphere outer diameter considerably and slightly increased the solid sphere diameter, while the sheet length slightly decreased. This result is in line with the result given in **Table 2.13**. When NaOH was used; increasing the concentration of the base catalyst increased the tube outer diameter without affecting their lengths, and also increased the solid sphere diameter. When  $\text{NH}_4\text{OH}$  was used; increasing the base concentration did not affect the tube diameter but increased the tube length considerably, and slightly decreased the hollow sphere outer diameter while the solid sphere diameter increased. An increase in tube size with an increase in base concentration, observed with both NaOH and  $\text{NH}_4\text{OH}$  was expected as an increase in template-precursor concentration would be expected to increase tube

outer diameter and/or length, due to formation of stronger and bigger needle-like templates at higher template precursor concentrations.

**Table 2.14.** Effect of base catalyst concentration on silica particle size.

Base	Base amount	Hollow Sphere O.D <sup>#</sup> (nm)	Solid Spheres (nm)	Tube O.D <sup>#</sup> (nm)	Tube length (μm)
KOH	85	84-425	140-600	-	sh* 6.8
KOH	170	50-1225	175-675	-	sh* 5.6
NaOH	85	84-360	80-380	38-120	0.4-6.3
NaOH	170	-	167-500	44-205	0.2-6.5
NH <sub>4</sub> OH	85	75-300	75-250	160-320	0.7-12.4
NH <sub>4</sub> OH	170	100-266	75-325	100-325	0.35-20.7

<sup>#</sup> - Outer diameter, \* - sheets.

#### 2.4.3. Variation of Water to Ethanol Amount

**Table 2.15** details the results of the effect of varying the water amount in the synthesis of silica materials in the presence of the different base catalysts. When KOH was used; increasing the water amount decreased formation of sheets and hollow spheres (considerably), and increased formation of amorphous material. However, the solid sphere yield was found not to be affected by varying the water amount. When NaOH was used; increasing the water amount was found to increase formation of solid spheres and of well-developed tubes (but remained constant between 25 and 50 % H<sub>2</sub>O). **Fig. 2.17** shows TEM images of tubes obtained with NaOH as base catalyst. When 2.3 % H<sub>2</sub>O was used (**Fig. 2.17a**), tubes were under-developed. Some of the tubes had closed ends while some looked like rods rather than hollow tubes (**Fig. 2.17b**). When the amount of water was increased to 25 % bigger tubes which partly looked like rods were obtained (shown in **Fig. 2.17c**).

Increasing the water amount to 50 % led to formation of better-developed tubes, as shown in **Fig. 2.17d** which shows thin but very well developed tubes. These results are similar to those obtained when  $\text{NH}_4\text{OH}$  was used as a base catalyst, as explained in Part A above. It was also found that increasing the water amount led to a decrease in formation of hollow spheres (considerably) and of amorphous material. The decrease in the tube/sheet and hollow sphere yield observed with an increase in water amount can be attributed to template dissolution. From this result one can deduce that the template crystals were present in large amounts at a water amount of 50 %.

**Table 2.15.** Effect of water amount (relative to ethanol) on silica particle distribution 85 mmol base (170 mmol for  $\text{NH}_4\text{OH}$  only) and 42.5 mmol oxalic acid, 25 °C.

Base	H <sub>2</sub> O relative to ethanol (%)	Tubes (%)	Hollow spheres (%)	Solid spheres (%)	Amorphous (%)
KOH	2.3	sh*15	20	35	30
KOH	25	sh*15	2	40	43
KOH	50	sh*10	0	35	55
NaOH	2.3	40	15	20	25
NaOH	25	40	5	40	15
NaOH	50	50	3	37	10
$\text{NH}_4\text{OH}$	2.3	35	35	15	15
$\text{NH}_4\text{OH}$	25	50	5	35	10
$\text{NH}_4\text{OH}$	50	50	10	30	10

\*- sheets

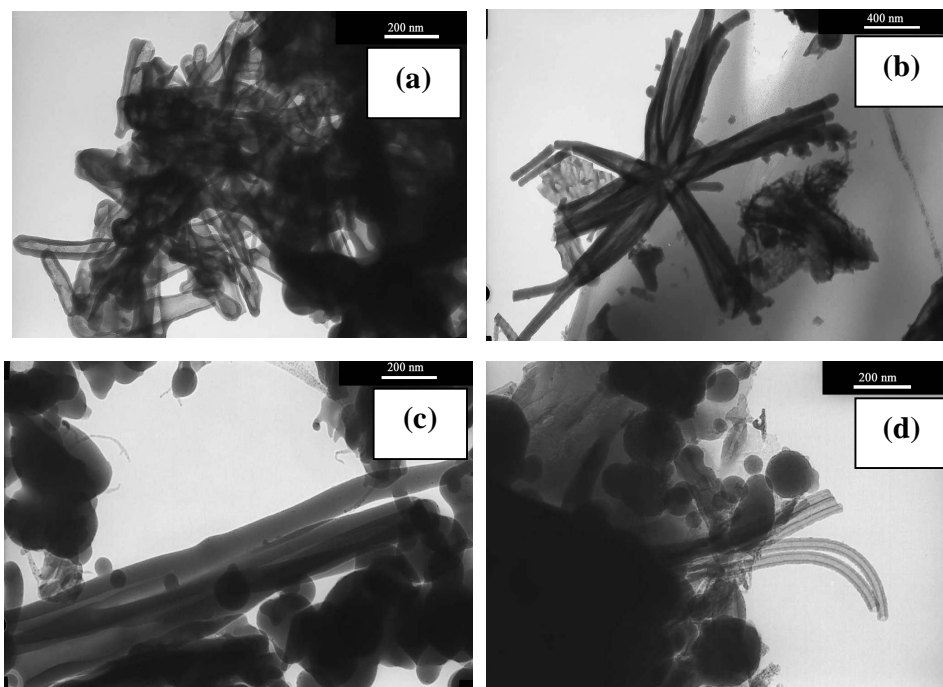


**Figure 2.17.** TEM images of tubes synthesised with NaOH as base catalyst in (a) and (b) 2.3 , (c) 25 and (d) 50 % water.

The effect of water amount on the particle size of silica materials synthesised with the different bases is presented in **Table 2.16**. When KOH was used; increasing the amount of water considerably increased the solid sphere size, while it reduced the sheet length. When NaOH was used; the hollow sphere diameter remained almost constant, the solid sphere diameters slightly decreased, while the tube outer diameter and length increased, when water was increased from 2.3 to 25 %. Increasing the water amount from 25- 50 % led to a drop in the tube outer diameter and length, and a corresponding considerable increase in the solid sphere diameter, while only a slight increase in hollow sphere outer diameter occurred. When  $\text{NH}_4\text{OH}$  was used; increasing the water amount was found to increase the tube outer diameter and length; the tube length dropped when the water amount was increased beyond 25 %, while the hollow sphere outer diameter remained more or less stable, and the solid spheres diameters increased with an increase in water amount to 25 %, and decreased with a further increase in water amount. The common behaviour of the tubes

obtained with both NaOH and NH<sub>4</sub>OH is in agreement with the results presented in **Table 2.15**. Thus template dissolution occurs with an increase in water amount beyond 25 %, to give a decrease in the diameter and length of tubes observed. However, the gradual decrease in sheet length with an increase in the water amount observed with KOH implies that the template formed in this case dissolved easily in the water, to give an increase in amorphous material. The increase in the solid sphere diameter, observed with both KOH and NaOH, with an increase in the amount of water (which occurred with an increase in water amount from 25 to 50 % with NaOH), despite an almost constant yield, is possibly due to the untemplated silica preferably coating on the solid spheres that were already formed. There were few template crystals available due to dissolution in the large amount of water present in the synthesis.

**Table 2.16.** Effect of water amount (relative to ethanol) on silica particle size.

Base	H <sub>2</sub> O amount (%)	Hollow Sphere O.D. <sup>#</sup> (nm)	Solid Spheres (nm)	Tube O.D. <sup>#</sup> (nm)	Tube length (μm)
KOH	2.3	50-605	200-800	-	sh* 7.0
KOH	25	-	150-1100	-	sh* 4.8
KOH	50	-	250-1567	-	sh* 4.0
NaOH	2.3	96-380	320-740	36-200	0.12-4.6
NaOH	25	50-350	80-600	60-320	1.56-9.8
NaOH	50	190-400	123-1333	44-300	0.7-6.9
NH <sub>4</sub> OH	2.3	165-388	75-200	52-120	0.45-22
NH <sub>4</sub> OH	25	150-400	75-375	38-307	0.21-25
NH <sub>4</sub> OH	50	100-375	75-325	100-325	0.35-20.7

<sup>#</sup> - outer diameter, \*-sheet

#### 2.4.4. The ‘Long Method’ v/s the ‘Short Method’ Synthesis Procedure

The effect of varying the synthesis procedure with the use of different base catalysts is presented in **Table 2.17**. It was found that, with all three base catalysts used, the tube (sheets in the case of KOH) yield increased, while both the hollow and solid spheres yields decreased when using the ‘short method’ synthesis procedure relative to the ‘long method’ procedure. As was expected, the amorphous material yield was found to have decreased when both NaOH and NH<sub>4</sub>OH were used. However the amorphous material yield was found to have increased when KOH was used. This could have been due to easy dissolution of the template when KOH was used. as a base catalyst. It was also found that the use of NH<sub>4</sub>OH as a base catalyst produced the highest amount of tubes when the ‘short method’ synthesis procedure was used, which could be attributed to the high base concentration used in this case.



**Table 2.17.** The effect of variation of the synthesis procedure with the use of different base catalysts on the particle distribution. Base 85 mmol (170 mmol for  $\text{NH}_4\text{OH}$ ), Oxalic acid 42.5 mmol, 2.3 %  $\text{H}_2\text{O}$ .

Base Used	$\text{H}_2\text{O}$ Amount (%)	Tubes (%)	Hollow spheres (%)	Solid spheres (%)	Amorphous (%)
KOH	Long	sh* 15	20	35	30
KOH	Short	sh*25	0	15	60
NaOH	Long	40	15	20	25
NaOH	Short	83	3	11	3
$\text{NH}_4\text{OH}$	Long	35	35	15	15
$\text{NH}_4\text{OH}$	Short	90	0	5	5

\*-sheets

**Table 2.18** shows the effect of variation of synthesis procedure on the silica particle size. For all three base catalysts employed in this study, it was found that the hollow sphere outer diameter decreased when the ‘short method’ synthesis procedure was used, which is in agreement with the decrease in hollow sphere yield obtained with these materials. In contrast the solid sphere and tube diameter increased. It was also found that the sheet and tube length obtained with KOH and NaOH, respectively, increased while the tube length obtained when  $\text{NH}_4\text{OH}$  was used remained more or less the same as the synthesis procedure was changed. The increase in tube diameter obtained with both NaOH and  $\text{NH}_4\text{OH}$ , and in the sheet/tube length observed with KOH and NaOH was expected, as more direct contact of oxalic acid with the base

occurs in the ‘short method’ than in the ‘long method’ synthesis procedure. This in turn leads to formation of bigger sheet/needle-like templates for the silica to build around, as it was explained in **Section 2.3.9** above.

KOH was found to produce bigger hollow spheres in the ‘short method’ synthesis procedure, and it was also observed that  $\text{NH}_4\text{OH}$  produced smaller solid spheres, while those obtained with KOH and NaOH were comparable. Also, bigger tubes were obtained with  $\text{NH}_4\text{OH}$  than with NaOH, and the tubes were also much longer than the sheets obtained with KOH. This could be due to the higher concentration of  $\text{NH}_4\text{OH}$  used when compared to KOH and NaOH.

**Table 2.18.** Effect of variation of synthesis procedure on silica particle size.

Base	Method	Hollow Sphere O.D. <sup>#</sup> (nm)	Solid Spheres (nm)	Tube O.D. <sup>#</sup> (nm)	Tube length (μm)
KOH	Long	50-605	200-800	-	sh* 7.0
KOH	Short	-	127-1567	-	sh*9.6
NaOH	Long	96-380	320-740	36-200	0.12-4.6
NaOH	Short	40-100	180-1133	50-275	0.12-11.8
NH <sub>4</sub> OH	Long	165-388	75-200	50-120	0.45-22
NH <sub>4</sub> OH	Short	-	20-512	88-400	1.3-21

<sup>#</sup>-Outer diameter, \*- sheets

#### 2.4.5. General Remarks on the Use of Different Base Catalysts

From this study, it can be deduced that increasing the amount of any of the template precursors (i.e. oxalic acid or base), increased tube/sheet formation while it decreased formation of amorphous material, hollow and solid spheres. This shows that the template (i.e. potassium/sodium/ammonium oxalate) prefers to form sheet/needle-like structures over spherical structures, especially when it is present in large amounts. The optimum water amount in the synthesis of tubes is between 25 and 50 %, as the largest and best-developed tubes were obtained with this amount of water. The solid sphere diameter significantly increased when the water amount was

increased beyond 25 %, probably due to template dissolution, which resulted in more silica forming into solid spheres.

In general, NaOH yielded more tubes than both KOH and  $\text{NH}_4\text{OH}$ , while KOH preferably produced hollow spheres. However, KOH showed poor ability to synthesise shaped silica morphologies, as extensive amounts of amorphous material were formed when it was used as a base catalyst. The reason for the higher amount of tubes in the case of both NaOH and  $\text{NH}_4\text{OH}$  when compared to KOH, and the formation of sheets and hollow spheres rather than tubes observed with KOH, stems from the shape their salts prefer to form in solution. **Fig. 2.18** shows SEM images of the salts of these bases that precipitated under the same conditions as the silica materials were synthesised, but in the absence of TEOS. Mainly spherical particles were obtained when potassium oxalate precipitated (**Fig. 2.18a** and **2.18b**), a mixture of spherical and oblong particles when sodium oxalate precipitated (**Fig. 2.18c** and **2.18d**), while needle-shaped particles were obtained when precipitated ammonium oxalate precipitated from solution (**Fig. 2.18e** and **2.18f**).

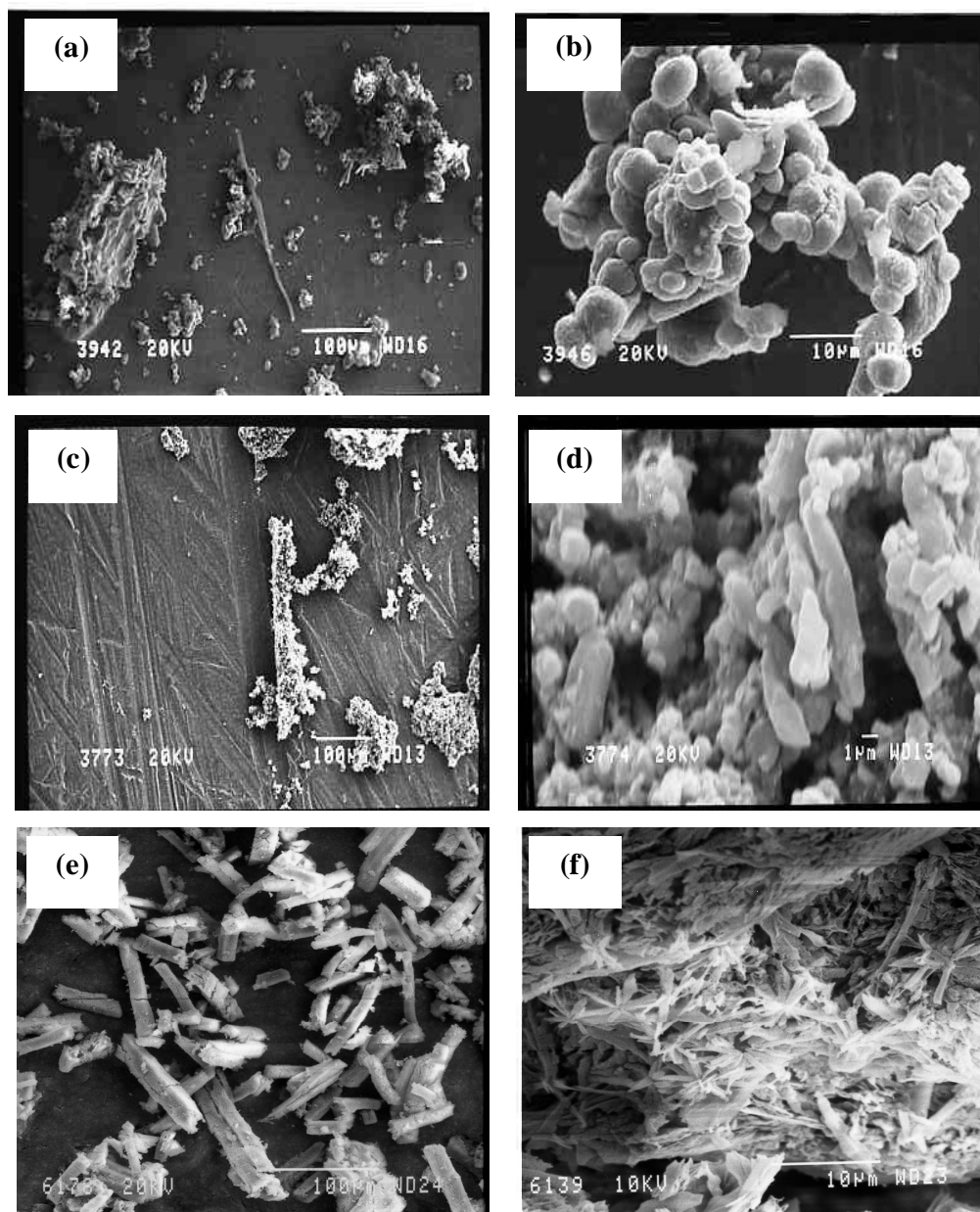


**Figure 2.18.** SEM images of (a) low and (b) higher magnification of Potassium oxalate, (c) low and (d) higher magnification of Sodium oxalate, and (e) low and (f) higher magnification of Ammonium oxalate salts precipitated in water/ethanol mixtures.

## 2.5. CONCLUSION

It is clear from this study that the morphology of silica gels synthesised by the templated sol-gel procedure greatly depends on the synthesis conditions employed. The optimum hydrolysis and ageing duration was found to be 2 h, as dissolving tubes and hollow spheres were obtained when the duration was increased. The ‘oxalate ion’ forms two different shapes of crystals in solution; the spherical crystals are responsible for the formation of hollow spheres, and the rod-/needle-like crystals are responsible for the formation of tubes. The needle-like crystals become present in large quantities when the amount of either the acidic or basic precursor is increased.

Since the major role of the organic co-solvent is to facilitate miscibility of TEOS with water, it therefore affects the rates of hydrolysis and condensation of TEOS, as formation of surface attached colloidal particles occurred when methanol was used. Also, the type of organic co-solvent used can increase or decrease the yield of shaped morphologies, depending on the amount of water and the solubility of oxalic acid or ammonium oxalate salt crystals in the organic co-solvent used. The amount of water used in the synthesis, also affects the morphology of the resultant silica gel. Thus when water is present in large quantities, template dissolution can occur, and this will result in a decrease in the yield of shaped morphologies. Template dissolution in the synthesis solution can also be increased by synthesis at elevated temperatures, thus resulting in lowered formation of shaped morphologies.

The effect of the type of base catalyst used on the morphology formed depends on the shape of the template crystals formed by the particular base used in solution, and the solubility of the template in the solvent used. While the ‘long method’ synthesis procedure allows ‘enough’ TEOS hydrolysis, the silica gels produced by the method showed lower yields of shaped morphologies due to reduced interaction of the acidic oxalate ion and the basic ion from the base catalyst by the hydrolysed TEOS.

It is thus clear from this study that while the synthesis conditions required to generate the different silica morphologies can be rationalised, control to completely synthesise either the hollow spheres or tubes is more difficult to achieve. Thus, control of silica morphology will certainly prove to be a challenge in future studies.

## 2.5. REFERENCES

1. P. Ball, *Made to Measure*, Princeton Press, Princeton, 1999
2. T. Asafa, C. Yoshina-Ishii, M.J. McLachlan and G.A. Ozin, *J. Mater. Chem.*, 10 (2000) 1751.
3. (a) P.M. Dove, J.J. DeYoreo and S. Weiner, Eds., *Reviews in Mineralogy and Geochemistry*, 54 (2003) (b) S. Mann, Ed, *Biomimetic Materials Chemistry*, Wiley Europe, 1997 (c) E.J. Lerner, *Amer. Inst. Physics*, Aug/Sept (2004) 16 (d) D. Braga, *Angew. Chem. Int. Ed.*, 43 (2003) 5544.
4. K.J.C. van Bommel, A. Friggeri and S. Shinkai, *Angew. Chem. Int. Ed.*, 42 (2003) 980.
5. F. Schuth, *Angew. Chem. Int. Ed.*, 42 (2003) 3604.
6. H. Nakamura and Y. Matsui, *J. Am. Chem. Soc.*, 117 (1995) 2651
7. F. Miyaji, S.A. Davis, J.P.H. Charmant and S. Mann, *Chem. Mater.*, 11 (1999) 3021
8. F. Miyaji, Y. Watanabe and Y. Suyama, *Mater. Res. Bull.*, 38 (2003) 1669
9. E. Mokoena, A.K. Datye and N.J. Coville, *J. Sol-Gel Science Technology.*, 28 (2003) 307.
10. C. Hippe, M. Wark, E. Lork and G. Schulz-Ekloff, *Microporous and Mesoporous Mater.*, 31 (1999) 235.
11. F. Miyaji, Y. Tatematsu and Y. Suyama, *J. Cer. Soc. Japan.*, 109 (2001) 924
12. J. Zygmunt, F. Krumeich and R. Nesper, *Adv. Mater.*, 18 (2003) 1538.
13. K.S.W. Sing, D.H. Everett, R.A.W. Haul, L. Moscou, R.A. Pierotti, J. Rouquérol, T. Siemieniowska, *Pure & Appl. Chem.* 57 (1985) 603.
14. G. Leofanti, M. Padovan, G. Tozzola, B. Venturelli, *Catal. Today*, 41 (1998) 207.
15. (a) W. Stober, A. Fink and E. Bohn, *J. Colloid Interface Sci.*, 26 (1968) 62 ,  
(b) D.L. Green, J.S. Lin, Y-F Lam, M.Z-C Hu, D.W. Schaefer and M.T. Harris, *J. Colloid Interface Sci.*, 299 (2003) 346.



16. J.D. Wright and N.A.J.M. Sommerdijk, *Sol-gel Materials: Chemistry and Applications*, Gordon and Breach Science Publishers, Amsterdam, 2001.
17. G. Sajeevkumar, R. Raveendran, B.S. Remadevi and A.V. Vaidyan, Bull. Mater. Sci., 27 (2004) 323.
18. X.S. Shajan and C. Mahadevan, Bull. Mater. Sci., 27 (2004) 327.

## **CHAPTER 3**

### **SYSTEMATIC STUDY OF THE USE OF D-GLUCONIC ACID AND OTHER HYDROXYACIDS IN THE SYNTHESIS OF SILICA GEL BY THE TEMPLATED SOL-GEL METHOD**

#### **3.1. INTRODUCTION**

Inorganic materials with well-defined shapes have attracted much attention due to their many potential applications (e.g. catalysis, adsorbents, chromatography, and medicine). Scientists working in materials as well as in other fields of chemistry have devoted a great deal of their effort towards the development of efficient and innovative fabrication methods in order to obtain these challenging materials. In one of the methods most commonly employed, formation of the inorganic material takes place under the influence of an organic template by transcription. A variety of organic templates have been successfully employed for this transcription process, e.g. surfactants<sup>1</sup>, organogels<sup>2</sup>, polymers<sup>3</sup>, and nanoparticles<sup>4</sup>, to produce materials with interesting shapes. It is generally accepted that for transcription to occur, interaction between the template surface and the precursor of the inorganic material or its prehydrolysed oligomer must be present<sup>5</sup>.

However, the use of such molecules has the potential drawback that the costs associated with scale-up are likely to be prohibitive. Thus the synthesis of silica tubes from tetraethylorthosilicate, by Nakamura and Matsui, using a relatively cheap template; DL-tartaric acid, in the presence of ethanol, ammonia and water, brought an alternative to using expensive templates. Their work has since sparked more research into cheaper templates which are easily accessible and easy to remove from the final silica product<sup>6</sup>.

In this work the use of D-gluconic, L-tartaric, stearic and cinnamic acid (chemical structures shown in **Fig. 3.1**) as template precursors for the synthesis of shaped silica gel is presented. The chapter is divided into two parts; part A deals with a systematic study on the effect of synthesis conditions on silica gels synthesised with the use of D-gluconic acid as a template precursor, while part B deals with the use of different hydroxyacids as template precursors for the synthesis of silica gel.

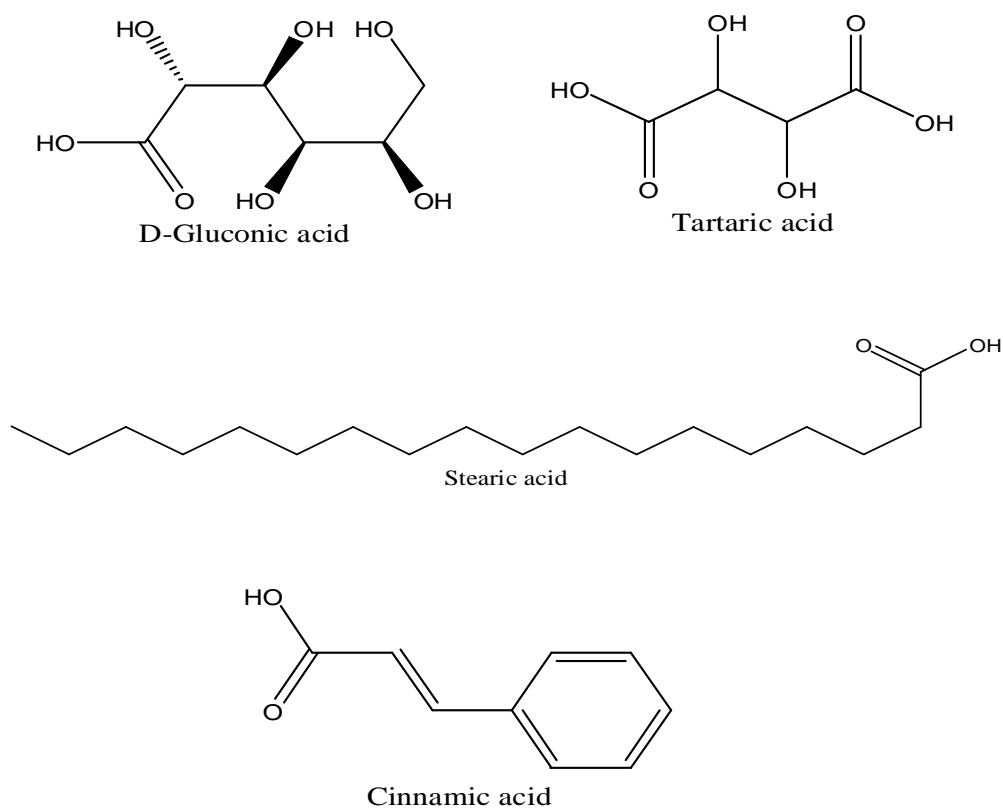


**Figure 3.1.** Chemical structures of template precursor molecules used in this study.

### 3.2. EXPERIMENTAL

#### 3.2.1. Reagents and Chemicals

Ethanol (Saarchem, 99.9%), methanol (Saarchem, 99%), isopropanol (Saarchem, 99%), 1-butanol (Sigma-Aldrich, 99.4%), distilled water, tetraethylorthosilicate (TEOS); (Aldrich, 98%), D-gluconic acid (Fluka, 50% in water, present in equilibrium with ~25 % gluconic acid lactone), L-tartaric acid (Merck), cinammic acid (BDH), stearic acid (BDH), and ammonium hydroxide (Fluka, 28%) were used as chemical sources. All chemicals were used as received. The synthesis procedure followed a standard approach and a typical synthesis is outlined below. Both the yield and product morphology were determined after each synthesis.

#### 3.2.2. Synthesis Procedure

##### *Part A: Systematic Study of the use of D-gluconic Acid in the Synthesis of Silica Gel by the Templated Sol-Gel Method*

In a typical synthesis, 85 mmol of template precursor, D-gluconic acid, was dissolved in a mixture of 0.7 ml of distilled water and 30 ml of ethanol. 6 ml of silicon precursor, TEOS, was then added to the mixture to form a sol, which was magnetically stirred at a speed of 300 rpm for 2 h at room temperature (25 °C). Finally, 12 ml of NH<sub>4</sub>OH (containing 175 mmol NH<sub>3</sub>) was added drop-wise over 30 min to the mixture to form a gel which was then aged for 2 h at room temperature. The gel was then washed immediately in aliquot amounts of ethanol and water dried in an oven at 70 °C for 48 h and then calcined under static air at 600 °C for 4 h.

- (a) *Variation of temperature:* The synthesis procedure outlined above was performed as described except that the synthesis temperature was varied (75 °C, 55 °C, and 25 °C).

- (b) ***Variation of amount of D-gluconic acid:*** The synthesis was carried out at room temperature. All parameters were kept constant, as described above except for the volume/amount of D-gluconic acid used 6.7, 13.4 and 26.8 ml containing 42.5, 85, and 170 mmol respectively.
- (c) ***Variation of  $\text{NH}_4\text{OH}$  volume:*** The synthesis was carried out at room temperature, all parameters were kept constant except for  $\text{NH}_4\text{OH}$  volume; 12, 24, and 36 ml  $\text{NH}_4\text{OH}$  was used containing 170, 340, and 510 mmol  $\text{NH}_3$  respectively.
- (d) ***Variation of amount of water:*** The synthesis was carried out at room temperature and all parameters except the amount of water were kept constant. The total solvent volume was kept constant at 30.7 ml. The percentage of water in ethanol used was 75, 50, 25, 10, and 2.3 % (by volume).
- (e) ***Variation of length of TEOS hydrolysis time:*** The synthesis was carried out at room temperature; all parameters were kept constant except for TEOS hydrolysis time which was varied from 1 min to 8 h.
- (f) ***Variation of length of ageing time:*** The synthesis was carried out at room temperature; all parameters were kept constant except for the length of ageing time, which was varied from 1 min to 8 h.
- (g) ***Variation of organic co-solvent:*** The synthesis was carried out at room temperature; the organic co-solvent and the amount of water relative to the organic co-solvent were varied. Methanol, ethanol, isopropanol, and 1-butanol were used as organic co-solvents, and the water amount relative to the organic co-solvent used was 2.3 % (by volume). All other parameters were kept constant.

**(h) Variation of synthesis procedure:** The ‘short method’ synthesis procedure was used. In this method, hydrolysis and condensation of TEOS were done simultaneously. The materials were synthesised at room temperature. An amount of 85 mmol of D-gluconic acid was dissolved in 30.7 ml of an ethanol and water mixture, containing 2.3 % water relative to the amount of ethanol amount. To the acidic mixture, 12 ml of ammonium hydroxide, containing 170 mmol  $\text{NH}_3$  was added all at once without stirring, and a white turbid solution was formed. Subsequently, 6 ml (27 mmol) of TEOS was added rapidly, the resulting gel stirred for 30 min, and was then aged for 2 h. After ageing, the gel was washed with copious amounts of hot water, dried at 100 °C for 48 h, and then calcined in static air at 600 °C for 6 h.

***Part B: A Study of the use of other Hydroxyacids in the Synthesis of Silica Gel by the Templated Sol-Gel Method***

**(i) Variation of acidic template precursor:** The ‘short method’ synthesis procedure described above in (h) was used to synthesise the materials at room temperature. D-gluconic acid (85 mmol), L-tartaric acid (85 mmol), cinnamic acid (85 mmol) and stearic acid (21.2 mmol) were dissolved in a 30.7 ml ethanol/water mixture containing 2.3 % water (stearic acid was dissolved in 45 ml diethyl ether). All other parameters remained the same.

### **3.2.3. Characterisation**

**3.2.3.1. Transmission Electron Microscopy.** Transmission electron microscopy images were observed with a JEOL-100S electron microscope with an acceleration voltage of 80 kV. Samples were prepared by sonicating about 100 mg of sample in 2 ml of ethanol for at least 5 minutes and then 2 drops of the suspension were placed on a Cu grid coated with carbon film. After approximately one minute, excess liquid was removed by touching one edge of the grid with a Whatman filter paper.

**3.2.3.2. N<sub>2</sub> Physisorption.** The nitrogen adsorption and desorption isotherms were measured at 77K using a Micromeritics ASAP 2010 instrument. The Brunauer-Emmet-Teller (BET) surface area was calculated from the adsorption isotherms and Barret-Joyner-Halenda (BJH) method was used to determine the pore size distribution. Degassing of the samples for 24 h at 0.1 Pa at 393 K preceded every measurement. Specific adsorption pore volumes were calculated by the BJH method that is assumed to cover the cumulative adsorption pore volume of pores in the range 1.7 to 300 nm in diameter.

**3.2.3.3. Powder X-Ray Diffraction.** X-Ray powder diffraction measurements were carried out on a Philips PW 1830 Diffractometer generator, equipped with a Ni-filtered CuK $\alpha$  radiation source. The measurements were carried out in the 1.5-60 ° 2 $\theta$  range at a generator voltage of 40 kV and current 20 mA. A scan rate of 2 ° per step was used.

**3.2.3.4. Thermal Analysis.** Thermogravimetric analyses were performed with a Perkin Elmer Pyris 1 TGA Thermogravimetric Analyser using nitrogen as the purge gas, at a flow rate of 20 ml per minute, and a heating rate of 5 °C per minute.

The amounts and sizes of the various silica shapes produced in the syntheses were estimated (as percentages) by standard measurement/counting procedures from TEM photographs. The distribution data was divided amongst four different morphological types: hollow spheres, solid spheres, tubes and irregularly shaped (referred to as ‘amorphous’ in the text and tables) material.

*Part A: Systematic Study of the use of D-gluconic Acid in the  
Synthesis of Silica Gel by the Templated Sol-Gel Method*

### 3.3. RESULTS AND DISCUSSION

#### 3.3.1. General Comments

Generally, silica gels synthesised in the presence of D-gluconic acid yielded more hollow spheres than tubes, and for this reason, only hollow and solid sphere sizes will be discussed.

**Fig. 3.2** shows a Powder X-ray diffractogram of the silica material synthesised in the presence of D-gluconic acid, before and after calcination. They both show the material to be amorphous. The peak that appears around 4  $2\theta$  degrees in the diffractogram for the uncalcined sample is due to residues of the template which were not removed during washing of the material.



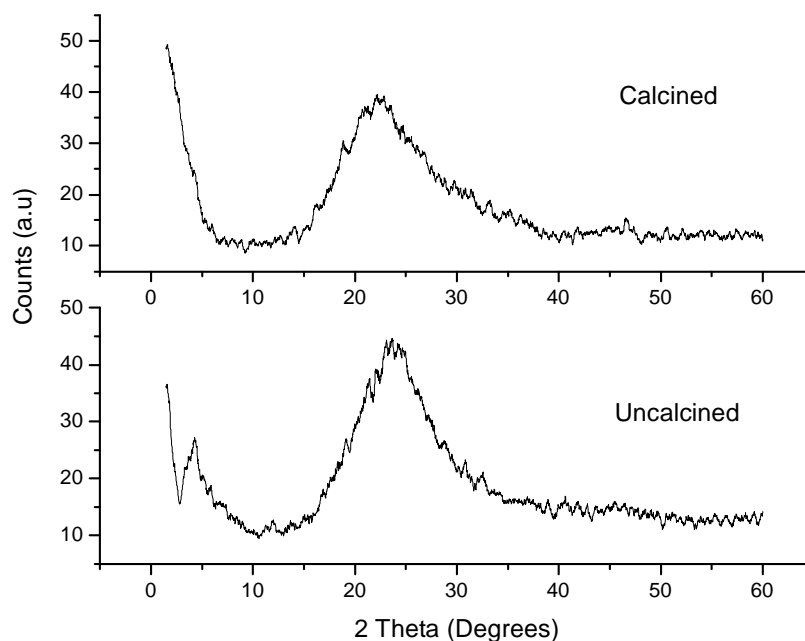


**Figure 3.2.** Powder X-ray diffractogram of a calcined and uncalcined typical material, synthesised at 25 °C with 85 mmol D-gluconic acid, 170 mmol  $\text{NH}_4\text{OH}$  in ethanol containing 2.3 %  $\text{H}_2\text{O}$ .

**Fig. 3.3** shows a typical isotherm of a calcined silica sample. It reveals a type IV isotherm which is typical of mesoporous materials<sup>7,8</sup>. As no limitation of adsorption at high relative pressure values was observed, the hysteresis loop was classified as of type H3, which is characteristic of solids consisting of aggregates of plate-like particles forming slit-shaped pores of nonuniform size and/or shape<sup>7,8</sup>. A BJH pore size distribution determined from the adsorption arm, shown in the inset in **Fig. 3.3**, indicated the presence of some micropores and a narrow distribution of mesopores with diameter of 2.9 nm. Similar results were noted in the pore size distribution determined from the desorption arm. In general, surface areas obtained from micropores were 3-8 % of the total surface area of the materials.

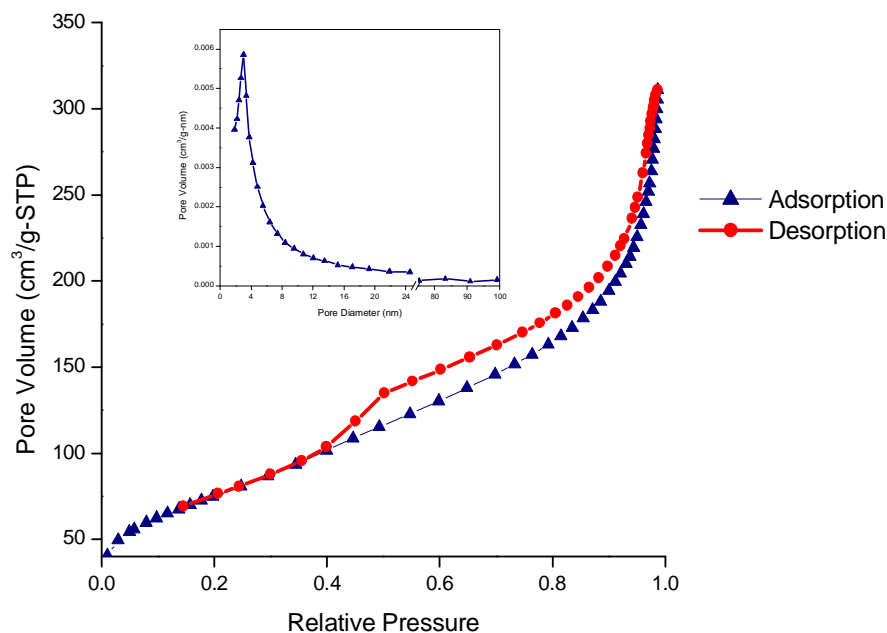


**Figure 3.3.** Nitrogen isotherm and BJH pore size distribution, calculated from the adsorption arm of the isotherm (inset) of a material synthesised at room temperature, with 85 mmol D-Gluconic acid, 170 mmol  $\text{NH}_4\text{OH}$  and 2.3 %  $\text{H}_2\text{O}$ .

**Figure 3.4** shows a thermogravimetric analysis profile of a typical material, carried out in a nitrogen atmosphere. It shows two weight losses, the first weight loss of 7 % occurring mainly as a result of loss of moisture in the sample, around 70 °C, and the second of 10 % occurring due to loss of the template, around 280 °C. No further weight loss was observed. Thus, by the end of the analysis, only 17 % of the original sample weight was lost, showing the thermal stability of the material.

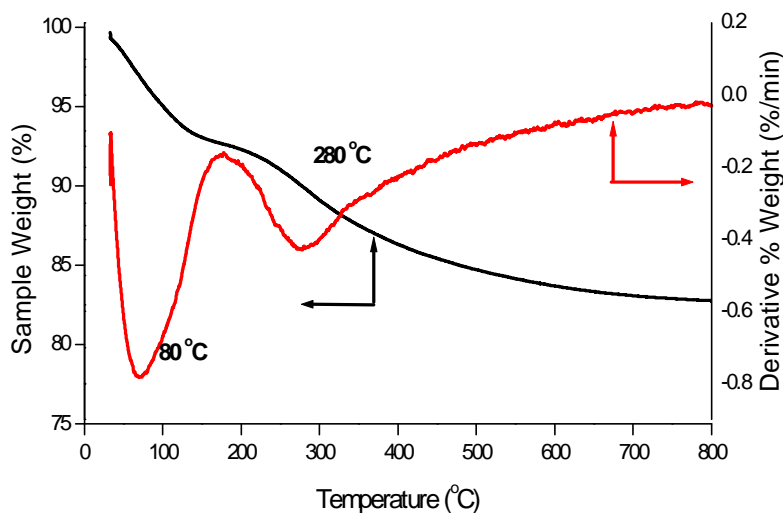


**Figure 3.4.** TGA profile of an uncalcined material synthesised at 25 °C with 85 mmol d-gluconic acid, 170 mmol  $\text{NH}_4\text{OH}$ , and 2.3 %  $\text{H}_2\text{O}$  in ethanol.

### 3.3.2. Effect of Temperature

**Tables 3.1** and **3.2** detail the results of varying the synthesis temperature on the particle distribution, particle size and physisorption properties of the synthesised silica gels. It was found that the hollow sphere yield increased with an increase in temperature, while the yield of the other morphologies decreased. Also, the hollow sphere outer diameter increased and reached a maximum at a synthesis temperature of 55 °C. The maximum hollow sphere outer diameter obtained at 55 °C corresponds with the maximum hollow sphere and minimum amorphous material yields obtained at the same temperature. The decrease in hollow sphere yield and diameter, with a corresponding increase in amorphous material obtained at 75 °C could be due to evaporation of ammonium hydroxide. A lower base concentration results in a decrease of the amount of template formed therefore decreasing the yield of shaped silica.

**Table 3.1.** Effect of temperature on silica particle distribution.

Temperature (°C)	Hollow spheres (%)	Solid spheres (%)	Tubes (%)	Amorphous (%)
25	30	20	10	40
55	65	0	5	30
75	60	0	5	35

The material synthesised at 25 °C was found to have the highest surface area, while the surface areas obtained with materials synthesised at 55 and 75 °C were the same. Also, the pore volumes of the synthesised materials were found to increase with an increase in the synthesis temperature. It was, however, expected that the material synthesised at 25 °C would show a low surface area, under the synthesis conditions, as a result of low hollow sphere and higher solid sphere yields obtained under the reaction conditions. The BJH pore size distributions of the materials, shown in **Fig. 3.5**, show that the materials synthesised at both 25 and 55 °C had narrow distributions of pores, with the lower temperature-synthesised material having the majority of the pores at a small size of 2.9 nm, while that synthesised at 55 °C had its majority at 3.7 nm. The material synthesised at 75 °C produced a silica gel with a broad pore size distribution centred between 9.6 and 17 nm. Thus the decrease in surface area with an increase in synthesis temperature above 25, despite the increase in pore volume observed, was due to the shift in the pore size distribution to higher pore diameters. Increasing the synthesis temperature from 55 to 75 °C did not change the surface area of the materials despite the similar particle yields observed with the two materials. The broad pore size distribution obtained with the higher temperature-synthesised material was expected to lower the surface area even further. This observation can, therefore, be attributed to an increase in pore volume observed with the higher temperature-synthesised material.

**Table 3.2.** Effect of synthesis temperature on silica particle size and physisorption properties.

Temperature (°C)	Hollow Spheres O.D* (nm)	Solid Spheres O.D*(nm)	BET Surface Area (m <sup>2</sup> /g)	Pore Volume (cm <sup>3</sup> /g)
25	100-940	150-1033	273	0.446
55	180-1680	0	183	0.538
75	80-1500	0	182	0.611

\*- Outer diameter.

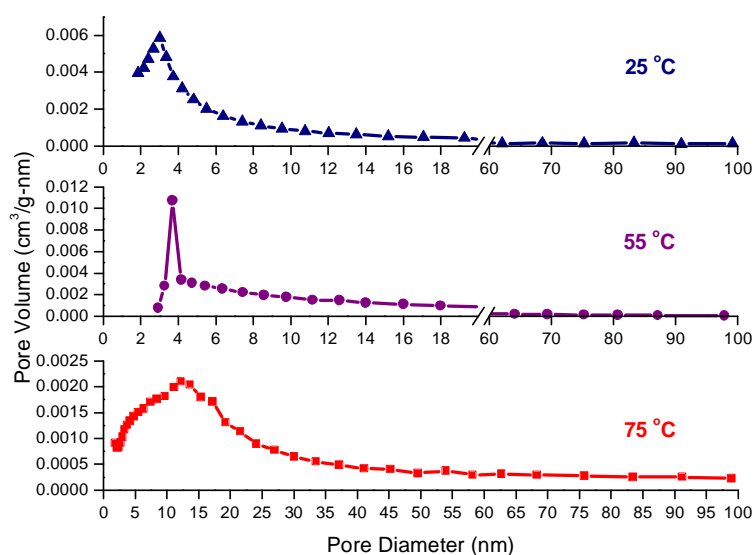


**Figure 3.5.** BJH pore size distributions (calculated from the adsorption arms of the isotherms) of silica gels synthesised at different temperatures.

The TEM images shown in **Fig. 3.6**, display the change in size of the hollow spheres as a result of an increase in temperature. One noticeable difference in the appearance of the hollow spheres synthesised at different temperatures is that those synthesised at 25 °C appeared clearer and had thicker walls than those synthesised at higher

temperatures. The hollow spheres synthesised at 75 °C had surface attached colloidal particles which made them appear cloudier and as if their walls were thicker.

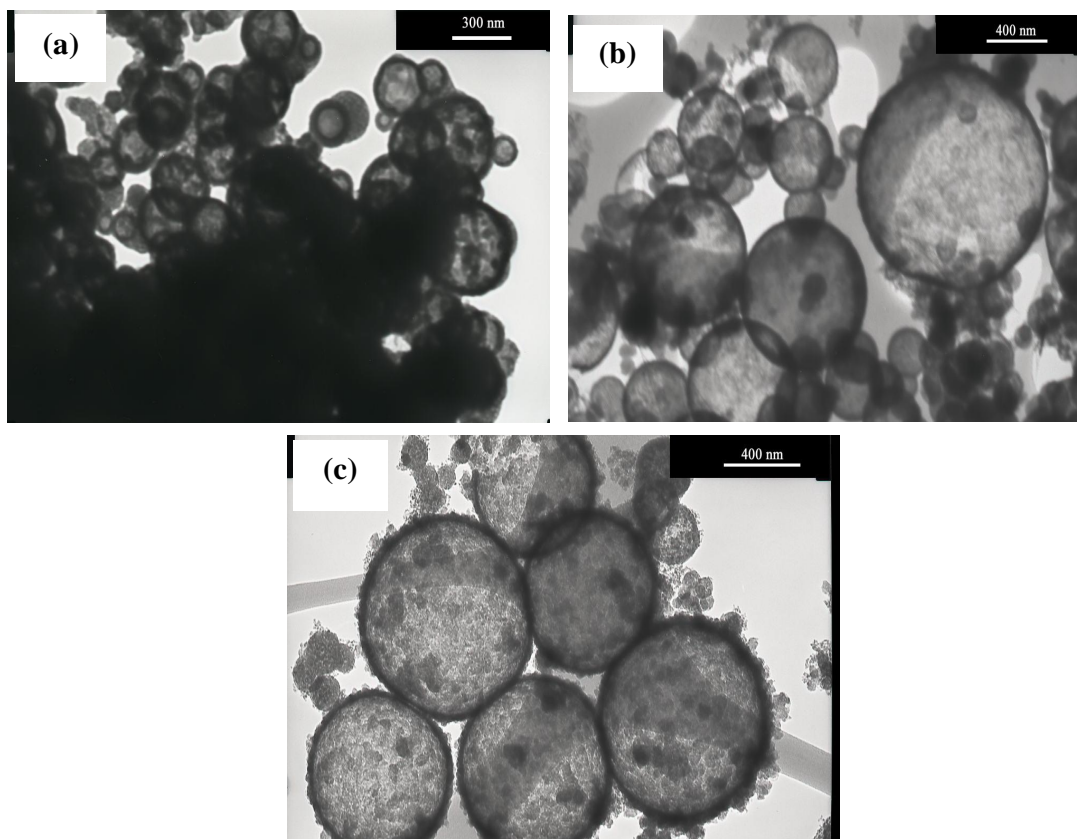


**Figure 3.6.** TEM images of hollow spheres synthesised at (a) 25 °C, (b) 55 °C and (c) 75 °C .

### 3.3.3. Effect of varying D- gluconic acid concentration

**Table 3.3** shows the effect of varying the amount of D-gluconic acid on the particle distribution of the silica gels. It was observed that increasing the acid amount led to a decrease in the hollow spheres and amorphous material yield, while an increase in the solid sphere yield and a slight increase in the tube yield was observed. It was also observed that increasing the acid amount from 85 to 170 mmol did not lead to a

change in the yields of the different morphologies. The decrease in hollow sphere yield with a corresponding increase in tube yield implies that the template prefers to form needle-like crystals, rather than spherical crystals, when present in large amounts. The increase in solid sphere yield could be due to changes in the pH of the synthesis solution as the acid amount was increased. Since D-gluconic acid is a monocarboxylic acid, it can react with ammonium hydroxide with the stoichiometric ratio of 1:1 to form ammonium D-gluconate, the latter is presumed to be the template. However, D-gluconic acid occurs in equilibrium with gluconic acid lactone, thus, only part of the used amount of the 'acid' could interact with ammonium hydroxide to form the template. Thus, the presence of the lactone could have inhibited complete formation of the template, hence increasing the amount of the acid beyond the stoichiometric amount of 85 mmol had no effect on the particle distribution.

Both the hollow and solid sphere diameters increased with an increased in D-gluconic acid amount to 85 mmol, and then decreased when the acid amount was increased further. The increase in the diameter of the hollow spheres was brought about by the presence of bigger template crystals at the higher concentration of the template. The increase in the solid sphere diameter which was followed by a decrease as the acid amount was increased further, and the decrease in the hollow sphere diameter at higher concentration of the acid could be due to pH changes as the acid amount was increased.

**Table 3.3.** Effect of variation of D-gluconic acid amount on silica particle distribution.

Acid amount (mmol)	Hollow spheres		Solid spheres		Tubes (%)	Amorphous (%)
	Yield (%)	O.D*(nm)	Yield (%)	O.D*(nm)		
43	50	140-770	5	100-350	0	45
85	30	100-940	20	150-1033	10	40
170	30	80-425	20	80-300	10	40

\*-Outer diameter

**3.3.4. Effect of varying NH<sub>4</sub>OH amount**

The effect of varying the base catalyst amount on particle distribution and size is presented in **Table 3.4**. It was observed that increasing the base amount beyond 170 mmol had no effect on the particle distribution, as the base had already exceeded the stoichiometric amount of 85 mmol. However an increase in the hollow sphere outer diameter with an increase in NH<sub>4</sub>OH amount was observed, with mostly bursting hollow spheres (indicated with arrows) obtained with 510 mmol, as shown in **Fig. 3.7**. A decrease which was followed by an increase in solid sphere diameter with an increase in ammonia amount was observed. The change in the particle size observed could have been brought by changes in the pH of the synthesis solution.



**Table 3.4.** Effect of varying  $\text{NH}_4\text{OH}$  amount on silica particle distribution and size.

<b><math>\text{NH}_4\text{OH}</math> (mmol)</b>	<b>Hollow spheres</b>		<b>Solid spheres</b>		<b>Tubes (%)</b>	<b>Amorphous (%)</b>
	<b>Yield (%)</b>	<b>O.D* (nm)</b>	<b>Yield (%)</b>	<b>O.D* (nm)</b>		
170	30	100-940	20	150-1033	10	40
340	30	100-1200	20	100-620	10	40
510	30	80-1320	20	125-1275	10	40

\*-Outer Diameter

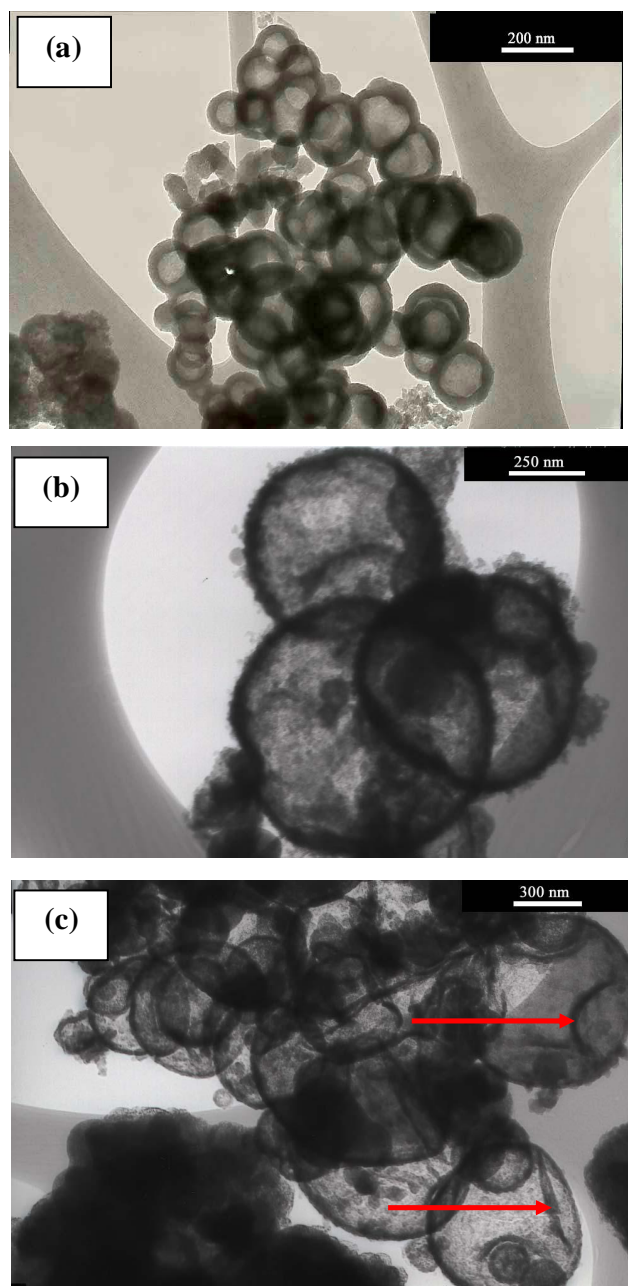


**Figure 3.7.** TEM images of hollow spheres synthesised in (a) 170, (b) 340, and (c) 510 mmol  $\text{NH}_4\text{OH}$ .

### 3.3.5. Effect of variation of water amount

**Table 3.5** shows the effect of variation of water amount on particle distribution and size. It was observed that increasing the amount of water up to 25 % led to a slight increase in the hollow sphere yield and a significant decrease in the amorphous material yield. Also while the tube yield remained the same with an increase in water up to 10 %, which later decreased with a further increase in water amount, the solid sphere yield increased with an increase in water from 2.3 to 25 % water amount. Increasing the water amount beyond 25 % led to a considerable decrease in the hollow sphere yield, a slight decrease in the solid sphere yield and a corresponding significant increase in the amorphous material yield. Increasing the water amount to 75 % and beyond resulted in formation of amorphous material only. It was also observed that increasing amount of water in the solvent gradually decreased the hollow sphere outer diameter, and a general decrease in solid sphere diameter was also observed. Template dissolution can be attributed to the decrease in the yield of shaped morphologies and the decrease in hollow sphere diameter observed as the water amount was increased. However, since the solid sphere diameter and yield have very little to do with the template crystals, their decrease can be attributed to poor hydrolysis of TEOS due to poor miscibility with water, the latter being a result of the low amount of organic co-solvent in the synthesis mixture.

**Table 3.5.** Effect of variation of water (relative to ethanol) amount on silica particle distribution and size.

Water amount (%)	Hollow Spheres (%)	O.D*(nm)	Solid Spheres (%)	O.D*(nm)	Tubes (%)	Amorphous (%)
2.3	30	100-940	20	150-1033	10	40
10	30	80-625	35	63-575	10	25
25	35	80-140	35	80-740	5	25
50	5	84-120	30	70-480	5	60
75	0	0	0	0	0	100

\*.-Outer Diameter.

### 3.3.6. The effect of hydrolysis and ageing time

The effects of the duration of both hydrolysis and ageing on the morphology of the synthesised silica gels were studied. It was observed that increasing the length of hydrolysis time had no effect on the yields of the morphologies but on their appearance and wall thickness. Increasing the hydrolysis time resulted in a reduction of the wall thickness of the hollow spheres; such that they looked enlarged. The hollow sphere wall thickness decreased and they eventually burst with prolonged hydrolysis time. **Fig. 3.8** shows TEM images of hollow spheres that resulted from different hydrolysis times. It shows that after 1 min of hydrolysis (shown in **Fig. 3.8a**), the resultant material contained undeveloped hollow spheres, and while after 2 h of hydrolysis well-defined hollow spheres were obtained, as shown in **Fig. 3.8b**. However, increasing hydrolysis time beyond 2 h, resulted in an increase in the inner diameter of the hollow spheres as a result of the reduction of their wall thickness, and the hollow spheres became cloudy, showing the presence of surface attached particles. This is clearly shown for data collected after 4 and 6 h of hydrolysis time (**Fig. 3.8c** and **3.8d**). After 8 h, the resultant hollow sphere wall thickness had been

reduced so much that the spheres started bursting, as shown in **Fig. 3.8e**. **Fig. 3.9** depicts the decrease in wall thickness of the hollow spheres with increasing duration of hydrolysis as measured by TEM.

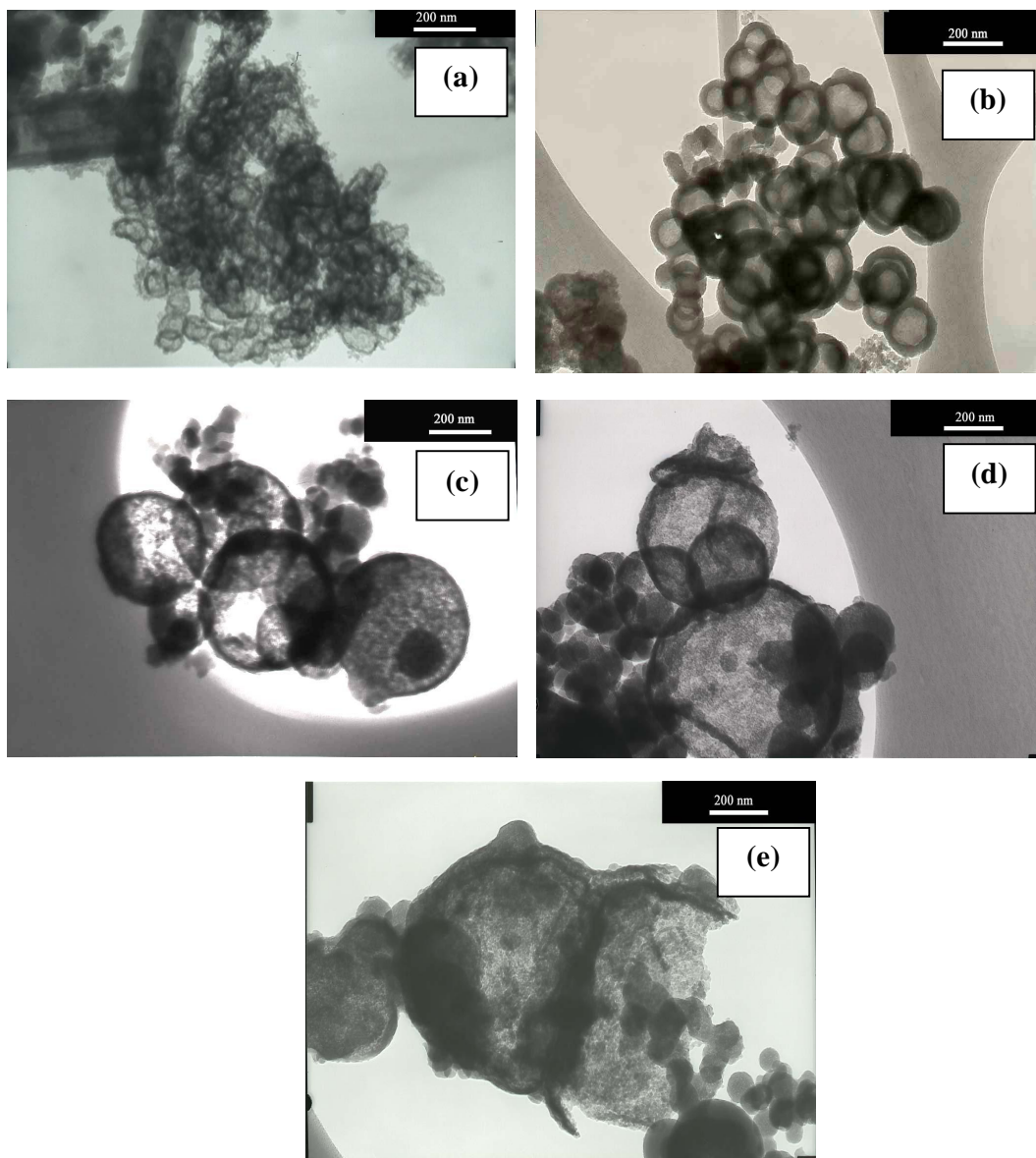


**Figure 3.8.** TEM images of hollow spheres synthesised after hydrolysis for different times. (a) 1 min; developing spheres, (b) 2 h; well-defined hollow spheres (c) 4 h; enlarged spheres, (d) 6h; cloudy and enlarged hollow spheres, and (e) 8 h; bursting sphere and (d) 8 h bursting sphere.

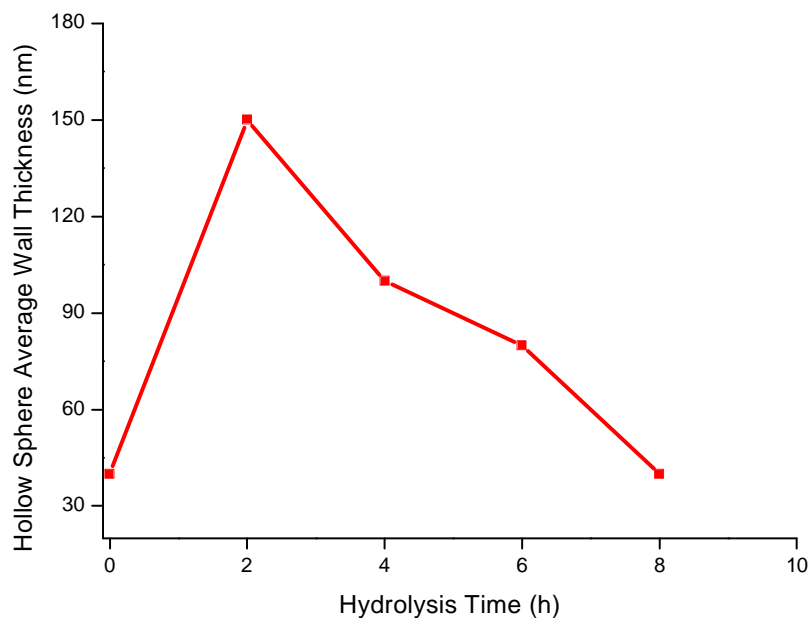


**Figure 3.9.** Effect of hydrolysis time on the hollow spheres average wall thickness.

The data suggest that hydrolysis of TEOS must be done for a reasonable amount of time, so as to allow formation of well-developed hollow spheres, which is 2 h in this case. Otherwise, if TEOS is allowed to hydrolyse for much longer periods, formation of small colloidal particles occur, which are not easily templated into shaped particles upon addition of the base catalyst, probably due to their small size and mass. These colloidal particles will then coat on the surface of the shaped silica material rather than be part of the silica hollow sphere framework. This leads to a decrease in wall thickness of the hollow spheres as observed with an increase in hydrolysis time.

A similar effect was observed on increasing the length of ageing time of the silica gels. **Fig. 3.10** shows TEM images of hollow spheres obtained after ageing for 1 min and 8 h. It shows that well-defined hollow spheres were already formed after only 1 min of ageing, as shown in **Fig. 3.10a**. The hollow sphere wall thickness was found

to gradually decrease and surface attached colloidal particles were formed on the hollow spheres with prolonged ageing time, as shown in **Fig. 3.10b** (8 h of ageing time). The decrease in the average wall thickness of the hollow spheres with an increase in duration of ageing is summarised in a form of a graph in **Fig. 3.11**.

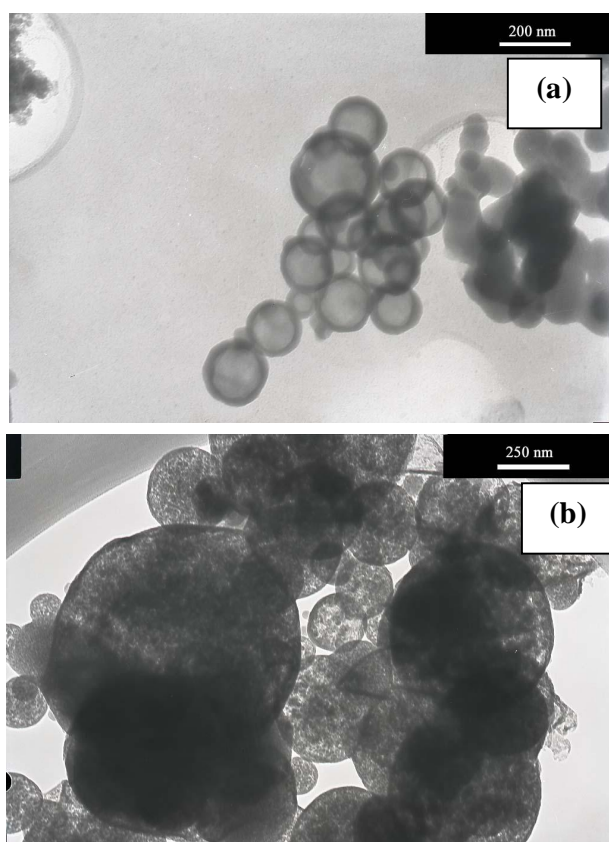


**Figure 3.10.** TEM images of hollow spheres aged for (a) 1 min, smooth and well-defined hollow spheres, and (b) 8 h, very cloudy, thin-walled hollow spheres.

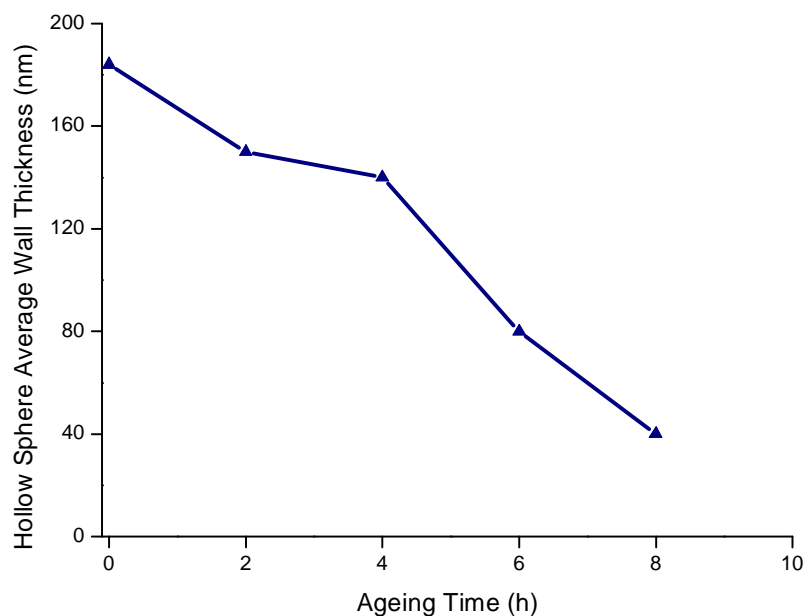


**Figure 3.11.** Effect of length of ageing time on hollow sphere average wall thickness.

The above results suggest that once the hollow spheres are formed, the silica reacts with the excess  $\text{OH}^-$  ions in solution and dissolution of the metastable silica occurs resulting in re-precipitation of colloidal particles on the surface of the hollow spheres. This shows that careful control of the duration of hydrolysis and ageing must be exercised in order to obtain a well-controlled and defined morphology of the resultant gels.

### 3.3.7. Variation of synthesis procedure: The ‘long method’ versus the ‘short method’ synthesis procedure

**Table 3.6** shows the effect of varying the synthesis procedure on the silica particle distribution. It was observed that the ‘short method’ synthesis procedure yielded very low amounts of shaped morphologies and hence a high amorphous material yield when compared to the ‘long method’. **Fig. 3.12** shows TEM images of tubes and



hollow spheres synthesised by the two synthesis procedures. It shows that the hollow spheres synthesised by the ‘short method’ were not as well-defined as those synthesised by the ‘long method’, as shown in **Fig. 3.12a** and **3.12c**. The tubes obtained from both procedures were not very well-developed, as shown in **Fig. 3.12b** and **3.12d**.

**Table 3.6.** Effect of variation of synthesis procedure on silica particle distribution.

Synthesis Procedure	Tubes (%)	Hollow spheres (%)	Solid spheres (%)	Amorphous (%)
‘Short method’	15	5	0	80
‘Long method’	10	30	20	40

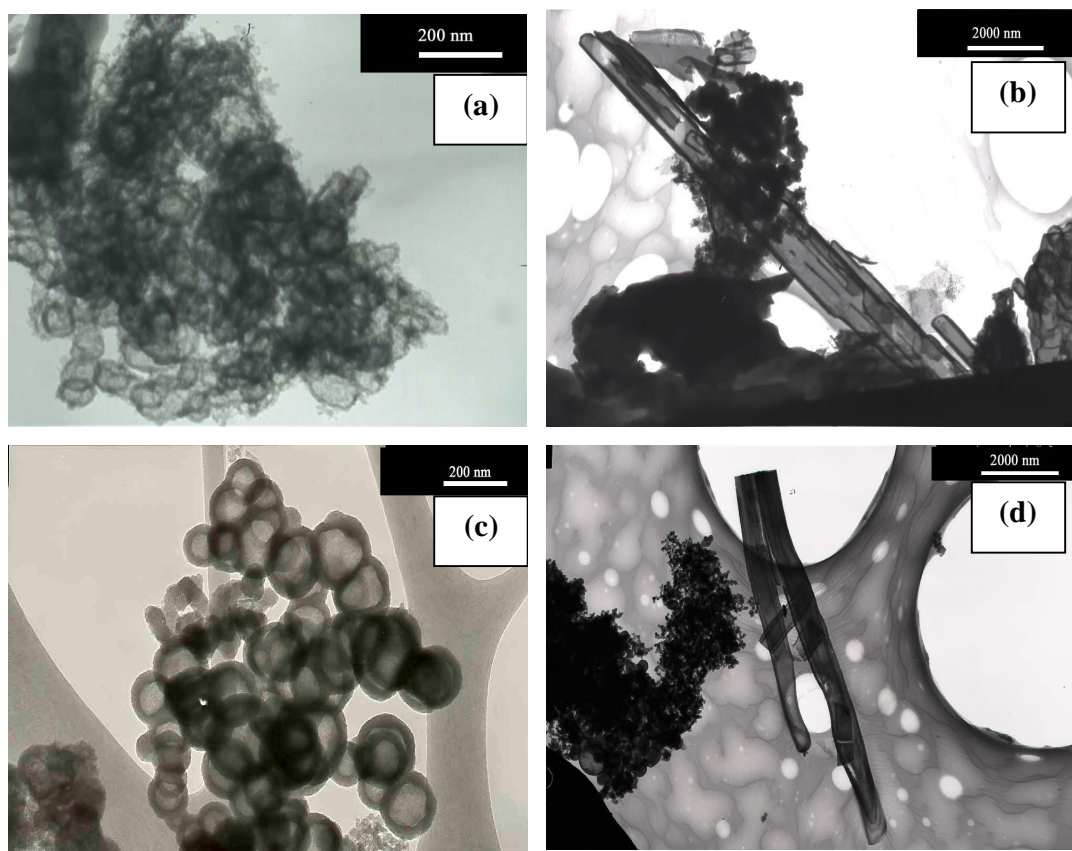


**Figure 3.12.** TEM images of hollow spheres and tubes synthesised by (a) and (b) the ‘short method’, (c) and (d) ‘long method’ synthesis procedures.

The effect of variation of synthesis procedure on particle size and physisorption properties is shown in **Table 3.7**. It was observed that the ‘long method’ synthesis procedure produced bigger hollow spheres and longer tubes than the ‘short method’ procedure, however, wider tubes were obtained with the latter procedure. It was also observed that the ‘short method’ procedure produced a very low surface area and pore volume material when compared to the ‘long method’ procedure. The BJH pore size distributions of the materials, shown in **Fig. 3.13**, show that the material synthesised from the ‘long method’ procedure had a narrow distribution, with the majority of the pores occurring at 2.9 nm, while that synthesised by the ‘short

method' showed a wide pore size distribution. Thus, these results imply that, since in the 'short method', TEOS was not allowed to hydrolyse enough before condensation of the sol, not only were the morphologies under-developed, but the pores were undeveloped as well. Thus hydrolysis of TEOS, allowed the fine-tuning of the pores and the hollow spheres, as observed with the 'long method'.

**Table 3.7.** Effect of variation of synthesis procedure on particle size and nitrogen physisorption properties of the silica gels.

Procedure	Hollow sphere O.D* (nm)	Tube O.D* (nm)	Tube length ( $\mu\text{m}$ )	BET Surface Area ( $\text{m}^2/\text{g}$ )	Pore Volume ( $\text{cm}^3/\text{g}$ )
'short method'	50-120	450-2000	3.1-17	32	0.136
'long method'	100-940	80-750	0.8-26	273	0.446

\*-Outer diameter

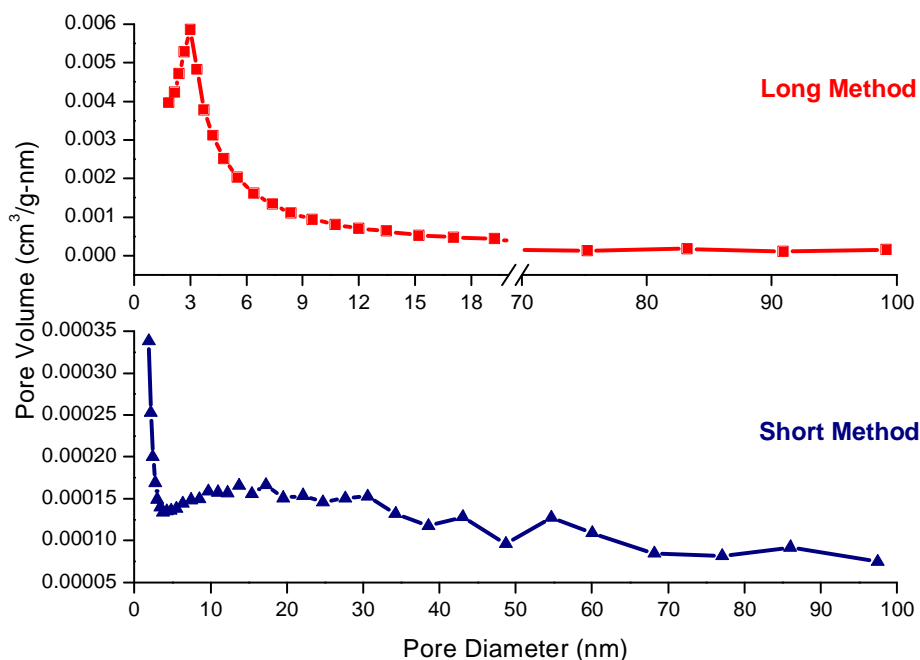


**Figure 3.13.** BJH pore size distributions (calculated from the adsorption arms of the isotherms) of materials synthesised by the ‘long method’ and ‘short method’ synthesis procedures.

### 3.3.8. Effect of variation of organic co-solvent

Methanol, ethanol, isopropanol and 1-butanol were used as co-solvents, and **Table 3.8** shows the effect of variation of the organic co-solvent on the particle distribution. It was found that synthesis in 1-butanol produced the highest amount of hollow spheres, while isopropanol produced the lowest amount. The hollow sphere yield obtained from synthesis in methanol and ethanol were almost the same, however, a higher yield of amorphous material was obtained with the latter. It was also observed that out of all the organic co-solvents employed in this study, methanol produced the lowest amount of amorphous material, which is reflected by the presence of only thick-wall smooth hollow spheres, shown in **Fig. 3.14a**, while thin-wall hollow

spheres with surface attached colloidal particles were obtained from synthesis in the other three co-solvents, shown in **Fig. 3.14b**, **3.14c**, and **3.14d**. Hollow spheres synthesised in both isopropanol and ethanol appeared cloudier than those synthesised in 1-butanol.

**Table 3.8.** Effect of variation of organic co-solvent on silica particle distribution.

Organic co-solvent	Hollow spheres (%)	Solid spheres (%)	Amorphous (%)
Methanol	45	45	10
Ethanol	40	20	40
Isopropanol	25	25	50
1-Butanol	80	0	20

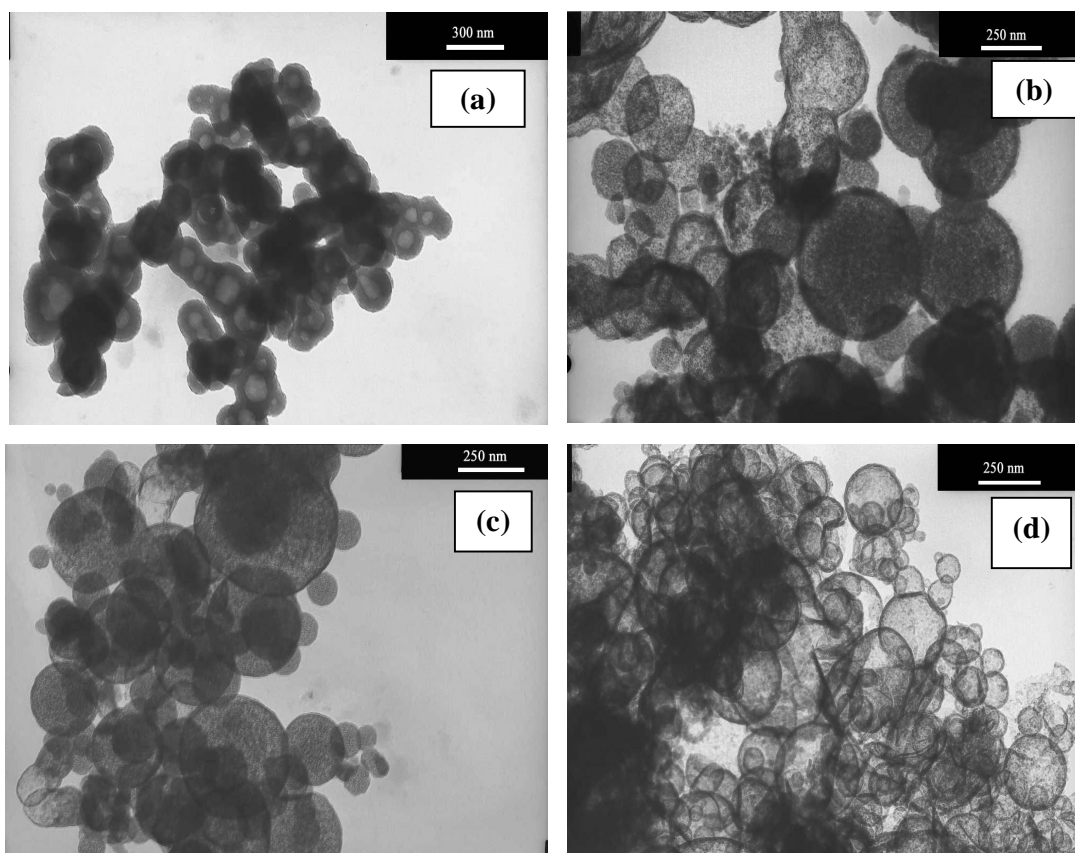


**Figure 3.14.** TEM images of hollow spheres synthesised in different organic co-solvents. (a) Methanol, (b) Ethanol, (c) Isopropanol, and (d) 1-Butanol.

The effect of variation of co-solvent on particle size and physisorption properties of the materials is summarised in **Table 3.9**. It shows that synthesis in ethanol produced bigger particles than in any other co-solvent, and that the particles obtained in methanol, isopropanol and 1-butanol were close in size. It was also observed that the synthesis in ethanol produced a lower surface area material than all other three co-solvents, while the highest surface area was obtained with methanol. The low surface area obtained from the synthesis in ethanol can be attributed to the bigger particle size observed in the resultant material. The pore volume of the synthesised silica gels was found to increase with an increase in the chain length of the organic co-solvent.

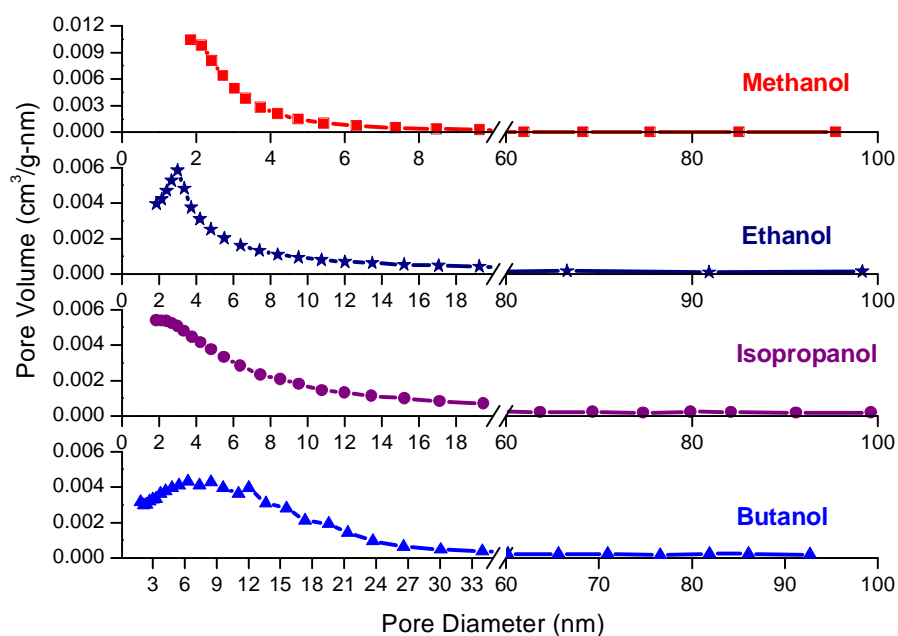
**Fig. 3.15** shows the BJH pore size distributions of the materials synthesised in the different organic co-solvents. It shows that the longer the chain length of the co-solvent, the broader the pore size distribution obtained. The high surface area obtained with 1-butanol, despite the very low amorphous material yield can be attributed to the absence of solid spheres and the high pore volume obtained with the material. The high surface area obtained from the material synthesised in methanol, despite the high solid sphere yield was due to the narrow pore size distribution which was found to occur at a smaller mesopore size of 2-4 nm. The high surface area obtained from the material synthesised in isopropanol was due to the large amount of amorphous material and the large pore volume obtained with the material.

The above results show that the choice of the organic co-solvent not only determines the morphology of the silica gels, by determining the existence of certain amounts of template crystals in the co-solvent, but also the porosity of the resultant silica gel as well, showing that the organic co-solvent affects the rate of TEOS hydrolysis.

**Table 3.9.** Effect of variation of organic co-solvent on silica particle size and surface area.

Organic co-solvent	Hollow spheres O.D* (nm)	Solid spheres (nm)	BET Surface Area (m <sup>2</sup> /g)	Pore Volume (cm <sup>3</sup> /g)
Methanol	80-540	80-800	386	0.305
Ethanol	100-940	150-1033	273	0.446
Isopropanol	80-575	40-500	372	0.631
1-Butanol	50-480	-	375	0.864

\*-Outer diameter

**Figure 3.15.** BJH pore size distributions (calculated from the adsorption arm of the isotherms) of silica gels synthesised in different organic co-solvents.



*Part B: A Study of the use of other Hydroxyacids in the Synthesis of Silica Gel by the Templated Sol-Gel Method*

### 3.4. RESULTS AND DISCUSSION

Silica gels were synthesised at room temperature, by the ‘short method’ procedure, using L-tartaric acid, stearic acid and cinnamic acid as template precursors. The materials were studied by TEM and nitrogen physisorption. It was observed that different morphologies were favored by the different template precursors. **Table 3.10** summarises the particle distribution obtained with the different template precursors. It was observed that cinnamic acid produced only amorphous material, while stearic acid produced a mixture of tubes, amorphous material and solid spheres, the latter produced in high yields. When L-tartaric acid was used, neither solid spheres nor amorphous material were obtained, only tubes and sheets with folds were observed. **Fig. 3.16** shows TEM images of the tubes obtained from using stearic acid and L-tartaric acid. It shows that solid tubes were obtained with both acids. The sheets with folds obtained with L-tartaric acid, shown in **Fig. 3.15c**, show the potential of this acid forming more tubes.

**Table 3.10.** Particle distributions of silica materials synthesised with the different template precursors.

<b>Template Precursor</b>	<b>Tubes (%)</b>	<b>Solid spheres (%)</b>	<b>Sheets (%)</b>	<b>Amorph. (%)</b>	<b>BET Surface Area (m<sup>2</sup>/g)</b>	<b>Pore Volume (cm<sup>3</sup>/g)</b>
L –Tartaric acid	5	0	95	0	492	0.516
Cinnamic acid	0	0	0	100	12	0.0525
Stearic Acid	5	90	0	5	13	0.0345

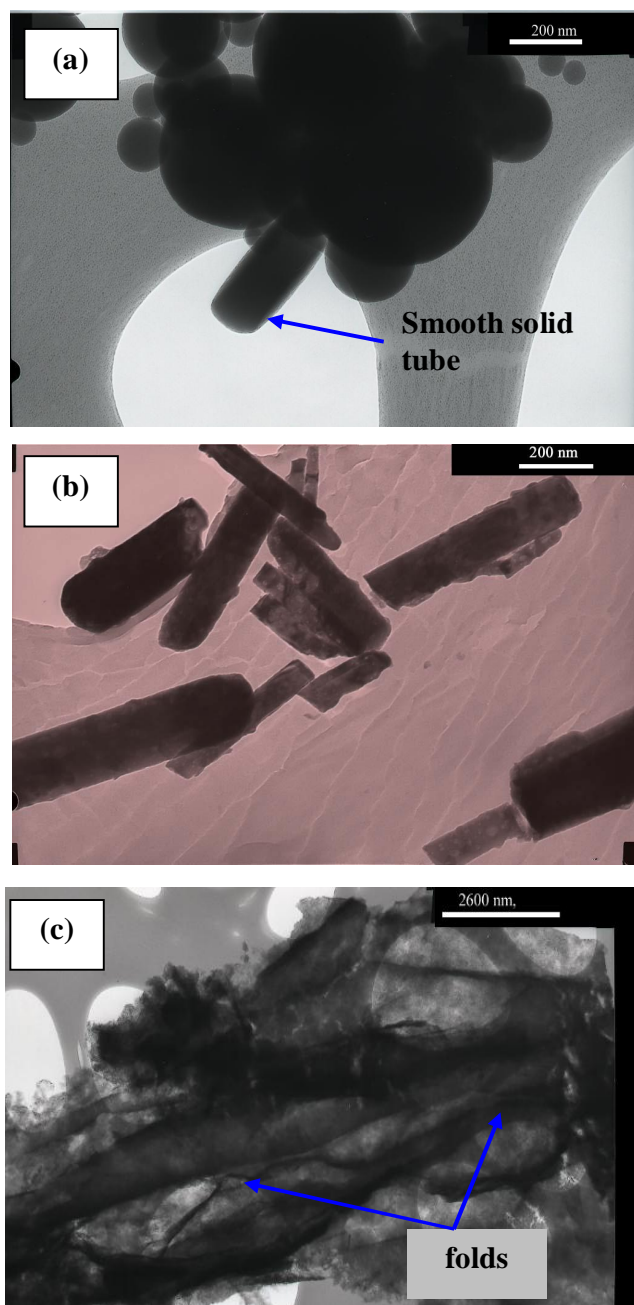


**Figure 3.16.** TEM images of (a) solid smooth tube obtained with stearic acid, (b) solid tubes and (c) sheet with folds obtained with L - tartaric acid.

**Figure 3.17** shows nitrogen adsorption-desorption isotherms and BJH pore size distributions of the materials synthesised using the different acids as template precursors. Isotherms obtained from silica gels synthesised with both stearic and cinammic acids showed no hysteresis, and were therefore classified as of type II, which is characteristic of nonporous or macroporous materials<sup>7,9</sup>. The macroporous nature of these materials is reflected by their low surface areas and pore volumes (shown in **Table 3.10**), and also from their BJH pore size distributions which do not touch the x-axis as the pore diameter increases. However, for the L-tartaric acid synthesised material, a type IV isotherm, which is characteristic of mesoporous materials<sup>7,9</sup>, was obtained, and its hysteresis loop was classified as an H4 hysteresis loop, which shows the existence of large mesopores embedded in a matrix with pores of much smaller size<sup>9</sup>. The mesoporosity of this material is shown by its high surface area and narrow pore size distribution which occurs at 2.9 nm.

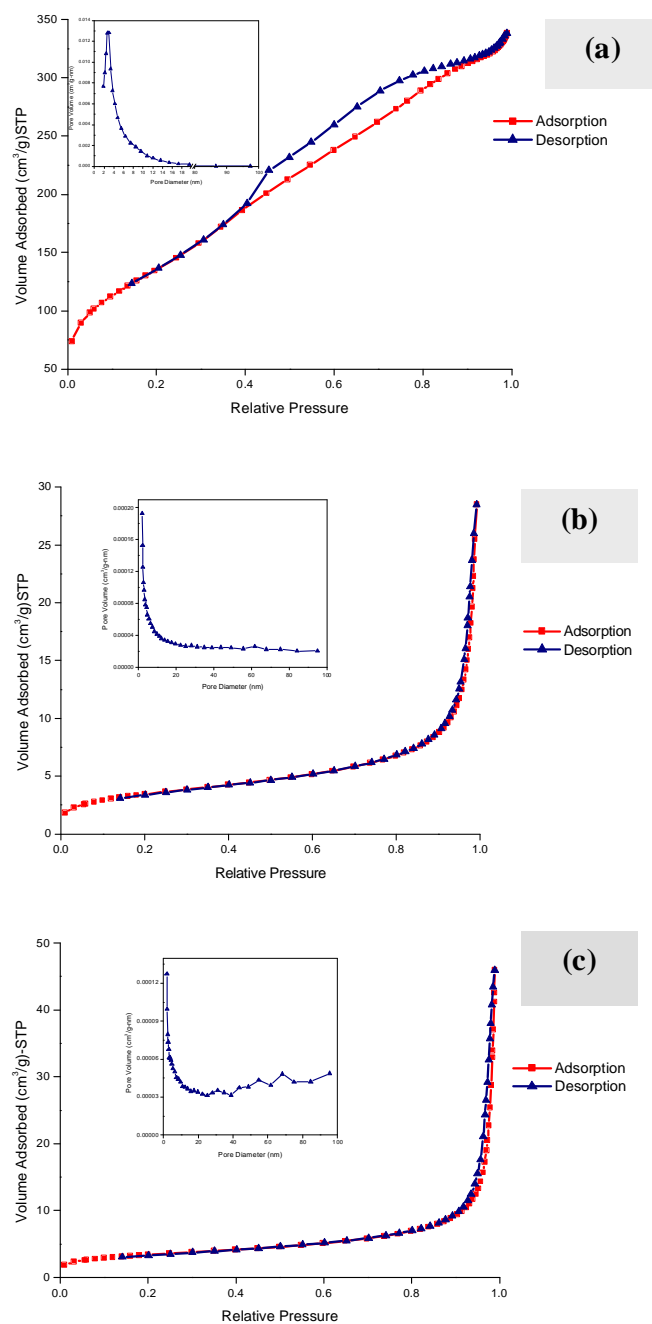


**Figure 3.17.** Nitrogen isotherms and (inset) BJH pore size distributions (calculated from the adsorption arms) of the materials synthesised with (a) L-tartaric acid, (b) cinammic acid and (c) stearic acid.

### 3.5. CONCLUSION

The study has demonstrated that the template precursor, and hence the template itself, together with the synthesis conditions determine the formation of particular morphologies.

The data have shown that an increase in temperature resulted in an increase in the hollow sphere yield and diameter, and the pore volume and diameter of the resultant silica gels, and that evaporation of ammonia at higher temperatures decreased the hollow sphere yields. Even though D-gluconic acid preferably formed hollow spheres, an increase in tube yield was found to occur at higher D-gluconic acid amounts; this shows that the template preferably formed needle-like template crystals at higher D-gluconic acid concentrations, which is a similar observation made when silica gels were synthesised in the presence of oxalic acid. Although no change in the yield of morphologies of the silica gels was observed with an increase in ammonia amount, the diameters of the hollow spheres were found to increase due to changes in the pH of the synthesis medium.

An increase in water amount up to 25 % was found to enhance formation of hollow spheres. However, an increase in water amount beyond 25 % was observed to lead to template dissolution which resulted in a decreased yield of shaped silica particles; which is similar to the results found with oxalic acid in Chapter 2. The excess water also led to poor hydrolysis of TEOS which led to a reduction of the solid sphere diameter. A high hollow sphere yield was obtained when 1-butanol was used as a co-solvent. However, surface attached colloidal particles were found on the hollow spheres, the same were found with both isopropanol and ethanol. Methanol produced thicker-walled smooth hollow spheres with smaller pore diameters. This shows that the choice of co-solvent not only determines the morphology of the silica gels but the porosity as well, due to different TEOS hydrolysis rates in the different co-solvents.

Increased duration of both hydrolysis and ageing resulted in decreased hollow sphere wall thickness and to formation of surface attached colloidal particles and bursting of the hollow spheres, as was found in the presence of oxalic acid in Chapter 2. However, unlike in the presence of oxalic acid, the ‘short method’ procedure produced a material with vast amounts of amorphous material and under-developed hollow spheres, with very low surface area and pore volume and wider pores.

While cinnamic acid produced only amorphous material, L-tartaric acid produced mainly sheets with folds, and stearic acid mainly solid spheres. Of all the three hydroxyacids, L-tartaric acid seemed to be a better candidate in forming shaped morphologies, particularly tubes from the sheets. The data also showed that not only did the template precursor affect the morphology of the resultant silica gels, but their porosity as well, as macroporous materials were obtained with both cinnamic and stearic acids while a mesoporous material was obtained with L-tartaric acid.

Thus, this whole study showed that materials with shaped morphologies can be obtained with the use of cheap template precursors, and that manipulation of the synthesis conditions can produce materials with enhanced yields of shaped morphologies.

**3.6. REFERENCES**

1. (a) M. Adachi, T. Harada, M. Harada, *Langmuir*, 15 (1999) 7097.  
(b) H. Imai, N. Takahashi, R. Tamura, H. Hirashima, *Langmuir*, 17 (2001) 17.
2. (a) J.H. Jung, Y. Ono, S. Shinkai, *Langmuir*, 16 (2000) 1643.  
(b) J.H. Jung, K. Nakashima, S. Shinkai, *Nanoletters*, 1 (2001) 145.  
(c) J.H. Jung, M. Amaike, K. Nakashima, S. Shinkai, *J. Chem. Soc., Perkin Trans.*, 2 (2001) 1938.  
(d) Y. Ono, K. Nakashima, M. Sano, Y. Kanekiyo, K. Inoue, J. Hojo, S. Shinkai, *Chem. Commun.*, (1998) 1477.  
(e) J.H. Jung, Y. Ono, S. Shinkai, *Angew. Chem. Int. Ed. Engl.*, 39 (2000) 1862.
3. (a) Y. Ono, Y. Kanekiyo, K. Inoue, J. Hojo, M. Nango, S. Shinkai, *Chem. Lett.*, (1999) 475.  
(b) K.J.C. van Bommel, J.H. Jung, S. Shinkai, *Adv. Mater.*, 13 (2001) 1472.
4. Y. Le, J.-F. Chen, J.-X. Wang, L. Shao, W.-C. Wang, *Mater. Lett.* 58 (2004) 2105.
5. R.A. Caruso, M. Antonietti, *Chem. Mater.*, 13 (2001) 3272.
6. (a) H. Nakamura, Y. Matsui, *J. Am. Chem. Soc.*, 117 (1995) 2651.  
(b) L. Wang, S. Tomura, F. Ohashi, M. Maeda, M. Suzuki, K. Inuka, *J. Mater. Chem.*, 11 (2001) 1465.  
(c) F. Miyaji, S.A. Davis, J.P.H. Charmant, S. Mann, *Chem. Mater.*, 11 (1999) 3021.  
(d) F. Miyaji, Y. Watanabe, Y. Suyama, *Mater. Res. Bull.*, 38 (2003) 1669.  
(e) E. M. Mokoena, A.K. Datye and N.J. Coville, *J. Sol-Gel Science Technology.*, 28 (2003) 307.
7. K.S.W. Sing, D.H. Everett, R.A.W. Haul, L. Moscou, R.A. Pierotti, J. Rouquérol, T. Siemieniowska, *Pure & Appl. Chem.* 57 (1985) 603.
8. G. Leofanti, M. Padovan, G. Tozzola, B. Venturelli, *Catal. Today*, 41 (1998) 207.
9. M. Kruk, M. Jaroniec, *Chem. Mater.*, 13 (2001) 3169.



## **PART II**

# **FISCHER-TROPSCH STUDIES OF SILICA SUPPORTED IRON CATALYST**

# CHAPTER 4

## FISCHER-TROPSCH SYNTHESIS: LITERATURE REVIEW

### 4.1. INTRODUCTION

The Fischer-Tropsch (FT) process can be defined as a hydrogenation of oxides of carbon producing higher hydrocarbons and/or oxygenated hydrocarbons in the presence of a catalyst<sup>1</sup>. The Fischer-Tropsch synthesis (FTS) is a practical way of converting coal and natural gas to gasoline, diesel oil, wax and chemicals such as olefins, alcohols and aldehydes. The hydrocarbon products are mostly liquid at ambient conditions but some are gaseous and some may even be solid. The FT process can be considered as a cheaper method for the production of liquid fuels and chemicals, when compared to crude oil, due to the continuously increasing price of the latter.

The fact that a hydrocarbon (methane) could be catalytically produced from carbon monoxide and hydrogen was observed by Sabatier in 1902 in his work using a Ni catalyst. In 1913 the Badische Anilin und Soda Fabrik (BASF)<sup>2</sup> revealed that mixtures of higher hydrocarbons and oxygenated compounds could be catalytically produced from a similar mixture under high pressures. Ten years later, Franz Fischer and Hans Tropsch obtained *synthol*, a mixture of hydrocarbons and oxygenated compounds, from the reaction of hydrogen and carbon monoxide over alkalised iron and other catalysts<sup>3</sup>. Since then more and more work has been done in the research and development of FT technology world-wide (a useful website for the location of publications relating to FT technology may be found at <http://www.fischer-tropsch.org>), however, the FT process today finds commercial application only in South Africa (PetroSA and Sasol) and Malaysia (Shell)<sup>4</sup>, and soon in Qatar and Nigeria.

## 4.2. THE FISCHER-TROPSCH REACTION

The chemistry taking place in a Fischer-Tropsch reactor is complex, but can be simplified into the following chemical reactions:

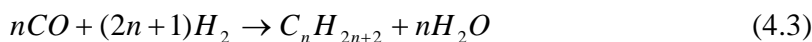
Methane formation:



Ethane formation:



Paraffin formation:

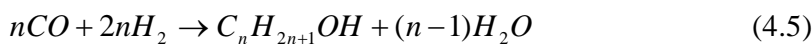


Olefin formation:



Depending on a number of factors, primarily the hydrogen to carbon monoxide ratio in the syngas and the type of catalyst employed, one or the other of reactions (4.3) and (4.4) predominates in the synthesis<sup>5</sup>. The reaction presented in eq. (4.3) is favoured by relatively high H<sub>2</sub> to CO ratios and catalysts with strong hydrogenating ability, while the reaction presented in eq (4.4) is favoured by a low H<sub>2</sub> to CO ratio and catalysts with less strong hydrogenating ability. Alcohols and acids can also form by the following chemical reactions:

Alcohol formation:



Acid formation:



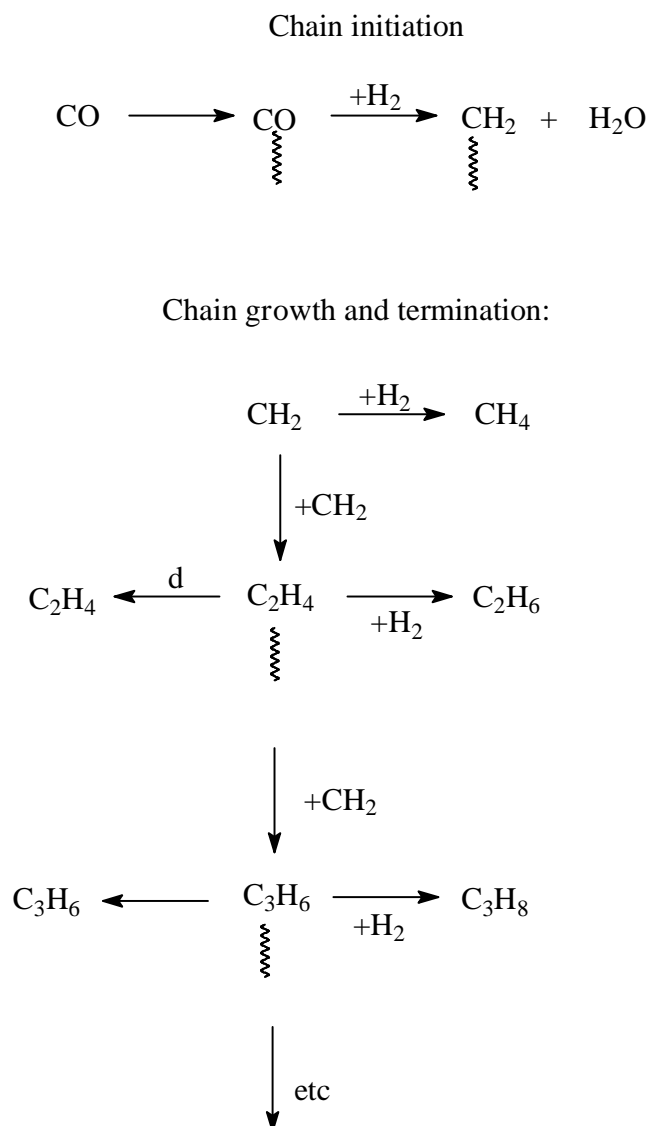
When an iron catalyst is employed, the water gas shift (WGS) reaction can take place:



The resultant  $H_2$  from the WGS reaction then goes back into the reactant stream and is used up in the FT reaction.

Thus, in general the main products of FTS are n-olefins (mainly  $\alpha$ -olefins, also internal olefins) and n-paraffins, and the typical side-products are oxygenates (1-alcohols, aldehydes, ketones and carboxylic acids) and branched compounds (mainly mono-methyl branched)<sup>6</sup>. Methane is considered to be an undesirable product in the FT reaction.

Different mechanisms have been proposed for hydrocarbon formation on the surface of a catalyst in the FT process<sup>1,7</sup>. All proposed mechanisms have in common the assumption that chain growth occurs by a step-wise procedure. Thus a mechanism of chain growth and termination was proposed<sup>6</sup> and the reaction sequence is illustrated in **Scheme. 4.1**. A 'CH<sub>2</sub>' unit can either react with H<sub>2</sub> to yield methane, which will desorb from the surface or can link up with another 'CH<sub>2</sub>' unit to form an adsorbed 'C<sub>2</sub>H<sub>4</sub>' species. Chain termination can occur whereby the adsorbed 'C<sub>2</sub>H<sub>4</sub>' species desorbs to yield ethylene, or it is hydrogenated to yield ethane. On the other hand, chain propagation can occur whereby the desorbed 'C<sub>2</sub>H<sub>4</sub>' unit links up with another 'CH<sub>2</sub>' unit to produce an adsorbed 'C<sub>3</sub>H<sub>6</sub>' unit. The reaction sequence can continue and thus hydrocarbons ranging from methane to high molecular mass waxes can be produced.



**Scheme 4.1.** Schematic representation of the mechanism for hydrocarbon chain growth and chain termination<sup>6</sup>.

The FT process is not selective since it is a polymerisation process<sup>8</sup>. Thus, the product distribution shows a wide spectrum of mainly linear hydrocarbons ranging from methane to heavy waxes. The wide variety of products can be a drawback, because expensive treatment facilities are needed to separate and upgrade them. The

actual composition/product distribution of a FT process depends on many reaction variables such as reaction conditions, the reactor system, as well as the catalyst formulation and physical properties of a catalyst. Thus, in this chapter some of these variables will be discussed.

### **4.3. FISCHER-TROPSCH CATALYSTS**

#### **4.3.1. Active Metals**

A catalyst is a very important component of the FT reaction, as the choice of the catalyst determines the distribution of the final products. Only the four metals iron, cobalt, nickel and ruthenium have been found to be sufficiently active for application in the FT synthesis. The relative cost of these metals in 2004 is shown in **Table 4.1**. Fe is the cheapest of all four metals while Ru is the most expensive. Ni was found to produce a lot of methane and its use as an FT catalyst has therefore been abandoned. The price of Ru is very high and it is available in amounts that are insufficient for large-scale industrial application. Thus, this leaves only Co and Fe as practical FT catalysts for industrial applications.

**Table 4.1.** Approximate relative cost of metals active for Fischer-Tropsch in 2004<sup>6</sup>.

Metal	Relative Cost
Fe*	1
Ni	250
Co	1000
Ru	48000

\* Fe as scrap metal.

#### 4.3.1.1. Iron

Iron catalysts are the most employed catalysts in the industrial FT process. Iron catalysts are cheaper, and their liquid hydrocarbon products are highly olefinic<sup>9,6</sup>, which makes them the most desirable catalysts for the production of olefins for use in the petrochemical industry. They have a high tolerance for sulphur<sup>9</sup>, which makes them suitable for use with coal-derived syngas.

Iron catalysts are also known to be highly responsive to promoters<sup>6</sup>, thus the activity and selectivity of an iron catalyst can be enhanced by their addition. Fe catalysts also have the ability to catalyse the WGS reaction. Thus, syngas with lower H<sub>2</sub> to Co ratios, as obtained from gasification of coal, can be used.

However, the lifetime of Fe catalysts in FT reactors is known to be short because these catalysts have a tendency to form carbides and oxides during the reaction. **Fig. 4.1** illustrates the phase changes that occur with time on stream in an iron catalyst reduced in H<sub>2</sub> and operating at 330 °C<sup>10</sup>. After reduction in H<sub>2</sub>, only Fe metal was found on the catalyst. However, as soon as H<sub>2</sub> was replaced by syngas, a change in the phase occurred; and the Fe metal was found to rapidly convert into a mixture of carbides and magnetite. Thus the activity of an iron catalyst declines with increased

time on stream mainly due to the phase changes, particularly into oxides, that occur in the catalyst.

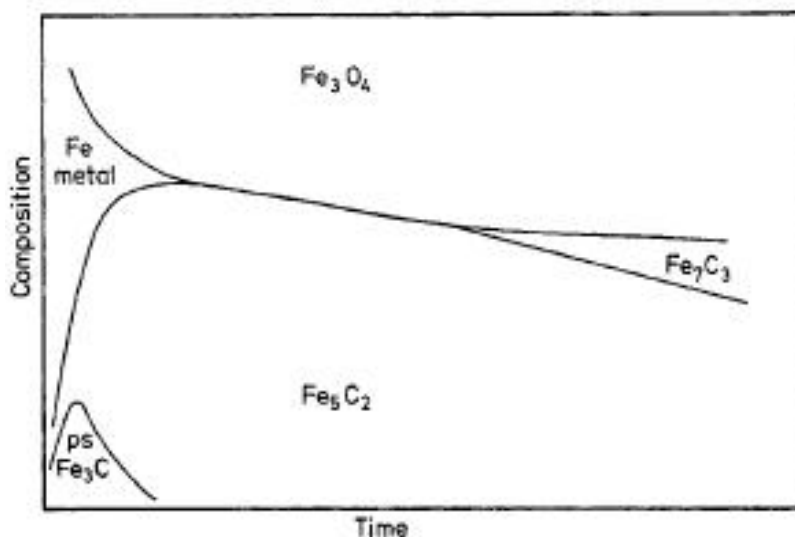


**Figure 4.1.** The change in composition of iron catalysts during FT reaction. The units are undefined as the rates of phase changes depend on alkali content<sup>10</sup>.

#### 4.3.1.2. Cobalt

Co-based catalysts provide the best compromise between performance and cost for the production of hydrocarbons by the FTS<sup>11</sup>. Because of the high cost of Co, the use of bulk Co catalysts is not economically feasible. Thus supported Co catalysts are employed industrially in the FT reaction. Typical support materials used are SiO<sub>2</sub><sup>12</sup>, Al<sub>2</sub>O<sub>3</sub><sup>13</sup>, TiO<sub>2</sub><sup>11,14</sup>, CeO<sub>2</sub><sup>14(a),15</sup> and ZrO<sub>2</sub><sup>14(a),15</sup>.

Unlike Fe catalysts, Co catalysts produce predominantly paraffins. The primary hydrocarbon products produced are also highly linear and methane selectivity is generally higher whereas the selectivity towards oxygenated hydrocarbons is lower compared to those produced by Fe catalysts.



An important advantage of using Co catalysts in FT reactions is the absence of water gas shift activity, so that significant amounts of CO<sub>2</sub> are not produced in the reactor. They also produce smaller quantities of oxygenates when compared to Fe catalysts, thus, increasing the catalyst lifetime and facilitating product processing<sup>16</sup>.

However, Co catalysts are not suitable for coal applications due to the catalyst poisoning from various impurities that are usually present, especially sulphur, and these impurities are difficult to remove to the required low levels. Thus, Fe catalysts are generally preferred when coal is used as a source of syngas. Also, Co-based catalysts reoxidise in the presence of water<sup>17</sup>.

#### 4.3.1.3. Nickel

Under FT conditions, supported and unsupported Ni catalysts were found to have parallel reactions which involved both methanation and FT routes<sup>18</sup>. Ni was found to be the most active catalyst for hydrogenation and consequently has a very high methane selectivity and low olefin selectivity at high temperatures, while at low temperatures was found to form volatile nickel carbonyls, which eventually lead to loss of Ni from the reactor<sup>1,19</sup>. Hence Ni catalysts are not employed in large scale FTS.

Ni supported on TiO<sub>2</sub> was found to exhibit better resistance towards poisoning and formation of nickel carbonyls, and enhanced activity towards formation of high molecular weight paraffinic products, when compared to unsupported Ni, however, high methane selectivity was still observed in this case<sup>20</sup>. For a Ni/Kieselghur catalyst, it was found that the reduction temperature affects the catalyst's methanation activity; a 90 % methane selectivity was obtained when the catalyst was reduced at 250 °C while only 30 % methane was observed when the catalyst was reduced at 175 °C<sup>21</sup>.

#### 4.3.1.4. Ruthenium

Ru is the most active FT catalyst and can produce a high molecular weight wax at temperatures as low as 150 °C. The wax produced contains less olefins and oxygenated products when compared to that produced by Fe and Co catalysts. The Ru catalyst is very stable, and is known to oxidise or carburise less under FT conditions when compared to other FT catalysts<sup>7(f),22</sup>. Another advantage of this catalyst is that no promoters are required to stabilise its activity<sup>23,24</sup>. Like with Ni catalysts, high selectivities towards methane are obtained at elevated temperatures. However, due to the high cost of Ru and its inadequate availability, it is not used in industrial applications, thus its application is limited to small scale research studies.

#### 4.3.1.5. Other FT catalysts

Other metals that have been investigated for the catalysis of the FT reaction are Rh, Os, Pd and Pt and have been found to have lower FT activity when compared to Fe, Co, Ni and Ru<sup>6,25</sup>. Also, Rh was found to produce large amounts of oxygenated products<sup>6</sup>, which can be an added disadvantage.

Mo was also found to be active for FTS and was found to be resistant to sulphur poisoning<sup>6</sup>. However, its activity was found to be low when compared to Fe catalysts. Studies as Sasol<sup>6</sup> showed that to achieve reasonable conversions the reaction has to be carried out around 400 °C. However, very high methane selectivity (~90 %) was obtained at that temperature, and promotion of this catalyst was able to reduce the selectivity to methane to 50 %.

A Cr-based catalyst has also been investigated but its activity was found to be lower than that of the Mo catalyst<sup>6</sup>.

Bimetallic catalysts<sup>26</sup> have been investigated for FT activity. The major objective of these investigations was to find metals that combine to form bimetallic clusters such that the metals are intimately connected both electronically and geometrically, and the resultant activity is greater than the sum of the two metal components. These include Fe-Co supported on  $\text{TiO}_2$ <sup>26(a)</sup>, Co-Pd on  $\text{Al}_2\text{O}_3$ <sup>26(b)</sup>, Ru-M (M= Fe, Cu, Co, Cr, Ce, V, Mn) on  $\text{Al}_2\text{O}_3$ <sup>26(c)</sup>, unsupported Co-M (M=Rh, Pd, Pt, Fe, Ni)<sup>26(d),(e)</sup>,  $\text{Ni}_x$ -Fe on  $\text{Al}_2\text{O}_3$ <sup>26(f)</sup>, Co-Re on  $\text{Al}_2\text{O}_3$ <sup>26(g)</sup>, Ag-Ru on  $\text{SiO}_2$ <sup>26(h)</sup>, and Fe-Mn<sup>26(i)</sup> catalysts.

#### 4.3.2. Promoters

The production of purified syngas, which is suitable as a feed gas to the FT reactors, is a major cost factor in industry. Whether coal or methane is used as a raw material, the cost of syngas can account for up to about 70 % of both capital and operating costs. Hence it is very important that the conversion of the syngas to (useful) hydrocarbon products in the FT reactors is as efficient and as complete as possible. In order to achieve this objective, the selectivity of the FT reaction should be controlled so as to minimise the production of undesired products such as methane. One way of controlling the product selectivity in an FT reaction is to introduce promoters in to the catalyst.

A promoter is considered as a component of the catalyst that does not take part in a catalytic reaction but changes the properties of the catalyst. The promoters may serve one or more of the following purposes; they may

- (i) supply a catalytic effect not possessed by the catalytic metal alone,
- (ii) facilitate catalyst preparation, conditioning, or regeneration,
- (iii) inhibit catalyst poisoning, and/or
- (iv) improve the physical nature of the support.

Two types of promoters are usually employed for improving the FT catalysts; chemical promoters and structural promoters, and these will be briefly discussed.

#### 4.3.2.1. Chemical Promoters

These types of promoters affect the electronic nature of the catalyst, and their presence may result in a change in the reduction levels of the metal catalyst and its activity and selectivity.

Fe catalysts are significantly affected by the presence of chemical promoters. For all Fe catalysts used in the FT reaction the promotion with the optimum amount of alkali metal is vital for satisfactory FT activity as well as the required selectivity. The presence of an alkali metal in an Fe catalyst has been shown to increase its selectivity towards long chain hydrocarbons and olefinic products, while methane selectivity was decreased. It has also been found by other researchers that the presence of an alkali increases the FT and WGS reaction rates.

Luo and Davis<sup>27</sup> have shown that potassium was a better promoter for an Fe catalyst than all Group 2 alkali metals, in that they obtained higher catalyst activity, higher wax production, lower methane selectivity and higher product olefinicity when they used potassium as a promoter. They showed that although the presence of the Group 2 alkali metals reduced methane formation and increased the probability of chain growth and the olefinicity of the products, the FT activity of the catalyst in the presence of the promoters decreased in the order  $K > Mg > unpromoted > Ba > Be > Ca$ . Similar results were obtained when potassium was compared with the Group 1 alkali metals<sup>28</sup>. It was found that although the presence of the Group 1 metals decreased methane selectivity, and increased the olefinicity of the products, the FT activity of the Fe catalyst decreased in the order  $K > Na > unpromoted > Li > Rb > Cs$  in their presence<sup>28</sup>.

The increase in catalytic activity on addition of potassium has been explained in terms of its structural and/or chemical promotional effects. Extensive characterization studies of catalysts, with and without potassium were made, and it

was found that potassium added in small amounts stabilizes the surface area of the precipitated iron oxyhydrides and protects it against recrystallization during calcination<sup>29,30</sup>. It was also observed<sup>29</sup> that a reduced potassium promoted catalyst had a much higher concentration of active sites than an unpromoted catalyst.

However, increased alkali levels can lead to an increased rate of carbon formation on the catalyst, which can result in increased catalyst consumption<sup>31</sup>. Also increased levels of alkali can lead to increased levels of organic acids in the hydrocarbon product, and these may cause corrosion problems and/or may be problematic in downstream refining operations<sup>31</sup>. It has also been showed that at high promoter concentrations the active sites may be covered by the promoter, resulting in a decline of the catalyst activity<sup>29</sup>.

Another chemical promoter that has been shown to bring about a significant change in the activity of an Fe catalyst is Cu. Cu facilitates the reduction of Fe and thus decreases the time required to reach steady state in FTS<sup>10</sup>. It also reduces catalyst sintering of an Fe catalyst by lowering its reduction temperature<sup>10</sup>. The presence of Cu lowers the rate of carbon formation on an iron catalyst and also increases the FT activity of the catalyst as a result of the increased higher degree of reduction of Fe<sup>32</sup>.

Unlike Fe catalysts, Co-based catalysts in general do not appear to be very sensitive to the chemical nature of the promoter. It was found that addition of small amounts of Ru to a Co-based catalyst increased the initial reduction and *in situ* regeneration of the catalyst, and that the FT activity as well as the selectivity towards higher molecular weight hydrocarbons increased<sup>14(c)</sup>. Re<sup>33</sup> was found to promote reduction of Co on Al<sub>2</sub>O<sub>3</sub>, while Pt was found to increase the reducibility and the FT activity of a Co/Al<sub>2</sub>O<sub>3</sub><sup>13(c)</sup> and of Co/Nb<sub>2</sub>O<sub>5</sub><sup>34</sup> catalysts. Pd and Rh were shown to increase the surface reducibility and FT activity of a Co/Nb<sub>2</sub>O<sub>5</sub> catalyst, and an increased selectivity towards C<sub>5</sub>+ hydrocarbons was observed on addition of Rh<sup>34</sup>. La was also found to decrease the selectivity towards methane in a Co/SiO<sub>2</sub> catalyst<sup>12(c)</sup>.

#### 4.3.2.2. Structural Promoters

The main purpose of this type of promoter is to enhance the surface area of the catalyst and hence the metal dispersion, while maintaining its stability in the reaction. Structural promoters also act as spacers between metal crystallites, thus inhibiting sintering of the crystallites with time on stream<sup>10</sup>. Also, particularly for Co catalysts, the presence of a support reduces the cost as the Co metal crystallites are distributed on the support. Typical materials used as structural promoters include inorganic oxides such as  $\text{SiO}_2$ <sup>6,12</sup>,  $\text{TiO}_2$ <sup>6,14,35</sup>,  $\text{Al}_2\text{O}_3$ <sup>6,13</sup>,  $\text{Nb}_2\text{O}_5$ <sup>34</sup>,  $\text{ZrO}_2$ <sup>14(a),15</sup>,  $\text{CeO}_2$ <sup>14(a),15</sup>,  $\text{MgO}$ <sup>36</sup> or a mixture of supports such as  $\text{MgO/SiO}_2$ <sup>37</sup> and  $\text{TiO}_2/\text{SiO}_2$ <sup>38</sup>, zeolites<sup>39</sup> and molecular sieves<sup>40</sup>, activated carbon<sup>41</sup>, carbon nanotubes<sup>42</sup> and nanofibers<sup>43</sup>.

The choice of the support can have a considerable effect on the final activity and selectivity of the catalysts due to interaction between the support and the active metal<sup>44</sup>. It was found that  $\text{SiO}_2$  seems to be a better support in comparison with other inorganic supports ( $\text{Cr}_2\text{O}_3$ ,  $\text{MgO}$ ,  $\text{Al}_2\text{O}_3$ ,  $\text{ZnO}$ ) as an Fe catalyst supported on  $\text{SiO}_2$  exhibited a higher catalytic activity and wax selectivity, and also improved mechanical stability<sup>10,45</sup>. The presence of a support in an alkali promoted Fe catalyst can reduce the basicity of the promoter, and this has been observed particularly with  $\text{SiO}_2$  and  $\text{Al}_2\text{O}_3$  supports<sup>6</sup>. Thus, if there is any silica or alumina present, the alkali can react with the support to form alkali-silicates or –aluminates, respectively, which will be less basic than the ‘free’ alkali, and hence the basicity of the working surface will be lowered. Even if the supports or other high surface area promoters added do not chemically interact at all with the alkali they will effectively dilute the alkali in that the alkali will not only be distributed on the Fe surface but also on the surface of the other component. Hence promoted impregnated and precipitated Fe catalysts containing large amounts of support do not show good FT and WGS activity, and they show increased selectivity towards low molecular weight hydrocarbons<sup>46</sup>. Strong metal-support interactions (SMSIs) can also occur between Fe and the

support. Usually when the catalyst is reduced at very high temperatures interaction of the support and Fe can occur, resulting in formation of irreducible species, which consequently reduce the catalyst activity<sup>10</sup>.

Studies with Al<sub>2</sub>O<sub>3</sub> and SiO<sub>2</sub> supported Co catalysts have shown that the porosity of the support can have an effect on the metal crystallite size and the selectivity of the catalyst. It has been found for a Co/Al<sub>2</sub>O<sub>3</sub> catalyst that the smaller the pore diameter of the support the smaller the Co crystallite size and the lower the selectivity towards methane<sup>47</sup>. The reason for the low methane selectivity observed with small pore diameters was attributed to the long reactant residence time in the small pores, which can lead to olefin readsorption and consequently to increased chain propagation. It has also been shown for a SiO<sub>2</sub> supported Co catalyst that the wider the pore diameter of the support, the larger the Co crystallite size becomes, and this leads to a reduced metal dispersion and reducibility, and consequently to a lower catalyst activity<sup>48</sup>. A study of supported Co catalysts containing 3 % (by weight) Co and tested at 1 atm and 225 °C showed that the specific activity of the catalysts containing different supports decreased in the order TiO<sub>2</sub> > SiO<sub>2</sub> > Al<sub>2</sub>O<sub>3</sub> > Carbon > MgO<sup>49</sup>. The study showed that the specific activity of the catalysts decreased with an increase in metal dispersion, and that lower molecular weight hydrocarbons were obtained with higher metal dispersion and lower reduction extents. The presence of TiO<sub>2</sub> in a Co catalyst was found to lead to relatively high hydrogenation activities due to a SMSI<sup>39(b)</sup>.

Evidence of strong metal-support interactions (SMSIs) has been found in studies of FT over supported Ni<sup>20</sup>, and Ru<sup>50</sup> catalysts. Higher activities were obtained with a Ni/TiO<sub>2</sub> catalyst when compared to unsupported Ni and Ni/Al<sub>2</sub>O<sub>3</sub> catalysts, and it was also found that a Ni/Al<sub>2</sub>O<sub>3</sub> catalyst deactivated with time on stream while Ni/TiO<sub>2</sub> showed little or no loss in activity, indicating a greater resistance to carbon deposition and/or metal sintering with the latter<sup>20</sup>.

#### 4.4. FISCHER-TROPSCH REACTION TEMPERATURE

Currently, two FT operating modes are used commercially: the high temperature FT (HTFT) process with iron-based catalysts, which is operated at temperatures between 300 and 350 °C, and is used for the production of low molecular mass olefins, gasoline (primarily) and diesel fuel range liquids, and the low temperature FT (LTFT) process with either Co or Fe based catalysts, which is operated at 200-250 °C temperature range, and is used for the production of high molecular weight waxes<sup>6,51</sup>.

Irrespective of the type of metal catalyst used, raising the FT reaction temperature shifts the selectivity to lower carbon number hydrocarbons. The reason being that at higher temperatures, desorption of growing hydrocarbon chains from the catalyst surface occurs, which leads to chain termination. Thus, the end result is a decrease in selectivity towards long chain hydrocarbons, and an increase in selectivity towards low molecular weight hydrocarbons, especially methane<sup>6</sup>.

As the temperature is increased, the system becomes more hydrogenating and so the ratio of olefin to paraffins decreases and the selectivity towards alcohols and acids decreases. For the LTFT operations the hydrocarbons are predominantly linear, while mostly branched hydrocarbons are formed in the HTFT process. The branched hydrocarbons are predominantly mono-methyl isomers, and in the HTFT process the degree of branching increases with an increase in temperature. While no aromatics are formed in the LTFT process, their amount increases with an increase in temperature in the HTFT process<sup>6</sup>.

#### 4.5. APPLICATION OF FISCHER-TROPSCH PRODUCTS

Potentially, the products from an FT reaction find many uses<sup>6</sup>. The olefins produced can be oligomerised, alkylated or hydroformylated to produce special final products



like hair shampoo. The oxygenates can be converted to paraffins in a hydrogenation step and fractionated into naphtha and diesel and optionally a kerosene/jet fuel. The naphtha may be further upgraded using conventional refining processes to produce gasoline. Alternatively, the oxygenates can be separated and processed to produce a wide range of chemical products. Wax product may either be hydrocracked to provide further naphtha, diesel and optionally kerosene/jet fuel, or hydroprocessed to produce high quality lubricant base oils. The wax product may also be processed to make speciality wax products, or converted into fatty acids which can be used for the production of soaps and edible fats.

Production of ethylene and propylene in FTS is possible and these products can be used as monomers to produce plastics while the butylene produced in the synthesis is also a useful petrochemical feedstock. The associated C<sub>2</sub> to C<sub>4</sub> paraffins may be separated and steam cracked to produce additional olefins, and the C<sub>3</sub> together with C<sub>4</sub> paraffins may be sold as liquefied petroleum gas.

#### 4.6. SCOPE OF THIS WORK

It has been shown that Fe based catalysts are the most simple catalysts to use in FTS, mainly due to their low cost, the fact that they are resistant to sulphur poisoning and that they are responsive to promoters<sup>6</sup>. Thus, their activity and selectivity can be controlled by addition of promoters. It has also been found that SiO<sub>2</sub> support is a superior support when compared to other inorganic oxide supports<sup>10,45</sup>. Hence the choice of iron and silica combination was done for this study.

Studies on Fe catalysts in the FTS have mostly been done on precipitated Fe catalysts containing SiO<sub>2</sub> as a binder/spacer rather than a support, mainly because it has been shown that Fe catalysts containing large amounts of support exhibit poor activities and selectivities<sup>46</sup>. Also, not much research has been reported on the use of

nanstructured silica gels as supports for the Fe FT catalyst. Thus, in this work SiO<sub>2</sub> was used as a support (85 wt %) for an Fe FT catalyst, and the effect of potassium promotion levels on the activity of the catalyst was studied. Two types of SiO<sub>2</sub> gels were used in this study: commercial and nanstructured silica gels.

The effect of varying potassium promotion levels of an Fe catalyst supported on the different silica gels on its activity and selectivity in the FT reaction was investigated in Chapter 6. In Chapter 7 studies on the effect of the silica gel morphology on the activity and selectivity of a potassium promoted Fe catalyst in the FT reaction were done. The size and geometry of the support are expected to have an influence on the distribution of the catalyst, and hence on its activity and selectivity.

---

#### 4.7. REFERENCES

1. R.B. Anderson, *The Fischer-Tropsch Synthesis*, Academic Press, New York, 1984.
2. Badische Anilin und Soda Fabrik, German Patent No. 293787, (1913).
3. H. Pichler, *Adv. Catal.* 4 (1952) 271.
4. (a) B. Jager, R. Espinoza, *Catal. Today* 23 (1995) 17.  
(b) A.A. Adesina, *Appl. Catal. A: Gen.* 138 (1996) 345.
5. B.H. Weil, J.C. Lane, *The Technology of the Fischer-Tropsch Process*, Constable & Co. LTD, London, 1949.
6. M.E. Dry, in *Studies in Surface Science and Catalysis: Fischer-Tropsch Technology*, Chapt 3 and Chapt 7, Vol 152, A. Steynberg and M.Dry, (eds.), Elsevier, New York, 2004.
7. (a) F. Fischer, H. Tropsch, *Brennst. -Chem.* 7 (1926) 97.  
(b) J.T. Kummer, T.W. de Witt, P.H. Emmett, *J. Am. Chem. Soc.* 70 (1948) 3632.  
(c) P.M. Maitlis, *Pure Appl. Chem.* 61 (1989) 1747.  
(d) H. Kölbl, K.D. Tillmetz, *J. Catal.* 34 (1974) 307.  
(e) B.H. Davis, *Fuel. Process. Technol.* 71 (2001) 157.  
(f) M.E. Dry, *Catal. Today* 6 (1990) 183.  
(g) M.E. Dry, *Appl. Catal. A: Gen.* 138 (1996) 319.
8. H. Schulz, *Appl. Catal. A: Gen.* 186 (1999) 3.
9. H.G. Schulz, G. Schaub, M. Claeys, T. Riedel, *Appl. Catal. A: Gen.* 186 (1999) 215.
10. M.E. Dry, in *Catalysis Science and Technology*, Chapt. 4, Vol 1, J.R. Anderson and M. Boudart (eds.), Springer-Verlag, New York, 1981, p 159.
11. E. Iglesia, *Appl. Catal.* 161 (1997) 59.
12. (a) M. Adachi, K. Yoshii, Y.Z. Han, K. Fujimoto, *Bull. Chem. Soc. Jpn.* 69 (1996) 1509.  
(b) A. Khodakov, A. Griboval-Constant, R. Bechara, V.L. Zholobenko, *J. Catal.* 206 (2002) 230.

- (c) G.H. Haddad, B. Chenand, J.G. Goodwin, J. Catal. 160 (1996) 43.
13. (a) R. Bechara, D. Balloy, D. Vanhove, Appl. Catal. A: Gen. 207 (2001) 343.  
(b) D. Schanke, A.M. Hillmen, E. Bergene, K. Kinnari, E. Rytter, E. Ådnanes, A. Holmen, Energy and Fuels 10 (1996) 867.  
(c) A. Holmen, D. Schanke, S. Vada, E.A. Blekkan, A.M. Hillmen, A. Hoff, J. Catal. 156 (1995) 85.
14. (a) M. Kraun, M. Baerns, Appl. Catal. A. Gen. 186 (1999) 189.  
(b) R.C. Reuel, C.H. Bartholomew, J. Catal. 85 (1984) 63.  
(c) E. Iglesia, S.L. Soled, R.A. Fiato, G.H. Via, J. Catal 143 (1993) 345.  
(d) E. Iglesia, S.L. Soled, R.A. Fiato, J. Catal 137 (1992) 212.
15. (a) L.A. Bruce, M. Hoang, A.E. Hughes, T.W. Turney, Appl. Catal. A: Gen. 100 (1993) 51.  
(b) J. van der Loosdrecht, M. van der Haar, A.M. van der Kraan, A.J. van Dillen, J.W. Geus, Appl. Catal. 150 (1997) 365.  
(c) M.K. Niemelä, A.O.I. Krause, T. Vaara, J. Lathinen, Top. Catal. 2 (1995) 45.  
(d) M.K. Niemelä, A.O.I. Krause, T. Vaara, J.J. Kiviaho, M.K.O. Reikainen, Appl. Catal. A. Gen. 147 (1996) 325.
16. M. J. Keyser, R.C. Everson, R.L. Espinoza, Appl. Catal. A: Gen. 171 (1998) 9.
17. P.J. van Berge, J. Van der Loosdrecht, S. Barradas, A.M. van der Kraan, Catal. Today 58 (2000) 321.
18. (a) S. Ho, J.M. Cruz, M. Houalla, D.M. Hercules, J. Catal. 135 (1992) 173.  
(b) C.H. Bartholomew, R.B. Pannell, J.L. Butler, J. Catal. 65 (1980) 335.  
(c) Y. Huang, J.A. Schwarz, Appl. Catal. 32 (1987) 59.  
(d) G.A. Hardjigeorgiou, J.T. Richardson, Appl. Catal. 21 (1986) 11.
19. H.H. Storch, N. Golumbic, R.B. Anderson, *The Fischer-Tropsch and Related Synthesis*, John Wiley, New York, 1951.
20. M.A. Vannice, R.L. Garten, J. Catal. 56 (1979) 236.
21. F.Fischer, K. Meyer, Brennstoff.-Chem. 8 (1927) 165.
22. M.E. Dry, Catal. Lett. 7 (1990) 241.

23. H. Schulz, *Topics in Catal.* 26 (2003) 73.
24. F. Fischer, H. Buffleb, *Brenstoff.-Chem.* 21 (1940) 285.
25. M.A. Vannice, *J. Catal.* 37 (1975) 449.
26. (a) D.J. Duvenhage, N.J. Coville, *Catal. Lett.* 104 (2005) 129.  
(b) H. Freund, *ACS National Meeting* 229 (2005) 108.  
(c) G.D. Zakumbaeva, L.B. Shapovalova, *Petroleum Chem.* 44 (2004) 334.  
(d) A.L. Lapidus, M.V. Tsapkina, B.P. Tonkonogov, A.Y. Krylova, *Khimiya Tverdogo Topliva (Russian)* (2004) 3.  
(e) D. Bazin, L. Gucci, *Stud. Surf. Sc. Catal.* 147 (2004) 343.  
(f) E. Boellaard, A.M. van der Kraan, J.W. Geus, *Appl. Catal. A: Gen.* 224 (2002) 1.  
(g) D.P. van der Wiel, M. Pruski, T.S. King, *J. Catal.* 188 (1999) 186.  
(h) A. Choplin, M. Leconte, J.M. Bassier, S.G. Shore, W.-L. Hsu, *J. Mol. Catal.* 21 (1993) 389.  
(i) B.-T. Teng, J. Chang, C.-H. Zhang, D.-B. Cao, J. Yang, Y. Liu, X.-H. Guo, H.-W. Xiang, Y.-W. Li, *Appl. Catal. A: Gen.* 301 (2006) 39.
27. M. Luo, B.H. Davis, *Appl. Catal. A: Gen.* 246 (2003) 171.
28. W. Ngatsoue-Hoc, Y. Zhang, R.J. O'Brien, M. Lou, B.H. Davis, *Appl. Catal. A: Gen.* 236 (2002) 77.
29. H. Kolbel, in *Actes du Deuxieme Congres International de Catalyse Vol 2*, Technip, Paris, 1960, p 2075.
30. H. Kolbel and H. Giering, *Brenstoff-Chem.* 44 (1963) 343.
31. D.B. Bukur, D. Mukesh and S.A. Patel, *Ind. Eng. Chem. Res.* 29 (1990) 194.
- 32 R.B. Anderson, in: P.H Emmet (Ed.), *Catalysis Vol. 4.*, Van Nostrand-Reinhold, New York, 1956, p 1.
33. A.M. Hillmen, D. Schanke, A. Holmen, *Catal. Lett.* 38 (1996) 143.
34. F.B. Noronha, A. Frydman, D.A.G. Aranda, C. Perez, R.R. Soares, B. Morawek, D. Castner, C.T. Campbell, R. Frety, M. Schmal, *Catal. Today* 28 (1996) 147.
35. E. Iglesia, *Appl. Catal.* 161 (1997) 59.

36. G.S. Sewell, E. van Steen, C.T. O'Connor, *Catal. Lett.* 37 (1996) 255.
37. R.J. O'Brien, L. Xu, S. Bao, A. raje, B.H. Davis, *Appl. Catal. A: Gen.* 196 (2000) 173.
38. B. Jonsomijt, T. Wongsalee, P. Prasenthdam, *Mater. Chem. Phys.* 97 (2006) 343.
39. (a) J. Eilers, S.A. Posthuma, S.T. Sie, *Catal. Lett.* 37 (1997) 253.  
(b) S. Bessel, *Appl. Catal. A: Gen.* 96 (1993) 253.  
(c) V.U.S. Rao, R.J. Gormley, *Catal. Today* 6 (1990) 207.
40. D. Yin, W. Li, W. Yang, H. Xiang, Y. Sun, B. Zhong, S. Peng, *Microporous and Mesoporous Mat.* 47 (2001) 15.
41. H.-J. Jung, P.L. Walker Jr, M.A. vannice, *J. Catal.* 75 (1982) 416.
42. (a) E. van Steen, F.F. Prinsloo, *Catal. Today* 71 (2002) 327.  
(b) M.C. Bahome, L.L. Jewell, D. Hildebrandt, D. Glasser, N.J. Coville, *Appl. Catal A: Gen.* 287 (2005) 60.
43. G.L. Bezemer, J.H. Bitter, H.P.C.E. Kuipers, H. Oosterbeek, J.E. Holewijn, X. Xu, F. Kaptein, A.J. van Dillen, K.P. de Jong, *J. Am. Chem. Soc.* 128 (2006) 3956.
44. M.A. Vannice, *Catal. Today* 12 (1992) 255.
45. C.H. Yang, J.G. Goodwin, *Can. J. Chem. Eng.* 61 (1983) 213.
46. K. Jothimurugesan, J.J. Spivey, S.K. Gangwal and J.G. Goodwin Jr, in *Studies in Surface Science and Catalysis: Natural Gas Conversion Vol 119.*, A.Parmaliana, D. Sanfilippo, F. Frusteri, A. Vaccari, F. Arena (eds.), Elsevier, New York, 1998, p215.
47. H. Xiong, Y. Zhang, S. Wang, J. Li, *Catal. Commun.* 6 (2005) 512.
48. D. Song, J. Li, *J. Mol. Catal. A : Chem.* 247 (2006) 206.
49. R.C. Reuel, C.H. Bartholomew, *J. Catal.* 85 (1984) 78.
50. M.A. Vannice, R.L. Garten, *J. Catal.* 63 (1980) 255.
51. M.E. Dry, *Catal. Today* 71 (2002) 227.

# **CHAPTER 5**

## **EXPERIMENTAL**

### **5.1. INTRODUCTION**

The catalysts prepared in this study were evaluated in a slurry operated continuously stirred tank reactor, for Fischer-Tropsch activity and selectivity.

In this study characterisation of the catalysts and supports was carried out by scanning and transmission electron microscopes, nitrogen physisorption, temperature programmed and elemental analysis techniques.

General preparation methods and characterisation techniques are described in this chapter. Specific catalyst preparation methods are discussed in the relevant subsequent chapters.

### **5.2. REAGENTS AND CHEMICALS USED**

#### **5.2.1 Supports**

The following supports were used in this work:

- (i) Commercial silica, Davisil silica gel, grade 645, 6-100 mesh (99+%, Aldrich), used as received.
- (ii) Silica tubes synthesised by the sol-gel method using oxalic acid as template precursor.
- (iii) Silica hollow spheres synthesised by sol-gel method using citric acid as template precursor.

*Synthesis of silica tubes:* The silica tubes were synthesized at 25 °C. Oxalic acid monohydrate (100g) was dissolved in a mixture of 154 ml ethanol and 154 ml deionised water. To the mixture was added 60 ml tetraethylorthosilicate, and the mixture stirred with an overhead stirrer set at 300 rpm, for 2 h. To the resulting sol, 120 ml ammonium hydroxide solution, containing 28 % aqueous ammonia, was added drop-wise with agitation of the sol for 45 min. The resulting gel was then aged for 2 h, washed with copious amounts of hot deionised water and then dried in a static air oven at 100 °C for 24 h. The dried silica gel was ground and sieved and only particles with sizes between 124 and 400 µm were collected. These were calcined in static air at 600 °C for 18 h to remove the template.

*Synthesis of silica spheres:* The synthesis of silica spheres was carried out at 25 °C. Citric acid (26 g) was dissolved in a mixture of 500 ml ethanol and 6 ml deionised water. To the mixture was added 73 g tetraethylorthosilicate, and the resulting sol kept un-agitated for 30 min. Then 240 ml ammonium hydroxide, containing 28% aqueous ammonia, was added drop-wise with agitation of the sol for 30 min. The resulting gel was then aged for 2 h, washed with copious amounts of hot deionised water and then dried in a static air oven at 100 °C for 24 h. The dried silica gel was ground and sieved and only particles with sizes between 124 and 400 µm were collected. These were then calcined in static air at 600 °C for 18 h to remove the template.

The supports were dried at 250 °C overnight prior to metal impregnation, to remove excess moisture.

### 5.2.2. Metals

Ferric nitrate ( $\text{Fe}(\text{NO}_3)_3 \cdot 9\text{H}_2\text{O}$ , 99.35 %, Shepherd) and potassium nitrate ( $\text{KNO}_3$ , 99.0 %, Allied) were used as sources of iron and potassium respectively.



### 5.2.3. Gases

Gases used for the FT synthesis were supplied by Air Products. Bulk H<sub>2</sub> (99.95 %) containing no sulphur compounds, was used without further purification. Bulk CO (99.5 %) was fed through a bed of lead oxide (22 %) on alumina (78 %) to remove iron carbonyl, prior to use in the reactor.

## 5.3. CATALYST PREPARATION

The catalysts were prepared by the incipient wetness impregnation method. Multiple-step impregnations with iron were done on the supports, with the mass of Fe(NO<sub>3</sub>)<sub>3</sub> hydrate and the water volume determined by the pore volume of the support used. The dry support was placed in a round bottom flask fitted to a burette and connected to a rotary evaporator. The metal ion solution was added dropwise to the dry support with concurrent rotation of the round-bottom flask. At the end of each impregnation step, the catalyst was dried on the rotary evaporator under vacuum at 90 °C.

The prepared iron impregnated catalyst was then divided into four equal parts and the parts were impregnated with KNO<sub>3</sub> so as to attain a 0, 0.1, 0.5 and 0.9 wt% potassium supported catalyst, respectively. The impregnation was done in a similar manner as with iron but as a single step procedure.

The catalysts were calcined in a fixed bed reactor, at 250 °C (heating rate of 5 °C/min), in air with a downward flow of 45 mL /min-g support for 6.5 h.

The catalysts were prepared such that at the end the nominal compositions were:

- (i) 15% Fe/0%K/85%SiO<sub>2</sub>
- (ii) 15%Fe/0.1% K/84.9% SiO<sub>2</sub>
- (iii) 15%Fe/0.5% K/84.5% SiO<sub>2</sub>

(iv) 15%Fe/0.9%K/84.1%SiO<sub>2</sub>

#### 5.4. THE FISCHER-TROPSCH REACTOR SYSTEM

The physical setup for the equipment for FT synthesis experiments is shown schematically in **Fig. 5.1** and its picture is shown in **Fig. 5.2**. It consists of a 1 L stainless-steel autoclave, operating as a continuously stirred tank reactor. Hydrogen and carbon monoxide were supplied from bulk containers and fed through two mass flow controllers (Brooks instruments), with the resulting syngas composition regulated by adjusting the flow rate of the appropriate gas. During operation, the syngas after passing through a 2 L mixing vessel, was delivered to the reactor through a dip tube extended below the impeller blade, the latter controlled externally by a DC variable speed drive motor with an integrated variable speed controller. A stainless steel mantle heater built around the autoclave was used to heat up the reactor, and this was controlled by a ramp-soak temperature controller (Omega PPL, USA). A K-type thermocouple T/C was inserted in the reactor vessel to determine the reactor temperature. A sintered metal filter **F** (0.5 µm) was installed to allow removal of heavy wax from the reactor, which could be collected in a hot trap **K<sub>1</sub>** maintained at 200 °C. A warm trap **K<sub>2</sub>** (maintained at 100 °C) and a cold trap **K<sub>3</sub>** (maintained at 0 °C) were used to collect light wax and water plus oil samples, respectively, by condensing from the vapour phase that was continuously withdrawn from the reactor vapour phase.

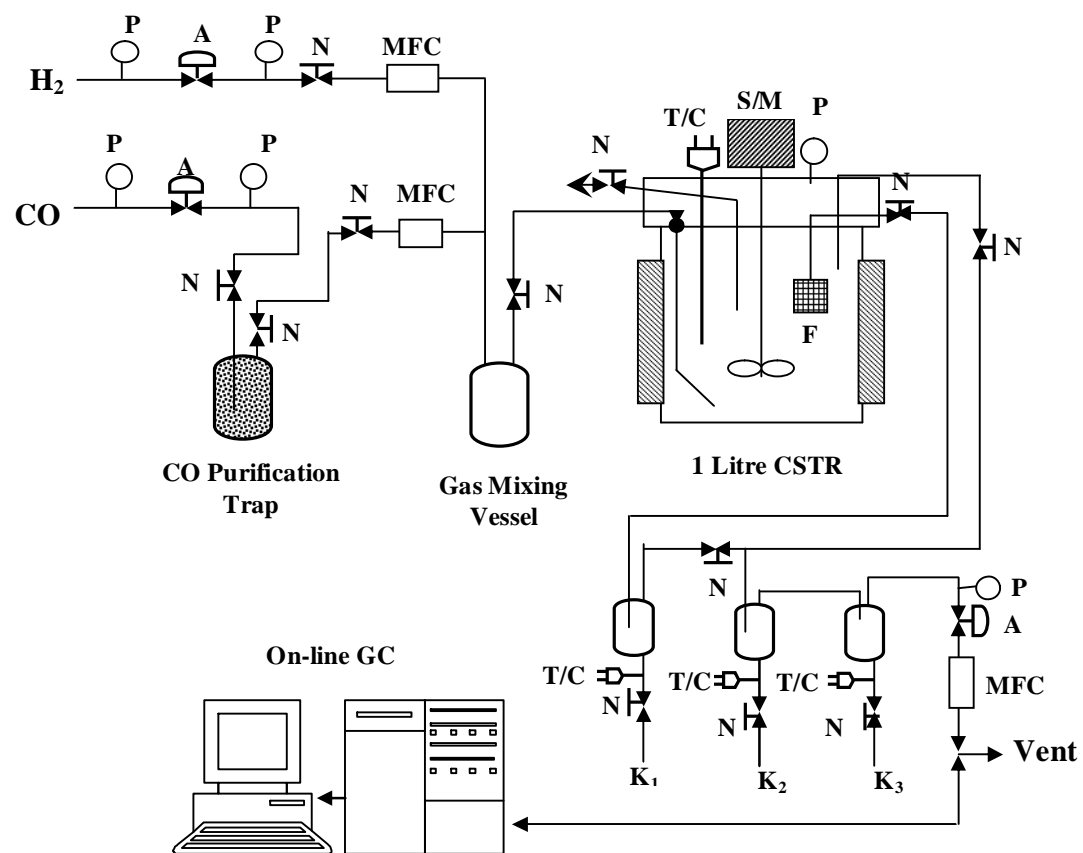


**Figure 5.1.** Schematic diagram of the slurry CSTR set-up used in the study. P- pressure gauge, A- pressure controller, N- needle valve, MFC- mass flow controller, T/C- thermocouple, S/M- stirrer motor, F- sintered metal filter, K<sub>1</sub>- heavy wax trap (200 °C), K<sub>2</sub>- light wax trap (100 °C), K<sub>3</sub>- liquid trap (0 °C)

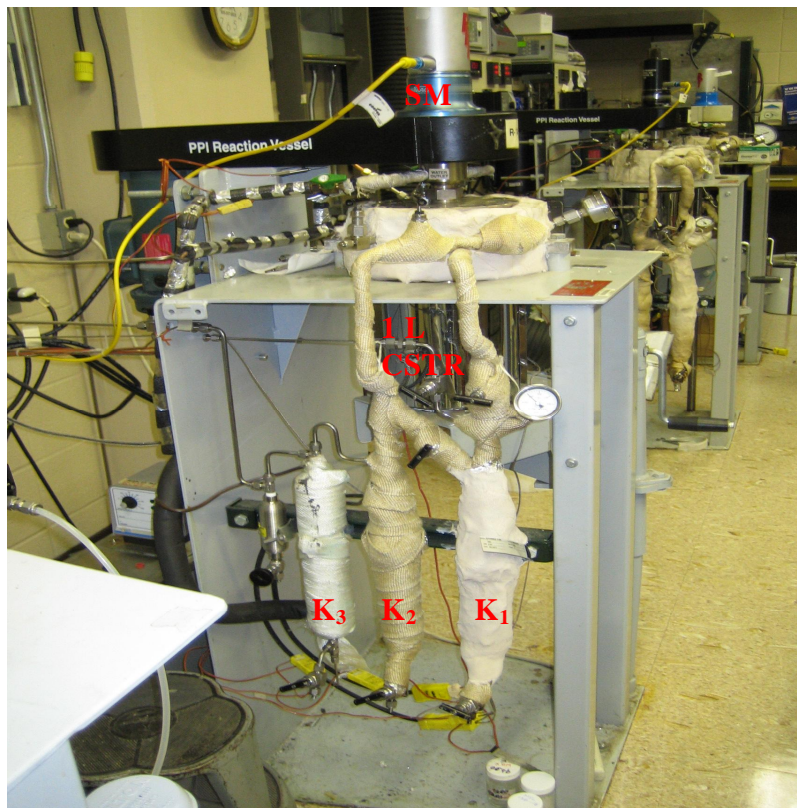


**Figure 5.2.** Picture of the reactor used for FT synthesis.  $K_1$ ,  $K_2$ ,  $K_3$ , S/M and 1L CSTR described in **Fig. 5.1**.

Incondensable tail gas from the cold trap went through a two-way valve which was manually operated to either allow the gas to flow to the GC for analysis or to be vented to the atmosphere.

## 5.5. FISCHER-TROPSCH SYNTHESIS

All catalysts were activated in situ in carbon monoxide atmosphere. A catalyst mass of 50 g was loaded in the 1 L autoclave reactor and suspended in 300 g Ethylflo164 oil (C-30 oil, BP Amoco), which is reported to be a 1-decene homopolymer. The

stirrer motor was operated at a speed of 750 rpm. Carbon monoxide was introduced at a weight hourly space velocity of 3.2 L/h (STP) per gram Fe and a pressure of 20 bar, and the reactor was heated to 270 °C at a rate of 2.2 °C/min. The catalyst was reduced at that temperature for 22 h. When the activation time was over, the reactor was cooled down to 250 °C. Once the reactor was at 250 °C, hydrogen was introduced, and the flow of the gases adjusted to provide a simulated synthesis gas with H<sub>2</sub>/CO ratio of 2/1, at a pressure of 20 bar, and a weight hourly space velocity 3.6 L/h (STP) per gram Fe. Gas, oil and wax samples were taken and analysed in 24-48 h intervals. However, heavy wax could not be filtered from the reactor as small amounts of it were produced and could therefore not reach the height of the sintered metal filter. Thus, the contents of the reactor after the reaction were instead analysed for heavy wax.

### 5.5.1. Product Analysis

The incondensable gaseous products from the cold trap were analysed online with an HP Refinery Gas Analyser (RGA) gas chromatograph (**Fig. 5.3**), providing molar compositions of C<sub>1</sub>-C<sub>7</sub> olefins and paraffins, as well as hydrogen, carbon monoxide and carbon dioxide. This GC was calibrated weekly with a standard gas. Water plus oil samples collected from the cold trap were separated, and the water analysed on an HP 5790 packed column GC (**Fig. 5.4**), providing area counts of olefins and paraffins of carbon numbers from 5 to 10. The mole percents of these products were calculated by multiplying the area count by a response factor. This factor is the sum of the area counts of the RGA C<sub>4</sub> mole percents divided by the sum of the area counts of the C<sub>4</sub>'s from the HP 5790 GC. The remaining oil samples were mixed with light wax from the warm trap and analysed on an Agilent 6890 Capillary GC (**Fig. 5.5**). The water and oil plus wax samples were injected neat on the GC. Heavy wax samples were diluted in o-xylene and analysed on an HP 5890 Series II capillary GC (**Fig. 5.6**).



**Figure 5.3.** Hewlett Packard Refinery Gas Analyser, used for analysing on-line gas samples, equipped with four TCD type detectors and four columns: 10 m x 0.32 mm molecular sieve 5Å @ 110 °C, 8 m x 0.32 mm Poraplot U @ 80 °C, 10 m x 0.32 mm Al<sub>2</sub>O<sub>3</sub> @ 140 °C, 10 m x 0.15 mm OV-1 @ 120 °C.



**Figure 5.4.** Agilent 6890 Capillary GC used for oil and wax analysis, equipped with an FID type detector, column: 60 m DB-5, 0.32 mm ID, 0.25 µm film. Programme: 35 °C hold 10 min, 4 °C/min to 325 °C, hold 52 min.

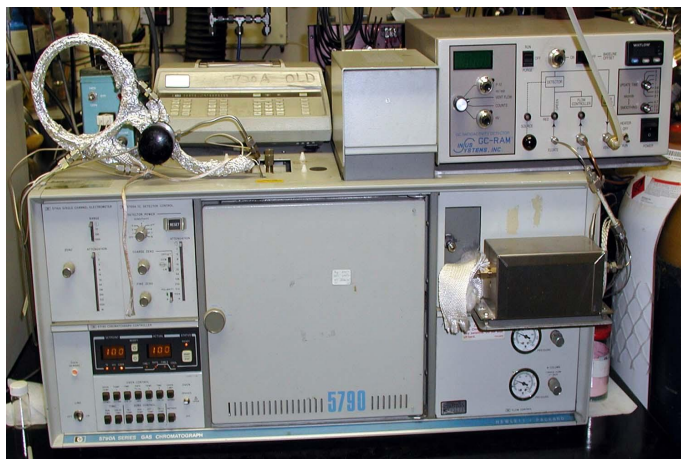


**Figure 5.5.** Hewlett Packard 5790 packed column GC for water samples analysis, equipped with a TCD type detector, column: 0.154m x 3.2 mm 80/100 mesh Porapak Q. Programme: 100 °C hold 1 min, 10 °C/min to 390 °C, hold 40 min.



**Figure 5.6.** Agilent 5890 Series II Capillary GC used for the analysis of heavy wax, equipped with an FID type detector. Column: 25 m HT-5 Aluminum clad 0.53mm I.D, 0.15  $\mu$ m film. Operation Programme: 50 °C no hold, 10 °C/min to 390 °C, hold 40 min.

The liquid products i.e. oil and wax mixtures, were analysed for iron content. Approximately 200 mg of the sample was put into solution using a combination of Perchloric and Nitric acids. The samples were diluted with deionised water and the resultant solution analysed using a Plasma-Therm 2500 Inductively Coupled Plasma-Optical Emission Spectrometer (ICP-OES) equipped with an Analytical Data Monitor (ADaM) data system.

### 5.5.2. Fischer-Tropsch Data Calculations

The raw data was stored in a Microsoft Access database. Any conversions, scaling and further manipulation of the data done was done entirely by SQL query of the database system, with the exception of the curve fitting for the calculation of chain growth probability (alpha) values, which was primarily done with the SAS system of Statistical Software. The system had a Microsoft Visual Basic 5.0 front end for data entry with reporting by Crystal Reports Professional Version 6. The following formulas were used during the SQL query to calculate useful information from the raw data:

The carbon monoxide conversion was calculated as being :

$$COconversion = \frac{n_{in} - n_{out}}{n_{in}} \times 100\% \quad (5.1)$$

where  $n_{in}$  and  $n_{out}$  are the molar flow rates of CO entering and exiting the reactor, respectively.

The Fischer-Tropsch reaction rate was calculated as being:

$$r_{FT} = r_{CO} - r_{CO_2} \quad (5.2)$$

where  $r_{CO}$  and  $r_{CO_2}$  are the CO and  $CO_2$  rates, respectively, in mol/h.g-Fe.



The rate of CO consumption was determined from the formula:

$$r_{CO} = \frac{n_{in}}{M} \times f \quad (5.3)$$

where  $n_{in}$  is the molar flow rate of CO entering the reactor,  $f$  is the CO fractional conversion, and  $M$  is the mass of Fe in the catalyst.

The rate of CO<sub>2</sub> formation or the water gas shift reaction rate was calculated as:

$$r_{CO_2} = \frac{n_{CO_2}}{M} \quad (5.4)$$

where  $n_{CO_2}$  is the molar flow rate of CO<sub>2</sub> produced, and  $M$  is the mass of Fe in the catalyst.

The selectivity towards methane was determined as being

$$S_{CH_4} = \frac{r_{CH_4}}{r_{FT}} \times 100\% \quad (5.5)$$

where  $r_{CH_4}$  and  $r_{FT}$  are the rate of methane formation and the rate of Fischer-Tropsch reaction, respectively, in mol/h.g-Fe.

The selectivity towards CO<sub>2</sub> was determined as being:

$$S_{CO_2} = \frac{n_{CO_2\_out}}{n_{CO\_in} - n_{CO\_out}} \times 100\% \quad (5.6)$$

where  $n_{CO_2\_out}$  is the molar flow rate of CO<sub>2</sub> produced,  $n_{CO\_in}$  and  $n_{CO\_out}$  are the molar flow rates of CO entering and exiting the reactor, respectively.

The catalyst efficiency was calculated using the following equation:

$$e = \frac{n_{CO\_in} - (n_{CO\_out} + n_{CO_2\_out})}{n_{CO\_in} - n_{CO\_out}} \times 100\% \quad (5.7)$$

where  $n_{CO\_in}$  and  $n_{CO\_out}$  are the molar flow rates of CO entering and exiting the reactor, respectively, and  $n_{CO_2\_out}$  is the molar flow rate of CO<sub>2</sub> produced.

The chain growth probability (alpha value) was obtained by performing a least square fit on an Anderson-Schultz-Flory (ASF) plot of products with carbon numbers from 1 to 20. Equation 5.8 was fitted with the exponential of the slope giving the required alpha value.

$$\ln(Wn / n) = n \ln \alpha + \ln((1 - \alpha)^2 / \alpha) \quad (5.8)$$

where  $Wn$  is the mass fraction of hydrocarbon with the  $n$ th carbon number, and  $\alpha$  is the chain growth probability.

The product distributions were calculated using equation 5.9, which represents the selectivity of the reaction to a specific component.

$$S_i = \frac{m_i}{\sum m_n} \quad (5.9)$$

where  $S_i$  is the mass fraction of component  $i$ , and  $m_i$  is the mass of component  $i$ .

The olefinicity of the products was determined as:

$$OlefinSelectivity = \frac{100 \times n_{totalOlefins}}{n_{totalOlefins} + n_{paraffins}} \quad (5.10)$$

---

$$\text{where } n_{\text{total Olefins}} = n_{1\text{-olefins}} + n_{\text{cis-2-olefins}} + n_{\text{trans-2-olefins}} \quad (5.11)$$

The 1-olefin selectivity was calculated as :

$$1 - \text{OlefinSelectivity} = \frac{n_{1\text{-Olefins}}}{n_{\text{totalOlefins}}} \quad (5.12)$$

where n is the molar flow rate of the respective product.

### 5.5.3. Catalyst Extraction

After the reaction, catalysts were extracted with hot o-xylene (Sigma-Aldrich, 98%), in a soxhlet extraction apparatus, for 24-48 h, to remove the heavy wax formed during the FT reaction. The extracted catalysts were then dried in a vacuum oven at 100 °C for 48 h, and then calcined in a static air furnace at 200 °C for 6 h prior to analysis.

## 5.6. SUPPORT AND CATALYST CHARACTERISATION

### 5.6.1. Transmission Electron Microscopy

Samples were prepared by sonicating about 100 mg of the sample in 2 ml ethanol for at least 5 minutes and then 2 drops of the suspension were placed on a lacey Cu grid coated with carbon film.

A JEOL 2010F High Resolution Transmission Electron Microscope (HRTEM) equipped with a field emission gun, an Oxford Energy Dispersive Spectra (EDS) detector with an Emispec Esvision computer control system and a Gatan CCD multiscan camera, and a Philips CM200 HRTEM equipped with a LaB<sub>6</sub> source and an EDS detector, were used to obtain high magnification images. Low resolution

transmission electron microscopy images were observed with a JEOL-100S electron microscope.

### 5.6.2. Scanning Electron Microscopy

The silica samples were coated with gold coating prior to analysis. A Hitachi S-2700 scanning electron microscope (SEM) fitted with a LaB<sub>6</sub> gun was used for photo imaging. The microscope was run at a voltage of 15 keV and a current of 75  $\mu$ A.

### 5.6.3. Ammonia Temperature Programmed Desorption

Generally about 200 mg of sample was placed on quartz wool fitted in a quartz U-shaped tube, and this was heated in a vertical furnace at a rate of 10  $^{\circ}$ C/min to 250  $^{\circ}$ C in a helium atmosphere, at a flow rate of 30 ml/min. The sample was kept at 250  $^{\circ}$ C for 30 min to remove any weakly adsorbed species and moisture. The furnace was then cooled down to 50  $^{\circ}$ C and NH<sub>3</sub> gas was passed over the sample at a rate of 30 ml/min for 30 min. The catalyst was then purged with He for 30 min, to remove gaseous NH<sub>3</sub> not adsorbed by the sample. The adsorbed NH<sub>3</sub> was then desorbed by increasing the temperature of the furnace at a rate of 10  $^{\circ}$ C/min to 300  $^{\circ}$ C. Data collection was started at the beginning of the desorption step, with the signal measured on an FID.

### 5.6.4. Carbon Monoxide Temperature Programmed Reduction

The TPR apparatus used in this study was the same as the one used by Duvenhage<sup>1</sup>. About 200 mg of catalyst was placed on quartz wool fitted in a quartz U-tube and was heated using a vertical furnace at a heating rate of 10  $^{\circ}$ C/min to 150  $^{\circ}$ C, in a nitrogen atmosphere with a flow rate of 12 mL/min, and was kept at 150  $^{\circ}$ C for 30 min to remove any weak adsorbates and moisture. The furnace was then cooled down to room temperature, carbon monoxide (2.5% CO/ Ar mixture) introduced at a

rate of 12 mL/min, and the furnace heated at a rate of 7.5 °C/min to 800 °C. The signal was measured on a low temperature dual filament TCD and recorded using a PC equipped with an I/O card.

#### **5.6.5. Nitrogen Physisorption**

BET surface areas, adsorption-desorption isotherms, and pore size distributions, the latter calculated by the Barret-Joyner-Halenda (BJH) method, were determined by nitrogen adsorption at -196 °C using a Micromeritics TRISTAR 3000 analyser. The samples were degassed at 160 °C, 100 mbar for 10 h prior to analysis.

#### **5.6.6. Elemental Analysis of Catalysts**

The fresh and used catalysts were ashed at 750 °C to remove any residual carbon (from coking) prior to analysis. The ashed samples were fused into glass beads using Lithium Tetraborate, and were then analyzed for Fe, K, C and SiO<sub>2</sub> using an PANalytical PW 2404 X-Ray spectrometer.

**5.7. REFERENCE**

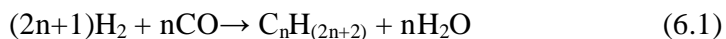
1. D.J. Duvenhage, *The Preparation, Characterisation, and Evaluation of Titania Supported Fe:Co Bimetallic Catalysts for Hydrogenation of CO*, PhD Thesis, University of the Witwatersrand, 1994.

# CHAPTER 6

## LOW TEMPERATURE FISCHER-TROSPCH SYNTHESIS REACTOR STUDIES OVER A COMMERCIAL SILICA AND SILICA TUBES SUPPORTED IRON CATALYSTS: EFFECT OF POTASSIUM LOADING.

### 6.1. INTRODUCTION

In Fischer-Tropsch (FT) synthesis, hydrocarbons are produced from CO and H<sub>2</sub> by a reaction which can be expressed as:



where the average value of n is  $1/(1-\alpha)$ ,  $\alpha$  being the rate of chain termination<sup>1</sup>.

When an iron catalyst is employed, the water gas shift reaction (equation (6.2)) can occur: water formed in the FT reaction (equation (6.1)), can react with CO from the feed gas to produce CO<sub>2</sub> and H<sub>2</sub>, the latter can then be used in the FT reaction.



This reaction is useful when a H<sub>2</sub> lean feed gas is used to make FT products.

Potassium has long been used as a promoter for iron catalysts. Numerous studies have shown that addition of small amounts of potassium to iron catalysts used for FT synthesis affects the performance of these catalysts in many ways. The presence of potassium (as K<sub>2</sub>O) has been reported to increase CO chemisorption while

decreasing H<sub>2</sub> chemisorption<sup>2(a)</sup>. This was explained by the fact that since K<sub>2</sub>O is a very strong base, it has the ability to donate electrons to Fe, and as CO tends to accept electrons from Fe on adsorption, the presence of K<sub>2</sub>O facilitates CO chemisorption on Fe resulting in a stronger Fe-C bond. On the other hand, H<sub>2</sub> at higher surface coverages donates electrons to Fe, and the presence of an electron-donating alkali would then weaken the iron-hydrogen bond. Thus, the net effect of potassium promotion is a strengthening of the Fe-C bond and a weakening of the C-O and Fe-H bonds. Potassium addition has also been reported to increase the synthesis gas consumption rate per volume of catalyst, the average molecular weight (chain-length) of the products (correspondingly decreasing the formation of methane and light gases), the olefin-to-paraffin ratio, the content of oxygenated products, the carbon deposition and catalyst deactivation rate, increase FTS activity at low potassium loading but decrease FTS activity at higher loadings, and decrease the H<sub>2</sub> to CO usage ratio due to an increase in the water-gas shift activity<sup>2,3</sup>.

Studies have been done on numerous supported iron FT catalysts. For precipitated FT catalysts, a comparison of silica with other inorganic supports (Cr<sub>2</sub>O<sub>3</sub>, MgO, Al<sub>2</sub>O<sub>3</sub>, ZnO) showed that silica-supported catalysts generally have higher activity and wax selectivity, and also improved mechanical stability<sup>4,5</sup>. Jothimurugesan et al<sup>6</sup> showed that increasing the level of precipitated silica in an iron FT catalyst increases the surface area of the catalyst, while it decreases the FT and the WGS activity. The authors also found that an increase in silica level increased the selectivity towards low molecular weight hydrocarbons at the expense of the selectivity towards heavier hydrocarbons.

Previous studies done on the effects of potassium promotion on silica supported iron catalysts mainly dealt with catalysts containing 60% or less of silica<sup>2,3,7,8</sup>. At that level silica can be considered as a binder, rather than a support, i.e. when the Fe/Si ratio > 4<sup>9</sup>. Anderson<sup>1</sup> stated that impregnated and precipitated promoted iron catalysts containing large amounts of supports do not show good FT activity,



possibly due to interaction of the support and the alkali promoter. Anderson's observation could explain the reason for the rarity of work on this type of catalyst. O'Brien et al <sup>10</sup> studied the activity of promoted iron catalysts on different supports in which the support made up about 80 % of the catalyst weight. However, they did not look at the effect of potassium loading. Rankin and Bartholomew<sup>11</sup> studied the effect of potassium loading on the activity of a silica supported iron catalyst (15 % Fe by weight); they varied the potassium loadings on the catalyst over a wide range (0.2-3 % K).

In this work we report the use of silica as a major component of the catalyst (85% by weight) where low potassium loadings were varied over a 0 to 0.9 weight % range. Low potassium loadings were chosen, as previous studies conducted on potassium promotion of iron FT catalysts showed that the effect of promotion on catalyst activity reaches a peak around K/Fe ratio of 0.05 by atomic mass<sup>2(a),3(c)</sup>. Thus, the objective of this work was to study the effect of potassium promotion on a highly silica supported iron FT catalyst, and to evaluate its effect of catalyst activity and product selectivity. This chapter is divided into two parts; part A deal with the effect of potassium loading on the activity and selectivity of a commercial silica-supported iron catalyst, while part B deals with the effect of potassium loading on an ammonium oxalate templated sol-gel synthesised silica support.

## 6.2. EXPERIMENTAL

### 6.2.1. Catalyst Preparation

#### *Part A: The effect of potassium loading on the activity and selectivity of a commercial silica supported iron catalyst.*

The catalysts were prepared by incipient wetness impregnation. Commercial silica, Davisil 645 (BET surface area 273 m<sup>2</sup>/g, pore radius 1.06 g/cm<sup>3</sup>; determined by N<sub>2</sub> physisorption) was dried at 250 °C overnight. Then 400 g of the support was impregnated with iron. The impregnation was done in two steps, using two 424 ml solution aliquots of Fe(NO<sub>3</sub>)<sub>3</sub>, each containing 35.3 g Fe. The dry support was placed in a round bottom flask fitted to a burette and connected to a rotary evaporator. The metal ion solution was added dropwise to the dry support with rotation of the round-bottom flask. At the end of each impregnation step, the catalyst was dried on the rotary evaporator under vacuum at 90 °C.

The prepared iron impregnated catalyst was then divided into four equal parts and the parts were impregnated over a single step with potassium. Potassium nitrate solutions, 100 ml, each containing 0, 0.124, 0.494 and 0.865 g potassium, respectively were used. The impregnations were done in a similar manner as with iron.

The catalysts were calcined in a fixed bed reactor, at 250 °C (heating rate of 5 °C/min), in air with a downward flow of 45 mL /min-g support for 6.5 h.

The nominal compositions (by weight) of the prepared catalysts were as follows:

- (i) 15 % Fe/0 % K/85 % SiO<sub>2</sub>
- (ii) 15 % Fe/0.1 % K/84.9 % SiO<sub>2</sub>
- (iii) 15 % Fe/0.5 % K/84.5 % SiO<sub>2</sub>

(iv) 15 %Fe/0.9 %K/84.1 %SiO<sub>2</sub>

***Part B: The effect of potassium loading on the activity and selectivity of a silica tubes supported iron catalyst.***

The catalyst support was prepared by the templated sol-gel method, at 25 °C, using ammonium oxalate as a template and a 1:1 mixture of water and ethanol as a solvent. Details of the synthesis of the support are outlined in Chapter 5. The support was crushed and sieved; only particles with sizes between 125 and 400 µm were collected. These were calcined at 600 °C for 18 h prior to metal impregnation.

The catalysts were prepared by incipient wetness impregnation. The prepared silica tubes support (BET surface area 100 m<sup>2</sup>/g, pore volume 0.332 g/cm<sup>3</sup>; determined by N<sub>2</sub> physisorption) was dried at 250 °C overnight to remove excess moisture. Then 166 g of the support was impregnated with iron. The impregnation was done in five steps, using five 55.2 ml Fe(NO<sub>3</sub>)<sub>3</sub> solution aliquots each containing 5.85 g Fe. The dry support was placed in a round bottom flask fitted to a burette and connected to a rotary evaporator. The metal ion solution was added dropwise to the dry support with rotation of the round-bottom flask. At the end of each impregnation step, the catalyst was dried on the rotary evaporator under vacuum at 90 °C.

The prepared iron impregnated catalyst was then divided into three parts and the parts were impregnated over a single step with potassium. Potassium nitrate solutions, about 28 ml, each containing 0.094, 0.657, 0.445 g potassium, respectively were used to impregnate the three catalyst parts. The impregnations were done in a similar manner as with iron.

The catalysts were calcined in a fixed bed reactor, at 250 °C (heating rate of 5 °C/min), in air with a downward flow of 45 mL /min-g support for 6.5 h.

The nominal compositions (by weight) of the prepared catalysts were as follows:

- (i) 15 %Fe/0.1 % K/84.9 % SiO<sub>2</sub>
- (ii) 15 %Fe/0.5 % K/84.5 % SiO<sub>2</sub>
- (iii) 15 %Fe/0.9 % K/84.1 % SiO<sub>2</sub>

### **6.2.2. Fischer-Tropsch Synthesis**

A catalyst mass of 50 g was loaded in a slurry CSTR reactor, with 300 g Ethylflo164 (C-30) oil, which is a commercial polyalphaolefin (Durasyn 164), as startup oil. The catalyst was activated at 270 °C for 22 h in CO, with a weight hourly space velocity of 3.2 L/h(STP)-per gram Fe and a pressure of 20 bar. When activation was complete, the reactor temperature was reduced to 250 °C, and H<sub>2</sub> was introduced, and its flow was controlled to provide a simulated synthesis gas with H<sub>2</sub>/CO ratio of 2/1, at a pressure of 20 bar, and a weight hourly space velocity of 3.6 L/h (STP) per gram Fe. The reaction was run for a total of 280 h. Gas, oil and wax samples were taken and analysed in 24-48 h intervals.

### **6.2.3. Extraction of used catalysts**

After the reaction, the catalysts were extracted with hot o-xylene, in a soxhlet extraction apparatus, for 24-48 h, to remove wax. The extracted catalysts were then dried in a vacuum oven at 100 °C for 48 h, and then calcined in a static air furnace at 200 °C for 6 h.

### **6.2.4. Catalyst Characterisation**

The calcined fresh catalysts were analysed for metal composition, while the calcined extracted catalysts were analysed for carbon content. All fresh and extracted catalysts were characterised by nitrogen physisorption.

*Part A: The effect of potassium loading on the activity and selectivity of a commercial silica supported iron catalyst.*

### 6.3. RESULTS AND DISCUSSION

The prepared catalysts were analysed for actual iron and potassium contents by ICP. **Table 6.1** summarises the intended nominal and actual analysed compositions of each catalyst employed in this work. The elemental analysis data reveal that the metal ratios obtained from the prepared catalysts are very close to those predicted from the catalyst preparation. For the purpose of simplicity, each catalyst will be referred to by its nominal potassium content.

**Table 6.1** Metal contents of the prepared promoted iron catalysts

Nominal metal content (wt %)	Actual Fe content (wt%)	Actual K content (wt%)
15Fe	14.89	-
15Fe/0.1K	14.74	0.13
15Fe/0.5K	14.49	0.48
15Fe/0.9K	14.32	0.85

#### 6.3.1. Carbon monoxide conversion

CO conversion is a rough measure of the overall FT activity and stability of an iron catalyst. **Fig. 6.1** shows a plot of CO conversion as a function of time on stream for all four catalysts. Contrary to numerous reports<sup>3(a),3(c),5,9,12</sup>, in this study the effect of potassium on the iron catalyst *did not lead to an increase* in CO conversion. The CO

conversion decreased with an increase in potassium loading, reached a minimum at 0.5 %K, and then increased slightly with further increase in potassium loading. It was noted that all four catalysts showed a small decrease of catalyst activity with time on stream, as shown in **Table 6.2**.

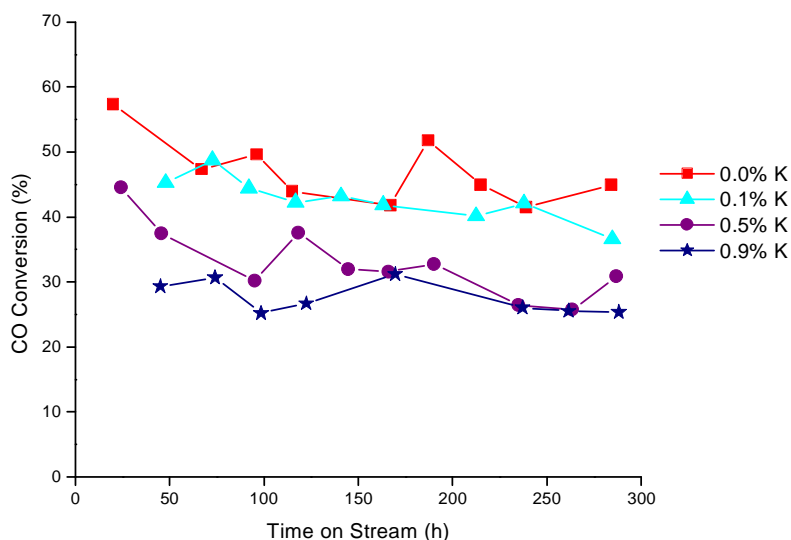


**Figure 6.1.** Effect of potassium loading on CO conversion over iron supported on Davisil SiO<sub>2</sub>.

**Table 6.2.** Effect of potassium loading on the decrease in catalyst activity with time on stream.

Catalyst	Overall Decrease in CO Conversion (%)	Overall Decrease in FT Reaction Rate (%)	Overall Decrease in WGS Reaction Rate (%)	Overall Decrease in CO <sub>2</sub> Selectivity (%)
0% K	12.4	0.0552	0.0746	1.98
0.1% K	8.62	0.260	0.168	4.89
0.5% K	3.98	0.071	0.142	7.52
0.9% K	6.62	0.170	0.184	7.30

Literature reports on the effect of potassium on iron FT catalyst give conflicting results (see details in **Table 6.3**). In several previous studies with iron catalysts, it was reported that the overall catalyst activity either increased with potassium loading or passed through a maximum as a function of potassium loading<sup>3(c),5,9,13</sup>. Further, Pichler<sup>14</sup> reported that  $K_2CO_3$  in the 0 -0.25 wt% range, had no effect on the catalyst activity, whereas other researchers found that the activity of potassium promoted iron catalyst was lower than that of an unpromoted catalyst<sup>2(a),15</sup>. Raje et al.<sup>3(d)</sup> observed a decrease in FT activity with an increase in potassium loading only at low CO conversions (0-60 %) while other researchers generally observed a decrease in FT activity with potassium promotion<sup>16</sup>. The contradiction and differences in the results found by previous researchers can be attributed to differences in parameters such as catalyst preparation and conditions under which the catalysts were prepared.

Arakawa and Bell<sup>2</sup> observed a decrease in  $H_2$  and CO uptake with an increase in potassium promotion, during their chemisorption studies on a potassium promoted alumina supported iron catalysts, although they also observed retention of adsorbed CO after attempts to desorb it from the catalyst surface. They attributed the decrease in  $H_2$  and CO uptake to a decrease of iron dispersion on the support as the K/Fe ratio increased. Also, as previously observed by other researchers<sup>2(a),5,17</sup>, the addition of potassium leads to enhanced carbon deposition on the catalyst surface during FT synthesis, and this leads to lowered catalyst activity. This carbon deposition eventually leads to catalyst deactivation through blocking of the active sites of the catalyst. Thus, a decrease in iron dispersion and an increase in carbon deposition with an increase in potassium promotion could lead to lowered catalyst activity with time.

**Table 6.3.** Details of reaction conditions used by other researchers.

Catalyst	Conditions	Finding	Ref
Precipitated Fe/K/Cu/SiO <sub>2</sub> K level: 0.007-0.1 atomic ratio	Activation: CO, 270 °C, Reaction: CSTR, 230 °C, H <sub>2</sub> /CO: 0.67, 12 bar	Activity increases with potassium loading and plateaus at 0.5 wt% loading	3(c)
Precipitated Fe/K SiO <sub>2</sub> supported K <sub>2</sub> O level: 12-32%, unsupported K <sub>2</sub> O level: 0-3.0%	Low temperature, no further details	<b>Supported catalyst:</b> activity increased with increasing potassium levels. <b>unsupported catalyst:</b> activity increased with increasing K levels but went through a peak at K <sub>2</sub> O level of 12%.	5,9
Sintered Fe <sub>3</sub> O <sub>4</sub> , K <sub>2</sub> O/100Fe: 0.06-0.94	Activation: H <sub>2</sub> , 400 °C Reaction: 227 °C, H <sub>2</sub> /CO: 1, 6.9 bar	Activity increases sharply with increasing potassium loading, then decreases beyond 0.5 wt% loading	13
Precipitated Fe	No details	K <sub>2</sub> CO <sub>3</sub> in the 0 - 0.25 wt% range had no effect on the catalyst activity	14
Fe supported on Al <sub>2</sub> O <sub>3</sub> , K/Fe=0 – 0.4	Activation: H <sub>2</sub> , 400 °C Reaction: Fluidised bed, 260 °C, H <sub>2</sub> /CO: 3, GHSV: 6 L/h-gFe.	Activity of a promoted catalyst was lower than that of an unpromoted catalyst	2(a)



**Table 6.3.** Details of reaction conditions used by other researchers (continued).

Catalyst	Conditions	Finding	Ref
Precipitated Fe <sub>2</sub> O <sub>3</sub> , K/Fe <sub>2</sub> O <sub>3</sub> =0.011	Activation: H <sub>2</sub> , 300 °C Reaction: Stirred tank reactor, 250 °C, H <sub>2</sub> /CO:3, 8.1 bar.	Activity of promoted catalyst was lower than that of an unpromoted catalyst	15
Precipitated Fe/SiO <sub>2</sub> K level: 0.36 - 2.2 atomic ratio	Activation: CO, 270 °C Reaction: CSTR, 270 °C, H <sub>2</sub> /CO: 0.67, 13.1 bar	A decrease in FT activity with increasing potassium loading at low CO conversions (0-60%)	3(d)
xK/3.9Fe/Al <sub>2</sub> O <sub>3</sub> (x=2.2, 5.5 wt %)	Activation: H <sub>2</sub> , 450 °C Reaction: Fixed bed reactor, 260 °C, H <sub>2</sub> /CO: 3, 1.01 bar	FT activity decreases with increasing potassium loading	16

### 6.3.2. Methane Selectivity

Methane selectivity as a function of time on stream is shown in **Fig. 6.2**. In agreement with previous work done by other researchers<sup>2(a),3(c),3(d),9,15,18,19</sup>, potassium promotion decreased methane selectivity and an increase in potassium loading led to a decrease in methane selectivity. However, in the present case, the decrease was not as significant as reported by previous researchers<sup>2,19</sup>; Arakawa and Bell found a decrease in methane selectivity from 57 % to 22 % when they increased the K/Fe ratio from 0 to 0.4 on an Al<sub>2</sub>O<sub>3</sub> supported iron catalyst (at 260 °C, H<sub>2</sub>/CO = 3 and GHSV = 6 LSTP/h-gFe), Bukur et al also found a decrease from 22 % down to 10 % with an increase of K/Fe ratio from 0 to 0.005 on a precipitated iron catalyst (at 250 °C, H<sub>2</sub>/CO = 1, 14.8 bar). The methane selectivity, for both promoted and unpromoted catalysts, was generally higher than what other researchers have found

(CH<sub>4</sub> selectivity of 1.5-5 % using a precipitated Fe/K/Cu/SiO<sub>2</sub> K level: 0.007-0.1 atomic ratio, in a CSTR at 230 °C, H<sub>2</sub>/CO: 0.67, 12 bar)<sup>3(c)</sup>, (CH<sub>4</sub> selectivity of 5-11 % using a precipitated 100/Fe/4.6Si catalyst with K levels : 0.36-2.2 atomic ratio, in a CSTR at 270 °C, H<sub>2</sub>/CO: 0.67, 13.1 bar)<sup>3(d)</sup>, (CH<sub>4</sub> selectivity of 5-6 % using a precipitated 100Fe/4.6Si/1.44K atomic ratio catalyst in a CSTR at 270 °C, H<sub>2</sub>/CO:0.67, 13.1 bar)<sup>18</sup>, probably due to different reaction conditions and the type of catalyst used. Jothimurugesan et al<sup>6</sup>, Dry<sup>5,9</sup> and Bukur et al<sup>20</sup> found, in their study of silica supported iron based FT catalysts, that an increase in the amount of SiO<sub>2</sub> support used led to an increase in methane selectivity and correspondingly to a decrease in long chain hydrocarbon selectivity.

Dry and Oosthuizen<sup>3(b)</sup> have shown from their study of CO<sub>2</sub> chemisorption on an alkali promoted SiO<sub>2</sub> supported iron catalyst, that there is a relationship between surface basicity (defined as the ratio of chemisorbed CO<sub>2</sub> to argon BET monolayer volume) of the catalyst and its selectivity for methane, whereas the relationship between methane selectivity and the catalyst K<sub>2</sub>O content was not linear. They found that methane selectivity decreased with an increase in the surface basicity of the catalyst. They therefore concluded that the catalyst surface basicity depends not only on the amount of potassium present but also on how well it is distributed over the catalyst surface. They demonstrated that chemical interaction between the basic alkali and the acidic support takes place, and that potassium silicates, which are less basic than pure K<sub>2</sub>O, are formed, rendering the SiO<sub>2</sub> supported promoted catalyst less basic. Thus, the reduction in surface basicity, due to the presence of SiO<sub>2</sub> in the catalyst, explained the observed increase in methane selectivity when the SiO<sub>2</sub> content was increased. In the present case, the SiO<sub>2</sub> comprised about 85 % of the total catalyst mass, implying that the surface basicity of the catalysts employed was low, resulting in high methane selectivities.

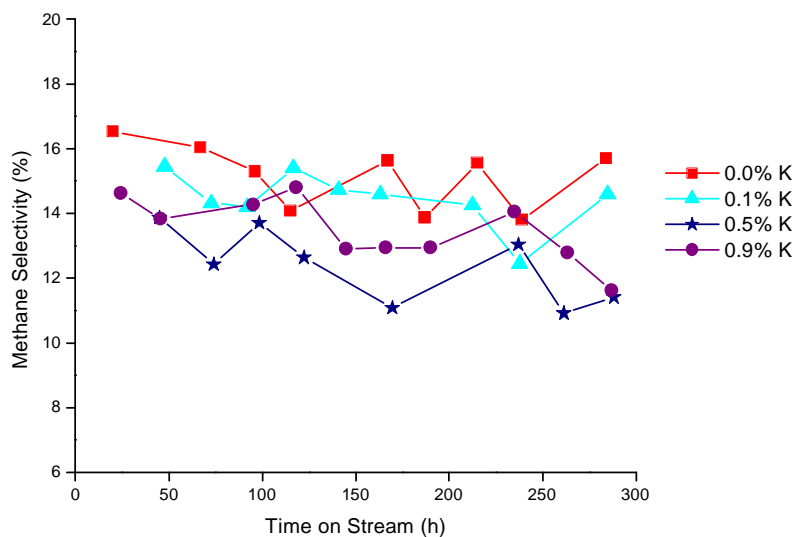


**Figure 6.2.** Effect of potassium loading on methane selectivity.

### 6.3.3. Reaction Rates and Catalyst Efficiency

The effect of potassium loading on the FT rate is shown in **Fig. 6.3**. Amongst all four catalysts, the unpromoted catalyst exhibited the highest FT rate. The FT rate decreased with an increase in potassium loading, but a switch in the trend was observed between the 0.5 % and 0.9 % K loaded catalysts. This result is in agreement with Dry's findings for a supported iron catalyst<sup>5,9</sup>. For all four catalysts, a slight decrease in the FT rate with time on stream was observed, depicted in **Table 6.2**.

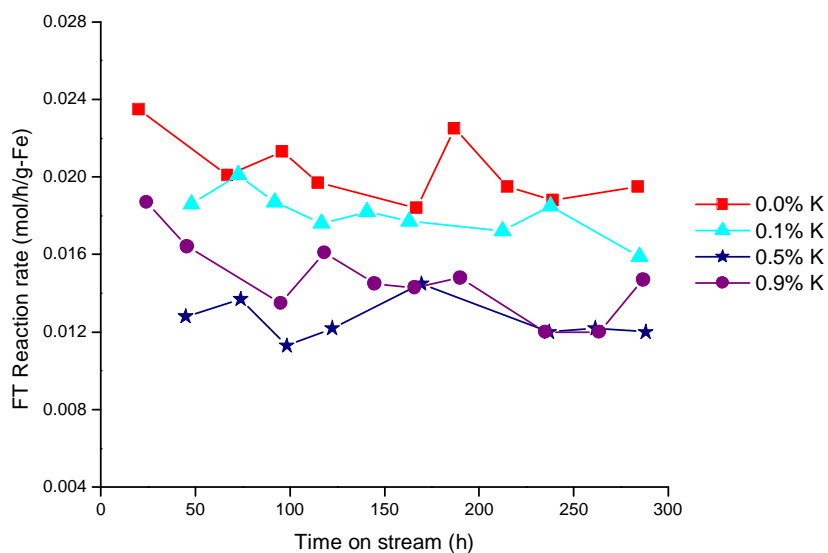


**Figure 6.3.** Effect of potassium loading on Fischer-Tropsch reaction rate.

The FT reaction on iron catalysts is always accompanied by the WGS reaction. The rate of WGS reaction, shown in **Fig. 6.4**, exhibited by all four catalysts showed a similar trend to the rate of the FT reaction. The unpromoted catalyst exhibited the highest WGS reaction rate, and the WGS reaction rate decreased with increasing potassium loading, with a switch in the trend observed between the 0.5 % and 0.9 % K loaded catalysts. The WGS reaction rate also decreased with time on stream, and this decrease was more apparent with the promoted catalysts than with the unpromoted one, see **Table 6.2**.

Another measure of the WGS activity of the catalyst is its selectivity towards  $\text{CO}_2$ . The effect of potassium loading on the  $\text{CO}_2$  selectivity is shown in **Fig. 6.5** and it exhibits the same pattern found for both the FT and WGS reaction rates. Contrary to previous studies<sup>2(a),3(a),15,19</sup>, the unpromoted catalyst had the highest selectivity towards  $\text{CO}_2$  when compared to promoted catalysts. Also, the  $\text{CO}_2$  selectivity decreased with an increase in potassium promotion, down to a minimum with 0.5 % K and then increased again with a further increase in potassium loading. It is also clear from the figure that the  $\text{CO}_2$  selectivity for all the catalysts decreased with time

on stream and that this decrease is more significant with the promoted catalysts, (see also **Table 6.2**).

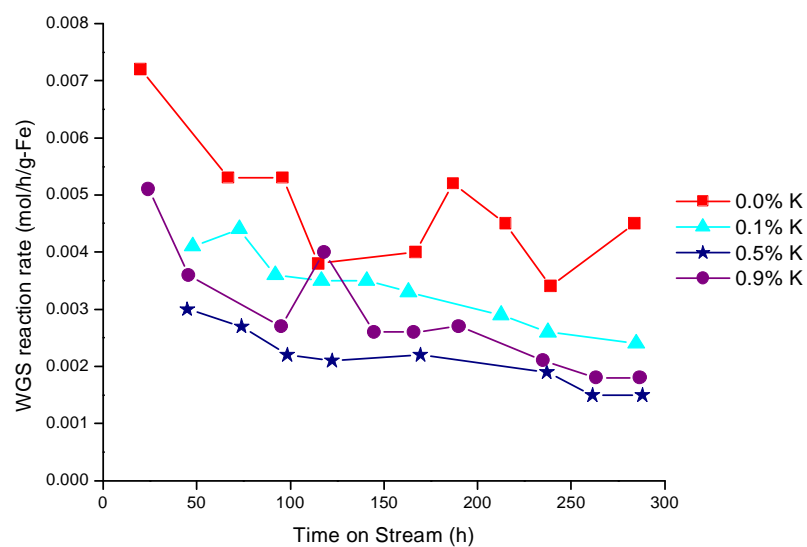


**Figure 6.4.** Effect of potassium loading on water-gas-shift reaction rate.

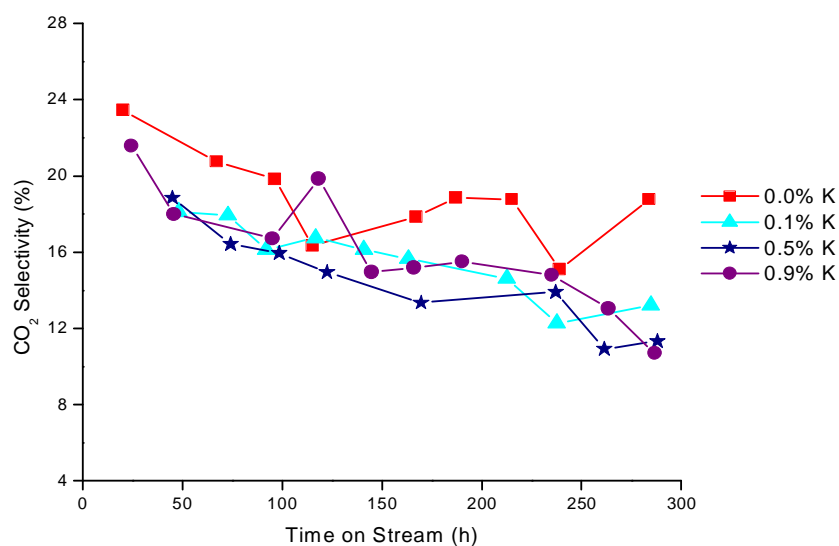


**Figure 6.5.** Effect of potassium loading on CO<sub>2</sub> selectivity.

Summarizing the above findings, it can be seen that CO conversion, FT and WGS reaction rates, and CO<sub>2</sub> selectivity exhibited by all the catalysts follow the same trend; they all decrease with increasing potassium loading, and no further increase was observed when potassium loading was increased beyond 0.5 %.

However, direct comparison of the rates of FT and WGS reactions exhibited by these catalysts must be treated circumspectly as all the catalysts in this study gave different CO conversions. Thus, to get a true reflection of the effect of potassium loading on an iron catalyst, a comparison of its activity in the FT reaction relative to the WGS reaction has to be made. This is illustrated in **Fig. 6.6**, which shows a plot of the catalyst efficiency, the ratio of the FT reaction rate relative to the WGS reaction rate, against reaction time. The catalyst efficiency is a good measure of how much CO was converted into hydrocarbons rather than CO<sub>2</sub>. The plot clearly shows that:

- (i) the unpromoted catalyst was less efficient in forming hydrocarbons,
- (ii) the catalyst efficiency for the promoted catalysts clearly increased with time on stream, and that
- (iii) the catalyst efficiency increased with potassium loading, reached a maximum with 0.5 % K and then decreased with a further increase in potassium loading.

Thus, although the 0.5 % K catalyst showed the lowest CO conversion, it was more effective in producing hydrocarbons than any of the other catalysts. This shows that a higher CO conversion does not necessarily imply a high production of useful hydrocarbons.

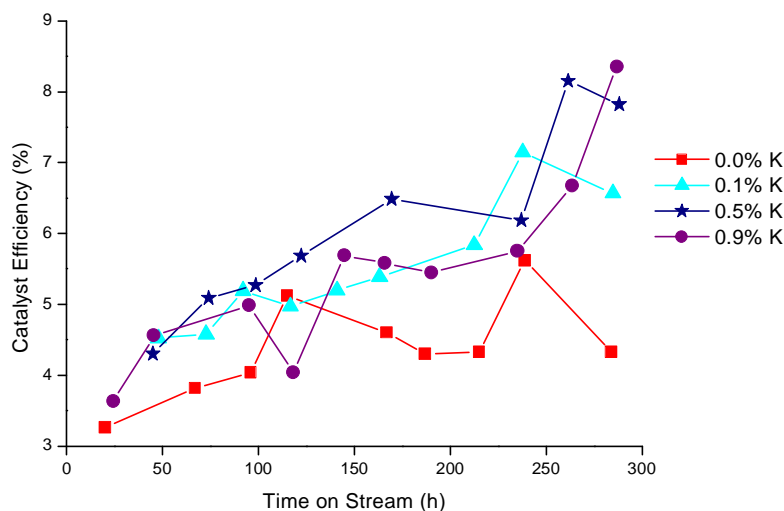


**Figure 6.6.** Effect of potassium loading on catalyst efficiency.

In his study on the reduction of Fe catalysts, Dry<sup>5,9</sup> found that the presence of SiO<sub>2</sub> in a precipitated Fe catalyst led to a lower degree of iron oxide reduction and that the degree of reduction was lowered from 100 to 57 % when SiO<sub>2</sub> levels were increased from 0 to 50 g per 100 g Fe. He attributed the decrease in the degree of Fe reduction in the presence of SiO<sub>2</sub> to the formation of an iron silicate complex during catalyst preparation, which is slower to reduce than iron oxide. Similar results were also found with a SiO<sub>2</sub> supported Ni catalyst<sup>21</sup>. Dry also found a mixture of Fe<sub>5</sub>C<sub>2</sub> and Fe<sub>3</sub>O<sub>4</sub> phases present in a fused catalyst after reduction in 100 % CO for 8 h. It has been shown that the unreduced Fe can still be reduced to carbides during FT reaction by CO in the feed gas<sup>22,23</sup>. Furthermore, potassium promoted iron catalysts have been shown to carburize more rapidly and completely than unpromoted iron catalysts<sup>2(a),5,9</sup>. There has been considerable debate about the active phase of iron in the FT synthesis. Some studies have indicated that FT synthesis requires an active oxide species<sup>24</sup>, while others have supported a carbide species<sup>25,26</sup>. On the other hand, it is believed that metallic Fe<sup>27</sup> and Fe<sub>3</sub>O<sub>4</sub><sup>28,29</sup> are more effective catalytic sites for the WGS reaction than Fe carbides. Thus, in the present case, it is speculated that

the increase in the catalyst efficiency, more clearly shown by potassium promoted catalysts, could be due to formation of more iron carbides during FT synthesis, thereby increasing hydrocarbon formation. When more carbidic sites are formed, obviously a corresponding decrease in the number of oxidic or metallic sites occurs. This is reflected by the decrease in WGS activity, and hence CO<sub>2</sub> selectivity, of the catalysts with time on stream, which is more apparent in the case of promoted catalysts.

#### 6.3.4. Product Distribution and Selectivity

The hydrocarbon product distribution is illustrated in **Fig. 6.7** in the form of an Anderson-Shultz-Flory (ASF) plot, a semi-logarithmic plot of product weight versus the number of carbons in the product. As found by other researchers<sup>15,19,30</sup> for all four catalysts employed in this study, the total product distributions cannot be described by a uniform chain growth probability factor  $\alpha$ , as the ASF plot shows two distinct regions of different slopes (which give two values of  $\alpha$ ). Under FT conditions, wax products are in the liquid state, so the catalyst pores are presumably filled with liquid. Thus, it has been postulated that when liquids are present inside the catalyst pores, the higher molecular weight products would have longer residence time within the catalyst pores, which could lead to alkene re-incorporation; i.e. readsorption of primary alkenes<sup>31,32</sup>. Alkene re-incorporation then results in further chain growth, which implies an increased chain growth probability, and hence the occurrence of two distinct chain growth probabilities.

The deviation of C<sub>20+</sub> products from the second slope could be due to hold-up of these components in the reaction slurry, as was previously observed by others<sup>15</sup>. These products make up about 14-23 % (depending on the catalyst used) of the total reactor hold-up liquid weight, the rest being C<sub>30</sub> start-up oil.



The effect of potassium loading on the chain growth probability is presented in **Table 6.4**. The values of both  $\alpha_1$  (for  $C_5$ - $C_{12}$ ) and  $\alpha_2$  (for  $C_{13}$ - $C_{20}$ ) obtained were higher for the promoted catalysts when compared to the unpromoted catalyst, and a slight increase in the chain growth probability with an increase in potassium loading was also observed. Furthermore, the chain growth probability of products  $C_{13}$ - $C_{20}$  obtained was higher than for lower molecular weight products  $C_5$ - $C_{12}$ . This is in agreement with previous findings by other researchers<sup>15,19</sup>.

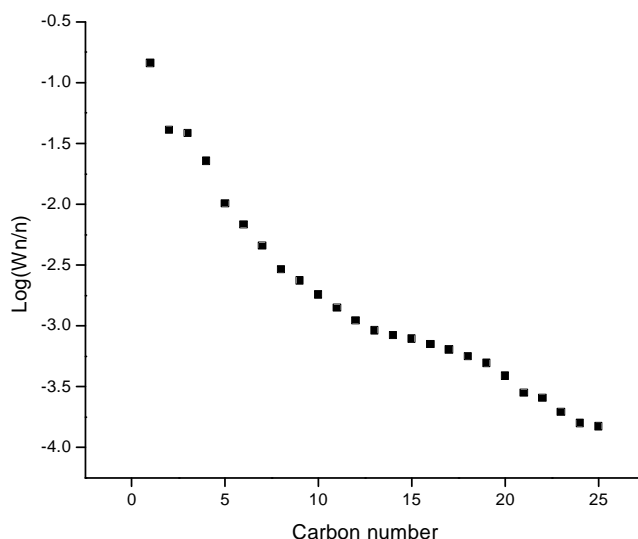


**Figure 6.7.** Anderson-Shultz-Flory plot for a 0.5 % potassium promoted catalyst.

The hydrocarbon product distributions of the four catalysts are shown in **Fig. 6.8**. The average molecular weight of hydrocarbon products increased on addition of potassium and increased with increasing potassium loading up to 0.5 %. It is clear that potassium (i.e. 0-0.5 %) lowered the formation of methane and gaseous hydrocarbons ( $C_2$ - $C_4$ ), and slightly increased selectivity towards higher molecular weight hydrocarbons. This is in agreement with previous studies<sup>2(a),3(c)3(d),9,15,18,19</sup>. In the present case the effect observed is very small and could be due to a promoter-support interaction which can lead to decreased catalyst surface basicity. The increase in selectivity for higher molecular weight hydrocarbons generally observed

is due to the increased CO and lowered H<sub>2</sub> surface coverage in the presence of potassium<sup>2(a),3(a),5,14,15</sup>. This implies that in the present case, as most of the potassium was bound to the support, as it usually occurs when silica is used as a support, the CO and H<sub>2</sub> surface coverages were only slightly affected by an increase in potassium loading.

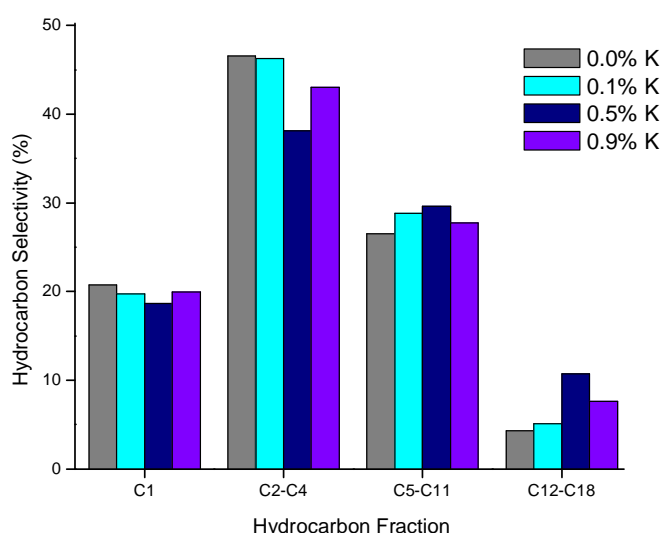


**Figure 6.8.** Effect of potassium loading on hydrocarbon product distribution.

The effect of potassium promotion on olefin selectivity, which is expressed as a mass fraction of olefins in the total hydrocarbon product of the same carbon number, is summarized in **Table 6.4**. The results show that for all four catalysts, the olefin content increased from C<sub>2</sub> to C<sub>4</sub>, reached a maximum at C<sub>4</sub>, and then decreased with increasing carbon number. This trend was also observed by other researchers<sup>5,9,15,19</sup>. The observed decrease in olefin selectivity results from secondary hydrogenation of olefins to paraffins. Ethylene is more reactive than other low molecular weight olefins, and is therefore easily hydrogenated into ethane. As explained earlier, alkene-reincorporation usually occurs with the higher molecular weight products. Thus the higher the molecular weight of the product, the slower they would diffuse

out of the catalyst pores, and therefore the longer the residence time the greater the likelihood that the primary olefin will be hydrogenated to paraffin. Hence the longer the chain length the lower the olefin selectivity of the product<sup>5,33</sup>.

The presence of potassium on an iron FT catalyst is known to increase olefin selectivity by suppressing secondary hydrogenation reactions of olefins into paraffins<sup>3(d),15,19</sup>. Indeed, our results show that olefin selectivity increases with potassium promotion. Since potassium increases CO chemisorption while decreasing H<sub>2</sub> chemisorption, as reported by other researchers<sup>2(a),2(b)</sup>, its presence results in a lower surface concentration of H<sub>2</sub>, and consequently to a lower hydrogenation activity<sup>9,19</sup>.

**Table 6.4.** Effect of potassium promotion on chain growth probability and olefin selectivity.

		0% K	0.1% K	0.5% K	0.9% K
Alpha	$\alpha_1$	0.67	0.69	0.76	0.70
	$\alpha_2$	0.71	0.75	0.77	0.81
<b>Olefin selectivity*</b>					
	C <sub>2</sub>	21	22	27	30
	C <sub>3</sub>	67	70	72	72
	C <sub>4</sub>	93	93	94	95
	C <sub>5</sub>	43	45	59	29
	C <sub>6</sub>	61	64	62	64
	C <sub>7</sub>	54	58	58	59
	C <sub>8</sub>	50	53	53	56
	C <sub>9</sub>	44	48	49	51
	C <sub>10</sub>	43	46	46	49
	C <sub>11</sub>	38	43	42	44
	C <sub>12</sub>	36	39	38	40
	C <sub>13</sub>	31	34	34	36
	C <sub>14</sub>	27	30	30	32
	C <sub>15</sub>	22	26	26	28
	C <sub>16</sub>	19	22	22	25

\* % Olefin = (100 x olefin/(olefin+paraffin))

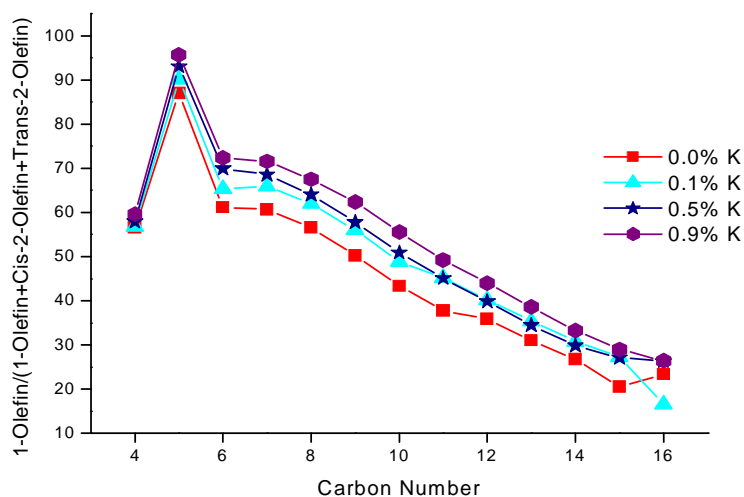


**Figure 6.9.** Effect of potassium loading on 1-olefin selectivity.

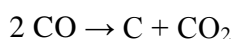
The isomerisation ability of the catalyst can be seen from its selectivity towards 1-olefins relative to 2-olefins (i.e. 1-olefin + cis-2-olefin + trans-2-olefin) produced. This is illustrated in **Fig. 6.9**. It can be observed that potassium suppressed isomerisation of 1-olefins and also that this effect increased with an increase in potassium loading. Also, for a given catalyst, the fraction of 1-olefins decreased with increasing carbon number, i.e. the isomerisation activity of the catalysts increased with carbon number. This is in agreement with previous findings<sup>5,9,19,34</sup>.

### 6.3.5. Catalyst Characterisation

**Table 6.5** shows the surface properties of the fresh and used catalysts. It shows that the surface area decreased upon addition of iron. A similar result was obtained in studies of a Co/SiO<sub>2</sub> catalyst<sup>35</sup>. The decrease can be attributed to pore blocking by the metal as it is accompanied by a significant decrease in pore volume. Also, a slight decrease in surface area with potassium loading can be observed. This is in line with the results found by Dry and Oosthuizen<sup>3(b)</sup>. They observed a marked decrease in surface area of the catalyst when Na and K were used as promoters

compared to Li and Ba. They also observed that the surface area decreased further with an increase in K loading. In their X-ray line broadening study of reduced K<sub>2</sub>O promoted iron catalyst, Dry et al<sup>36</sup> found that samples containing K<sub>2</sub>O had larger iron crystallites than those without K<sub>2</sub>O. They then concluded that the loss of surface area when potassium is used as a promoter is therefore due to crystal growth, rather than pore blocking.

A significant decrease in the surface area of all the catalysts was observed in the used catalysts. Egiebor and Cooper<sup>37</sup> observed the same behaviour in their Fe/Cu/SiO<sub>2</sub> catalysts, and they attributed the decrease in surface area of the catalyst after an FT reaction due to deposition of carbon onto the surface of the catalyst, and sintering of the catalyst particles during synthesis. Indeed, carbon was found on the catalysts after the reaction, as is shown in **Table 6.5**. The catalyst which gave the highest catalyst efficiency (0.5 %K) had the most carbon content after the reaction. The carbon was deposited as a result of the Boudouard reaction:



This type of carbon is totally different from the high molecular weight wax, which limits the diffusion of reactants and is soluble in hydrocarbon products, and was thus easily removed by soxhlet extraction using hot o-xylene. The Boudouard carbon deposits permanently on the catalyst surface thereby decreasing the number of active sites.

The reason for the observed higher surface area in the 0.5 %K used catalyst compared to the 0.1 % K used catalysts is due to the high content of the high surface area amorphous carbon, i.e. Boudouard carbon, on the 0.5 % K catalyst.

**Table 6.5.** Physisorption data and carbon content of fresh and used catalysts.

Catalyst or support	Fresh Catalyst		Used Catalyst		C/Fe ratio
	BET	Single Point	BET	Single Point	
	Surface	Pore	Surface	Pore	
	Area (m <sup>2</sup> /g)	Volume (cm <sup>3</sup> /g)	Area (m <sup>2</sup> /g)	Volume (cm <sup>3</sup> /g)	
Davisil	273	1.078	-	-	-
0.0% K	254	0.787	229	0.756	0.328
0.1% K	250	0.772	190	0.684	0.386
0.5% K	242	0.758	208	0.745	0.426
0.9% K	239	-	189	0.670	0.406

## 6.4. CONCLUSION

The effects of potassium promotion on the activity and selectivity of a catalyst cannot always be predicted as they depend on catalyst preparation, composition and conditions under which the catalyst is tested. For the catalyst system studied, the presence of the alkali promoter reduced the catalyst activity and the methane selectivity while it increased the selectivity towards olefins and higher molecular weight hydrocarbons. However, it seems there is a maximum promotion level that can be used to obtain optimum catalyst activity, because using loadings higher than about 0.5 % decrease the promotional effect of the alkali promoter.

Unfortunately, strong metal-support interactions, which reduce the promotional effect of the promoter, cannot be avoided when silica is used as a support.

*Part B: The effect of potassium loading on the activity and selectivity of silica tubes supported iron catalyst.*

## 6.5. RESULTS AND DISCUSSION

The prepared catalysts were analysed for actual iron and potassium contents by ICP. **Table 6.6** summarises the intended nominal and actual analysed compositions of each catalyst employed in this work. Although the attained iron levels were slightly lower than it was intended, the potassium levels were close to those predicted from the catalyst preparation. For the purpose of simplicity, each catalyst will be referred to by its nominal potassium content.

**Table 6.6.** Metal contents of the prepared promoted iron catalysts

Nominal metal content (wt %)	Actual Fe content (wt%)	Actual K content (wt%)
15Fe/ 0.1K	12.36	0.12
15Fe/0.5K	12.28	0.45
15Fe/0.9K	12.20	0.80

### 6.5.1. Carbon monoxide conversion

**Fig. 6.10** shows the CO conversion profiles of the catalysts. In agreement with previous studies done on potassium promoted Fe FT catalysts<sup>3(a),3(c),5,9,12</sup>, an increase in potassium loading to 0.5 wt % led to an increase in carbon monoxide conversion, which decreased with a further increase in potassium loading. Dry<sup>5</sup> showed that the influence of increasing the potassium content of catalysts is not always consistent



and that it depends on the type of catalyst and the conditions under which it is being tested. He showed this by testing a fused iron catalyst at low temperature in a fixed bed reactor and found that the catalyst activity decreased with an increase in potassium content, while the catalyst activity increased with an increase in potassium content and then flattened out at higher conversions when tested at higher temperatures in a fluidized bed reactor. Thus the catalyst activity can either increase or decrease with potassium promotion depending on the reaction conditions.

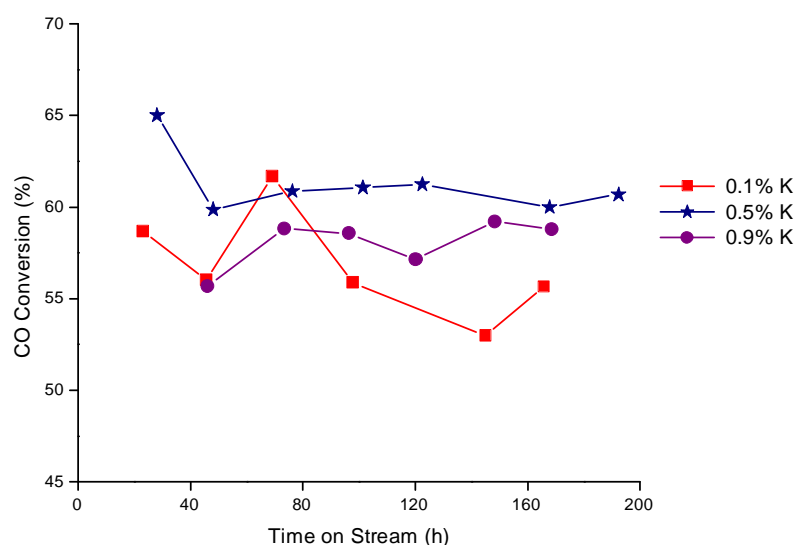


**Figure 6.10.** Effect of potassium loading on CO conversion over Fe supported on silica tubes.

The CO conversion not only increased with an increase in potassium content but it passed through a maximum at 0.5 % K promotion. This result is similar to those obtained by others<sup>2(a),3(c),3(d),13</sup>, however the maximum was not found to occur at the same promotion level. A decrease in catalyst activity with further increase in potassium content can be attributed to a decrease in iron dispersion on the support as the K/Fe ratio increased<sup>2(a)</sup>, as discussed in Part A above.

### 6.5.2. Methane Selectivity

The effect of potassium promotion on an FT reaction is usually seen from its effect on the catalyst selectivity towards methane, and this is shown in **Fig. 6.11**. An increase in potassium loading from 0.1 to 0.5 % led to an increase in methane selectivity, which decreased slightly with a further increase in potassium loading to 0.9 %. This is surprising as an increase in potassium levels in a catalyst is known to decrease its selectivity towards methane<sup>2(a),3(c),3(d),9,12,15,18,19</sup>. However, Bartholomew and Rankin<sup>11</sup> found an increase in potassium loading to decrease methane formation at reaction temperatures between 200-225 °C, whereas they found it to decrease methane formation at 250 °C.

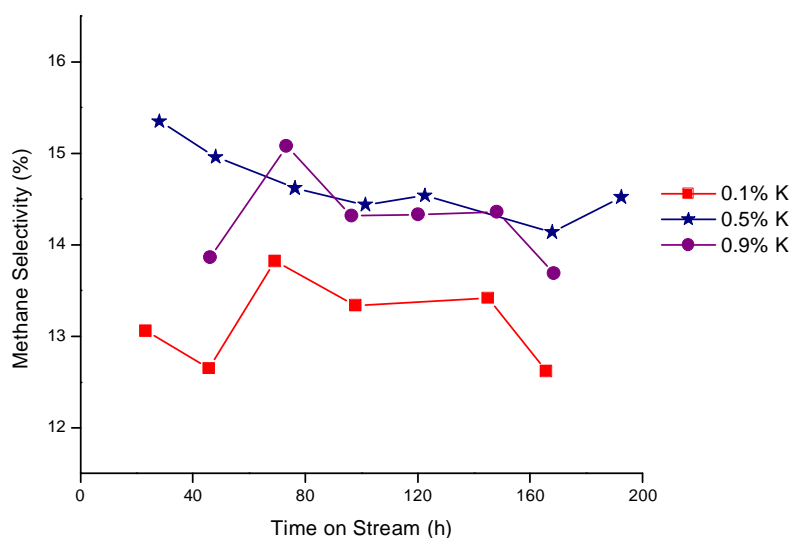


**Figure 6.11.** Effect of potassium loading on methane selectivity.

### 6.5.3. Reaction Rates

Although, in relation to the CO conversion profiles of these catalysts, an increase in FT reaction rates with an increase in potassium loading would be expected, only a small change in the FT reaction rates was observed (**Fig. 6.12a**). However, in

agreement with previous studies<sup>2(a),3(a),15,19</sup>, an increase in potassium loading led to an increase in WGS reaction rate, shown in **Fig. 6.12b**. The WGS activity of the catalysts can also be seen by their selectivity towards CO<sub>2</sub>, shown in **Fig 6.13**, which increases with an increase in potassium loading, and showed no further increase with an increase in potassium loading beyond 0.5 wt %.

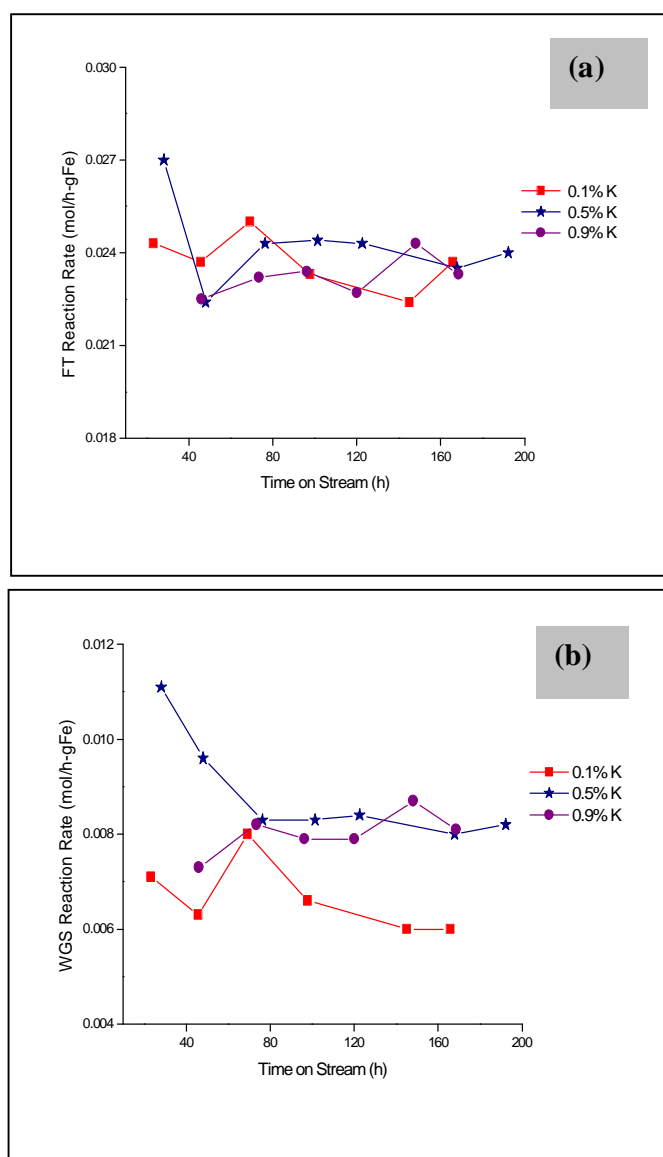


**Figure 6.12.** Effect of potassium loading on (a) Fischer-Tropsch and (b) water-gas shift reaction rates.

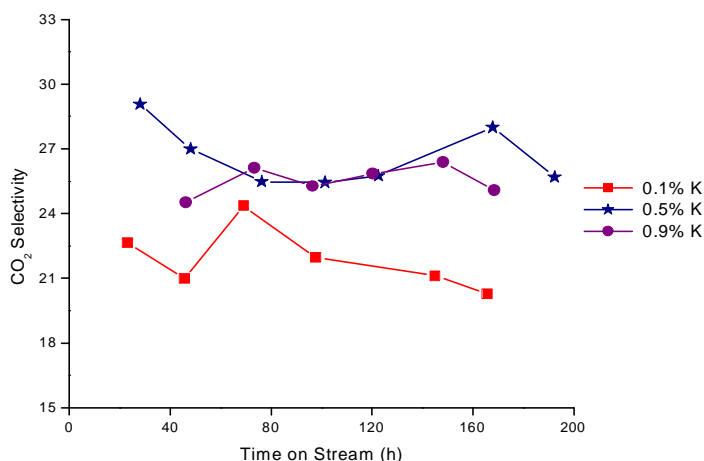


**Figure 6.13.** Effect of potassium loading on CO<sub>2</sub> selectivity.

#### 6.5.4. Product Distribution and Selectivity

The hydrocarbon product distribution is illustrated in **Fig. 6.14** in the form of an Anderson-Shultz-Flory (ASF) plot. Similarly to catalysts reported in part A section 6.3.4. above and previous work done by other researchers<sup>15,19,30</sup>, the total product distributions for all three catalysts employed in this study cannot be described by a uniform chain growth probability factor  $\alpha$ , as the ASF plot shows two distinct regions of different slopes (which give two values of  $\alpha$ ). The deviation of C<sub>20+</sub> products from the second slope could be due to hold-up of these components in the reaction slurry, as was previously observed by others<sup>15</sup>, because chromatographic analysis of the reactor hold-up liquid showed the presence of products with C<sub>19</sub>-C<sub>60</sub> carbon numbers. These products made up about 14-19.5 % of the total reactor hold-up liquid weight, depending on the catalyst used (see **Table 6.7**), the rest being C<sub>30</sub> start-up oil.

The effect of potassium loading on the chain growth probability is presented in **Table 6.8**. A slight increase in the chain growth probability with an increase in

potassium loading was observed. Furthermore, the chain growth probability of products  $C_{13}$ - $C_{20}$  obtained was higher than for lower molecular weight products  $C_5$ - $C_{12}$ . This is in agreement with previous findings by other researchers<sup>15,19</sup>. The occurrence of two distinct chain growth probabilities due to alkene-reincorporation was explained in part A section 6.3.4. above.

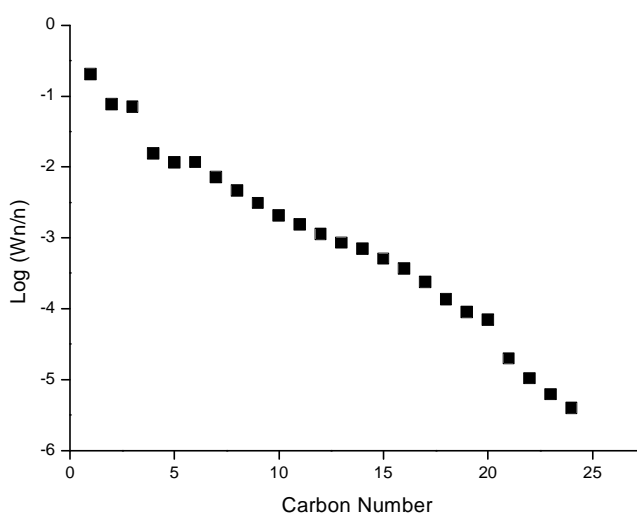


**Figure 6.14.** Anderson-Schultz-Flory distribution plot of 0.5 % K loaded catalyst.

The effect of potassium loading on product distribution is shown in **Fig. 6.15**. An increase in potassium loading led to an increase in methane selectivity, while a decrease in  $C_2$ - $C_4$  hydrocarbons was observed. Also an increase in selectivity towards heavier hydrocarbons ( $C_{12+}$ ) was observed. Previous studies have shown that a decrease in methane selectivity, caused by an increase in potassium loading, is usually accompanied by an increase in selectivity towards heavier hydrocarbons<sup>2,3(c),3(d),5,15,19</sup>. However in those studies a decrease in methane selectivity was also accompanied by a decrease in selectivity towards  $C_2$ - $C_4$  hydrocarbons, whereas in the present case a decrease in selectivity towards  $C_2$ - $C_4$  hydrocarbons occurred with an increase in methane selectivity. This decrease in light

gases with an increase in potassium loading accounts for an increase in selectivity towards heavier hydrocarbons despite an increase in methane selectivity. The increase in selectivity towards heavier hydrocarbons with an increase in potassium loading was further confirmed by an increase in the weight percentage of C<sub>19+</sub> hydrocarbon products held-up in the C<sub>30</sub> startup oil at the end of the reaction, shown in **Table 6.7**.

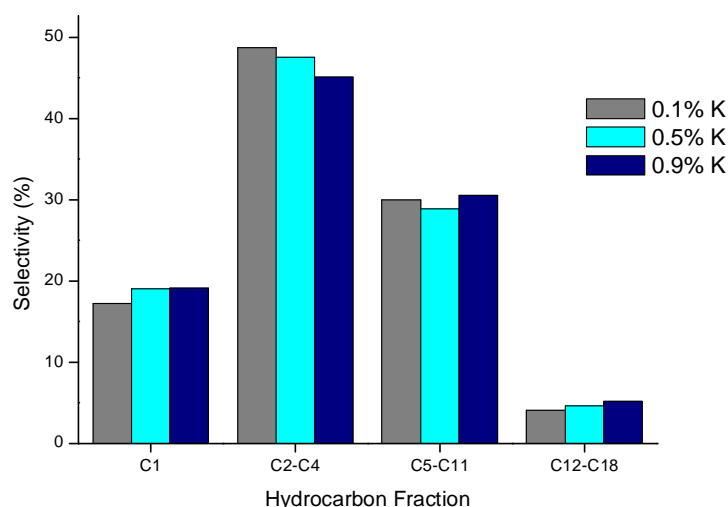


**Figure 6.15.** Effect of potassium loading on hydrocarbon product distribution.

**Table 6.7.** Amount of C<sub>19+</sub> hydrocarbons in reactor contents at the end of reaction.

Catalyst	Amount C <sub>19+</sub> (wt %)
0.1% K	14.51
0.5% K	15.36
0.9% K	19.36

The effect of potassium promotion on olefin selectivity is summarized in **Table 6.8**. The results show that olefin selectivity increased with an increase in potassium

promotion, which implies that an increase in potassium loading suppressed secondary hydrogenation of olefins to paraffins, as was previously found by others<sup>3(d),15,19</sup>. This is due to a reduced surface hydrogen concentration, as explained in part A section 6.3.4. above. The results also show that for all three catalysts, the olefin content increased from C<sub>2</sub> to C<sub>4</sub>, reached a maximum at C<sub>4</sub>, and then decreased with increasing carbon number. This trend was also observed by other researchers<sup>5,9,15,19</sup>. The observed decrease in olefin selectivity results from secondary hydrogenation of olefins to paraffins as discussed in part A section 6.3.4 above. The unexpected drop of selectivity towards C<sub>5</sub> olefins was probably due to loss of these olefins during sampling or due to error by the gas chromatograph during analysis.

**Table 6.8.** Effect of potassium promotion on chain growth probability and olefin selectivity.

		0.1% K	0.5% K	0.9% K
<b>Chain growth Probability</b>				
	A <sub>1</sub> (C <sub>5</sub> -C <sub>12</sub> )	0.67	0.64	0.69
	A <sub>2</sub> (C <sub>13</sub> -C <sub>20</sub> )	0.70	0.73	0.71
<b>Olefin selectivity* (%)</b>				
	C <sub>2</sub>	23	23	28
	C <sub>3</sub>	70	71	73
	C <sub>4</sub>	69	71	72
	C <sub>5</sub>	30	29	29
	C <sub>6</sub>	62	63	65
	C <sub>7</sub>	56	59	61
	C <sub>8</sub>	50	54	57
	C <sub>9</sub>	46	49	53
	C <sub>10</sub>	44	48	51
	C <sub>11</sub>	40	43	47
	C <sub>12</sub>	38	39	44
	C <sub>13</sub>	33	35	39
	C <sub>14</sub>	30	32	36
	C <sub>15</sub>	27	28	32

\*Olefin selectivity (100xOlefin/(Olefin+Paraffin))

The effect of potassium loading on selectivity towards 1-olefins relative to 2-olefins is shown in **Fig. 6.16**. In agreement with previous studies done on potassium promoted iron catalysts<sup>5,9,19,34</sup>, an increase in potassium loading increases selectivity towards 1-olefins, implying that isomerisation of 1-olefins to cis- and trans- olefins is suppressed by an increase in potassium levels. Furthermore, for a given catalyst, the fraction of 1-olefins decreased with increasing carbon number, i.e. the isomerisation activity of the catalysts increased with carbon number. The unexpected dip in the



selectivity towards C<sub>5</sub> olefins is due to loss of the C<sub>5</sub> olefins during sampling or due to instrumental error in the analysis of that group of hydrocarbon products.

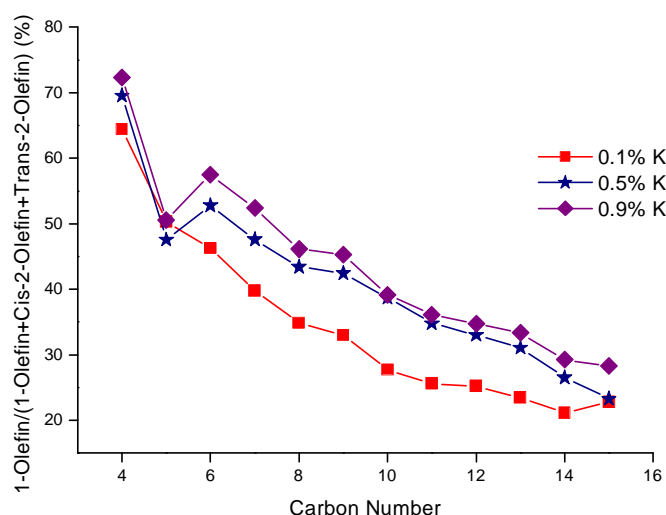


**Figure 6.16.** Effect of potassium loading on 1-olefin selectivity.

### 6.5.5. Catalyst Characterisation

**Table 6.9** shows the surface properties of the fresh and used catalysts. It shows that the surface area decreased slightly upon addition of both iron and potassium, this can be attributed to pore blocking<sup>35</sup> and crystal growth<sup>36</sup>, respectively.

A significant decrease in the surface area of all the catalysts was observed in the used catalysts. Egiebor and Cooper<sup>37</sup> observed the same behaviour in their Fe/Cu/SiO<sub>2</sub> catalysts, and they attributed the decrease in surface area of the catalyst after an FT reaction due to i) deposition of carbon on the surface of the catalyst, which plugs the surface pores leading to the internal surfaces of the catalyst, and (ii) sintering of the catalyst particles during synthesis, which caused the catalyst particles to agglomerate and form bigger particles with a lower reduced surface area. Indeed, carbon was

found on the catalysts after the reaction, as it is shown in **Table 6.9**, and that the catalyst which gave the highest FT activity had more carbon content after the reaction. Similarly to the Davisil silica supported catalysts, studied in the previous chapter, this carbon was deposited by the Boudouard reaction.

An unexpected increase in the pore volume of the 0.1 and 0.5 % K catalysts after the reaction was observed; it is not clear what led to an increase rather than a decrease in pore volume of the catalysts.

**Table 6.9.** Physisorption data and carbon content of the fresh and used catalysts

Catalyst or Support	Fresh Catalyst		Used Catalyst		
	BET	Single Point	BET	Single Point	C/Fe ratio
	Surface	Pore	Surface	Pore	
	Area (m <sup>2</sup> /g)	Volume (cm <sup>3</sup> /g)	Area (m <sup>2</sup> /g)	Volume (cm <sup>3</sup> /g)	
Silica tubes	109	0.35	-	-	-
0.1% K	105	0.254	78	0.264	0.15
0.5% K	100	0.267	78	0.288	0.29
0.9% K	99	0.269	74	0.262	0.22

## 6.6. CONCLUSION

Dry<sup>5</sup> mentioned that the effect of potassium promotion in an FT catalyst cannot be predicted with ease. Thus, a different behaviour in the catalyst activity was observed in the presence of silica tubes compared to the commercial silica support used in part A of this chapter. However, the bottom line appears to be that, there exists a maximum promotion level that can be used to obtain optimum catalyst activity for

the tubular silica materials, because using potassium loadings higher than 0.5 wt % decreased the catalyst activity. This could be explained in two ways (i) potassium containing catalysts have a higher concentration of active sites than unpromoted catalysts; thus at higher potassium concentrations, the active sites may be covered with the excess potassium, thereby leading to a decline in catalyst activity<sup>2(b)</sup>, or (ii) that the decline in catalytic activity at high potassium levels can be due to diffusion restrictions in the porous catalysts. At higher alkali levels, the wax formed within the catalyst pores becomes progressively longer chained and thus more viscous. The diffusion rates of the reactants through the wax to the active sites are therefore lowered and consequently the overall reaction rate is lowered<sup>9</sup>.

Nanostructured inorganic supports, particularly those synthesised by the simple and inexpensive sol-gel process, are applied extensively in many industrial applications. However, their use as supports in the FT reaction has not been thoroughly researched. This study shows that there is hope in using these materials as supports in the FT reaction.

## 6.7. REFERENCES

1. R.B. Anderson, *The Fischer-Tropsch Synthesis*, Academic Press, New York, 1984.
2. (a) H. Arakawa and A.T. Bell, *Ind. Eng. Chem.*, 22 (1983) 97.  
(b) H. Kolbel, in *Actes du Deuxieme Congres International de Catalyse Vol 2.*, Technip, Paris, 1960, p2075.  
(c) M.E. Dry, T. Shingles, L.J. Boshoff and G.J. Oosthuizen, *J. Catal.*, 15 (1969) 190.  
(d) H. Kolbel, W.K. Muller, E. Schottle and H. Hammer, *Angew. Chem.*, 2 (1963) 554.
3. (a) R.B. Anderson, B. Sellgman, J.F. Schultz, R. Kelly and M.A. Elliot, *Ind. Eng. Chem.*, 44 (1952) 391.  
(b) M.E. Dry and G.J. Oosthuizen, *J. Catal.*, 11 (1968) 18.  
(c) M. Luo, R.J. O'Brien, S. Bao and B.H. Davis, *Appl. Catal. A Gen.*, 239 (2003) 111.  
(d) A.P. Raje, R.J. O'brien and B.H. Davis, *J. Catal.*, 180 (1998) 36.
4. C.H. Yang and J.G. Goodwin, *Can. J. Chem. Eng.*, 61 (1983) 213.
5. M.E. Dry, in *Catalysis Science and Technology.*, Chapt. 4, Vol 1, J.R. Anderson and M. Boudart (eds.), Springer-Verlag, New York, 1981, p 159.
6. K. Jothimurugesan, J.J. Spivey, S.K. Gangwal and J.G. Goodwin Jr, in *Studies in Surface Science and Catalysis: Natural Gas Conversion Vol 119.*, A.Parmaliana, D. Sanfilippo, F. Frusteri, A. Vaccari, F. Arena (ed.), Elsevier, New York, 1998, p215.
7. D.B. Bukur and C. Sivaraj, *Appl. Catal. A: Gen.*, 231 (2002) 201.
8. M.E. Dry and C.S. van Botha, *J. Catal.*, 17 (1970) 341.
9. M.E. Dry, in *Studies in Surface Science and Catalysis Vol 152: Fischer-Tropsch Technology.*, Chapt 3 and 7, A. Steynberg and M. Dry, (eds.), Elsevier, New York, 2004.
10. R.J. O'Brien, L. Xu, S. Bao, A. Raje and B.H. Davis, *Appl. Catal. A: Gen.*, 196

- (2000) 173.
11. J.L. Rankin and C.H. Bartholomew, *J. Catal.*, 100 (1986) 526.
  12. M. Luo, and B.H. Davis, *Appl. Catal. A: Gen.*, 246 (2003) 171.
  13. R.B. Anderson, in: P.H. Emmet (Ed.), *Catalysis Vol. 4.*, Van Nostrand-Reinhold, New York, 1956, p 29.
  14. H. Pichler, in *Advances in Catalysis.*, Vol 4 W.G. Frankenberg, V.I. Komarewsky and E.K. Rideal (eds.), Academic, New York, 1952, p 271.
  15. R.A. Dector and A. Bell, *J. Catal.*, 97 (1986) 121.
  16. G.B. McVicker and M.A. Vannice, *J. Catal.*, 63 (1980) 25.
  17. H.P. Bonzel and H. Krebs, *Surf. Sc.*, 94 (1980) 119.
  18. W. Ngatsoue-Hoc, Y. Zhang, R.J. O'Brien, M. Luo and B.H. Davis, *Appl. Catal. A: Gen.*, 236 (2002) 77.
  19. D.B. Bukur, D. Mukesh and S.A. Patel, *Ind. Eng. Chem. Res.*, 29 (1990) 194.
  20. D.B. Bukur, X. Lang, D. Mukesh, W.H. Zimmerman, M.P. Rosynek and C. Li, *Ind. Eng. Chem. Res.*, 29 (1990) 1588.
  21. G.C.A. Schuit and L.L. van Reijen, *Adv. Catal.*, Vol 10, Eley, Frankenburg and Komarewsky (eds.) Academic Press, New York, 1958.
  22. N. Sirimanothan, H.H. Hamdeh, Y. Zhang and B.H. Davis, *Catal. Letters.*, 82 (2002) 181.
  23. K.R.P.M. Rao, F.E. Huggins, G.P. Huffman, R.J. Gormley, R.J. O'Brien and B.H. Davis, *Energy and Fuels.*, 10 (1996) 546.
  24. J.P. Reymond, P. Mériaudeau and S.J. Teichner, *J. Catal.*, 75 (1982) 39.
  25. R.J. O'Brien, L. Xu, R. Spicer and B.H. Davis, *Energy and Fuels.*, 10 (1996) 921.
  26. M.D. Shroff, D.S. Kalakkad, K.E. Coulter, S.D. Köhler, M.S. Harrington, N.B. Jackson, A.G. Sault and A. Datye, *J. Catal.*, 156 (1995) 185.
  27. J.F. Schultz, W.K. Hall, B. Seligman and R.B. Anderson, *J. Am.Chem. Soc.*, 77 (1955) 213.
  28. V.U.S. Rao, G.J. Steigel, G.J. Cinquegrane and R.D. Srivastava, *Fuel Process.*

- Technol., 30 (1992) 83.
29. B. Jagor and R. Espinoza, Catal. Today., 23 (1995) 17.
30. G.A. Huff and C.N. Satterfield, J. Catal., 85 (1984) 370.
31. E. Iglesia, S.C. Reyes and R.J. Madon, J. Catal., 129 (1991) 238.
32. E. Iglesia, S.C. Reyes, R.J. Madon and S.L. Soled, Adv. Catal., 39 (1993) 221.
33. L.Tau, H.A. Dabbagh and B.H. Davis, Energy Fuels., 4 (1990) 94.
34. K. Herzog and J. Gaube, J. Catal., 115 (1989) 337.
35. D. Song, J. Li, J. Mol. Catal A: Chem. 247 (2006) 206.
36. M.E. Dry, G.M. Leuteritz, W.J. van Zyl, J. S. Afr. Chem. Inst. 16 (1963) 15.
37. N.O. Egiebor, W.C. Cooper, Can. J. Chem. Eng. 63 (1985) 81.

# CHAPTER 7

## LOW TEMPERATURE FISCHER-TROPSCH SYNTHESIS STUDIES OVER A SILICA SUPPORTED IRON CATALYST: EFFECT OF SILICA SUPPORT TYPE

### 7.1. INTRODUCTION

The Fischer-Tropsch (FT) reaction is a method of production of hydrocarbons from synthesis gas<sup>1,2,3</sup>. The synthetic fuels produced via FT have high cetane numbers, low sulphur and aromatic contents, and this makes them suitable for diesel engines and the environment<sup>4</sup>. The product spectrum of the FT reaction is very broad and consequently many studies have been carried out in an attempt to control and limit the product selectivity. The products most desired are those with low methane content, high olefin-to-paraffin ratio and high wax content. This control is usually achieved by modification of the catalyst, the reactor, and/or reaction conditions<sup>5,6</sup>.

Often, unsupported catalysts are preferred for the FT reaction, particularly when iron is used as the active metal, because it has been shown that the presence of a support, reduces the activity of the catalyst<sup>1,6</sup>. However, the presence of a catalyst support offers the advantage of improved catalyst stability, cost reduction because less of the metal is used, increased metal dispersion and hence increased surface area<sup>6,7</sup>.

Many researchers have studied the use of supported metal catalysts in an FT reaction. Supports such as  $\text{SiO}_2$ <sup>8</sup>, zeolites<sup>8(c),(d)</sup>,  $\text{Al}_2\text{O}_3$ <sup>8(a),(d)</sup>,  $\text{TiO}_2$ <sup>8(a)</sup>,  $\text{MgAl}_2\text{O}_3$ <sup>9</sup>, and mixtures such as  $\text{MgO/SiO}_2$ <sup>9</sup>,  $\text{TiO}_2/\text{SiO}_2$ <sup>10</sup> have been used, which all have microporous and mesoporous structures, providing an advantage of high metal dispersion. Highly ordered mesoporous silicas, such as MCM-41<sup>11</sup>, FSM-16<sup>12</sup>, SBA-

15<sup>13</sup> and HMS<sup>14</sup>, with well-defined periodic mesopores, have also been studied as catalyst supports.

The chemical nature of the support can have an influence in the orientation of the metal crystals, and the chemical nature of the support, its surface acid-base properties and its texture, and these properties can affect the reaction. It has been shown for a Co catalyst that the specific methane selectivity diminishes when the pore size increases<sup>15,16</sup>. With a microporous support, the chain growth probability and paraffin formation could be favoured since product diffusion from the catalyst pores is slow and the residence time of the formed products is enhanced. However, it can be difficult to predict the influence of the support porosity since the metal particle size can be modified by the pore size. For a silica support, the pore size and the acid properties can influence the metal-support interaction that can lead to formation of a metal-support complex, which is not easily reduced.

The sol-gel procedure can be used, especially for the synthesis of silica gel<sup>17,18,19</sup>. This process allows for the mastering of the surface area, the porosity and particle size of the silica product<sup>17,20,21</sup>. For synthesis of silica, the hydrolysis of an alkylosilane and the condensation of the formed silanol molecules can proceed simultaneously in an aqueous solution. The addition of an acid or base to the alkylosilane is preferred as it leads to a fast and complete hydrolysis. Hydrolysis in acidic medium results in low branched polymer networks with high specific surface areas, while in basic medium condensation is favoured; the siloxane networks are more branched and the specific surface areas are lower<sup>22</sup>. These types of materials have been evaluated as supports for FT catalysts, e.g silica aerogels<sup>23</sup>. Recently it has been shown that templates can be used to transfer structural information from the template to inorganic supports such that the shape (and even the chirality) of the newly formed support can now be predicted<sup>24,25</sup>. One of the procedures used to transfer shape to inorganic supports in the sol-gel process is via the use of organic crystals<sup>26</sup> and inorganic ([Pt(NH<sub>3</sub>)<sub>4</sub>(HCO<sub>3</sub>)<sub>2</sub>)]<sup>27</sup> crystals as templates. The shape of



the inorganic support formed in the synthesis has been shown to relate to the shape of the crystalline template which can be spheres and/or rods/tubes/fibres.

Supports with shaped morphologies (carbon nanotubes<sup>28</sup>, carbon nanofibers<sup>29</sup>, and silica tubes<sup>30</sup> and hollow spheres<sup>30,31</sup>) have been evaluated in the FT synthesis, and have shown remarkable activity and selectivity. However, not much literature is available on the use of silica tubes and hollow spheres as supports for an Fe FT catalyst, as to the best of our knowledge, these materials have only been reported to have been used as binders rather than as supports<sup>30</sup>. In this work we report the use of templated sol-gel synthesised silica tubes and hollow spheres as supports for a low temperature potassium promoted iron FT catalyst, and we compare them to a commercial silica support.

## 7.2. EXPERIMENTAL

### 7.2.1. Catalyst Support Preparation

Three types of silica supports were employed in this study, namely:

- (i) commercial Davisil silica Grade 645,
- (ii) silica tubes synthesized by the sol-gel method, using ammonium oxalate as template, and
- (iii) silica spheres synthesized by the sol-gel method using ammonium citrate as template.

*Preparation of Commercial Davisil silica:* The support was calcined at 250 °C in a static air furnace, for not less than 12 h, prior to catalyst preparation.

*Synthesis of silica tubes:* The silica tubes were synthesized at 25 °C. Oxalic acid monohydrate (100 g) was dissolved in a mixture of 154 ml ethanol and 154 ml deionised water. To the mixture was added 60 ml tetraethylorthosilicate, and the mixture stirred with an overhead stirrer set at 300 rpm, for 2 h. To the resulting sol, 120 ml ammonium hydroxide solution, containing 28 % aqueous ammonia, was added drop-wise with agitation of the sol for 45 min. The resulting gel was then aged for 2 h, washed with copious amounts of hot deionised water and then dried in a static air oven at 100 °C for 24 h. The dried silica gel was ground and sieved and only particles with sizes between 124 and 400 µm were collected. These were calcined in static air at 600°C for 18 h prior to impregnation with metals.

*Synthesis of silica spheres:* The synthesis of silica spheres was carried out at 25 °C. Citric acid (26 g) was dissolved in a mixture of 500 ml ethanol and 6 ml deionised water. To the mixture was added 73 g tetraethylorthosilicate, and the resulting sol kept un-agitated for 30 min. Then 240 ml ammonium hydroxide, containing 28% aqueous ammonia, was added drop-wise with agitation of the sol for 30 min. The resulting gel was then aged for 2 h, washed with copious amounts of hot deionised water and then dried in a static air oven at 100 °C for 24 h. The dried silica gel was ground and sieved and only particles with sizes between 124 and 400 µm were collected. These were calcined in static air at 600°C for 18 h prior to impregnation with metals.

### 7.2.2. Catalyst preparation

The catalysts were prepared by the incipient wetness impregnation method. Multiple-step impregnations with iron were done, and the details are tabulated in **Table 7.1**. The dry support was placed in a round bottom flask fitted to a burette and connected to a rotary evaporator. The metal ion solution was added dropwise to the dry support with rotation of the round-bottom flask. At the end of each impregnation step, the catalyst was dried on the rotary evaporator under vacuum at 90 °C.

The impregnation of the support with Fe metal was then followed by a single step impregnation of the catalysts with potassium. The procedure was done in a similar manner as that of iron. The potassium impregnated iron catalysts were then dried on a rotary evaporator under vacuum at 90 °C.

The impregnations were done so as to attain 15 % Fe and 0.5 % K (by weight) loaded catalysts.

The catalysts were calcined in a fixed bed reactor, at 250 °C (heating rate of 5 °C/min), in air with a downward flow of 45 mL/min-g support for 6.5 h.

**Table 7.1.** Details of catalyst preparation procedure.

SiO <sub>2</sub> Support	Mass support (g)	*Steps Fe	Volume solution per step (mL)	Mass Fe per step (g)	*Steps K	Volume solution (mL)	Mass K per step (g)
Davisil	100	2	106	8.83	1	106	0.494
Tubes	90	5	29	3.18	1	29	0.445
Spheres	80	2	77	7.06	1	77	0.395

\*steps= impregnation steps

### 7.2.3. Fischer-Tropsch Synthesis

Pretreatment of iron catalysts is a crucial step in an FT process as its conditions can have a huge impact on the catalyst activity and selectivity and also on the performance of the catalyst during the course of the reaction. Anderson<sup>1</sup> showed that without pre-treatment, the iron catalyst is inactive and that H<sub>2</sub>, CO or syngas can reduce an iron catalyst at 200-300 °C. It has been reported that iron catalysts activated in CO lead to an initial high catalyst activity, increased hydrocarbon

production rate, higher selectivity towards long-chain hydrocarbons, and higher product olefinicity, when compared to those activated in either syngas or H<sub>2</sub><sup>1,32</sup>. Hence CO was chosen as an activation gas in this study.

A catalyst mass of 50 g was loaded in a slurry CSTR reactor, with 300 g Ethylflo164 (C-30) oil. The catalyst was activated at 270 °C for 22 h in CO, with space velocity of 24 sL/h and a pressure of 20 bar. When the activation time was over, the reactor temperature was reduced to 250 °C, and H<sub>2</sub> was introduced, and its flow was controlled to provide a simulated synthesis gas with H<sub>2</sub>/CO ratio of 2/1, at a pressure of 20 bar, and a space velocity of 27 sL/h (WHSV 3.6 L/h (STP) per gram Fe). The reaction was run for a total of about 180 h. Gas, oil and wax samples were taken and analysed after 24-48 h intervals.

Calculations relating to the FT synthesis are explained in detail in Chapter 5.

#### **7.2.4. Extraction of used catalysts**

After the reaction, the catalysts were extracted with hot o-xylene in a soxhlet extraction apparatus, for 24-48 h, to remove wax. The extracted catalysts were then dried in a vacuum oven at 100 °C for 48 h, and then calcined in a static air furnace at 200 °C for 6 h.

#### **7.2.5. Catalyst Characterisation**

The calcined fresh catalysts were analysed for metal composition, while the calcined extracted catalysts were analysed for carbon content. The supports and the fresh and extracted used catalysts were characterised by nitrogen physisorption, scanning and transmission electron microscopes.

## 7.3. RESULTS AND DISCUSSION

### 7.3.1. Characterisation of supports

The morphology of the silica supports used is summarized in **Fig. 7.1**. SEM and TEM images of the used supports are shown in **Figs 7.2** and **7.3**. The amount of the different particles in the supports were estimated from TEM analysis. The Davisil silica support consisted entirely of undeveloped, irregularly shaped particles (shown in **Fig. 7.2a** and **7.3a**), while the templated sol-gel synthesised silica supports consisted of a mixture of morphologies; tubes, solid and hollow spheres, and undeveloped particles (**Fig. 7.2b** and **7.2c**, and **Fig 7.3b** and **7.3c**). Note that for the sake of simplicity; the templated sol-gel synthesised supports were named *based on the shape of the majority of the particles found in them*.

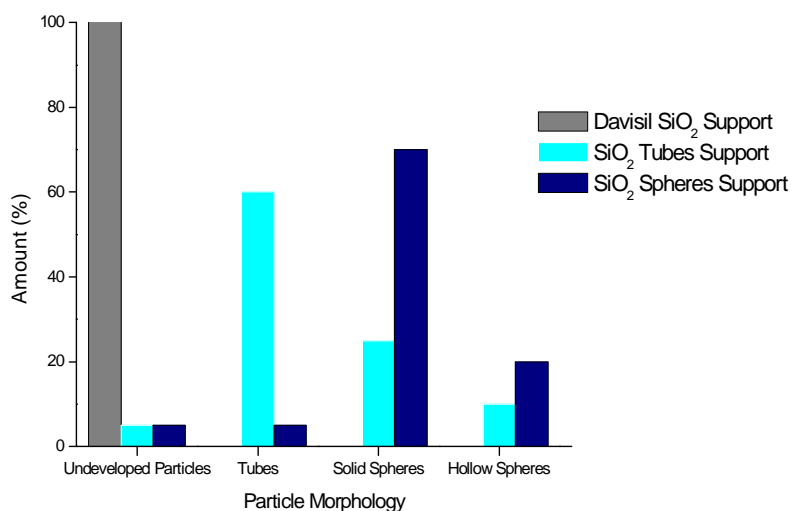


**Figure 7.1.** The distribution of morphology in the silica supports.

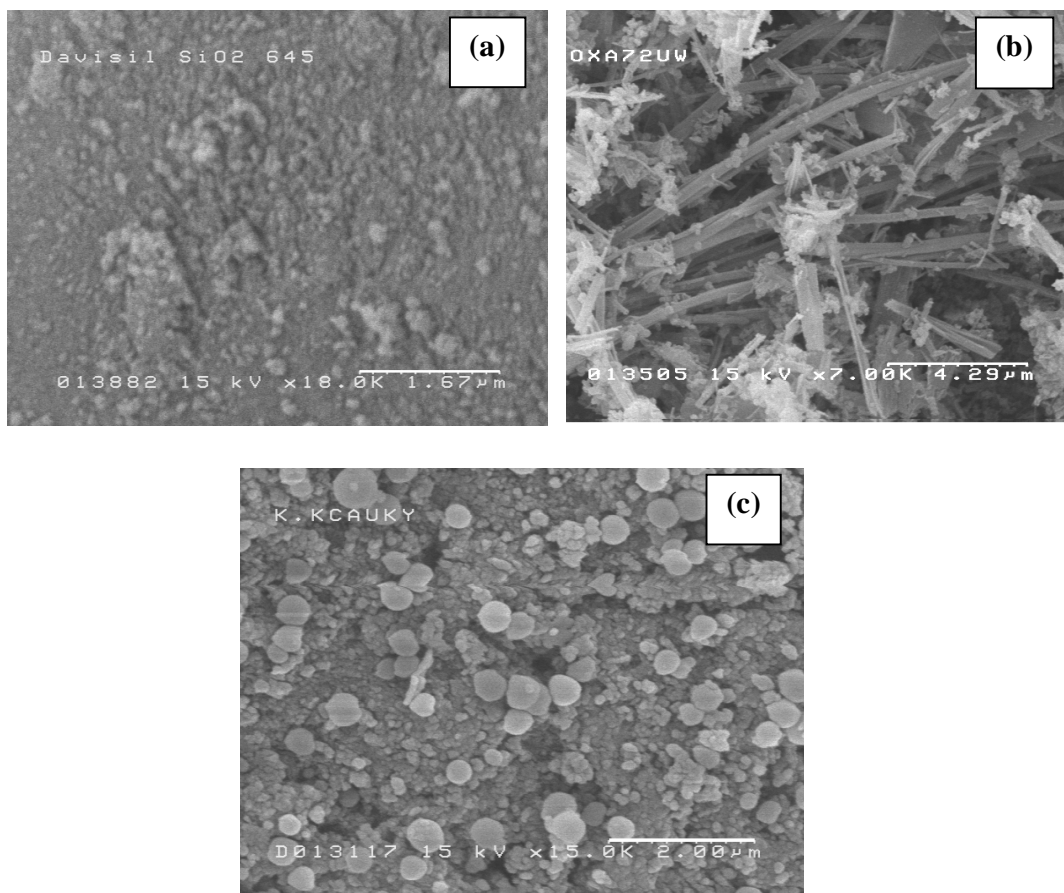


**Figure 7.2.** SEM images of the supports used. (a) commercial Davisil silica, (b) ammonium oxalate templated silica tubes, and (c) ammonium citrate templated silica spheres.

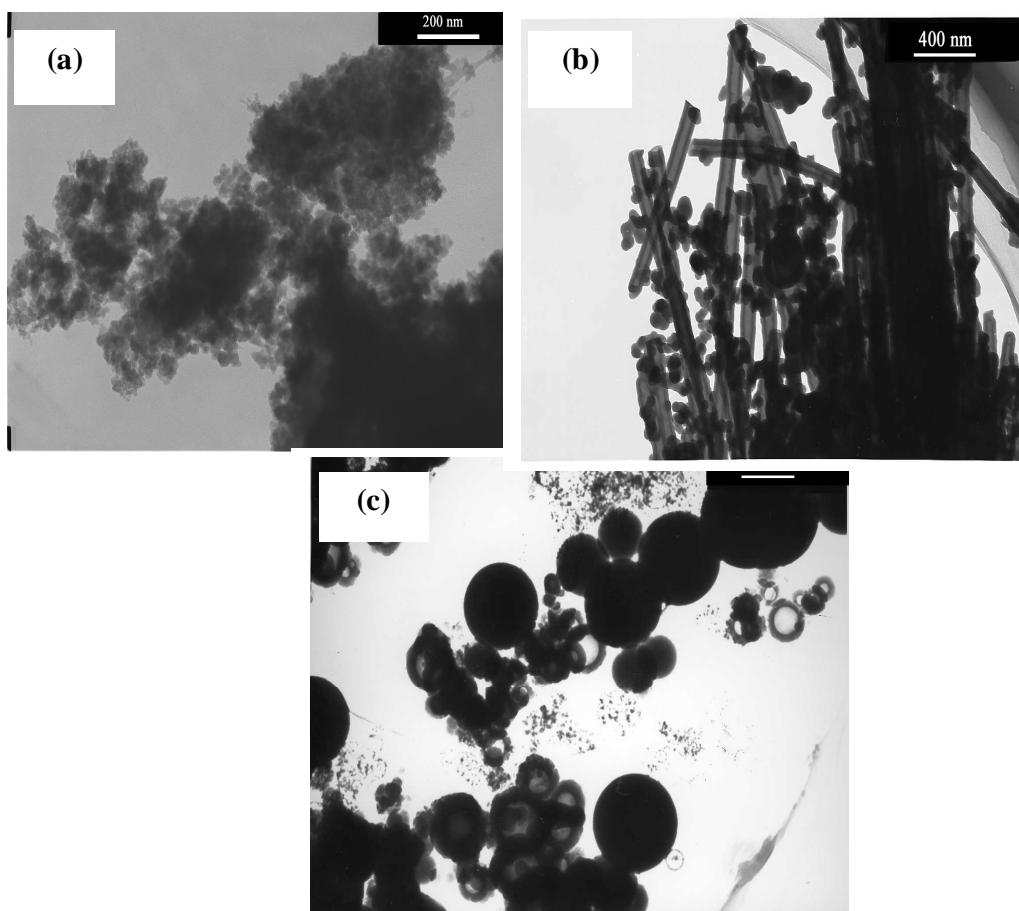


**Figure 7.3.** TEM images of the supports used. (a) commercial Davisil silica, (b) ammonium oxalate templated silica tubes, and (c) ammonium citrate.

The total surface area determined by application of the BET method from nitrogen adsorption isotherms at -196 °C were obtained for each support after calcination in air at 250 °C. The adsorption-desorption isotherms and the pore size distributions, calculated by the BJH method from the adsorption branches of the isotherms, are shown in **Fig. 7.4** and listed in **Table 7.2**. All the supports exhibited a type IV isotherm (shown in **Fig. 7.4a**), which is typical of mesoporous materials<sup>33,34</sup>. For the templated sol-gel synthesised silicas, as no limitation of adsorption at high relative pressure values was observed, their hysteresis loops were classified as of type H3,

which are characteristic of solids consisting of aggregates of plate-like particles forming slit-shaped pores of nonuniform size and/or shape<sup>33,34</sup>. The hysteresis obtained from the silica tubes support was very narrow, which implies the support contains wide-pores<sup>35</sup>. The Davisil silica exhibited a hysteresis loop with adsorption limitation at high relative pressure values, and thus the hysteresis loop was classified as of type H1, which is characteristic of solids consisting of particles crossed by nearly cylindrical channels of aggregates of spheroidal particles of uniform size and shape<sup>34</sup>. The BJH pore size distribution of the supports, **Fig 7.4b**, shows that the Davisil silica and the silica spheres supports have nearly well-defined distributions, as the majority of pores lie between 5.7 and 10 nm for the Davisil silica and between 5.9 and 10 nm for the silica spheres. Although the pore size distribution for the silica tubes shows that the support has pores with radii of 1.1 nm, it also has a wide range of pore sizes, with radii up to 80 nm.



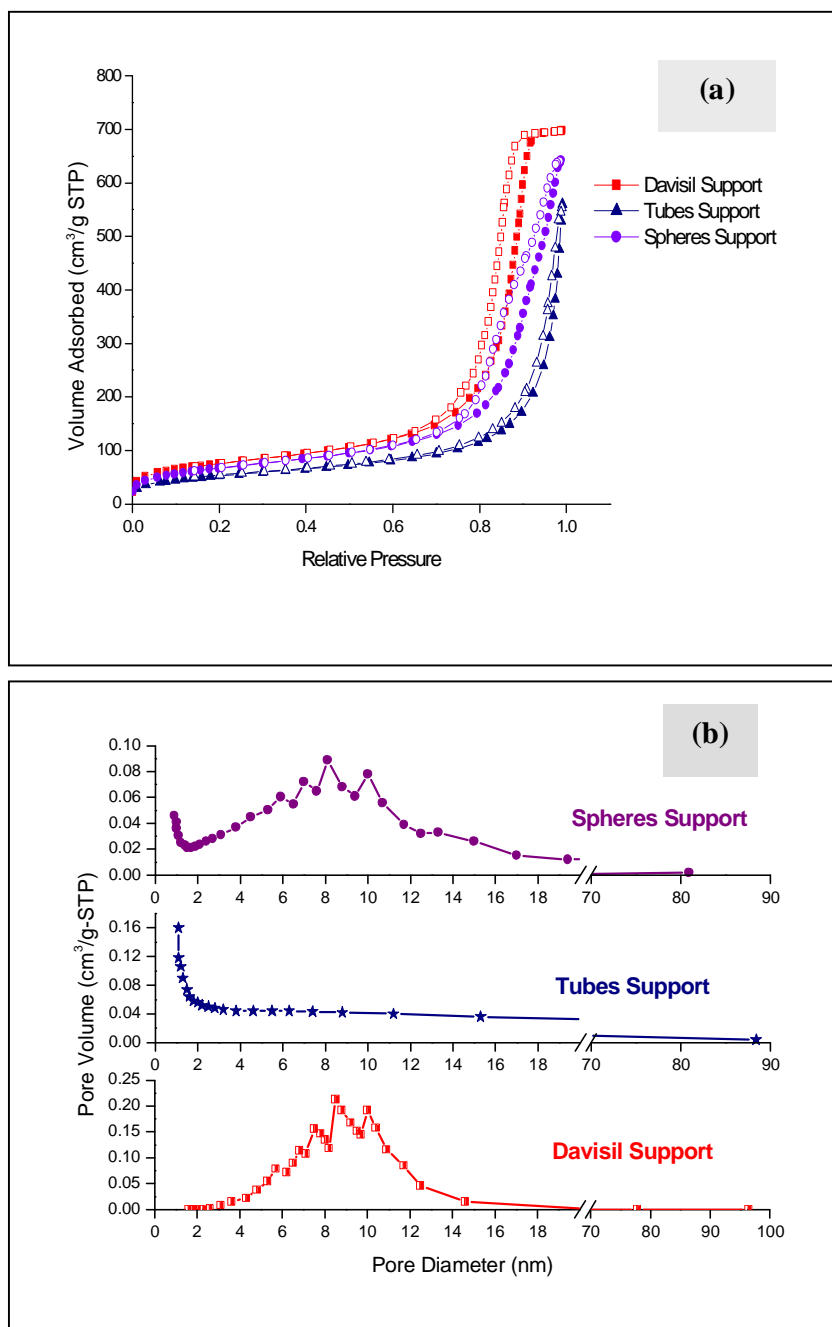


**Figure 7.4.** (a) Nitrogen adsorption-desorption isotherms (closed symbols-adsorption, open symbols-desorption) and (b) BJH pore size distributions of the supports, calculated from the adsorption arm.

It was observed that the Davisil silica support had the highest surface area and pore volume, followed by the silica spheres, with the lowest surface area and pore volume given by the silica tubes. The low surface area of the silica tubes, despite the low pore volume, can be attributed to the presence of wide pores in the wide pore size distribution of the support.

**Table 7.2.** Physisorption data of the supports.

Support	BET Surface Area	Single Point
	(m <sup>2</sup> /g)	Pore Volume (cm <sup>3</sup> /g)
Davisil Support	273	1.078
Tubes Support	109	0.347
Spheres Support	245	0.972

The prepared catalysts were analysed for actual iron and potassium contents by ICP. Table 7.3 summarises the actual analysed compositions of each catalyst employed in this work. Although the attained iron levels were lower than was intended, the potassium levels were close to those predicted from the catalyst preparation method.

**Table 7.3.** Actual metal contents of the prepared promoted iron catalysts.

Catalyst	Actual Fe content	Actual K content
	(wt%)	(wt%)
Davisil	14.49	0.48
Tubes	12.28	0.45
Spheres	12.82	0.40

### 7.3.2. Carbon monoxide conversion

The effect of silica support type on CO conversion is shown in **Fig. 7.5**. The catalysts supported on sol-gel synthesised silica gave high CO conversions, with tubes giving the highest CO conversion. Although a slight overall decrease of 4.65 and 4.30 % in the CO conversion exhibited by the Davisil silica and the silica tubes supported catalysts, respectively, was observed, a rapid decrease occurred in the case of the silica spheres supported catalyst with an overall decrease of 15.58 %, i.e. disregarding the first 48 h of the reaction.

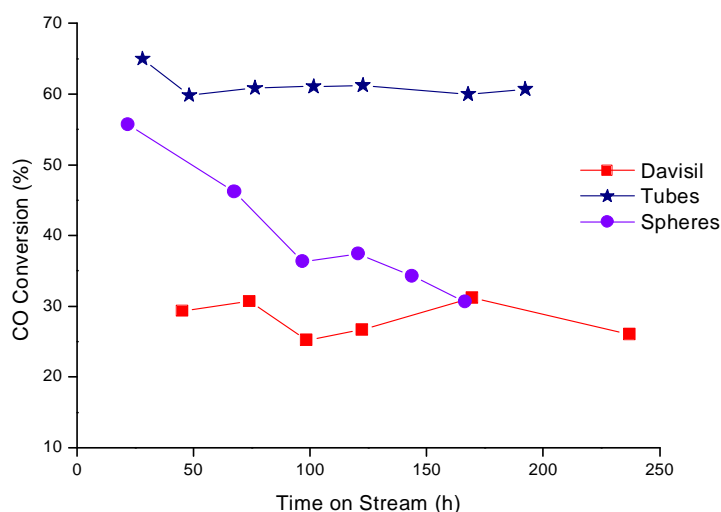


**Figure 7.5.** Effect of silica support type on carbon monoxide conversion.

During the reactions small amounts of the metal were lost from the catalyst into the product stream. **Fig 7.6** shows the cumulative amount of Fe found in the liquid products sampled during the reaction. It shows a rapid increase in metal loss in the first 24-48 h, followed by a steady increase afterwards. The former observations correspond with the high CO conversion observed in the first 24-48 h of the reaction with all the catalysts. It has been shown that unsupported iron catalysts generally give higher CO conversions and FT activity than supported catalysts<sup>7(e)</sup>. Thus the

high CO conversion observed at the beginning of the reaction could be due to the loosely bound iron particles, which acted as unsupported iron catalyst, and once these particles were removed from the reactor, the catalyst system then became more or less stable, except for the silica spheres supported catalyst. It is clear in the figure that the amount of Fe lost from the catalysts during the reaction is comparable for all three catalysts, thus the rapid decline in activity observed with the silica spheres supported catalyst was clearly not due to loss of the metal, as the loss of metal occurred at a similar rate to that of the other two catalysts.

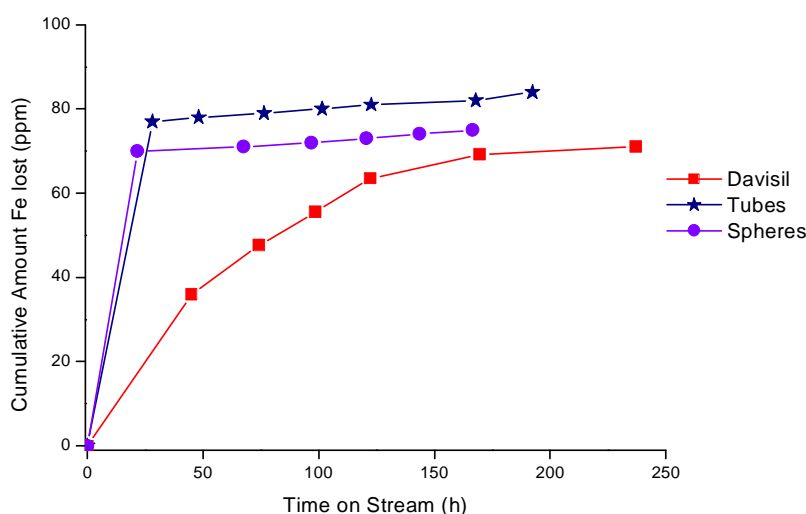


**Figure 7.6.** Cumulative amount of iron lost during reaction.

### 7.3.3. Reaction Rates

The water-gas shift (WGS) reaction is an important reaction in an FT process when an iron catalyst is employed. **Fig. 7.7** shows the FT reaction rate (**Fig. 7.7a**) and the WGS reaction rate (**Fig. 7.7b**) of the catalysts as a function of time on stream. The catalysts supported on templated sol-gel synthesised silicas gave higher FT and WGS reaction rates than the Davisil silica supported catalyst. The high reaction rates observed with the former correlate with their high CO conversions. A slight decrease

in the reaction rates of all the catalysts, with time on stream, was observed, and this is tabulated in **Table 7.4**. From the table it is clear that the decrease in the WGS activity of all the catalysts occurred more rapidly than that of their FT activity. This decrease is responsible for the decrease in the CO conversion observed with the catalysts. The decrease in the rates of the FT and WGS reactions could be due to carbon deposition and/or sintering of the catalysts, as will be described later.

It has been shown that iron-containing catalysts are not stable during FT synthesis, but are converted into carbides by the feedgas<sup>32(a),36</sup>. Also carbide species<sup>32(b),37</sup> are believed to be the active species for the FT reaction while metallic Fe<sup>38</sup> and Fe<sub>3</sub>O<sub>4</sub><sup>39,40</sup> are believed to be more effective catalytic sites for the WGS reaction than Fe carbides. Thus the different rates of decline of the FT and the WGS reactions could be due to formation of carbides, which should enhance the FT activity of the catalyst, while a corresponding decrease in iron oxides and/or metallic iron should decrease the WGS activity of the catalyst. Although ideally the FT activity of the catalysts should have been enhanced, it was counteracted by carbon deposition and sintering of the catalysts (to be shown later). Hence a decrease in the FT activity was observed instead and its rate of decline was smaller than that of the WGS reaction.

**Table 7.4.** Overall change in FT reaction rate, WGS reaction rate and catalyst efficiency with time on stream.

<b>Catalyst</b>	<b>Overall Decrease in FT Reaction Rate (mol/h-gFe)</b>	<b>Overall Decrease in WGS Reaction Rate (mol/h-gFe)</b>	<b>Overall Increase in Catalyst Efficiency (%)</b>
Davisil	$17 \times 10^{-2}$	$20 \times 10^{-2}$	2.51
Tubes	$14 \times 10^{-2}$	$19 \times 10^{-2}$	2.30
Spheres	$29 \times 10^{-2}$	$55 \times 10^{-2}$	6.80

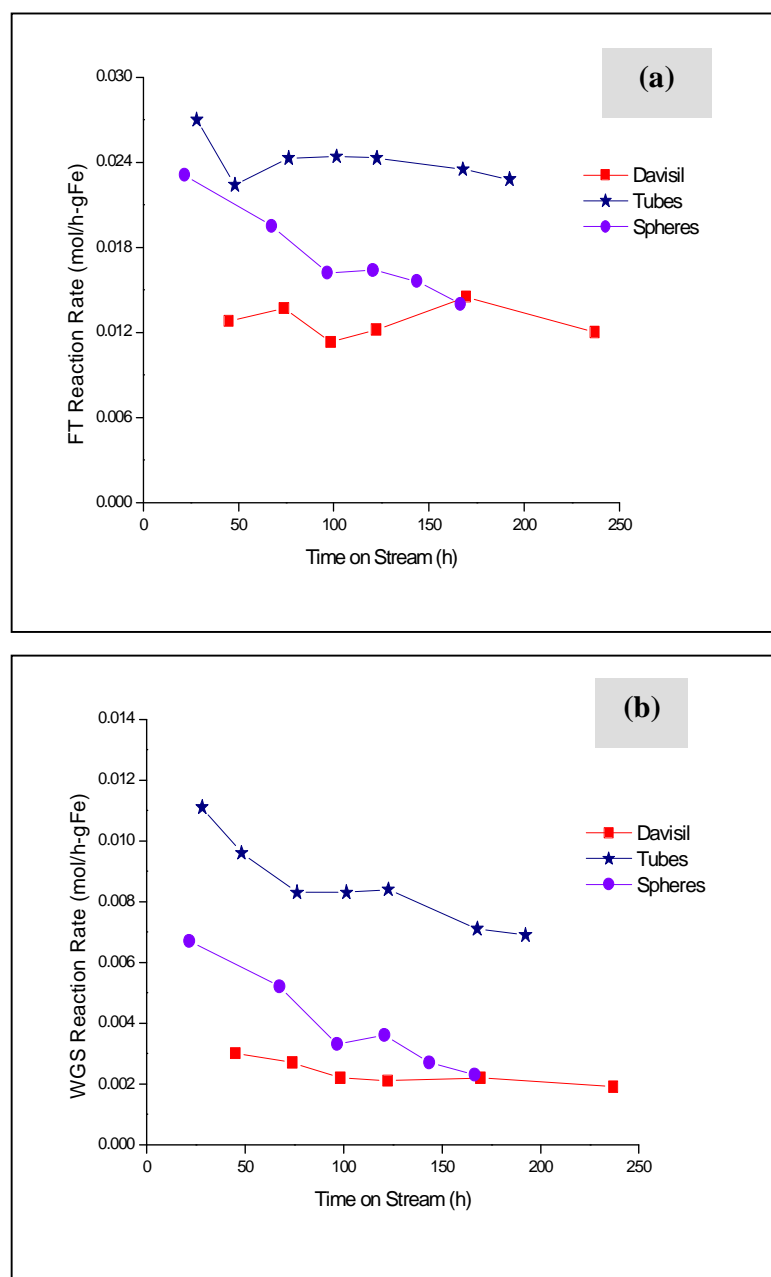


**Figure 7.7.** The effect of silica support type on the rate of the (a) Fischer-Tropsch reaction and (b) water gas shift reaction.

The catalyst efficiency, which is proportional to the ratio of the FT reaction rate to that of the WGS reaction rate, of all the catalysts under study (shown in **Fig. 7.8**) shows that, although the Davisil silica supported catalyst gave the lowest CO conversion, it was more efficient in producing hydrocarbons compared to the sol-gel synthesised silica supported catalysts, while the silica tubes supported catalyst showed the lowest catalyst efficiency despite its high CO conversion. Also, the catalyst efficiency exhibited by all the catalysts showed a slight increase (shown in **Table 7.4**) with time on stream. This increase was related to the higher rate of decline in WGS activity compared to FT activity observed in all the catalysts.

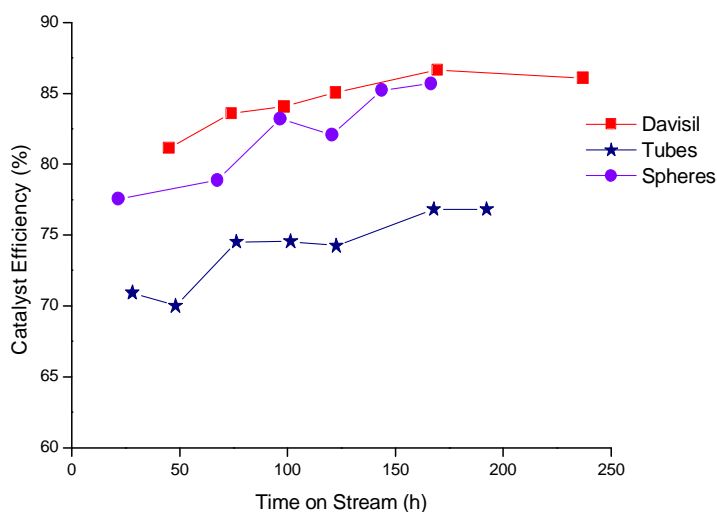


**Figure 7.8.** The effect of silica support type on the catalyst efficiency for production of hydrocarbons.

#### 7.3.4. Carbon dioxide selectivity

In agreement with the catalyst efficiency that indicate the production of hydrocarbons, the CO<sub>2</sub> selectivity profile of the catalysts (**Fig. 7.9**) clearly shows that the sol-gel synthesised silica supported catalysts had higher selectivity towards CO<sub>2</sub>



production compared to the Davisil silica supported catalyst, with the highest CO<sub>2</sub> selectivity obtained with the silica tubes supported catalyst.

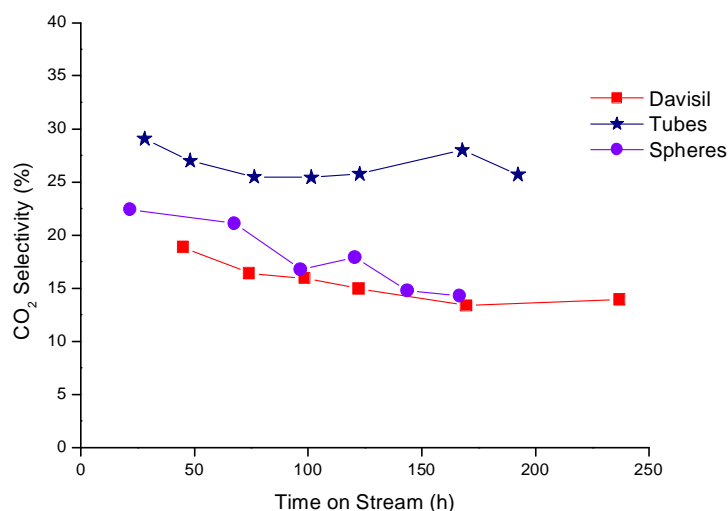


**Figure 7.9.** The effect of support type on carbon dioxide selectivity.

### 7.3.5. Methane Selectivity

The catalyst selectivity towards methane is shown in **Fig. 7.10**. Although there was no major difference in the selectivity towards methane shown by the three catalysts employed, it is clear that the templated sol-gel synthesised silica supported catalysts produced more methane than the Davisil silica supported catalyst, with the tubes producing the highest selectivity towards methane.

Two factors that can influence catalyst selectivity towards methane are the support acidity and the support/catalyst pore size. In their study of CO<sub>2</sub> chemisorption on alkali promoted SiO<sub>2</sub> supported iron catalyst; Dry and Oosthuizen<sup>41</sup> have shown that methane selectivity decreased with an increase in the surface basicity of the catalyst. The surface basicity of a catalyst depends on the acidity/basicity of the support and the level of alkali promotion. However NH<sub>3</sub>-TPD analysis of the supports, shown in **Fig. 7.11**, showed no distinguishable detail in their acidic sites.

It has been shown for a cobalt catalyst that the catalyst selectivity towards methane decreases with an increase in the catalyst pore size<sup>15,16</sup>. Since the silica tubes support showed a wide pore size range, it was expected to have a low methane selectivity; however, this was not the case. Thus the high methane selectivity exhibited by this catalyst can be correlated to its high CO conversion, and not its acidity or pore size.

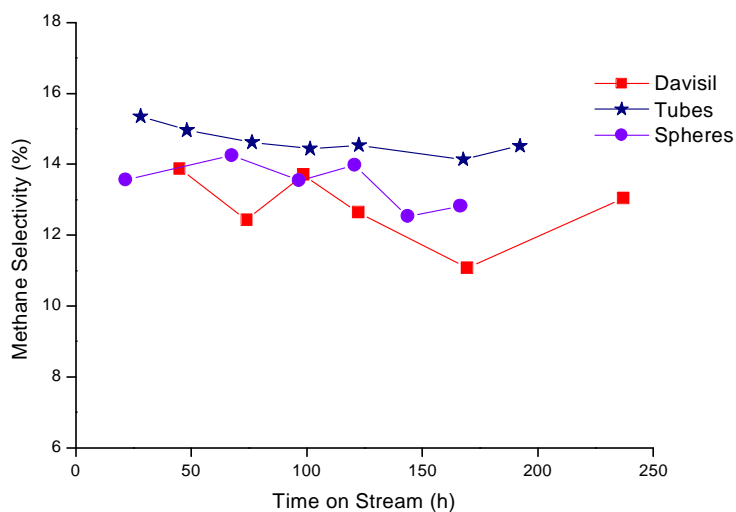


**Figure 7.10.** Effect of silica support type on methane selectivity.

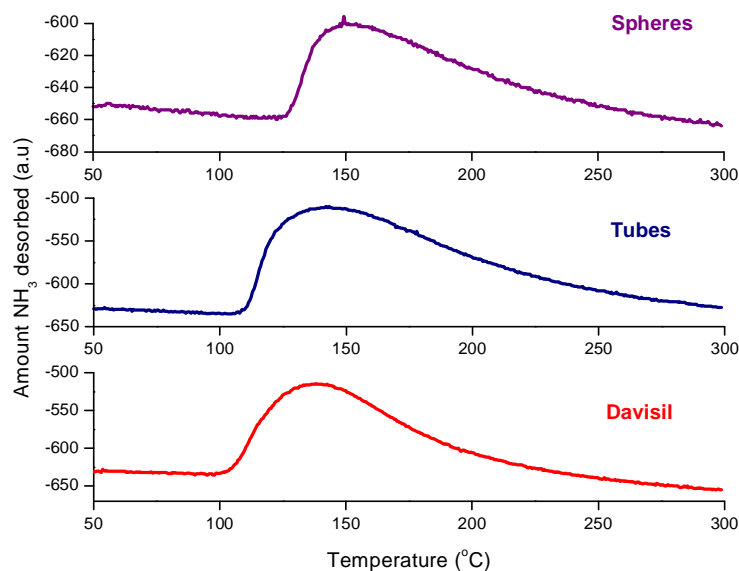


**Figure 7.11.** Ammonia-TPD of the used supports

### 7.3.6. Product Distribution and Selectivity

The effect of the catalyst support on the product distribution is shown in **Fig. 7.12**. Due to low formation of reactor heavy wax (C<sub>19+</sub>), which could not be sampled during the reaction, only distributions of hydrocarbons of carbon number up to 18 are shown in the figure. The reactor contents were analysed at the end of the reaction to determine the resultant percentage of C<sub>19+</sub> hydrocarbons in C<sub>30</sub> oil and the percentages are shown in **Table 7.5**. When compared to the templated sol-gel synthesised silica supported catalysts, it was observed that the Davisil silica supported catalyst showed the lowest selectivity towards light gases (C<sub>1</sub>-C<sub>4</sub>), and a corresponding high selectivity towards long chain hydrocarbons (C<sub>12+</sub>). In agreement with this observation, **Table 7.5** shows that the Davisil silica supported catalyst produced the highest amount of reactor heavy wax (C<sub>19+</sub>) when compared to the other catalysts.

Some researchers in their study of silica and alumina supported cobalt catalysts found an increase in FT reaction rate, a decrease in methane selectivity, and an increase in selectivity towards long chain hydrocarbons with an increase in support/catalyst pore diameter<sup>42,43</sup>. However, other researchers<sup>44,45</sup> found an increase in support/catalyst pore size to lead to an increase in methane selectivity and a corresponding decrease in longer chain hydrocarbons; the authors attributed this to the longer residence time of olefins in narrow pores leading to olefin readsorption, which eventually leads to chain propagation. The differences in these findings could have been brought about by the different catalyst systems and reaction conditions used.

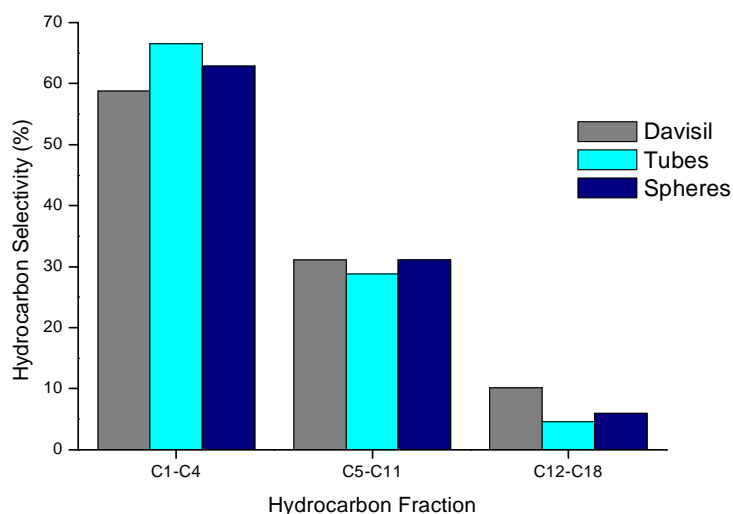


**Figure 7.12.** Effect of silica support type on hydrocarbon product distribution.

**Table 7.5.** Amount of C<sub>19+</sub> hydrocarbons in reactor contents at the end of the reaction.

Catalyst	Amount C <sub>19+</sub> (weight %)
Davisil	21.05
Tubes	15.36
Spheres	18.31

The hydrocarbon product distribution is illustrated in **Fig. 7.13** in the form of an Anderson-Shultz-Flory (ASF) plot. All three catalysts showed a similar ASF plot, so only the one obtained from the silica spheres supported catalyst is shown. It shows that the total product distribution for the catalysts employed in this study cannot be described by a uniform chain growth probability factor  $\alpha$ , which is similar to work reported by previous researchers<sup>36(a),46,47</sup>. The deviation of C<sub>20+</sub> products from the second slope could be due to hold-up of these components in the reaction slurry, as was previously observed by others<sup>36(a)</sup>, as chromatographic analysis of the reactor hold-up liquid showed the presence of products with C<sub>19</sub>-C<sub>60</sub> carbon numbers. These products made up about 15-21 % of the total reactor hold-up liquid weight, depending on the catalyst used (see **Table 7.5**), the rest being C<sub>30</sub> start-up oil.

The effect of the silica support type on the chain growth probability is presented in **Table 7.6**. The Davisil silica supported catalyst gave the highest chain growth probabilities compared to the templated sol-gel synthesised silica supported catalysts. Furthermore, for all three catalysts, the chain growth probability obtained for C<sub>13</sub>-C<sub>20</sub> products was higher than for lower molecular weight products C<sub>5</sub>-C<sub>12</sub>. This is in agreement with previous findings by other researchers on iron catalysts<sup>36(a),47</sup>. The occurrence of two distinct chain growth probabilities is due to alkene-reincorporation, as was explained in Chapter 6.

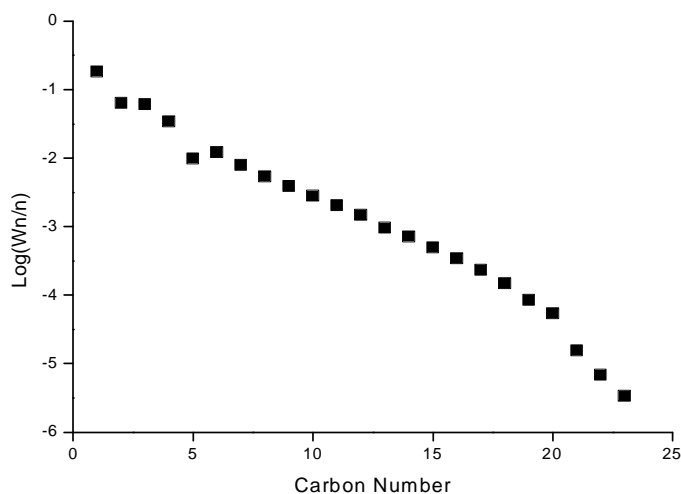


**Figure 7.13.** The Anderson-Schulz-Flory plot of a silica spheres supported potassium promoted iron catalyst.

The selectivity of the catalysts towards olefins is shown in **Table 7.6**. As is usually found with iron FT catalysts<sup>6,32(c),36(a),47,48</sup>, for all three catalysts the selectivity towards olefins increased from C<sub>2</sub> to C<sub>4</sub>, reached a maximum at C<sub>4</sub>, and then decreased with increasing carbon number. The deviation from the linear olefin content distribution in **Table 7.6** for C<sub>5</sub> is due to instrumental error. No major differences in the olefin selectivity exhibited by all three catalysts were observed.

**Table 7.6.** Effect of silica support type on chain growth probability and olefin selectivity.

		Davisil	Tubes	Spheres
<b>Chain growth Probability</b>				
	$\alpha_1$ (C <sub>5</sub> -C <sub>12</sub> )	0.766	0.644	0.709
	$\alpha_2$ (C <sub>13</sub> -C <sub>20</sub> )	0.771	0.703	0.725
<b>Olefin selectivity* (%)</b>				
	C <sub>2</sub>	27	23	26
	C <sub>3</sub>	72	71	70
	C <sub>4</sub>	94	71	70
	C <sub>5</sub>	64	29	26
	C <sub>6</sub>	62	63	61
	C <sub>7</sub>	58	59	57
	C <sub>8</sub>	53	54	51
	C <sub>9</sub>	49	49	47
	C <sub>10</sub>	46	48	45
	C <sub>11</sub>	42	43	41
	C <sub>12</sub>	38	39	38
	C <sub>13</sub>	34	35	33
	C <sub>14</sub>	30	32	29
	C <sub>15</sub>	25	28	25

### 7.3.7. Characterisation of catalysts

#### *Nitrogen Physisorption*

The pore size distributions of the catalysts, calculated by the BJH method from the adsorption arm of their isotherms, are shown in **Fig. 7.14**. It shows the catalyst pore size distributions were similar to those of the supports; the silica tubes supported catalysts showed a wide pore size distribution (as explained in the nitrogen

physisorption of the supports), while the silica spheres and Davisil silica supported catalysts showed an almost well-defined pore size distribution, with the majority of pores ranging between 8 and 10 nm.

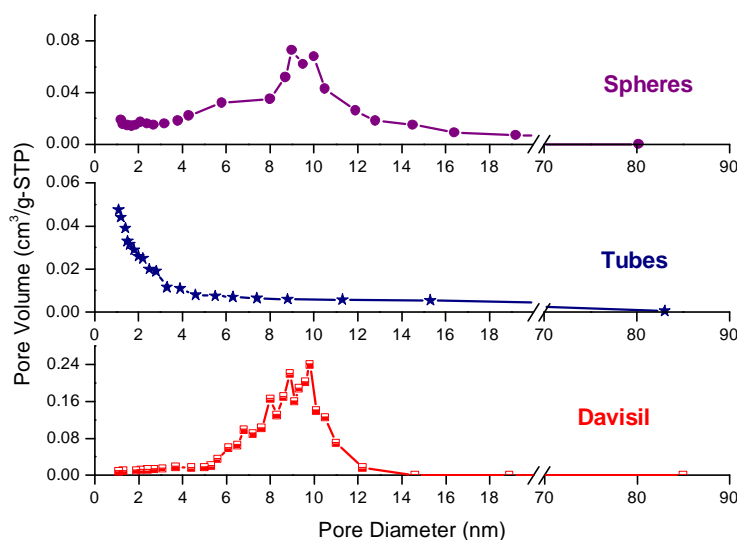


**Figure 7.14.** BJH pore size distributions of fresh catalysts calculated from the adsorption arm.

The surface areas and pore volumes of the supports, and the fresh and used catalysts are presented in **Table 7.7**. It was observed that the surface areas and pore volumes of all three supports decreased after addition of iron and potassium, and this decrease was more pronounced for the narrow pore supports (silica spheres and Davisil silica). As explained in the previous two chapters, addition of iron to a support leads to pore blocking while promotion of an iron catalyst with potassium promotes crystal growth of the iron particles, resulting in reduced surface areas of the support<sup>41,49</sup>.

The surface areas of all three catalysts were found to have decreased markedly after the reaction, and the pore volumes of both the Davisil silica and silica spheres supported catalysts decreased, while that of the silica tubes supported catalysts



increased. The pore volumes of the catalysts were expected to decrease after the reaction; thus it is not clear why the silica tubes catalyst behaved differently. The decrease in surface area of the catalysts could be due to sintering during the reaction.

**Table 7.7.** Physisorption data and carbon content of the fresh and used catalysts.

Catalyst or Support	Fresh Catalyst		Used Catalyst		C/Fe ratio
	BET Surface Area (m <sup>2</sup> /g)	Single Point Pore Volume (cm <sup>3</sup> /g)	BET Surface Area (m <sup>2</sup> /g)	Single Point Pore Volume (cm <sup>3</sup> /g)	
Davisil Support	273	1.078	-	-	-
Fe/K/Davisil	243	0.758	208	0.745	0.426
Tubes Support	109	0.347	-	-	-
Fe/K/Tubes	100	0.267	79	0.288	0.153
Spheres Support	245	0.972	-	-	-
Fe/K/Spheres	169	0.570	124	0.528	0.167

### *Catalyst Morphology*

**Figure 7.15** shows the TEM images of the Davisil silica supported catalyst, before and after the reaction. As the Davisil silica support was made entirely of small undeveloped particles, these particles could not be easily distinguished from the iron nanoparticles, it seemed as if the iron particles were well mixed with the support. As the iron nanoparticles were not easily distinguishable from the rest of the support, they were assumed to have an almost spherical shape, similar to that of the support, (**Fig. 7.15a**). After the reaction, although no clear evidence of damage to the support was found, localised formation of dark spots was observed. The latter could be agglomerations of the iron nanoparticles.

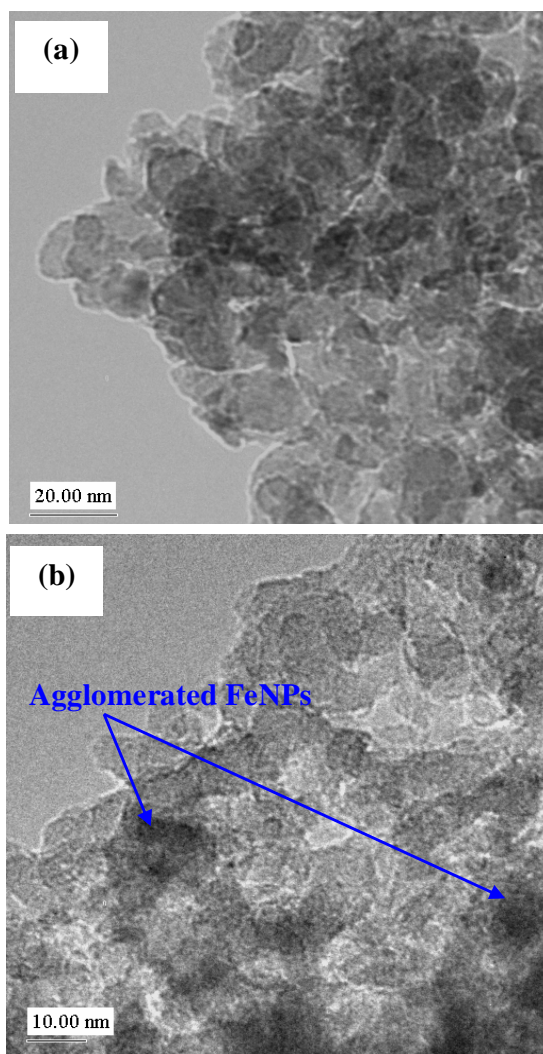


**Figure 7.15.** HRTEM images of (a) fresh and (b) used Davisil silica supported catalyst.

The TEM images of the silica tubes supported catalyst are shown in **Fig. 7.16**. On this catalyst, each iron nanoparticle had a needle-like shape, with lengths of about 10-12 nm. These particles connected end-to-end to each other to form ‘columns’, with the ‘columns’ lying close and parallel to each other (**Fig. 7.16b**). The shape and arrangement of these iron nanoparticles seemed to ‘mimic’ the shape of the dominant particle morphology of the support; i.e. tubes. These groups of iron nanoparticles

were found to occur both in the cavities of the tubes and outside the tubes. **Fig. 7.17** shows HRTEM images of the used silica tubes supported catalyst. The iron nanoparticles were found to have lost their needle-like shapes and the ‘column’ arrangement (**Fig. 7.17a** and **7.17b**), and were agglomerated with localised formation of elongated, denser regions. However, the silica tubes still remained undamaged after the reaction, **Fig. 7.17c**)

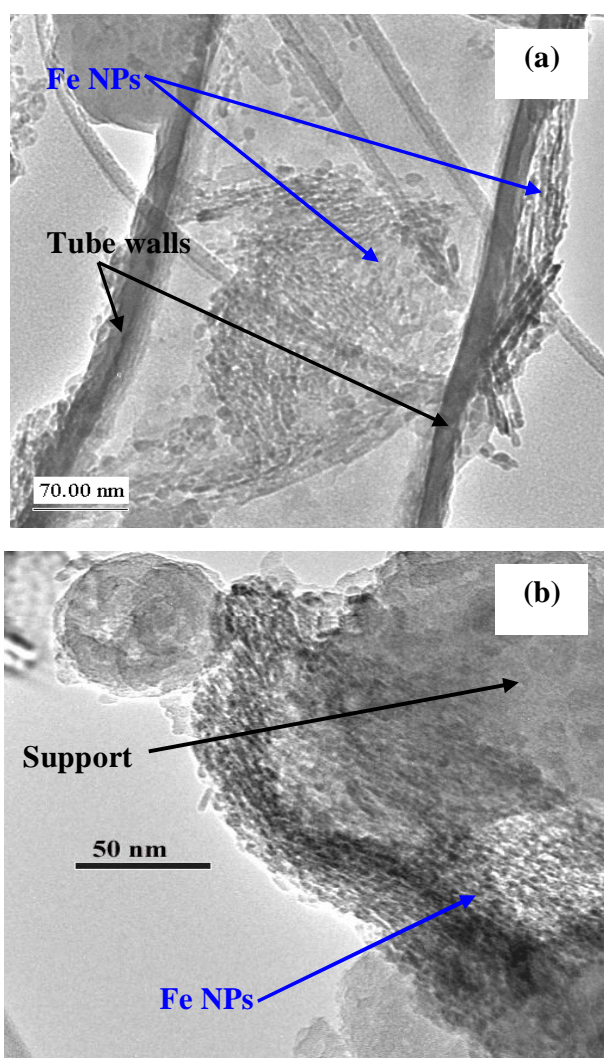


**Figure 7.16.** HRTEM images of a fresh silica tubes supported iron catalyst, showing (a) Fe nanoparticles occurring both inside and outside a silica tube, and (b) column arrangements of needle-like Fe nanoparticles.

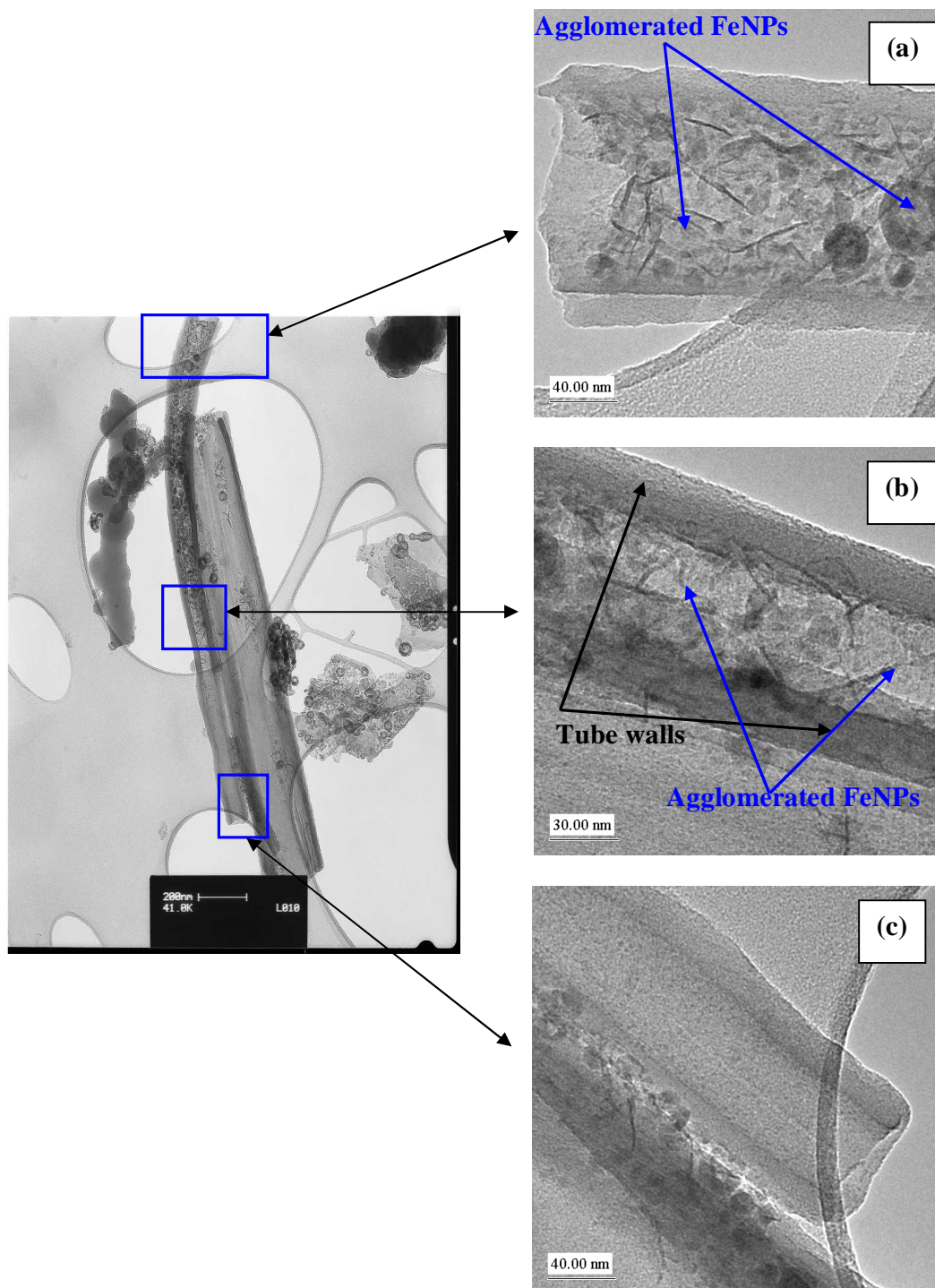


**Figure 7.17.** HRTEM images of a used silica tubes supported catalyst, (a) showing agglomerated Fe NPs inside a tube, (b) agglomerated Fe NPs some occurring outside the tube walls, and (c) silica tube not damaged during the reaction.

The TEM images of the silica spheres supported catalyst are shown in **Fig. 7.18**. Similarly to the silica tubes supported catalyst, the iron nanoparticles were found to be on the surface of the support (**Fig. 7.18a**). These had a semi-hexagonal shape, with diameters of about 5-7 nm, and were joined to each other in a chain-like arrangement (**Fig. 7.18b**). After the reaction, the support morphology was found not to have been altered (**Fig. 7.18c**). However, the iron nanoparticles were found to have lost their semi-hexagonal shape and chain-like arrangement (**Fig. 7.18d**), and were agglomerated with localised formation of denser particles.

For all the three catalysts, potassium particles could not be identified from HRTEM-EDX, which implies that they were too small and/or finely dispersed on the catalyst support.



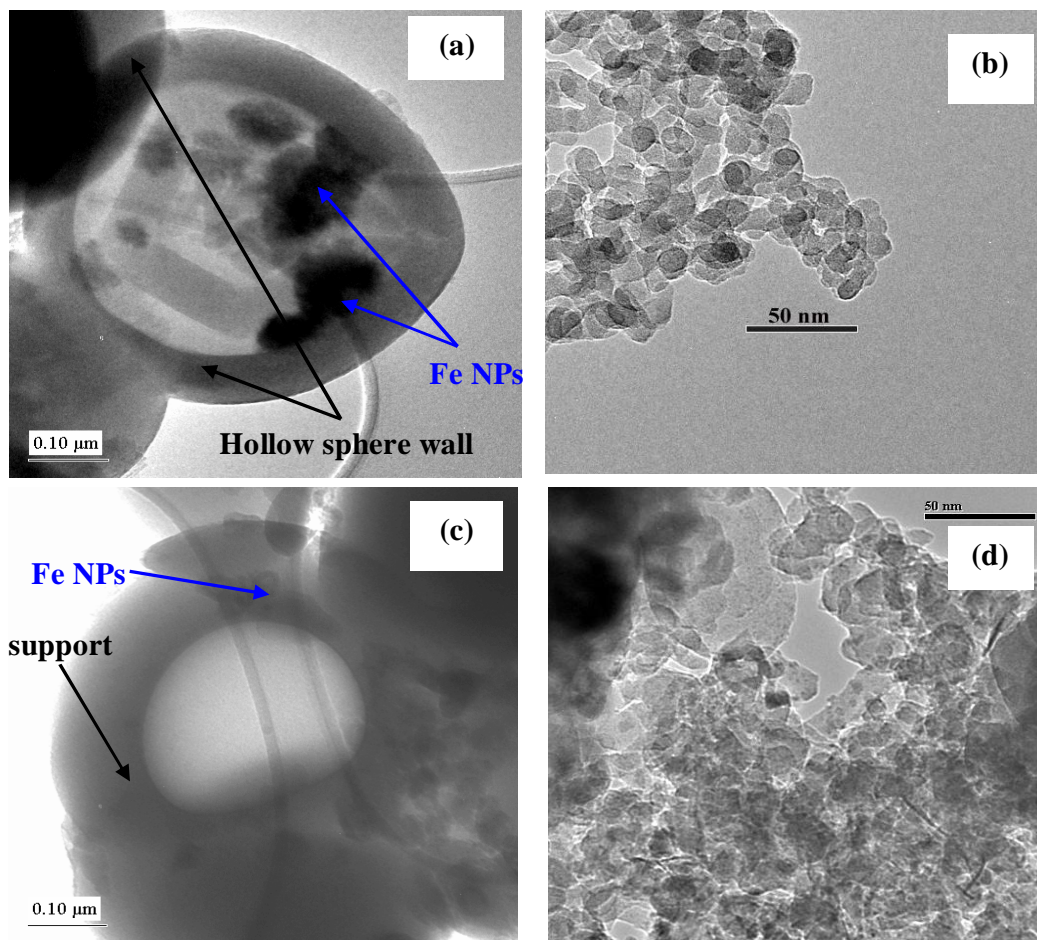


**Figure 7.18.** HRTEM images of a fresh and used silica spheres supported iron catalyst. Fresh catalyst (a) Fe nanoparticles on spheres, and (b) high magnification image showing semi-hexagonal Fe nanoparticles, Used catalyst (c) silica sphere still intact, and (d) high magnification image showing disorganised and agglomerated Fe nanoparticles.

For the templated sol-gel synthesised supported catalysts, agglomeration of some of the iron nanoparticles after the reaction led to formation of ‘doughnut shaped’ particles, shown in **Fig. 7.19**. The core and the shell of these particles were found to be made of crystalline iron phases, determined by EDX, and these particles were found to be surrounded by a thin layer of amorphous carbon, as shown in **Fig 7.19b**.

Although these particles were not observed in the Davisil silica supported catalyst, these could have been formed and mixed up with the support, as even the iron nanoparticles prior to the reaction could not be singled out from the support.

These ‘doughnut shaped’ particles are similar to those obtained by other researchers in their studies of potassium promoted precipitated iron catalysts after FT synthesis. In their study, Shroff and coworkers<sup>37,50</sup> found iron carbide cores surrounded by a layer of polycrystalline carbon in a passivated catalyst, while magnetite cores with small amounts of iron carbide embedded in them and surrounded by polycrystalline carbon were found in unpassivated catalysts. Davis<sup>51</sup> observed the presence of magnetite particles surrounded by graphitic carbon after 28 h on stream. He also found particles containing mixtures of magnetite and iron carbide surrounded by graphitic carbon after 461 h on stream, but it is not clear if these samples were passivated or not. Graham *et al*<sup>52</sup>, in their HRTEM/EDX study of a precipitated iron catalyst, observed Fe carbide cores surrounded by a layer of a mixture of magnetite and hematite which was subsequently surrounded by a layer of amorphous carbon, they reported that their sample was removed from the reaction after 168 h and was kept under an inert atmosphere after its removal, through wax extraction until it was analysed. Dry<sup>53</sup> found that finer catalyst particles consisted solely of small iron carbide particles embedded in a matrix of carbon, whereas larger catalysts particles consisted of cores of magnetite surrounded by a mixture of iron carbide and carbon, again, it is not clear if these samples were passivated or not. Dry explained the formation of the magnetite cores in the bigger particles as arising from the reaction of the iron with the synthesis gas. As the syngas entered the porous iron nanoparticles the FT reaction occurred, which formed water as one of the products, and the deeper the gas penetrated into the particle, the more the oxidising residual gas became. Thus the cores of the larger particles could be oxidised while the outer layers remain in a reducing atmosphere. Differences in the iron phases observed after the FT reaction by these researchers were suggested to arise from the differences in the catalyst particle sizes, the syngas composition and flow rate, and also the catalyst

passivation procedures. Thus, some of the particles could have been oxidised before they were analysed. In our case, the catalysts were not passivated at all after the reaction.

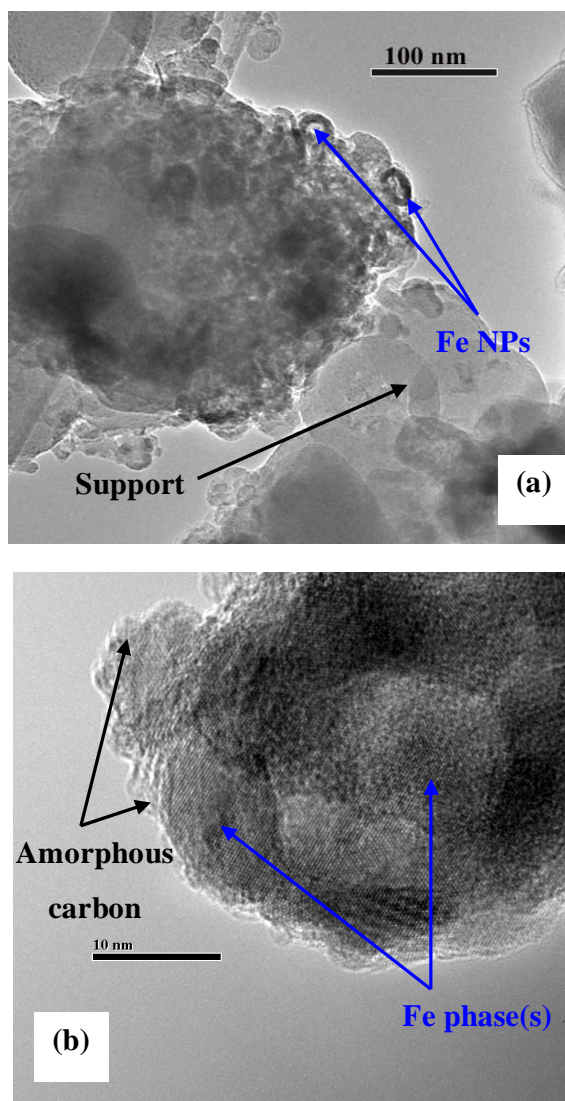


**Figure 7.19.** HRTEM image showing (a) agglomerated Fe nanoparticles, and (b) a high magnification of a 'doughnut shaped' particle.



Even though the doughnut shaped iron particles were not observed in the Davisil silica supported catalyst, the catalyst was found to contain some particles of amorphous carbon after the reaction, as shown in **Fig. 7.20**.

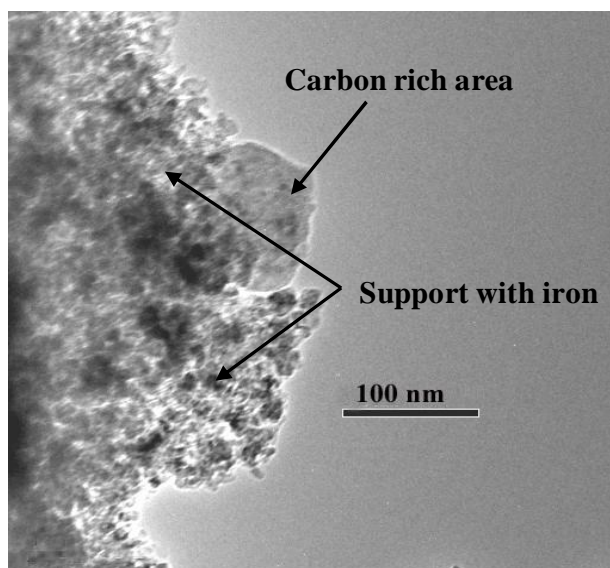
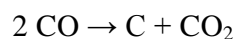


**Figure 7.20.** HRTEM image of Davisil silica supported catalyst after FT synthesis, showing amorphous carbon particle.

Elemental analysis of all three catalysts after the reaction (**Table 7.7**) showed that the Davisil silica-supported catalyst contained the highest amount of carbon, while the silica tubes supported catalyst contained the lowest carbon amount. Carbon deposition on a catalyst during FT reaction occurs by the Boudouard reaction:



The presence of alkali on a catalyst is known to increase the intrinsic rate of carbon deposition in the FT reaction<sup>48</sup>. However, in the presence of silica, the rate of carbon deposition is decreased due to the reduced basicity of the alkali, the latter resulting from metal-support interactions.

Despite the sintering of the catalysts observed after reaction, the templated sol-gel silica supports showed remarkable stability, as no evidence of structural damage was observed, despite the harsh conditions encountered by the catalyst during the reaction, i.e. high temperature and mechanical force from the impeller blades.

### *Catalyst Reduction*

The influence of catalyst support type on the reduction behaviour in carbon monoxide of a silica supported iron catalyst was studied by temperature programmed reduction (TPR), see **Fig 7.21**. The occurrence of multiple reduction peaks indicates the presence of a number of reducible species. The reduction profiles obtained from the Davisil silica and the silica spheres supported catalysts are similar to those obtained by Jin and Datye<sup>54</sup> in their reduction studies of a Stöber spheres-supported iron catalyst. The first peak (which for the Davisil silica and the silica spheres supported catalysts, occurs around 250 and 270 °C, respectively) is due to an  $\text{Fe}^{3+} \rightarrow \text{Fe}^{2+}$  transformation. The second peak (which occurs at 330 °C for the silica spheres supported catalyst, and appears as a shoulder around 300 °C for the Davisil silica supported catalyst) can be attributed to the transformation of  $\text{Fe}^{2+}$  to  $\chi$ - and  $\epsilon$ -carbides. However, for the silica tubes-supported catalyst, the  $\text{Fe}^{3+} \rightarrow \text{Fe}^{2+}$  and  $\text{Fe}^{2+}$  to  $\chi$ - and  $\epsilon$ -carbides transformations occurred almost simultaneously and could not be separated, as these reductions appeared as a single broad peak centered around 320 °C. For all three catalysts two humps occurred between 450 and 550 °C and between 650 and 750 °C. During the reduction of an iron catalyst, the transformation of  $\chi$  to  $\theta$ -carbide (cementite) and  $\alpha$ -Fe should be expected to occur between 400 and 500 °C. However, these transformations do not involve carbon consumption. These two reactions humps are due to carbon deposition by the Boudouard reaction<sup>54</sup>.

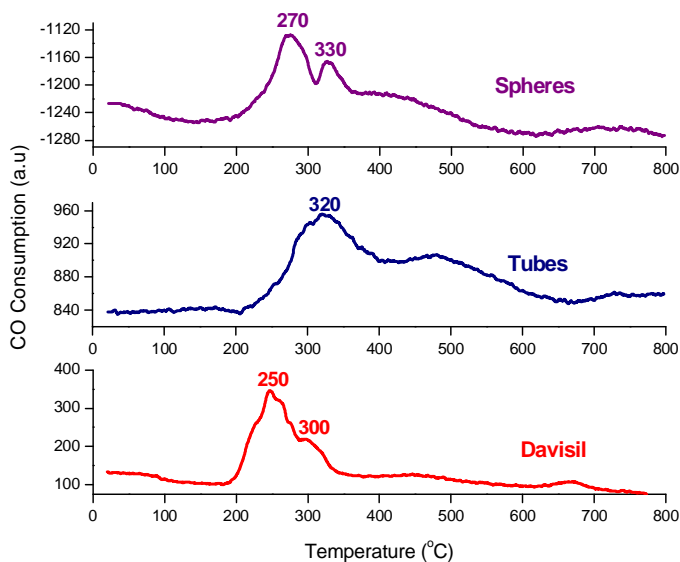


**Figure 7.21.** CO TPR profile of silica supported iron catalysts.

It was observed that iron reduction in the Davisil silica-supported catalyst occurred earlier than with the other catalysts. It was also observed that the second transformation, i.e. from Fe<sup>2+</sup> to  $\chi$ - and  $\varepsilon$ - carbides, in the profile of the templated sol-gel synthesised silica supported catalysts overlapped with the carbon deposition stage. This could mean that there were strong metal-support interactions in the templated sol-gel synthesised silica supported catalysts, as these interactions tend to form complexes which can be only be reduced at higher temperatures.

## 7.4. CONCLUSION

Templated sol-gel synthesised silica materials were employed as supports for a FT catalyst, and these proved to work successfully. Overall, the Davisil silica support still seemed to be a better support when compared to the templated sol-gel

synthesised silica supports, in terms of its efficiency to produce hydrocarbons, its lower methane selectivity and its higher selectivity towards long chain hydrocarbons.

Despite the rapid decline in activity of the silica spheres supported catalyst, intermediate results (i.e. activity and selectivity) were obtained from this catalyst when compared to the Davisil silica and silica tubes supported catalysts. This is not surprising as this catalyst showed intermediate porosity and surface area. This could imply that the porosity of the support outweighs its morphology in dictating the reducibility of the metal, and hence the catalyst activity and selectivity.

The rapid deactivation of the silica spheres supported catalyst was clearly not due to loss of metal in the reaction slurry or support disintegration. The deactivation could have been due to pore blocking, which could have been cleared during wax extraction, or even due to metal support interaction which may lead to formation of silicates, thereby reducing the amount of the active phase.

The templated sol-gel synthesised supports exhibited remarkable stability despite the mechanical force, created by the impeller blades used in the reaction. The structures remained undamaged after use in the reaction. However, careful control of the pore size of supports synthesised by the templated sol-gel method still remains a challenge.

## 7.5. REFERENCES

1. R.B. Anderson, *The Fischer-Tropsch Synthesis*, Academic Press, New York, 1984.
2. M.M.G. Senden, A.D. Punt, A. Hoek, *Stud. Surf. Sci. Catal.* 119 (1998) 961.
3. A.C. Vosloo, *Fuel. Proc. Technol.* 71 (2001) 149.
4. C. Knottenbelt, *Catal. Today* 71 (2002) 437.
5. H. Schulz, *Appl. Catal. A: Gen.* 186 (1999) 3.
6. M.E. Dry, in *Catalysis Science and Technology*, Chapt. 4, Vol 1, J.R. Anderson and M. Boudart (eds.), Springer-Verlag, New York, 1981, p 159.
7. (a) A.K. Datye, M.D. Shroff, Y. Jin, R.P. Brooks, J.A. Wilder, M.S. Harrington, A.G. Sault, N.B. Jackson, *Stud. Surf. Sci. Catal.* 101 (1996) 1421.  
(b) D.B. Bukur, X. Lang, D. Mukesh, W.H. Zimmerman, M.P. Rosynek and C. Li, *Ind. Eng. Chem. Res.*, 29 (1990) 1588.  
(c) C.H. Bartholomew, R.B. Pannel, J.L. Butler, *J. Catal.* 65 (1980) 335.  
(d) C.H. Bartholomew, R.B. Pannel, J.L. Butler, D.G. Mustard, *Ind. Eng. Chem. Prod. Res. Dev.* 20 (1981) 296.  
(e) G.B. Mc Vicker, M.A. Vannice, *J. Catal.* 63 (1980) 25.
8. (a) R.C. Reuel and C.H. Bartholomew, *J. Catal.* 85 (1984) 63.  
(b) S. Sun, N. Tsubaki, K. Fujimoto, *Appl. Catal. A: Gen.* 202 (2000) 121.  
(c) L.B. Backman, A. Rautanen, A.O.I. Krause, M. Lindblad, *Catal. Today* 43 (1998) 11.  
(d) S. Bessel, *Appl. Catal. A : Gen.* 96 (1993) 253.
9. R.J. O'Brien, L. Xu, S. Bao, A. Raje, B.H. Davis, *Appl. Catal. A : Gen.* 196 (2000) 173.
10. B. Jongsomijt, T. Wongsalee, P. Prasethdam, *Mater. Chem. Phys.* 97 (2006) 343.
11. C.T. Kresge, M.E. Leonowicz, W.J. Roth, J.C. Vartuli, J.S. Beck, *Nature* 359 (1992) 710.
12. S. Inagaki, Y. Fukushima, K. Kuroda, *J. Chem Soc, Chem. Commun.* (1993) 680.

13. E. Zhao, J. Feng, Q. Huo, N. Melosh, G.H. Fredrickson, B.F. Chmelka, G.D. Stucky, *Science* 279 (1998) 548.
14. H.H. Nijs, P.A. Jacobs, *J. Catal.* 65 (1980) 328.
15. D. Vanhove, Z. Zhuyong, P. Makambo, M. Blanchard, *Appl. Catal.* 9 (1984) 327.
16. J.A. Lapszewicz, H.J. Loeh, J.R. Chipperfield, *J. Chem. Soc., Chem. Commun.*, (1993) 913.
17. J.D. Wright, N.A.J.M. Sommerdijk, *Sol-gel Materials Chemistry and Applications*, Taylor and Francis, London, 2001.
18. L.L. Hench, J.K. West, *Chem. Rev.* 90 (1990) 33.
19. E.F. Vansant, P. Van Der Voort, K.C. Vrancken, in *Studies in Surface Science and Catalysis*, Vol. 93: Characterization and chemical modification of the silica surface, Chapt 1 and 3, Elsevier, Amsterdam, 1995.
20. J.C. Ro, I.J. Chung, *J. Non-Cryst. Solids* 130 (1991) 8.
21. A.M. Buckley, M. Greenbalt, *J. Non-Cryst. Solids* 143 (1992) 1.
22. J.Y. Ying, J.B. Benzinger, A. Navrotsky, *J. Am. Ceram. Soc.* 76 (1993) 2571.
23. B.C. Dunn, P. Cole, D. Covington, M.C. Webster, R.J. Pugmire, R.D. Ernst, E.M. Eyring, N. Shah, G.P. Huffman, *Appl. Catal. A : Gen.* 278 (2005) 233.
24. K.J.C. van Bommel, A. Friggeri and S. Shinkai, *Angew. Chem. Int. Ed.*, 42 (2003) 980.
25. F. Schuth, *Angew. Chem. Int. Ed.*, 42 (2003) 3604.
26. (a) H. Nakamura and Y. Matsui, *J. Am. Chem. Soc.*, 117 (1995) 2651.  
(b) F. Miyaji, S.A. Davis, J.P.H. Charmant and S. Mann, *Chem. Mater.*, 11 (1999) 3021.  
(c) F. Miyaji, Y. Watanabe and Y. Suyama, *Materials Research Bulletin*, 38 (2003) 1669.  
(d) E. M. Mokoena, A.K. Datye and N.J. Coville, *J. Sol-Gel Science Technology.*, 28 (2003) 307.
27. C. Hippe, M. Wark, E. Lork and G. Schulz-Ekloff, *Microporous and Mesoporous Materials.*, 31 (1999) 235.

28. (a) F. Rodriguez-Reinoso, Carbon 36 (1998) 159.  
(b) E. van Steen, F.F. Prinsloo, Catal.Today 71 (2002) 327.  
(c) M.C. Bahome, L.L. Jewell, D. Hildebrandt, D. Glasser, N.J. Coville, Appl. Catal. A : Gen. 287 (2005) 60.
29. G. L.Benzemer, A. van Laak, A.J. van Dillen, K.P. de Jong, Stud. Surf. Sc. Catal. 147 (2004) 259.
30. E. M. Mokoena, Synthesis and use of silica materials as supports for the Fischer-Tropsch reaction, PhD thesis, University of the Witwatersrand, 2005.
31. S. Naito, K. Minoshima, T. Miyao, Top. Catal. 39 (2006) 131.
32. (a) G. Bian, A. Oonuki, Y. Kobayashi, N. Koizumi, M. Yamada, Appl. Catal. A : Gen. 219 (2001) 13.  
(b) R.J. O' Brien, L. Xu, R. Spicer and B.H. Davis, Energy and Fuels, 10 (1996) 921.  
(c) M. Luo, B.H. Davis, Fuel Proc. Tech. 83 (2003) 49.  
(d) R.J. O'Brien, L. Xu, R. Spicer, S. Bao, D.R. Milburn, B.H. Davis, Catal. Today, 101 (1997) 1.  
(e) H.W. Pennline, M.F. Zarochak, J.M. Stencel, J.R. Diehl, Ind. Eng. Chem. Res., 26 (1987) 595.  
(f) D.B. Bukur, M. Koranne, X. Lang, K.R.P.M. Rao, G.P. Huffman, Appl. Catal. A: Gen., 126 (1995) 85.  
(g) D.B. Bukur, K. Okabe, M.P. Rosynek, C.P. Li, D.J. Wang, K.R.P.M. Rao, C.P. Huffman, J. Catal., 155 (1995) 353.  
(h) D.B. Bukur, X. Lang, J.A. Rossin, W.H. Zimmerman, M.P. Rosynek, E.B. Yeh, C. Li, Ind. Eng. Chem. Res., 28 (1989) 1130.  
(i) J.W. Niemantsverdriet, A.M. van der Kraan, J. Catal., 72 (1981) 385.

- 
33. K.S.W. Sing, D.H. Everett, R.A.W. Haul, L. Moscou, R.A. Pierotti, J. Rouquérol, T. Siemieniewska, *Pure & Appl. Chem.* 57 (1985) 603.
34. G. Leofanti, M. Padovan, G. Tozzola, B. Venturelli, *Catal. Today*, 41 (1998) 207.
35. R.K. Iler, *The Chemistry of Silica: Solubility, Polymerisation, Colloid and Surface Properties, and Biochemistry*, Wiley, New York, 1979.
36. (a) R.A. Dector and A. Bell, *J. Catal.* 97 (1986) 121.  
(b) G.B. Raup, W.N. Delgass, *J. Catal.* 58 (1979) 348.  
(c) J.A. Amelse, J.B. Butt, L.H. Schwartz, *J. Phys. Chem.* 82 (1978) 558.  
(d) L.J.E. Hofer, E.M. Cohn, W.C. Peebles, *J. Am. Chem. Soc.* 71 (1949) 189.  
(e) J.W. Niemantsverdriet, A.M. van der Kraan, W.L. van Dijk, H.S. van der Baan, *J. Phys. Chem.* 84 (1980) 3363.
37. M.D. Shroff, D.S. Kalakkad, K.E. Coulter, S.D. Köhler, M.S. Harrington, N.B. Jackson, A.G. Sault and A. Datye, *J. Catal.*, 156 (1995) 185.
38. J.F. Schultz, W.K. Hall, B. Seligman and R.B. Anderson, *J. Am. Chem. Soc.*, 77 (1955) 213.
39. V.U.S. Rao, G.J. Steigel, G.J. Cinquegrane and R.D. Srivastava, *Fuel Process. Technol.*, 30 (1992) 83.
40. B. Jagor and R. Espinoza, *Catal. Today*, 23 (1995) 17.
41. M.E. Dry and G.J. Oosthuizen, *J. Catal.*, 11 (1968) 18.
42. D. Song, J. Li, *J. Mol. Catal. A : Chem.* 247 (2006) 206.
43. A.Y. Khodakov, A.G. Constant, R. Bechara, V.L. Zholobenko, *J. Catal.*, 206 (2002) 239.
44. H.F. Xiong, Y.H. Zhang, S.G. Wang, J.L. Li, *Catal. Commun.*, 6 (2005) 512.
45. R.J. Madon, E. Iglesia, *J. Catal.* 139 (1993) 576).
46. G.A. Huff and C.N. Satterfield, *J. Catal.* 85 (1984) 370.
47. D.B. Bukur, D. Mukesh and S.A. Patel, *Ind. Eng. Chem. Res.* 29 (1990) 194.
48. M.E. Dry, in *Studies in Surface Science and Catalysis Vol 152: Fischer-Tropsch Technology*, Chapt 3 and 7, A. Steynberg and M. Dry, (eds.), Elsevier, New York, 2004.



49. M.E. Dry, G.M. Leuteritz, W.J. van Zyl, J. S. Afr. Chem. Inst. 16 (1963) 15.
50. M.D. Shroff, A.K. Datye, Catal. Lett., 37 (1996) 101.
51. B.H. Davis, *Technology Development for iron Fischer-Tropsch Catalysts*, Final Report, US DoE, Contract No. DE-AC22-94055—13, 1999, p129.
52. U.M. Graham, A. Dozier, R.A. Khatri, R. Srinivasan, B.H. Davis, (to be published).
53. M. Dry, Catal. Lett., 7 (1990) 241.
54. Y. Jin, A.K. Datye, J. Catal. 196 (2000) 8.

# **CHAPTER 8**

## **GENERAL CONCLUSION**

### **PART I**

Sol-gel processing offers a facile synthesis of silica gels and the use of organic templates together with the process, provides a cheaper alternative to other conventional methods for the synthesis of nanostructured silica gels. In this work nanostructured silica gels were synthesised by the sol-gel method using simple hydroxyacids as structure directing template precursors. The following synthesis variables were investigated:

- (i) type and amount of the hydroxyacid (acidic templated precursor),
- (ii) type and amount of base catalyst (basic template precursor),
- (iii) synthesis temperature,
- (iv) duration of hydrolysis and ageing,
- (v) solvent concentration (the water relative to co-solvent amount),
- (vi) the organic co-solvent, and
- (vii) the synthesis procedure.

The variation of synthesis conditions resulted in the production of materials with different properties and morphologies.

The use of different template precursors yielded materials with mixtures of morphologies; hollow tubes (and/or sheets), hollow spheres, together with solid spheres and amorphous material usually obtained in the absence of a structure directing template.

The morphology of the synthesised silica gels was found to be determined by the various shapes of the template crystals occurring in solution, the latter being largely determined by the type of the acidic and the basic template precursors (i.e. the hydroxyacid and base catalyst) employed. Studies with oxalic acid showed that at high template precursor concentrations, more needle-like template crystals occurred when compared to spherical templates, and this led to increased formation of tubes. Also, at high template concentrations, the needle-like template crystals formed were wider and/or longer, which resulted in formation of wider and/or longer tubes, while at low template concentration silica ions condensed to give alternate morphologies; i.e. amorphous materials and/or solid spheres.

Dissolution of the template occurred both at elevated temperatures ( $\geq 55$  °C) and at high water concentrations ( $> 50$  %). Template dissolution was evidenced by the reduction in the yield of shaped particles and either an increase in the amorphous material yield or the appearance of surface attached colloidal particles. It was also found that the amount of water in the solvent affected the yield, development and size of the shaped morphologies. The solvent concentration at which well-developed tubes with maximum tube yield and size (in the case of oxalic acid), and maximum yield of hollow spheres (in the case of D-gluconic acid) were formed was about 25-50 %. This showed that the maximum size and highest concentration of the template crystals occurred in 25-50 % water, and also that this concentration of the solvent was adequate for optimum hydrolysis and condensation of the silica sols.

The variation of the organic co-solvent affected the yield of the morphologies and the porosity of the resultant gels. However, no major change in the tubes sizes was observed. The result showed that the choice of the organic co-solvent did affect the rate of hydrolysis and/or condensation reactions, hence surface attached colloidal particles were observed only in the synthesis with methanol.

When ageing of the silica gels was done for too long (i.e. > 2 h), dissolution of the tubes and hollow spheres occurred as a result of the reaction of the metastable silica with the excess  $\text{OH}^-$  ions in solution. This reaction resulted in precipitation of the reacted silica ions on the surface of the tubes and the hollow spheres. Prolonged hydrolysis of the silica sols led to formation of tiny colloidal particles, which upon addition of the base catalyst, could not assemble themselves on the surface of the template, probably due to their small mass and size, but coated on the surface of the formed hollow spheres and tubes without becoming part of their framework. This then resulted in formation of thin walled hollow spheres and tubes.

Variation of the synthesis procedure greatly affected the morphology and the properties of the silica gels. Pre-formation of the template prior to addition of TEOS produced materials with much lower surface areas, higher tube yields and bigger tube sizes when compared with materials synthesised by forming the template together with the silica gel. Pre-formation of the template prior to addition of TEOS resulted in formation of high amounts of wider and longer needle-like templates as the interaction of the acidic and basic precursors to form the template crystals was unhindered by the presence of the silica precursor. Hence this procedure gave high tube yields and size. However, the ‘short method’ did not allow ‘enough’ time for TEOS hydrolysis, thereby forming materials with broad pore size distributions, low pore volumes and surface areas.

The study showed that although synthesis of exclusively one type of morphology is a challenge, enhancement of the yield of desired morphologies can be done by manipulation of the synthesis conditions.

The following studies can be suggested for the future:

- i) isolation of the different morphologies,
- ii) control of template crystallite size so as to be able to synthesise nanostructured materials with controlled and desirable size,

- ii) control of porosity of the silica gels, e.g. by using a combination of templates (a carboxylic acid as a structure-directing template and a template to impart porosity in the gel such as hexadecyltrimethylammonium chloride) to synthesise nanostructured materials with controlled and desirable porosity,
- iii) investigations on the mechanism of formation of the nanostructures, and
- iv) tailoring the chemical composition of the nanostructured materials by functionalisation, for potential applications. For example, introduction of inorganic molecules such as Al and Ti into the SiO<sub>2</sub> framework, attachment of organometallic complexes on the surface of the nanostructures, or synthesis of inorganic-organic networks by co-condensation of siloxane and organosiloxane precursors.

## PART II

The effect of varying the potassium promotion levels and of the support morphology on the catalyst activity and selectivity in the FT reaction was studied. The study showed that for both the Davisil silica and the silica tubes catalysts, the optimum promotion level was 0.5 % K. Inferior catalyst activity was observed when the potassium promotion was increased beyond this level. In the catalysts containing high potassium loading, i.e. 0.9 %, the active catalyst sites could have been possibly covered by the large amount of the alkali, and/or carbon deposition was enhanced, leading to lower catalyst activity. An increase in potassium loading in both the catalyst systems resulted in increased selectivity towards olefins, 1-olefins and to high molecular weight hydrocarbons.

Nanostructured silica supported catalysts exhibited higher activity and lower efficiency for formation of hydrocarbons when compared with the Davisil silica supported catalyst. It is suggested that the difference observed lies in the fact that the different morphologies and porosities of the supports affected the size, shape and

orientation of the metal crystallites. This in turn affected the reducibility of the metal and the metal-support interaction.

The study showed that nanostructured silica gels have a potential for application as a support for FT catalysts as they remained strong and stable throughout the reaction, despite the large mechanical force and harsh conditions encountered. Although the Davisil silica supported catalyst exhibited superior efficiency to produce hydrocarbons when compared to the nanostructured silica supported catalysts, direct comparison of the activities of these catalysts should be avoided as the reaction conditions used in this study were not optimised for all the three catalysts.

For a conclusion to be made about the effect of the morphology of the support on the activity and selectivity of the catalysts, the following studies should be done:

- i) metal dispersion and extent of metal reduction of the catalysts should be analysed,
- ii) the phase of the active metal should be monitored during the reaction, possibly by a technique such as (*in situ*) Mössbauer spectroscopy,
- iii) supports with different ranges of compositions of structured morphologies should be tested, and lastly
- iv) for a direct comparison of the supports to be done, the catalysts should be tested at the conditions giving optimum performance of the catalysts.